

DISSERTATION ZUR ERLANGUNG DES DOKTORGRADES  
DER FAKULTÄT FÜR CHEMIE UND PHARMAZIE  
DER LUDWIG-MAXIMILIANS-UNIVERSITÄT MÜNCHEN

Synthesis, Characterization,  
Quantum-Chemical Analysis  
and Linkage Isomerism of  
Nitritoferrates(III) and Related Metallates(III)

Jan Heinemann

aus

Neuburg a. d. Donau, Germany

2021

## **Erklärung**

Diese Dissertation wurde im Sinne von § 7 der Promotionsordnung vom 28. November 2011 von Herrn Prof. Dr. Peter Klüfers betreut.

## **Eidesstattliche Versicherung**

Diese Dissertation wurde eigenständig und ohne unerlaubte Hilfe erarbeitet.

München, den 05.10.2021

---

Jan Heinemann

Dissertation eingereicht am 07.10.2021

1. Gutachter: Prof. Dr. Peter Klüfers
2. Gutachter: Prof. Dr. Hans-Christian Böttcher

Mündliche Prüfung am 24.11.2021

“We all change, when you think about it, we’re all different people; all through our lives, and that’s okay, that’s good, you gotta keep moving, so long as you remember all the people that you used to be. I will not forget one line of this, not one day, I swear. I will always remember when The Doctor was me.”

- 11<sup>th</sup> Doctor, Doctor Who

# Contents

<b>1</b>	<b>Introduction</b>	<b>1</b>
1.1	Nitrite: usage, properties and biology . . . . .	1
1.2	Binding behavior and complexes of nitrite . . . . .	3
1.3	Photoinduced linkage isomerism . . . . .	5
1.4	Aim of this work . . . . .	8
<b>2</b>	<b>Results</b>	<b>9</b>
2.1	Synthesis of the ligands . . . . .	9
2.1.1	Synthesis of the bisphosphane oxides . . . . .	9
2.1.2	Synthesis of H <sub>2</sub> Bn <sub>2</sub> edda . . . . .	9
2.1.3	Synthesis of H <sub>2</sub> <i>t</i> Bu <sub>2</sub> salen and H <sub>2</sub> <i>t</i> Bu <sub>4</sub> salen . . . . .	9
2.1.4	Synthesis of Hbpmea . . . . .	9
2.1.5	Synthesis of tpya . . . . .	9
2.1.6	Synthesis of Ag <sup>15</sup> NO <sub>2</sub> . . . . .	10
2.2	Synthesis of the precursor compounds . . . . .	11
2.2.1	Synthesis of (HNEt <sub>3</sub> ) <sub>2</sub> [FeCl(fpin) <sub>2</sub> ] ( <b>P1</b> ) . . . . .	11
2.2.2	Synthesis of [FeCl <sub>2</sub> L <sub>2</sub> ](ClO <sub>4</sub> ) (L = dppe(O) <sub>2</sub> , dppp(O) <sub>2</sub> , dppf(O) <sub>2</sub> ) ( <b>P2-4</b> ) . . . . .	12
2.2.3	Synthesis of the aminocarboxylate precursor compounds ( <b>P5-8</b> ) . . . . .	12
2.2.4	Synthesis of [Fe <sub>2</sub> Cl <sub>2</sub> (Hbpmea) <sub>2</sub> (μ-O)]Cl <sub>2</sub> · 2MeCN ( <b>P9</b> · 2MeCN) . . . . .	15
2.2.5	Synthesis of the salen precursor compounds ( <b>P10-P12</b> ) . . . . .	17
2.2.6	Synthesis of [Fe(bipzpy)X <sub>3</sub> ] (X = Cl, Br) ( <b>P13</b> and <b>P14</b> ) . . . . .	17
2.2.7	Synthesis of [FeCl <sub>3</sub> (Me <sub>3</sub> tacn)] ( <b>P15</b> ) . . . . .	18
2.2.8	Synthesis of [FeCl <sub>2</sub> (tpya)](ClO <sub>4</sub> ) ( <b>P16</b> ) . . . . .	19
2.3	Nitrito compounds with O-Donor co-ligands . . . . .	20
2.3.1	Synthesis of nitrito complexes with perfluoropinacolate ( <b>1a-M</b> (M = Al, Sc, Cr, Fe, Ga, In, Tl, Bi) and <b>1b</b> ) . . . . .	20
2.3.2	Synthesis of nitritoiron complexes with bisphosphane oxides ( <b>2-4</b> ) . . . . .	30
2.4	Nitrito compounds with N,O-Donor co-ligands . . . . .	34
2.4.1	Synthesis of nitritoiron complexes with aminocarboxylato ligands ( <b>5-8</b> ) . . . . .	34
2.4.2	Synthesis of [Fe <sub>4</sub> (μ-bpmea) <sub>2</sub> ( <i>Z</i> -NO <sub>2</sub> -κO) <sub>2</sub> ( <i>E</i> -NO <sub>2</sub> -κO) <sub>4</sub> (μ <sub>3</sub> -O) <sub>2</sub> ] · 2MeCN ( <b>9</b> · 2MeCN) . . . . .	38
2.4.3	Synthesis of nitritoiron complexes with salen and its derivatives ( <b>10-12</b> ) . . . . .	41
2.5	Nitrito compounds with N-Donor co-ligands . . . . .	45
2.5.1	Synthesis of [Fe(bipzpy)X <sub>2</sub> (NO <sub>2</sub> -κ <sup>2</sup> O, O')] · MeCN (X = Cl, Br) ( <b>13</b> · MeCN and <b>14</b> · MeCN) . . . . .	45
2.5.2	Synthesis of nitrito complexes with Me <sub>3</sub> tacn ( <b>15a</b> · 0.5DCM and <b>15b</b> · 2DCM) . . . . .	46
2.5.3	Synthesis of [Fe <sub>2</sub> (NO <sub>2</sub> -κO) <sub>2</sub> (tpya) <sub>2</sub> (μ-O)](ClO <sub>4</sub> ) <sub>2</sub> · 2C <sub>3</sub> H <sub>6</sub> O ( <b>16a</b> · 2C <sub>3</sub> H <sub>6</sub> O) and [(NO <sub>2</sub> -κO)(tpya)Fe(μ-O)Fe(NO <sub>2</sub> -κ <sup>2</sup> O, O')](tpya)](ClO <sub>4</sub> ) <sub>2</sub> · 3C <sub>3</sub> H <sub>6</sub> O ( <b>16b</b> · 3C <sub>3</sub> H <sub>6</sub> O) . . . . .	50
2.5.4	Synthesis of [Fe <sub>2</sub> Cl <sub>2</sub> (NO <sub>2</sub> -κ <sup>2</sup> O, O') <sub>2</sub> (py) <sub>4</sub> (μ-O)] · py ( <b>17</b> · py) . . . . .	53

2.6	Computer-chemical calculations . . . . .	55
2.6.1	Validation of the computer-chemical results <i>via</i> structural optimization . . . . .	55
2.6.2	Spin density distribution in <b>1a-Fe</b> and <b>1a-Cr</b> . . . . .	58
2.6.3	Quantum-chemical scan calculations . . . . .	60
2.7	Photoinduced linkage isomerism experiments . . . . .	69
2.7.1	Photoirradiation on <b>1a-Fe</b> . . . . .	69
2.7.2	Photoirradiation on <b>2</b> · MeCN . . . . .	70
2.7.3	Photoirradiation on <b>7</b> . . . . .	72
2.7.4	Photoirradiation on <b>15b</b> . . . . .	73
2.7.5	Photoirradiation on <b>6</b> and <b>8</b> . . . . .	75
<b>3</b>	<b>Discussion</b> . . . . .	<b>76</b>
3.1	Tactics for the successful synthesis of novel nitritoiron complexes . . . . .	76
3.1.1	Selection of solvents, ligands and oxidation state of the central metal . . . . .	76
3.1.2	Synthesis method of choice . . . . .	78
3.2	Synthesis of the precursor compounds . . . . .	79
3.2.1	Halogenidoiron(III) complexes known to literature . . . . .	79
3.2.2	Novel halogenidoiron(III) complexes . . . . .	80
3.3	Synthesis and characterization of novel nitrito complexes . . . . .	81
3.3.1	Nitrito complexes with perfluoropinacol as co-ligand . . . . .	81
3.3.2	Nitritoiron complexes with bisphosphane oxides as co-ligand . . . . .	82
3.3.3	Nitritoiron complexes with aminocarboxylato co-ligands . . . . .	82
3.3.4	$[\text{Fe}_4(\mu\text{-bpmea})_2(\text{Z-NO}_2\text{-}\kappa\text{O})_2(\text{E-NO}_2\text{-}\kappa\text{O})_4(\mu_3\text{-O})_2] \cdot 2\text{MeCN}$ ( <b>9</b> · 2MeCN) . . . . .	83
3.3.5	Nitritoiron complexes with salen and its derivatives . . . . .	83
3.3.6	Nitritoiron complexes with bipzpy . . . . .	85
3.4	Nitritoiron complexes containing oxido bridges . . . . .	85
3.5	Observed binding modes and absence of nitrito- $\kappa\text{N}$ in the case of the nitritoiron(III) complexes . . . . .	88
3.6	Binding modes in $(\text{HNEt}_3)_2[\text{M}^{\text{III}}(\text{fpin})_2(\text{NO}_2)]$ ( <b>1a-M</b> with M = Al, Sc, Cr, Fe, Ga, In, Tl, Bi) . . . . .	89
3.7	Quantum-chemical calculations . . . . .	91
3.7.1	Structure optimization . . . . .	91
3.7.2	Scan calculations I: general statements and methodology . . . . .	92
3.7.3	Scan calculations II: scan graphs of the <b>1a-M</b> (M = Al, Sc, Cr, Fe, Ga, In, Tl) series . . . . .	94
3.7.4	Scan calculations III: scan graphs of nitritoiron complexes . . . . .	95
3.8	Photoinduced linkage isomerism of selected compounds . . . . .	97
3.8.1	Requirements for the tested substances and PLI of nitritoiron complexes . . . . .	97
3.8.2	PLI of <b>1a-Fe</b> . . . . .	97
3.8.3	PLI of <b>2</b> · MeCN . . . . .	99
3.8.4	PLI of <b>7</b> . . . . .	99
3.8.5	PLI of <b>15b</b> . . . . .	100
3.8.6	PLI of <b>6</b> and <b>8</b> . . . . .	101
<b>4</b>	<b>Summary and outlook</b> . . . . .	<b>102</b>

<b>5</b>	<b>Experimental part</b>	<b>107</b>
5.1	Common working techniques . . . . .	107
5.2	Analytical methods . . . . .	107
5.2.1	Elemental analysis . . . . .	108
5.2.2	IR spectroscopy . . . . .	108
5.2.3	NMR spectroscopy . . . . .	108
5.2.4	UV-Vis spectroscopy . . . . .	108
5.2.5	Single-crystal X-ray diffraction . . . . .	108
5.2.6	PLI experiments . . . . .	109
5.2.7	Quantum-chemical calculations . . . . .	109
5.3	Reagents and solvents . . . . .	110
5.4	Synthesis of the ligands . . . . .	112
5.4.1	Phosphane oxides . . . . .	112
5.4.2	H <sub>2</sub> Bn <sub>2</sub> edda . . . . .	115
5.4.3	H <sub>2</sub> <i>t</i> Bu <sub>2</sub> salen . . . . .	117
5.4.4	H <sub>2</sub> <i>t</i> Bu <sub>4</sub> salen . . . . .	118
5.4.5	Hbpmea . . . . .	119
5.4.6	tpya . . . . .	120
5.4.7	Ag <sup>15</sup> NO <sub>2</sub> . . . . .	122
5.5	Synthesis of the halogenidoiron(III) precursor compounds . . . . .	123
5.5.1	(HNEt <sub>3</sub> ) <sub>2</sub> [FeCl(fpin) <sub>2</sub> ] ( <b>P1</b> ) . . . . .	123
5.5.2	[FeCl <sub>2</sub> (dppe(O) <sub>2</sub> ) <sub>2</sub> ](ClO <sub>4</sub> ) ( <b>P2</b> ) . . . . .	124
5.5.3	[FeCl <sub>2</sub> (dppp(O) <sub>2</sub> ) <sub>2</sub> ](ClO <sub>4</sub> ) ( <b>P3</b> ) . . . . .	125
5.5.4	[FeCl <sub>2</sub> (dppf(O) <sub>2</sub> ) <sub>2</sub> ](ClO <sub>4</sub> ) ( <b>P4</b> ) . . . . .	126
5.5.5	(NBnMe <sub>3</sub> )[FeCl <sub>2</sub> (qu) <sub>2</sub> ] ( <b>P5</b> ) . . . . .	127
5.5.6	(NEt <sub>4</sub> )[Fe(Bn <sub>2</sub> edda)Cl <sub>2</sub> ] ( <b>P6</b> ) . . . . .	128
5.5.7	(NEt <sub>4</sub> ) <sub>2</sub> [Fe <sub>2</sub> Cl <sub>2</sub> (μ-heida) <sub>2</sub> ] · 2MeCN ( <b>P7</b> · 2MeCN) . . . . .	129
5.5.8	(NBnMe <sub>3</sub> ) <sub>2</sub> [FeCl <sub>2</sub> (nta)] ( <b>P8</b> ) . . . . .	130
5.5.9	[Fe <sub>2</sub> Cl <sub>2</sub> (Hbpmea) <sub>2</sub> (μ-O)]Cl <sub>2</sub> · 2MeCN ( <b>P9</b> · 2MeCN) . . . . .	131
5.5.10	[FeCl(salen)] ( <b>P10</b> ) . . . . .	132
5.5.11	[FeCl( <i>t</i> Bu <sub>2</sub> salen)] ( <b>P11</b> ) . . . . .	133
5.5.12	[FeCl( <i>t</i> Bu <sub>4</sub> salen)] ( <b>P12</b> ) . . . . .	134
5.5.13	[Fe(bipzpy)Cl <sub>3</sub> ] ( <b>P13</b> ) . . . . .	135
5.5.14	[Fe(bipzpy)Br <sub>3</sub> ] ( <b>P14</b> ) . . . . .	136
5.5.15	[FeCl <sub>3</sub> (Me <sub>3</sub> tacn)] ( <b>P15</b> ) . . . . .	137
5.5.16	[FeCl <sub>2</sub> (tpya)](ClO <sub>4</sub> ) ( <b>P16</b> ) . . . . .	138
5.6	Synthesis of nitrito complexes with O-donor co-ligands . . . . .	139
5.6.1	(HNEt <sub>3</sub> ) <sub>2</sub> [M(fpin) <sub>2</sub> (NO <sub>2</sub> )] (M = Al, Sc, Cr, Fe, Ga, In, Tl, Bi) ( <b>1a-M</b> ) . . . . .	139
5.6.2	(PPN) <sub>2</sub> [Fe <sub>2</sub> (fpin) <sub>2</sub> (NO <sub>2</sub> -κ <sup>2</sup> O, O') <sub>2</sub> (μ-OCH <sub>3</sub> ) <sub>2</sub> ] ( <b>1b</b> ) . . . . .	143
5.6.3	[Fe(dppe(O) <sub>2</sub> ) <sub>2</sub> (NO <sub>2</sub> -κO) <sub>2</sub> ](ClO <sub>4</sub> ) · MeCN ( <b>2</b> · MeCN) . . . . .	144
5.6.4	[Fe(dppp(O) <sub>2</sub> ) <sub>2</sub> (NO <sub>2</sub> -κO) <sub>2</sub> ](ClO <sub>4</sub> ) · 2MeCN ( <b>3</b> · 2MeCN) . . . . .	145
5.6.5	[Fe(dppf(O) <sub>2</sub> ) <sub>2</sub> (NO <sub>2</sub> -κO) <sub>2</sub> ](ClO <sub>4</sub> ) · 3MeCN ( <b>4</b> · 3MeCN) . . . . .	146
5.7	Synthesis of nitrito complexes with N,O-donor co-ligands . . . . .	147
5.7.1	(NBnMe <sub>3</sub> )[Fe(NO <sub>2</sub> -κO) <sub>2</sub> (qu) <sub>2</sub> ] · 2MeCN ( <b>5</b> · 2MeCN) . . . . .	147
5.7.2	(NEt <sub>4</sub> )[Fe(Bn <sub>2</sub> edda)(NO <sub>2</sub> -κO) <sub>2</sub> ] ( <b>6</b> ) . . . . .	148
5.7.3	(NEt <sub>4</sub> ) <sub>2</sub> [Fe <sub>2</sub> (μ-heida) <sub>2</sub> (NO <sub>2</sub> -κO) <sub>2</sub> ] ( <b>7</b> ) . . . . .	149
5.7.4	(NBnMe <sub>3</sub> ) <sub>2</sub> [Fe(NO <sub>2</sub> -κ <sup>2</sup> O, O')(NO <sub>2</sub> -κO)(nta)] ( <b>8</b> ) . . . . .	150

Table of Contents

---

5.7.5	[Fe <sub>4</sub> (μ-bpmea) <sub>2</sub> (NO <sub>2</sub> -κ <sup>2</sup> O, O') <sub>2</sub> (NO <sub>2</sub> -κO) <sub>4</sub> (μ <sub>3</sub> -O) <sub>2</sub> ] · 2MeCN ( <b>9</b> · 2MeCN) . . . . .	151
5.7.6	{[Fe(NO <sub>2</sub> -κO)(salen)] <sub>2</sub> } · 2MeCN ( <b>10</b> · 2MeCN) . . . . .	152
5.7.7	[Fe(NO <sub>2</sub> -κ <sup>2</sup> O, O')(tBu <sub>2</sub> salen)] ( <b>11</b> ) . . . . .	153
5.7.8	[Fe(NO <sub>2</sub> -κ <sup>2</sup> O, O')(tBu <sub>4</sub> salen)] ( <b>12</b> ) . . . . .	154
5.8	Synthesis of nitrito complexes with N-donor co-ligands . . . . .	155
5.8.1	[Fe(bipzpy)Cl <sub>2</sub> (NO <sub>2</sub> -κ <sup>2</sup> O, O')] · MeCN ( <b>13</b> · MeCN) . . . . .	155
5.8.2	[Fe(bipzpy)Br <sub>2</sub> (NO <sub>2</sub> -κ <sup>2</sup> O, O')] · MeCN ( <b>14</b> · MeCN) . . . . .	156
5.8.3	[Fe(Me <sub>3</sub> tacn)(NO)(NO <sub>2</sub> -κO) <sub>2</sub> ](NO <sub>3</sub> ) · 0.5DCM ( <b>15a</b> · 0.5DCM) . . . . .	157
5.8.4	[Fe <sub>2</sub> (Me <sub>3</sub> tacn) <sub>2</sub> (NO <sub>2</sub> -κO) <sub>4</sub> (μ-O)] ( <b>15b</b> ) . . . . .	158
5.8.5	[Fe <sub>2</sub> (NO <sub>2</sub> -κO) <sub>2</sub> (tpya) <sub>2</sub> (μ-O)](ClO <sub>4</sub> ) <sub>2</sub> · 2C <sub>3</sub> H <sub>6</sub> O ( <b>16a</b> · 2C <sub>3</sub> H <sub>6</sub> O) and [(NO <sub>2</sub> -κO)(tpya)Fe(μ-O)Fe(NO <sub>2</sub> -κ <sup>2</sup> O, O')(tpya)](ClO <sub>4</sub> ) <sub>2</sub> · 3C <sub>3</sub> H <sub>6</sub> O ( <b>16b</b> · 3C <sub>3</sub> H <sub>6</sub> O) . . . . .	159
5.8.6	[Fe <sub>2</sub> Cl <sub>2</sub> (NO <sub>2</sub> -κ <sup>2</sup> O, O') <sub>2</sub> (py) <sub>4</sub> (μ-O)] · py ( <b>17</b> · py) . . . . .	160
<b>6</b>	<b>Appendix</b> . . . . .	<b>161</b>
6.1	Packing diagrams of the crystal structures . . . . .	161
6.2	Crystallographic tables . . . . .	192
<b>7</b>	<b>Bibliography</b> . . . . .	<b>205</b>

## List of Figures

1.1	Denitrification pathway from nitrate to elemental nitrogen in the natural nitrogen cycle. . . . .	2
1.2	The different non-bridging and bridging binding modes of nitrito ligands. . . . .	4
1.3	Number of crystallized nitrito Complexes. . . . .	5
1.4	Visualization of the photoinduced linkage isomerism of SNP. . . . .	6
1.5	Visualization of the first PLI with a conversion rate of 100 %. . . . .	6
1.6	Visualization of the energy hypersurfaces of the excited state and the ground state for a $ML_5(NO)$ substance with two different MS. . . . .	7
2.7	Ortep plot of $(HNEt_3)_2[FeCl(fpin)_2]$ in crystals of <b>P1</b> . . . . .	11
2.8	Ortep plot of $(NBnMe_3)[FeCl_2(qu)_2]$ in crystals of <b>P5</b> . . . . .	13
2.9	Ortep plot of $(NEt_4)[Fe(Bn_2edda)Cl_2]$ in crystals of <b>P6</b> . . . . .	14
2.10	Ortep plot of $(NEt_4)_2[Fe_2Cl_2(\mu\text{-heida})_2] \cdot 2MeCN$ in crystals of <b>P7</b> $\cdot 2MeCN$ . . . . .	15
2.11	Ortep plot of $[Fe_2Cl_2(Hbpmea)_2(\mu\text{-O})]Cl_2 \cdot 2MeCN$ in crystals of <b>P9</b> $\cdot 2MeCN$ . . . . .	16
2.12	Ortep plot of $[Fe(bipzpy)Cl_3]$ in crystals of <b>P13</b> . . . . .	18
2.13	Ortep plot of $[Fe(bipzpy)Br_3]$ in crystals of <b>P14</b> . . . . .	18
2.14	Ortep plot of $[FeCl_2(tpya)](ClO_4)$ in crystals of <b>P16</b> . . . . .	19
2.15	Ortep plot of $(HNEt_3)_2[Fe(fpin)_2(NO_2\text{-}\kappa^2O, O')]$ in crystals of <b>1a-Fe</b> . . . . .	22
2.16	Ortep plot of $(HNEt_3)_2[Cr(fpin)_2(NO_2\text{-}\kappa O)]$ in crystals of <b>1a-Cr</b> . . . . .	23
2.17	Ortep plot of $(HNEt_3)_2[Cr(fpin)_2(NO_2\text{-}\kappa^2O, O')]$ in crystals of <b>1a-Cr</b> . . . . .	24
2.18	Ortep plot of $(HNEt_3)_2[Al(fpin)_2(NO_2\text{-}\kappa O)]$ in crystals of <b>1a-Al</b> . . . . .	25
2.19	Ortep plot of $(HNEt_3)_2[Tl(fpin)_2(NO_2\text{-}\kappa^2O, O')]$ in crystals of <b>1a-Tl</b> . . . . .	26
2.20	Ortep plot of $(HNEt_3)_2[Bi(fpin)_2(NO_2\text{-}\kappa O)]$ in crystals of <b>1a-Bi</b> . . . . .	27
2.21	Ortep plot of $(PPN)_2[Fe_2(fpin)_2(NO_2\text{-}\kappa^2O, O')(\mu\text{-OMe})_2]$ in crystals of <b>1b</b> . . . . .	29
2.22	CShM calculations of the hexacoordinated $(HNEt_3)_2[M^{III}(fpin)_2(NO_2)]$ substances. . . . .	30
2.23	Ortep plot of $[Fe(dppe(O)_2)_2(NO_2\text{-}\kappa O)_2](ClO_4) \cdot MeCN$ in crystals of <b>2</b> $\cdot MeCN$ . . . . .	32
2.24	Ortep plot of $[Fe(dppp(O)_2)_2(NO_2\text{-}\kappa O)_2](ClO_4) \cdot 2MeCN$ in crystals of <b>3</b> $\cdot 2MeCN$ . . . . .	32
2.25	Ortep plot of $[Fe(dppf(O)_2)_2(NO_2\text{-}\kappa O)_2](ClO_4) \cdot 3MeCN$ in crystals of <b>4</b> $\cdot 3MeCN$ . . . . .	33
2.26	Ortep plot of $(NBnMe_3)[Fe(NO_2\text{-}\kappa O)_2(qu)_2] \cdot 2MeCN$ in crystals of <b>5</b> $\cdot 2MeCN$ . . . . .	35
2.27	Ortep plot of $(NEt_4)[Fe(Bn_2edda)(NO_2\text{-}\kappa O)_2]$ in crystals of <b>6</b> . . . . .	36
2.28	Ortep plot of $(NEt_4)_2[Fe_2(\mu\text{-heida})_2(NO_2\text{-}\kappa O)_2]$ in crystals of <b>7</b> . . . . .	37
2.29	Ortep plot of $(NBnMe_3)_2[Fe(NO_2\text{-}\kappa^2O, O')(NO_2\text{-}\kappa O)(nta)]$ in crystals of <b>8</b> . . . . .	38
2.30	Ortep plot of $[Fe_4(\mu\text{-bpmea})_2(Z\text{-}NO_2\text{-}\kappa O)_2(E\text{-}NO_2\text{-}\kappa O)_4(\mu_3\text{-}O)_2] \cdot 2MeCN$ in crystals of <b>9</b> $\cdot 2MeCN$ . . . . .	40
2.31	Ortep plot of the $Fe_4O_4$ core in crystals of <b>9</b> $\cdot 2MeCN$ . . . . .	41
2.32	Ortep plot of $[Fe(NO_2\text{-}\kappa O)(salen)]_2 \cdot 2MeCN$ in crystals of <b>10</b> $\cdot 2MeCN$ . . . . .	43
2.33	Ortep plot of $[Fe(NO_2\text{-}\kappa^2O, O')(tBu_2salen)]$ in crystals of <b>11</b> . . . . .	43
2.34	Ortep plot of $[Fe(NO_2\text{-}\kappa^2O, O')(tBu_4salen)]$ in crystals of <b>12</b> . . . . .	44
2.35	Ortep plot of $[Fe(bipzpy)Cl_2(NO_2\text{-}\kappa^2O, O')] \cdot MeCN$ in crystals of <b>13</b> $\cdot MeCN$ . . . . .	46
2.36	Ortep plot of $[Fe(bipzpy)Br_2(NO_2\text{-}\kappa^2O, O')] \cdot MeCN$ in crystals of <b>14</b> $\cdot MeCN$ . . . . .	46
2.37	Time-resolved <i>in-situ</i> IR spectrum of the reaction of <b>P15</b> with silver nitrite. . . . .	48

List of Figures

---

2.38	Evolution of nitrous oxide during the reaction of <b>P15</b> with silver nitrite. . .	48
2.39	Ortep plot of $[\text{Fe}(\text{Me}_3\text{tacn})(\text{NO})(\text{NO}_2\text{-}\kappa\text{O})_2](\text{NO}_3) \cdot 0.5\text{DCM}$ in crystals of <b>15a</b> $\cdot 0.5\text{MeCN}$ . . . . .	49
2.40	Ortep plot of $[\text{Fe}_2(\text{Me}_3\text{tacn})_2(\text{NO}_2\text{-}\kappa\text{O})_4(\mu\text{-O})] \cdot 2\text{DCM}$ in crystals of <b>15b</b> $\cdot 2\text{DCM}$ . . . . .	50
2.41	Ortep plot of $[\text{Fe}_2(\text{NO}_2\text{-}\kappa\text{O})_2(\text{tpya})_2(\mu\text{-O})](\text{ClO}_4)_2 \cdot 2\text{C}_3\text{H}_6\text{O}$ in crystals of <b>16a</b> $\cdot 2\text{C}_3\text{H}_6\text{O}$ . . . . .	52
2.42	Ortep plot of $[(\text{NO}_2\text{-}\kappa\text{O})(\text{tpya})\text{Fe}(\mu\text{-O})\text{Fe}(\text{NO}_2\text{-}\kappa^2\text{O}, \text{O}')(\text{tpya})](\text{ClO}_4)_2 \cdot 3\text{C}_3\text{H}_6\text{O}$ in crystals of <b>16b</b> $\cdot 3\text{C}_3\text{H}_6\text{O}$ . . . . .	53
2.43	Ortep plot of $[\text{Fe}_2\text{Cl}_2(\text{NO}_2\text{-}\kappa^2\text{O}, \text{O}')_2(\text{py})_4(\mu\text{-O})] \cdot \text{py}$ in crystals of <b>17</b> $\cdot \text{py}$ . . . . .	54
2.44	Spin population in <b>1a-Fe</b> . . . . .	59
2.45	Spin population in <b>1a-Cr-}\kappa\text{O}</b> . . . . .	60
2.46	Spin population in in <b>1a-Cr-}\kappa^2\text{O}, \text{O}'</b> . . . . .	60
2.47	Scan graph of the anion in <b>1a-Fe</b> . . . . .	61
2.48	Scan graph of the anion in <b>1a-Sc</b> . . . . .	61
2.49	Scan graph of the anion in <b>1a-Cr</b> . . . . .	62
2.50	Scan graph of the anion in <b>1a-Al</b> . . . . .	64
2.51	Scan graph of the anion in <b>1a-Ga</b> . . . . .	64
2.52	Scan graph of the anion in <b>1a-In</b> . . . . .	64
2.53	Scan graph of the anion in <b>1a-Tl</b> . . . . .	64
2.54	Two possible arrangements of the nitrito ligand in the compounds <b>7</b> and <b>11</b> . . . . .	65
2.55	Scan graph of the anion in <b>7</b> . . . . .	66
2.56	Scan graph of <b>11</b> . . . . .	66
2.57	Scan graph of <b>12</b> . . . . .	67
2.58	Scan graph of <b>13</b> . . . . .	68
2.59	Scan graph of <b>14</b> . . . . .	68
2.60	Difference spectrum of the photoirradiation experiment of <b>1a-Fe</b> . . . . .	70
2.61	Difference spectra of the photoirradiation experiment of <b>2</b> $\cdot \text{MeCN}$ . . . . .	71
2.62	Depopulation of the MS state of <b>2</b> $\cdot \text{MeCN}$ . . . . .	71
2.63	Evolution and shift of the nitrosyl-related vibrational band in <b>2</b> $\cdot \text{MeCN}$ . . . . .	71
2.64	Difference spectra of the photoirradiation experiment of <b>7</b> . . . . .	72
2.65	Comparison of the IR spectra of <b>7</b> before and after the irradiation experiment. . . . .	72
2.66	IR spectra of the irradiated of <b>7</b> while increasing the temperature. . . . .	73
2.67	Difference spectra of the photoirradiation experiment of <b>15b</b> . . . . .	74
2.68	Depopulation of the MS state of <b>15b</b> . . . . .	74
2.69	IR spectra of the irradiated compound <b>15b</b> while increasing the temperature. . . . .	74
2.70	Rising $\text{N}_2\text{O}$ and $\text{CO}_2$ -related IR band in the photoirradiation experiment of <b>6</b> . . . . .	75
2.71	Rising $\text{CO}_2$ -related IR band in the photoirradiation experiment of <b>8</b> . . . . .	75
3.72	Visualization of the stereochemically active valence-shell lone pair in <b>1a-Bi</b> . . . . .	91
4.73	$[\text{Fe}_2(\mu\text{-heida})_2(\text{NO}_2\text{-}\kappa\text{O})_2]^{2-}$ , the anion of <b>7</b> , as first example for an fully reversible, PLI active nitritoiron complex with a conversion rate of nearly 100%. . . . .	103
6.74	Packaging diagram of <b>P1</b> . . . . .	161
6.75	Packaging diagram of <b>P5</b> . . . . .	162
6.76	Packaging diagram of <b>P6</b> . . . . .	163
6.77	Packaging diagram of <b>P7</b> $\cdot 2\text{MeCN}$ . . . . .	164

---

6.78	Packaging diagram of <b>P9</b> · 2MeCN. . . . .	165
6.79	Packaging diagram of <b>P13</b> . . . . .	166
6.80	Packaging diagram of <b>P14</b> . . . . .	167
6.81	Packaging diagram of <b>P16</b> . . . . .	168
6.82	Packaging diagram of <b>1a-Al</b> , <b>1a-Cr</b> ( $\kappa O$ ) and <b>1a-Ga</b> . . . . .	169
6.83	Packaging diagram of <b>1a-Tl</b> . . . . .	170
6.84	Packaging diagram of <b>1a-Bi</b> . . . . .	171
6.85	Packaging diagram of <b>1a-Sc</b> , <b>1a-Cr</b> ( $\kappa^2 O, O'$ ), <b>1a-Fe</b> and <b>1a-In</b> . . . . .	172
6.86	Packaging diagram of <b>1b</b> . . . . .	173
6.87	Packaging diagram of <b>2</b> · MeCN. . . . .	174
6.88	Packaging diagram of <b>3</b> · 2MeCN. . . . .	175
6.89	Packaging diagram of <b>4</b> · 3MeCN. . . . .	176
6.90	Packaging diagram of <b>5</b> · 2MeCN. . . . .	177
6.91	Packaging diagram of <b>6</b> . . . . .	178
6.92	Packaging diagram of <b>7</b> . . . . .	179
6.93	Packaging diagram of <b>8</b> . . . . .	180
6.94	Packaging diagram of <b>9</b> · 2MeCN. . . . .	181
6.95	Packaging diagram of <b>10</b> · 2MeCN. . . . .	182
6.96	Packaging diagram of <b>11</b> . . . . .	183
6.97	Packaging diagram of <b>12</b> . . . . .	184
6.98	Packaging diagram of <b>13</b> · MeCN. . . . .	185
6.99	Packaging diagram of <b>14</b> · MeCN. . . . .	186
6.100	Packaging diagram of <b>15a</b> · 0.5DCM. . . . .	187
6.101	Packaging diagram of <b>15b</b> · 2DCM. . . . .	188
6.102	Packaging diagram of <b>16a</b> · 2C <sub>3</sub> H <sub>6</sub> O. . . . .	189
6.103	Packaging diagram of <b>16b</b> · 3C <sub>3</sub> H <sub>6</sub> O. . . . .	190
6.104	Packaging diagram of <b>17</b> · py. . . . .	191

## List of Tables

1	Hydrogen bonds in crystals of <b>P1</b> . . . . .	12
2	Hydrogen bonds in crystals of <b>P9</b> · 2MeCN. . . . .	16
3	IR vibrations of the nitrito ligands in compounds <b>1a-M</b> . . . . .	21
4	Hydrogen bonds in crystals of <b>1a-M</b> . . . . .	28
5	IR vibrations of the nitrito ligands in <b>2-4</b> . . . . .	31
6	IR vibrations of the nitrito ligands in compounds <b>6-8</b> . . . . .	34
7	IR vibrations of the nitrito ligands in compound <b>9</b> · 2MeCN. . . . .	39
8	IR vibrations of the nitrito ligands in <b>10</b> · 2MeCN, <b>11</b> and <b>12</b> . . . . .	41
9	IR vibrations of the nitrito ligands in compounds <b>13</b> · MeCN and <b>14</b> · MeCN. . . . .	45
10	IR vibrations of the nitrito ligands in compounds <b>15a</b> · 0.5DCM and <b>15b</b> · 2DCM. . . . .	47
11	IR vibrations of the nitrito- $\kappa O$ ligands in <b>16</b> . . . . .	51
12	Hydrogen bonds in crystals of <b>17</b> · py. . . . .	54
13	Comparison of the experimental data and calculated values of the complex anions in <b>1a-Al</b> and <b>1a-Sc</b> . . . . .	56
14	Comparison of the experimental data and calculated values of the complex anions in <b>1a-Cr</b> . . . . .	56
15	Comparison of the experimental data and calculated values of the complex anions in <b>1a-Fe</b> and <b>1a-Ga</b> . . . . .	56
16	Comparison of the experimental data and calculated values of the complex anions in <b>1a-In</b> and <b>1a-Tl</b> . . . . .	57
17	Comparison of the experimental data and calculated values of the complex anion in <b>7</b> . . . . .	57
18	Comparison of the experimental data and calculated values of <b>11</b> and <b>12</b> . . . . .	58
19	Comparison of the experimental data and calculated values compounds <b>13</b> and <b>14</b> . . . . .	58
20	Hydrogen bonds in crystals of <b>1a-M</b> . . . . .	90
21	List of the used solvents and reagents with their corresponding purities and their manufacturers. . . . .	111
22	Crystallographic data of <b>P1</b> , <b>P5</b> and <b>P6</b> . . . . .	192
23	Crystallographic data of <b>P7</b> · 2MeCN, <b>P9</b> · 2MeCN and <b>P13</b> . . . . .	193
24	Crystallographic data of <b>P14</b> and <b>P16</b> . . . . .	194
25	Crystallographic data of <b>1a-Al</b> , <b>1a-Sc</b> and <b>1a-Cr</b> . . . . .	195
26	Crystallographic data of <b>1a-Fe</b> , <b>1a-Ga</b> and <b>1a-In</b> . . . . .	196
27	Crystallographic data of <b>1a-Tl</b> and <b>1a-Bi</b> . . . . .	197
28	Crystallographic data of <b>1b</b> , <b>2</b> · MeCN and <b>3</b> · 2MeCN. . . . .	198
29	Crystallographic data of <b>4</b> · 3MeCN, <b>5</b> · 2MeCN and <b>6</b> . . . . .	199
30	Crystallographic data of <b>7</b> , <b>8</b> and <b>9</b> · 2MeCN. . . . .	200
31	Crystallographic data of <b>10</b> · 2MeCN, <b>11</b> and <b>12</b> . . . . .	201
32	Crystallographic data of <b>13</b> · MeCN, <b>14</b> · MeCN and <b>15a</b> · 0.5DCM. . . . .	202
33	Crystallographic data of <b>15b</b> · 2DCM, <b>16a</b> · 2C <sub>3</sub> H <sub>6</sub> O and <b>16b</b> · 3C <sub>3</sub> H <sub>6</sub> O. . . . .	203
34	Crystallographic data of <b>17</b> · py. . . . .	204

---

## List of Schemes

1	Reactions of nitrous acid with primary amines as well as with secondary amines and amides. . . . .	2
2	Proposed reaction mechanism for the reduction of nitrite by the cytochrome <i>cd</i> <sub>1</sub> nitrite reductase (NiR) in <i>P. aeruginosa</i> . . . . .	3
3	Decomposition of nitrite in slightly (a) and strongly (b) acidic environment. .	76
4	Decomposition of nitrite in presence of iron(II). . . . .	77
5	Reaction of thiols, thioethers and phosphanes with nitrite. . . . .	77
6	Alternative synthesis methods for nitritoiron complexes. . . . .	78
7	Presumed reaction mechanism for the formation of the oxido bridge in compound <b>15b</b> . . . . .	87
8	Proposed PLI mechanism of the nitrito ligand in <b>1a-Fe</b> . . . . .	98
9	Proposed PLI mechanism of the nitrito ligand in <b>2</b> · MeCN. . . . .	99
10	Proposed PLI mechanism of the nitrito ligand in <b>7</b> . . . . .	100

**List of Abbreviations**

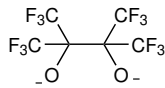
$\lambda$	wavelength
$\delta$	chemical shift
$\nu$	frequency
A	acceptor
ATR	attenuated total reflection
calcd.	calculated
D	donor
<i>d</i>	distance
DCM	dichloromethane
DMF	dimethyl formamide
EA	elemental analysis
ELF	electron localization function
<i>et al.</i>	<i>et alii</i>
equiv.	equivalent
ESI	electrospray ionization
GS	ground state
IR	infrared
L	ligand
M	metal
m	medium
MeCN	acetonitrile
MeOH	methanol
MLCT	metal-to ligand charge transfer
MS	metastable state
NiR	nitrite reductase
NMR	nuclear magnetic resonance
Ph	phenyl
PLI	photoinduced linkage isomerism
ppm	parts per million
PPN	bis(triphenylphosphine)iminium
QTAIM	quantum theory of atoms in molecules
rt	room temperature
s	strong
sh	shoulder
TS	transition state
UV/Vis	ultraviolet-visible
vs	very strong
vw	very weak
w	weak

**The Enemark-Feltham notation for metal-nitrosyl complexes**

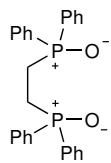
Since nitric oxide is considered a 'non-innocent ligand' its properties do not allow the assignment of an oxidation state to the central metal, the Enemark-Feltham notation is used for those compounds.<sup>[1]</sup> Here, the nitrosylmetal fragment is referred to as  $\{M(NO)_n\}^m$  whereby  $n$  is the number of nitrosyl ligands and  $m$  is the sum of the electrons in the metal's  $d$  orbitals and those in the  $\pi^*$  orbitals of the nitrosyl ligands.

List of numbered compounds

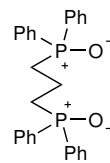
Ligands



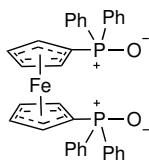
**fpin**



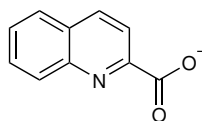
**dppe(O)<sub>2</sub>**



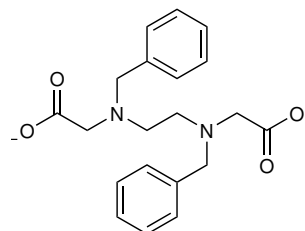
**dppp(O)<sub>2</sub>**



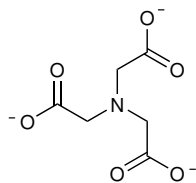
**dpfp(O)<sub>2</sub>**



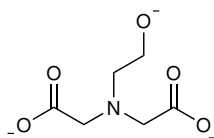
**qu**



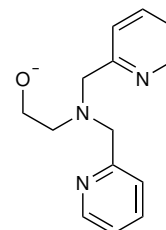
**Bn<sub>2</sub>edda**



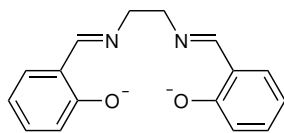
**nta**



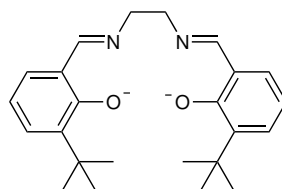
**heida**



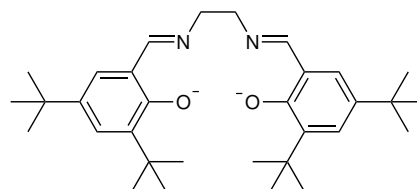
**bpmea**



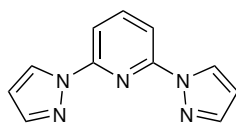
**salen**



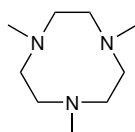
**tBu<sub>2</sub>salen**



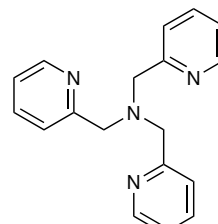
**tBu<sub>4</sub>salen**



**bipzpy**

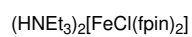
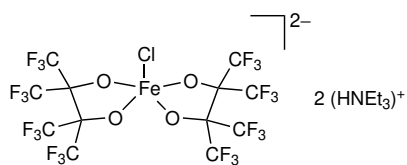


**Me<sub>3</sub>tacn**

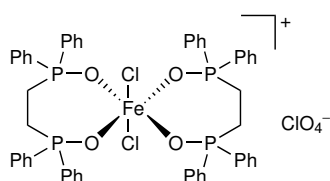


**tpya**

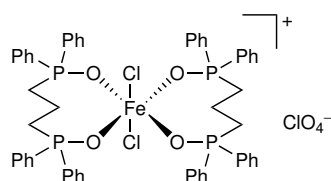
## Precursor compounds



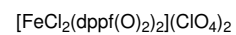
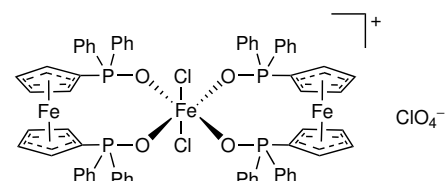
P1



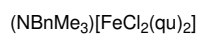
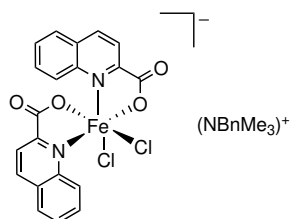
P2



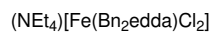
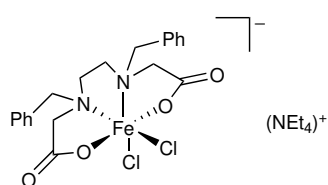
P3



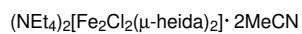
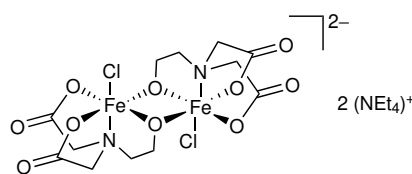
P3



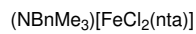
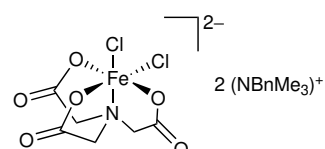
P5



P6

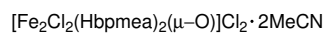
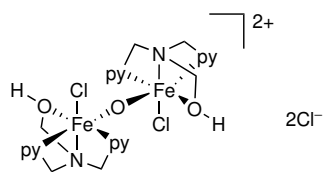


P7 · 2MeCN

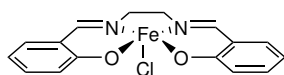


P8

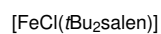
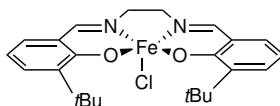
List of numbered compounds



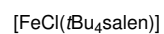
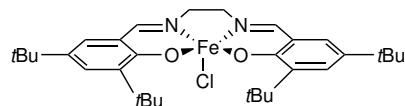
**P9** · 2MeCN



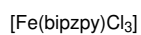
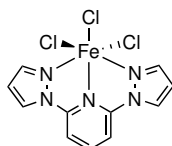
**P10**



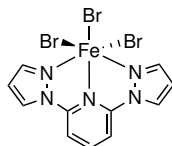
**P11**



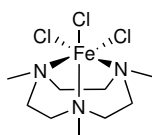
**P12**



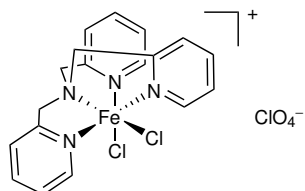
**P13**



**P14**

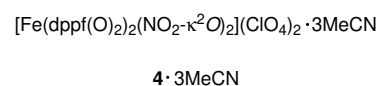
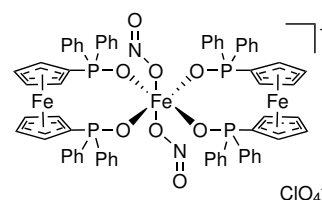
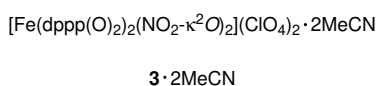
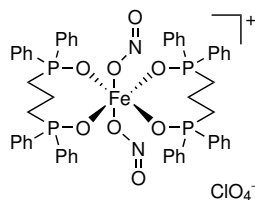
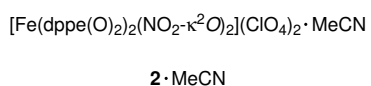
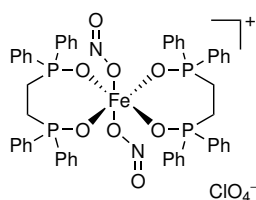
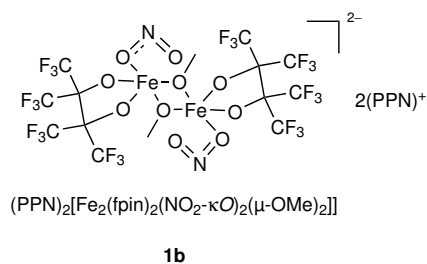
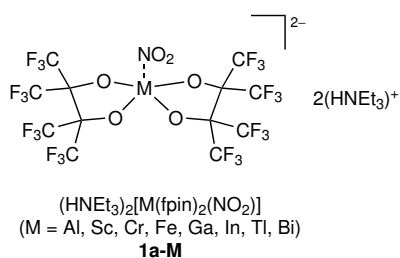


**P15**

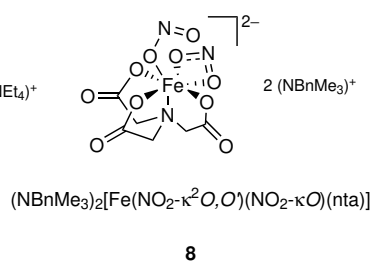
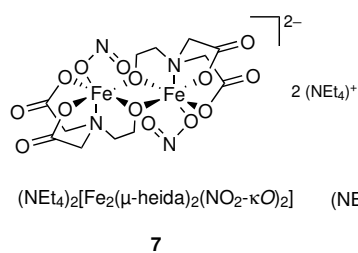
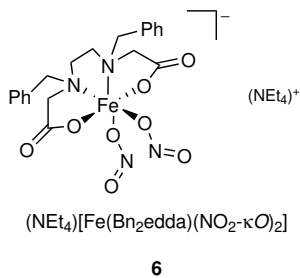
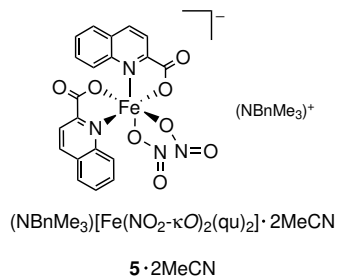


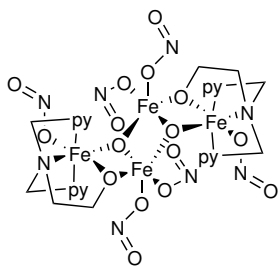
**P16**

Nitrito-iron complexes with O-donor co-ligands



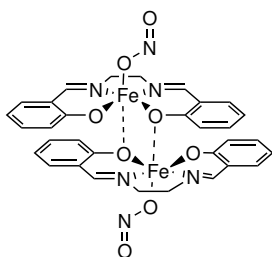
Nitrito-iron complexes with N,O-donor co-ligands





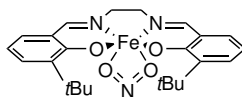
$[\text{Fe}_4(\mu\text{-bpmea})_2(\text{Z-NO}_2\text{-}\kappa\text{O})_2(\text{E-NO}_2\text{-}\kappa\text{O})_4(\mu_3\text{-O})_2] \cdot 2\text{MeCN}$

**9** · 2MeCN



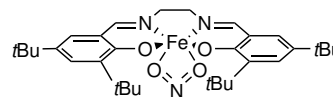
$[\{\text{Fe}(\text{NO}_2\text{-}\kappa\text{O})(\text{salen})\}]_2 \cdot 2\text{MeCN}$

**10** · 2MeCN



$[\text{Fe}(\text{NO}_2\text{-}\kappa^2\text{O},\text{O}')(\text{tBu}_2\text{salen})]$

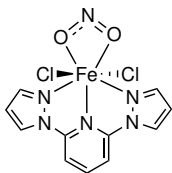
**11**



$[\text{Fe}(\text{NO}_2\text{-}\kappa^2\text{O},\text{O}')(\text{tBu}_4\text{salen})]$

**12**

### Nitrito-iron complexes with N-donor co-ligands



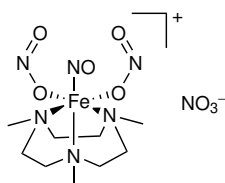
$[\text{Fe}(\text{bipzpy})\text{Cl}_2(\text{NO}_2\text{-}\kappa^2\text{O},\text{O}')] \cdot \text{MeCN}$

**13** · MeCN



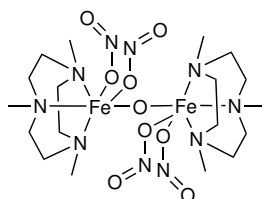
$[\text{Fe}(\text{bipzpy})\text{Br}_2(\text{NO}_2\text{-}\kappa^2\text{O},\text{O}')] \cdot \text{MeCN}$

**14** · MeCN



$[\text{Fe}(\text{Me}_3\text{tacn})(\text{NO})(\text{NO}_2\text{-}\kappa\text{O})_2](\text{NO}_3) \cdot 0.5\text{DCM}$

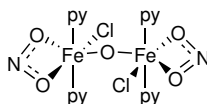
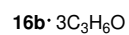
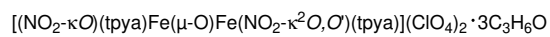
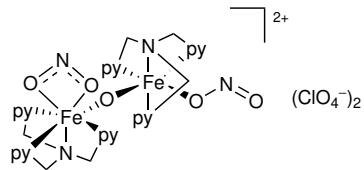
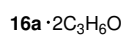
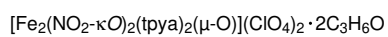
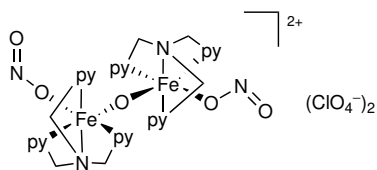
**15a** · 0.5DCM



$[\{\text{Fe}(\text{Me}_3\text{tacn})(\text{NO}_2\text{-}\kappa\text{O})_2\}]_2(\mu\text{-O}) \cdot 2\text{DCM}$

**15b** · 2DCM

List of numbered compounds



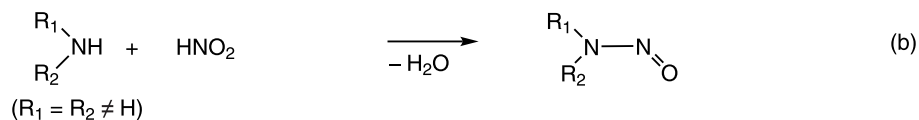
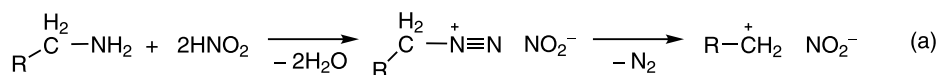
# 1 Introduction

## 1.1 Nitrite: usage, properties and biology

Nitrite salts are important compounds in synthetic chemistry, pharmacy, as well as in the construction sector and food industry.<sup>[2-7]</sup> Especially in the latter, they are indispensable since they are a key ingredient in curing salt. The curing of meat is a preservation technique which has been known for over 3000 years to elongate meat products' shelf life. At first, mainly sodium nitrate was added to sodium chloride but in the late 19<sup>th</sup> century, E. Polenske discovered that the nitrate is converted into nitrite during the curing process.<sup>[8,9]</sup> After that, nitrite became more and more popular as an ingredient in curing salts.<sup>[9-12]</sup>

The main benefit of nitrite in this application is based on its capacity to inhibit the growth of hazardous bacteria like *Clostridium botulinum* and *Clostridium perfringens* that are responsible for many food poisonings.<sup>[11,13,14]</sup> Furthermore, nitrite is the cause for the characteristic curing-flavor and the appetizing red color of cured meat products. This bright red color is a consequence of the reaction between nitrite and the heme unit of myoglobin which results in the formation of red nitrosomyoglobin.<sup>[8,10,11]</sup>

Unfortunately, this reaction behavior is also the reason for the toxicity of nitrite salts. They are able to oxidize the iron(II) in the blood's hemoglobin resulting in the formation of methemoglobin which is unable to act as oxygen carrier. The resulting condition is known as methemoglobinaemia and is potentially fatal if not treated early enough.<sup>[15,16]</sup> Furthermore, nitrites decompose quickly in slightly acidic environment – as found in the gastrointestinal system – or catalyzed by transition metals.<sup>[17-19]</sup> The decomposition products react with amides as well as with primary and secondary amines which are all parts of amino acids, peptides and proteins.<sup>[4]</sup> Primary amines react with the nitrites and form diazonium salts which are able to eliminate nitrogen under formation of carbenium ions that are considered to be strongly alkylating agents (Scheme 1 (a)). Secondary amines and amides react to *N*-nitrosamines and *N*-nitrosamides, respectively (Scheme 1 (b)).<sup>[4]</sup> In further decomposition steps, *inter alia*, formaldehyde and carbenium ions are formed. All those substances are classified either as toxic, teratogenic or highly carcinogenic.<sup>[20,21]</sup> For all these reasons, cured products should be consumed only in moderation and the allowed amount of nitrite in curing salt is limited by food regulations.<sup>[22,23]</sup>



**Scheme 1:** Reactions of nitrous acid with primary amines (a) as well as with secondary amines and amides (b).<sup>[4]</sup>

Contrary to its hazardous properties, nitrite is also essential for life since it is a key compound in nitrification and denitrification processes of the biological nitrogen cycle which describes the circulation of nitrogen within the atmosphere and different ecosystems. With the oxidation number of the N atom of +III, nitrite has its place as an intermediate between nitrate (+V) and nitric oxide (+II). Beside its part in the nitrification, where ammonium is oxidized to nitrate, nitrite is an important part of denitrification processes. In these, nitrate is reverted into elemental nitrogen which is a way for certain bacteria to produce energy under anaerobic conditions. A simplified overview of the main denitrification processes is depicted in Figure 1.1. Among other enzymes, nitrite reductases (NiR) are of great interest since they allow the controlled depletion of the molecule to nitric oxide.<sup>[24,25]</sup>

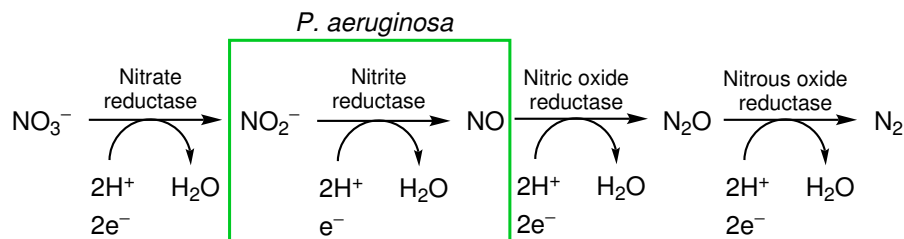


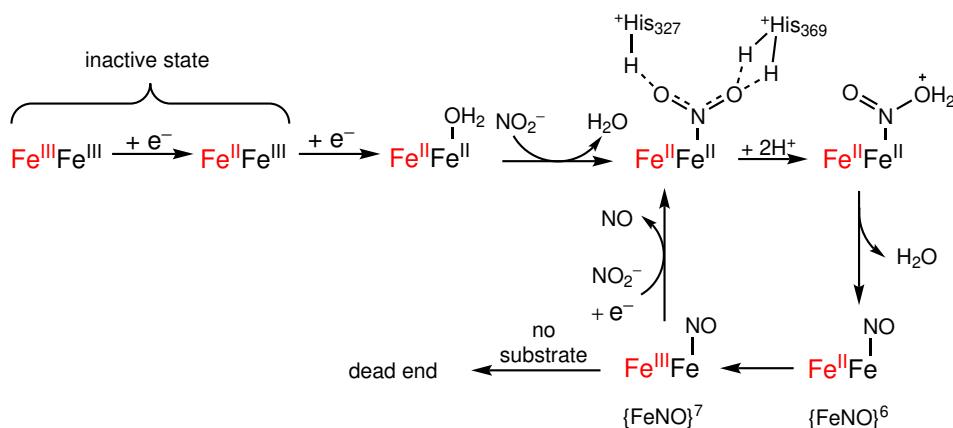
**Figure 1.1:** Denitrification pathway from nitrate to elemental nitrogen in the natural nitrogen cycle.<sup>[25]</sup>

Organisms like *Pseudomonas aeruginosa*, denitrifying bacteria that occur in most places on earth, are able to metabolize nitrite under anaerobic conditions with formation of nitric oxide.<sup>[26]</sup> For that, it uses the heme-based cytochrome *cd*<sub>1</sub> nitrite reductase (NiR) which will now be discussed in more detail.

The bifunctional multiheme enzyme is made up of two subunits each of which contain one heme *d*<sub>1</sub> and one heme *c* center. Beside its second function, to catalyze the reduction of oxygen to water, the enzyme's main function is to catalyze the reduction of nitrite to nitric oxide. The enzyme is located in the bacterial periplasm of various denitrifying bacteria and, due to slightly deviating structures, the rate constants for the catalyzed reaction are different for each bacterial strain.<sup>[24,27]</sup> Scheme 2 depicts the proposed reaction mechanism for cytochrome *cd*<sub>1</sub> NiR in *P. aeruginosa*.<sup>[24]</sup>

After a two-electron reduction, the enzyme is able to exit its inactive resting state. The

whole catalytic conversion of nitrite occurs on the heme  $d_1$  iron center while heme  $c$  (marked with a red color in Scheme 2) acts as an electron donor in later steps. First of all, a nitrite is able to replace an aqua ligand on the heme  $d_1$  iron. The  $\kappa N$ -bound nitrito ligand is stabilized by three hydrogen bonds of two neighboring histidine moieties which are able to donate two protons to the ligand. Elimination of a water molecule results in the formation of a nitrosyl complex. According to the Enemark-Feltham notation the product can be described as an  $\{\text{FeNO}\}^6$  compound that is reduced by the heme  $c$  in the following step, forming an  $\{\text{FeNO}\}^7$  complex.<sup>[1]</sup> If no other substrate is available, the enzyme is stuck in a dead end but, when further nitrite anions are present, the protein can be reduced to reform the nitrito- $\kappa N$  complex and start a new catalytic cycle. However, it is not clear whether the reduction occurs prior to the ligand exchange or afterwards.<sup>[24]</sup>



**Scheme 2:** Proposed reaction mechanism for the reduction of nitrite by the cytochrome  $cd_1$  nitrite reductase (NiR) in *P. aeruginosa*. The heme  $c$  center is marked with a red color.<sup>[24]</sup>

## 1.2 Binding behavior and complexes of nitrite

Knowledge about the ambidentate behavior of nitrito ligands is almost as old as coordination chemistry itself. In 1893 Alfred Werner used, *inter alia*, a series of nitrito cobalt compounds to deduce his theory of transition metal complexes.<sup>[28,29]</sup> Only one year later, Sophus Mads Jørgensen discovered that nitrite can coordinate in different ways on central metals by studying the chemistry of  $[\text{Co}(\text{NH}_3)_5(\text{NO}_2)]\text{Cl}_2$ .<sup>[30]</sup>

Beside five different non-bridging binding modes, many bridging binding modes are described in the literature.<sup>[31–33]</sup> According to IUPAC recommendations all those binding modes are referred to as "nitrito" ligands. The often used term "nitro ligand" in the case of N-bound nitrite is better described with the term nitrito- $\kappa N$  isomer (a). An advantage of the kappa convention is that it shows directly the coordinating atom of the ligand. In addition, the danger of confusing the nitrite with the nitrosyl ligand (such as in sodium nitroprusside) is minimized. Beside the  $N$ -binding, nitrite is able to form three types of O-coordination. The monodentate O-coordination can be subdivided into two cases. Ei-

ther the non-coordinating oxygen is pointing away from the central metal in the case of an *E*-nitrito- $\kappa O$  mode (b) or towards the metal as an *Z*-nitrito- $\kappa O$  isomer (c). Furthermore, the bidentate nitrito- $\kappa^2 O, O'$  mode (d) represents a symmetric chelating coordination. The fifth and last non-bridging binding mode, nitrito- $\kappa^2 N, O$  (e), is observed only as a transition state in isomerization reactions and has not been obtained as a stable species to date.

Nitrites can also act as a bridging ligand between up to three metal centers (Figure 1.2). Here, the  $\mu$ -nitrito- $1\kappa O:2\kappa N$  bridging mode marks, by far, the most represented one.<sup>[31,32]</sup> It is notable that in this case the formation of bridged *cis* and *trans* isomers (Figure 1.2 f and g) are possible.<sup>[31]</sup> The latter is discussed to be an intermediate in the reaction of cytochrome *c* oxidase with nitrite.<sup>[34]</sup> Other bridging binding modes of nitrite have been structurally characterized but are relatively rare. Especially in the case of iron, only three structurally characterized nitrito-bridged complexes are known so far.<sup>[35,36]</sup> Further, the bridging  $\mu$ -nitrito- $\kappa O$  and  $\mu$ -nitrito- $1:2\kappa N\kappa^2 O, O'$  binding modes (Figure 1.2 h and i) are observed in various multinuclear metal complexes.<sup>[37]</sup>

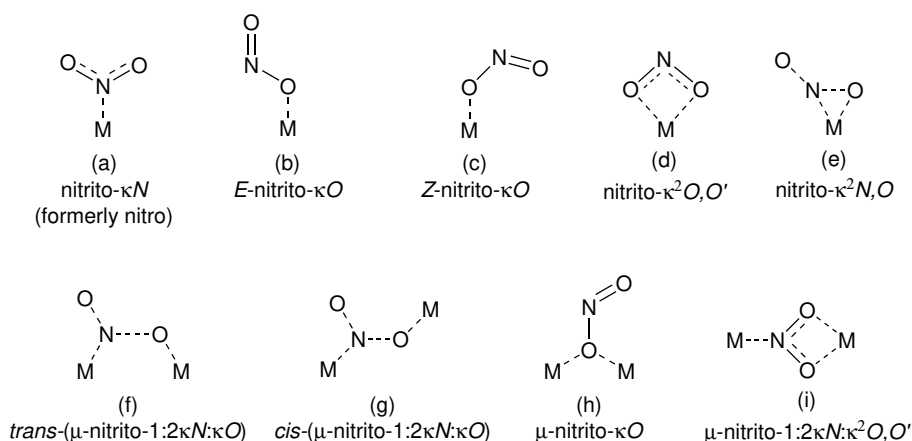


**Figure 1.2:** The different non-bridging and selected bridging binding modes of nitrito ligands.<sup>[31–33]</sup>

Some factors that determine the nitrite's binding mode have already been described in the literature. A review of Hitchman and Rowbottom from 1982 revealed the strong influence of the steric demand of other ligands as well as kinetic and thermodynamic effects.<sup>[38]</sup> They also assumed the central metal's electronic structure is influenced on the nitrito ligand's binding behavior but were unable to prove their assumption due to the lack of examples of early 3d transition metal complexes with nitrite.<sup>[38]</sup> In addition, later studies showed the hydrogen bond situation is influencing the binding mode of nitrite, too.<sup>[39]</sup> In addition, nitrite exhibits a special position in the spectrochemical row. In its O-bound forms the nitrite acts as weak field ligand while N-bonded nitrite is considered as a strong field ligand.<sup>[40]</sup>

While in the case of Co, Ni and Cu many nitrito complexes are known, their amount decreases with the atomic number within the first transition row. Figure 1.3 shows an

overview of structurally resolved nitrito complexes with transition metals according to the CCDC and ICSD databases.<sup>[37,41]</sup> Especially in the case of iron, the corresponding number decreases further if only non-heme complexes with nitrito ligands are taken into account.

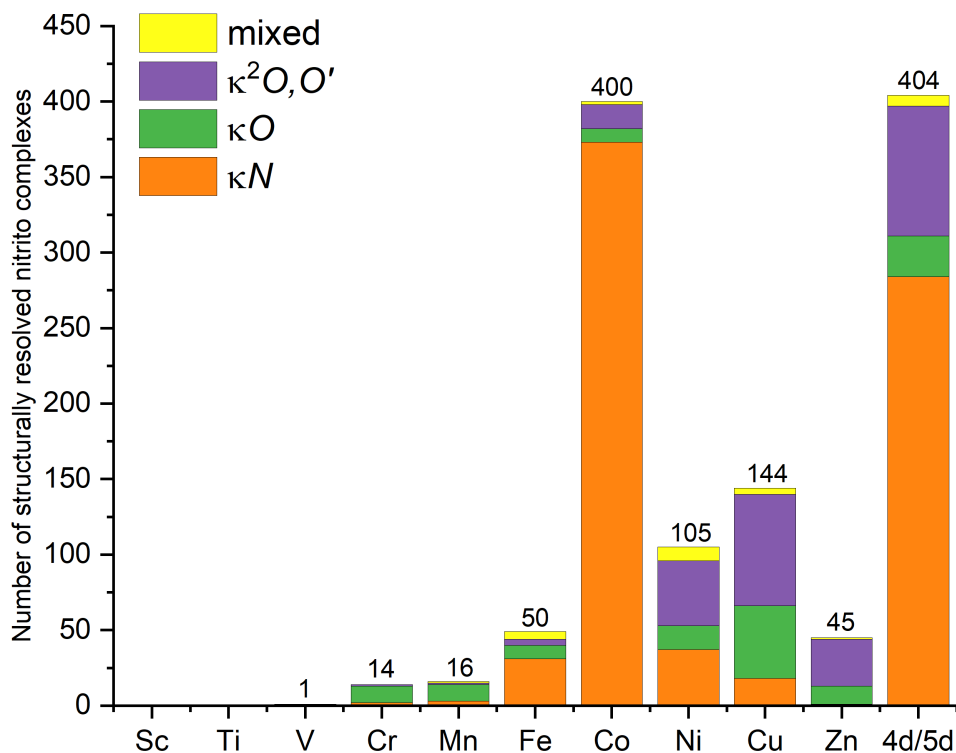


**Figure 1.3:** Number of structurally resolved nitrito complexes with transition metals according to the CCDC and ICSD databases.<sup>[37,41]</sup>

### 1.3 Photoinduced linkage isomerism

Some ambidentate ligands possess the ability to switch between their various binding modes. If the isomerism is triggered by the absorption of visible or ultraviolet light, the effect is called photoinduced linkage isomerism (PLI). One of the most famous PLI-active substances is sodium nitroprusside ( $\text{Na}_2[\text{Fe}(\text{CN})_5\text{NO}] \cdot 2\text{H}_2\text{O}$ ; SNP), the ground state (GS) of which marks an N-bound nitrosyl ligand. Irradiation with light triggers an isomerization into the two metastable states MS1 (isonitrosyl or  $\kappa O$  isomer) and MS2 (side-on or  $\kappa^2 N, O$  isomer).<sup>[42–45]</sup> However, the conversion rates of those reactions are very low, making it unusable for practical applications.<sup>[46,47]</sup>

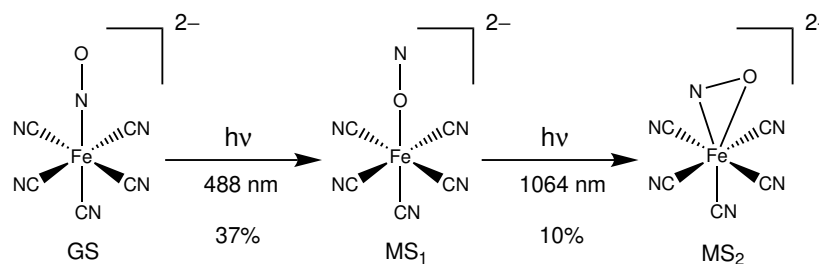


**Figure 1.4:** Visualization of the photoinduced linkage isomerism of SNP with formation of the two metastable states MS<sub>1</sub> (isonitrosyl or  $\kappa O$  isomer) and MS<sub>2</sub> (side-on or  $\kappa^2 N, O$  isomer).<sup>[47]</sup>

The PLI of nitrito ligands was first demonstrated in 1944 by Adell with IR spectroscopic methods on the already mentioned  $[\text{Co}(\text{NH}_3)_5(\text{NO}_2)]\text{Cl}_2$ . The author showed photochemical  $\kappa O$ -to- $\kappa N$  isomerization by irradiation of the compound with light of a wavelength of 436 nm.<sup>[48]</sup> In 1979 the first powder-diffraction study on this compound illustrated that isomerization can be triggered either by changing temperatures or by irradiation with light.<sup>[49]</sup> In 1997, the first photocrystallographic investigation was performed on SNP, giving definite proof of the existence of the MS1 and MS2.<sup>[45]</sup> Finally, at the end of the 2000s, Raithby *et al.* were the first authors to archive a conversion rate of 100% PLI with  $[\text{NiCl}(\text{dppe})(\text{NO}_2-\kappa N)]$  (Figure 1.5).<sup>[46]</sup> Since then, a few other examples with nickel, palladium and platinum which also undergo such high isomerization rates were found.<sup>[47]</sup>

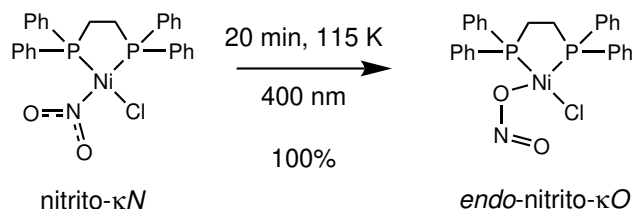


**Figure 1.5:** Visualization of the first PLI with a conversion rate of 100%.<sup>[46]</sup>

Possible applications of PLI-active substances are found in ultrafast optical switching and information storage devices.<sup>[50–52]</sup> In medicine those substances have potential use in photodynamic therapies.<sup>[47,53]</sup> Another benefit of the PLI effect is that substances can be generated which are not accessible by standard reaction ways.<sup>[50]</sup> A huge drawback for the application of PLI-active nitrosyl complexes is that their conversion rates are low in most cases. The reason for that is the high stability of the  $\kappa N$  GS compared to the low stabilities of the two possible MS. Furthermore, the activation barriers between the isomers in the case of nitrosyl ligands are relatively low which facilitates the relaxation back to the GS.<sup>[45]</sup> At this point, the great advantage of nitrito ligands comes into effect. Due to the less spherical shape, the re-isomerization is hindered by much higher activation barriers which leads to better conversion rates.

According to Hatcher *et al.* there are few parameters which have a positive influence on the occurrence of a PLI in solid-state samples. First of all, the wavelength of the light

used needs to be determined exactly since different wavelength are able to convert one MS into another or lead to a back-isomerization to the GS. Furthermore, the irradiation has to trigger either a  $d \rightarrow d$  transition or a MLCT, such as the  $d(M) \rightarrow \pi^*(NO)$  transition in nitrosyl complexes, to alter the bond situation between central metal and the ambidentate ligand.<sup>[54]</sup> Another important factor is the temperature. Above a certain temperature ( $T_{krit.}$ ) only the ground state exists; below that the excited states have a defined lifetime within a certain temperature range.<sup>[47]</sup>

Regarding the energy hypersurface of the PLI active substance, a relaxation from an excited state to an MS only occurs if the potential of the excited state has a minimum close to the saddle point between GS and MS on the ground state's potential surface. If the minimum of the excited state is within the ground state's potential pot, the system relaxes back to the GS.<sup>[47,54,55]</sup> A simplified visualization of this is shown in Figure 1.6.

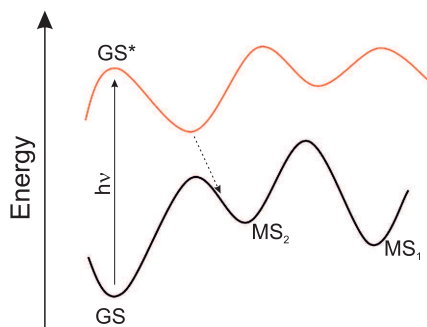


**Figure 1.6:** Visualization of the energy hypersurfaces of the excited state (red line) and the ground state (black line) for a  $ML_5(NO)$  substance with two different MS. Simplified redraw from reference<sup>[54]</sup>.

The switching ligand also needs a flexible environment. Strong interactions with other co-ligands, such as hydrogen-bonds, lead to a reduced conversion rate. In the case of photocrystallographic investigations, both the ground state substance and the metastable state have to be monocrystalline.<sup>[47]</sup> Hence it is necessary that the isomerization must not cause tensions that lead to a degradation of the crystal. For that, bulky auxiliary ligands which form a "reaction-cave" by embedding the nitrite lead to good conversion rates.<sup>[47,56]</sup>

## 1.4 Aim of this work

Although iron is one of the best investigated central metals and nitrite has been known as a ligand since the beginning of coordination chemistry, the number of structurally characterized nitritoiron compounds in literature is low. The same applies for nitrito complexes containing early-to-middle 3d central metals and p-block elements. For this reason, the first part of this work deals with the synthesis and full characterization of novel nitrito complexes with a special focus on the ferric compounds. For that, specific reaction conditions and suitable ligands are defined to obtain a reproducible reaction scheme. At first, halogenidoiron(III) precursor complexes with various N- and O-donating co-ligands are either newly synthesized or prepared according to literature-known procedures. Afterwards, these compounds are reacted with silver nitrite to exchange the chlorido ligands with nitrito ligands. It is shown, that this synthesis method also allows to synthesize a row of nitrito complexes with a variety of different trivalent central metals all of which exhibit the same general formula  $(\text{HNEt}_3)_2[\text{M}^{\text{III}}(\text{fpin})_2(\text{NO}_2)]$  ( $\text{M} = \text{Al}, \text{Sc}, \text{Cr}, \text{Fe}, \text{Ga}, \text{In}, \text{Tl}, \text{Bi}$ ; fpin = perfluoropinacolate). All synthesized halogenidoiron and nitrito complexes are characterized by IR and UV-vis spectroscopic means as well as by elemental analysis. Novel compounds or those which the solid state structures are not described in the literature are further analyzed by single-crystal X-ray diffraction. To facilitate the identification of the nitrite-related IR vibrational bands for the following PLI experiments, in most cases the  $^{15}\text{NO}_2^-$ -enriched substances are synthesized to verify the bands *via* the isotope-induced shift. Regarding the nitritoiron(III) complexes, in some cases the formation of bridging oxido ligands is observed. For a further investigation, *in-situ*- and gas-phase infrared spectroscopic methods are applied to reconstruct the corresponding reaction mechanism.

The second part of this thesis deals with the ambidentate properties of the nitrito ligand. For a closer investigation, quantum-chemical methods are applied on a selection of the synthesized nitrito complexes. At first, the best fitting functionals for the calculations are determined by comparison of the computed values from structural optimizations with the results of the single-crystal X-ray analyses. Afterwards, a method is developed which is based on relaxed potential energy surface scans that helps to investigate the stability of various nitrito isomers and the heights of the respective activation barriers. Applying the scan calculations on the different nitrito complexes helps to further refine this method. In connection with the scan calculations, especially the series of mononuclear complexes with various trivalent central metals allows a special view on the central metal's influence on the binding mode of the nitrito ligands. The scan calculations are discussed as a helpful tool for the prediction of future candidates for PLI experiments. Finally, PLI measurements are performed on six of the synthesized nitritoiron(III) complexes. In two cases a direct comparison between the previously implemented scan calculations and the results of the PLI measurement is possible.

## 2 Results

### 2.1 Synthesis of the ligands

#### 2.1.1 Synthesis of the bisphosphane oxides

The bisphosphane oxide ligands  $\text{dppe}(\text{O})_2$ ,  $\text{dppp}(\text{O})_2$  and  $\text{dppf}(\text{O})_2$  were synthesized by oxidizing the respective bisphosphanes with a surplus of hydrogen peroxide in dichloromethane.<sup>[57]</sup> The undefined amount of co-crystallized peroxides and residual water that remained in the crude substance of  $\text{dppf}(\text{O})_2$  was removed by stirring the dichloromethane solution together with a mole-sieve-filled tea bag.<sup>[58,59]</sup> All substances were characterized by elemental analysis,  $^1\text{H}$  and  $^{31}\text{P}\{^1\text{H}\}$  NMR as well as IR spectroscopy.<sup>[57-59]</sup>

#### 2.1.2 Synthesis of $\text{H}_2\text{Bn}_2\text{edda}$

The aminocarboxylate  $\text{H}_2\text{Bn}_2\text{edda}$  was synthesized according to a modified procedure of Ménage *et al.* by adding a basic *N,N'*-dibenzylethylenediamine solution to a cooled mixture of bromoacetic acid and sodium bicarbonate.<sup>[60]</sup> The product was characterized by elemental analysis,  $^1\text{H}$  and  $^{13}\text{C}\{^1\text{H}\}$  NMR as well as by IR spectroscopy. The analytical methods revealed that the air-stable compound was obtained with 3.9 equivalents of water.

#### 2.1.3 Synthesis of $\text{H}_2\text{tBu}_2\text{salen}$ and $\text{H}_2\text{tBu}_4\text{salen}$

The salen-based ligands were synthesized according to the literature-known procedure of Boyle *et al.* by refluxing ethylenediamine with the respective substituted salicylaldehyde in methanol. For characterization, elemental analysis,  $^1\text{H}$  and  $^{13}\text{C}\{^1\text{H}\}$  NMR as well as by IR spectroscopy were used.<sup>[61]</sup>

#### 2.1.4 Synthesis of $\text{Hbpmea}$

$\text{Hbpmea}$  was synthesized according to the procedure of Ording-Wenker *et al.* by adding sodium triacetoxyborohydride to a solution of ethanolamine and pyridine-2-carboxyaldehyde in dichloromethane. The ligand was characterized by elemental analysis,  $^1\text{H}$  and  $^{13}\text{C}\{^1\text{H}\}$  NMR as well as by IR spectroscopy.<sup>[62]</sup>

#### 2.1.5 Synthesis of $\text{tpya}$

$\text{tpya}$  was synthesized according to the procedure of Britovsek *et al.* by the addition of a surplus of sodium triacetoxyborohydride to a solution of pyridine-2-carboxyaldehyde and 2-(aminomethyl)pyridine in dichloromethane. The ligand was characterized by elemental analysis,  $^1\text{H}$  and  $^{13}\text{C}\{^1\text{H}\}$  NMR as well as by IR spectroscopy.<sup>[63]</sup>

### 2.1.6 Synthesis of $\text{Ag}^{15}\text{NO}_2$

$\text{Ag}^{15}\text{NO}_2$  was synthesized according to the procedure of Kundu *et al.* by adding an aqueous silver nitrate solution to an aqueous solution of  $^{15}\text{N}$ -enriched sodium nitrite. The light-sensitive  $\text{Ag}^{15}\text{NO}_2$  was characterized by elemental analysis and IR spectroscopy. The successful isotope enrichment was confirmed by comparison with the IR spectrum of the non-enriched silver nitrite.<sup>[64]</sup>

## 2.2 Synthesis of the precursor compounds

### 2.2.1 Synthesis of $(\text{HNEt}_3)_2[\text{FeCl}(\text{fpin})_2]$ (**P1**)

$(\text{HNEt}_3)_2[\text{FeCl}(\text{fpin})_2]$  (**P1**) was prepared by adding perfluoropinacol and triethylamine to a solution of iron(III) chloride in methanol. Dry crystals of (**P1**) are air-stable and can be stored for months at room temperature. **P1** was characterized by elemental analysis, single-crystal X-ray diffraction, IR and UV-Vis spectroscopy.

Since the compound is almost colorless, the UV-Vis spectrum featured no absorption bands in the visible region. Only two bands at 248 nm and 332 nm are observed.

**P1** crystallizes in the monoclinic space group  $P2_1/c$  with four formula units in the unit cell. The asymmetric unit cell consists of one formula unit. The molecular structure of **P1** is depicted in Figure 2.7 with its relevant distances and angles in the caption. The central metal is fivefold coordinated by one chlorido ligand and two chelating perfluoropinacolato ligands which form five-membered chelate rings. The two bidentate ligands are contorted to each other resulting in the formation of a distorted square pyramid. The mean Fe–O distance in the complex anion is 1.961(2) Å. Two triethylammonium counter-ions form each one classical hydrogen bond towards the opposing oxygen atoms O2 and O3. Further details regarding hydrogen bonds are listed in Table 1.

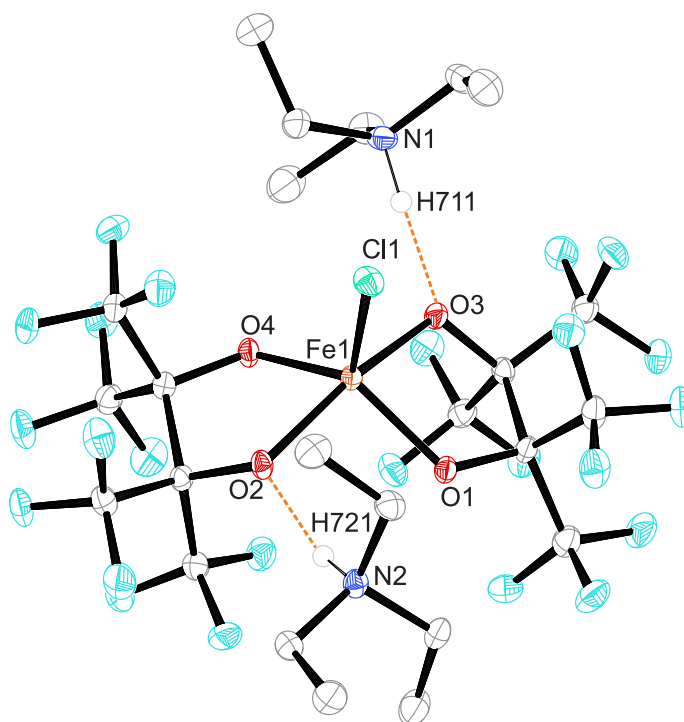


**Figure 2.7:** Ortep plot of  $(\text{HNEt}_3)_2[\text{FeCl}(\text{fpin})_2]$  in crystals of **P1**. For clarity, the C-bound hydrogen atoms are not depicted. The thermal ellipsoids are drawn at 50% probability. Interatomic distances (Å) and bond angles ( $^\circ$ ). The standard deviation of the last decimal is given in parentheses: Fe1–O1 1.924(1), Fe1–O2 1.991(2), Fe1–O3 2.011(2), Fe1–O4 1.919(1), Fe1–Cl1 2.2443(7); O1–Fe1–O3 80.88(7), O4–Fe1–O2 81.43(7), O4–Fe1–O1 131.61(7), O1–Fe1–O2 92.48(7), O4–Fe1–O3 90.54(7), O2–Fe1–O3 162.08(7), O4–Fe1–Cl1 115.31(5), O1–Fe1–Cl1 113.06(5), O2–Fe1–Cl1 99.27(5), O3–Fe1–Cl1 98.65(5).

**Table 1:** Distances and angles of hydrogen bonds in **P1**. The standard deviation of the last decimal is given in parentheses. Values without standard deviation refer to hydrogen atoms which were calculated on idealized positions, riding on their parent atoms.

D–H···A	$d(\text{D–H})/\text{\AA}$	$d(\text{H}\cdots\text{A})/\text{\AA}$	$d(\text{D}\cdots\text{A})/\text{\AA}$	$\angle(\text{D–H}\cdots\text{A})/^\circ$
N1–H711···O3	0.98	1.81	2.784(3)	173.7
N2–H721···O2	0.98	1.95	2.895(3)	160.3

### 2.2.2 Synthesis of $[\text{FeCl}_2\text{L}_2](\text{ClO}_4)$ ( $\text{L} = \text{dppe}(\text{O})_2, \text{dppp}(\text{O})_2, \text{dppf}(\text{O})_2$ ) (**P2-4**)

Compounds of the general formula  $[\text{FeL}_2\text{Cl}_2](\text{ClO}_4)$  ( $\text{L} = \text{dppe}(\text{O})_2, \text{dppp}(\text{O})_2, \text{dppf}(\text{O})_2$ ) (**P2-4**) were synthesized by adding the respective bisphosphane oxides and sodium perchlorate to a solution of iron(III) chloride in acetonitrile. The compounds are air-stable and show no signs of decomposition after being stored at room temperature for months. **P2-4** were characterized by elemental analysis as well as IR and UV-Vis spectroscopy. Since the molecular structures of the complex anions in **P2** and **P4** are known in the literature, no single-crystal X-ray diffraction analysis was performed.<sup>[65,66]</sup> Compound **P3** is very soluble in acetonitrile but attempts to obtain crystals for X-ray diffraction only resulted in the precipitation of a yellow powder.

The UV-Vis spectra of all precursor compounds with bisphosphane oxide ligands in acetonitrile solutions features only absorption bands below 360 nm. **P4** shows an additional band at 459 nm.

### 2.2.3 Synthesis of the aminocarboxylate precursor compounds (**P5-8**)

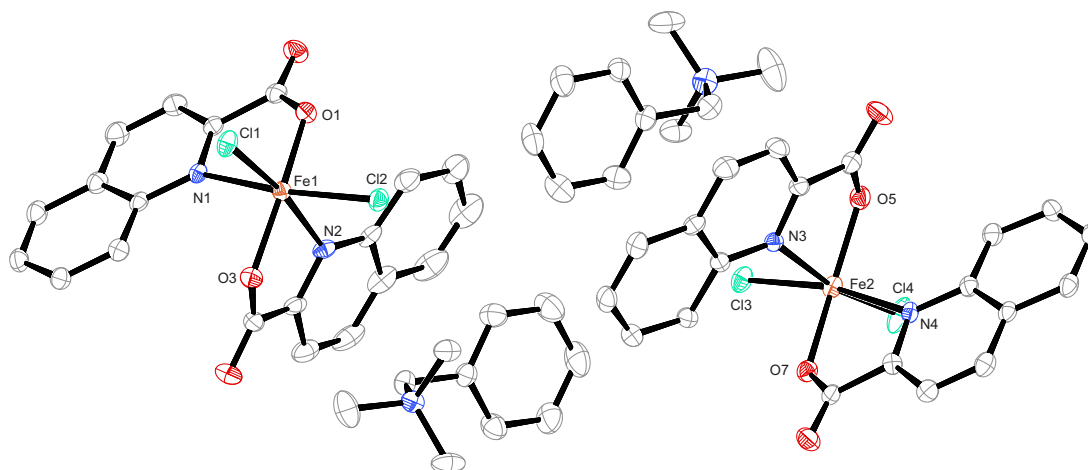
Preparation of the aminocarboxylate precursor compounds (**P5-8**) was performed by a modified procedure published by Walters *et al.*<sup>[67]</sup> Compounds **P5**, **P6** and **P8** are air-stable and can be stored for months at room temperature. **P7** · 2MeCN is thermally stable but highly hygroscopic and has to be stored under exclusion of ambient moisture. All aminocarboxylate precursor compounds were characterized by elemental analysis, single-crystal X-ray diffraction, IR and UV-Vis spectroscopy.

UV-Vis spectra of all aminocarboxylate complexes were recorded from solutions of the substances in acetonitrile. **P5-8** exhibit no absorptions in the visible region which is in accordance with their pale-yellow color. **P5** possesses absorption maxima in the UV region of the spectrum at 299 nm, 300 nm and 337 nm. The solution of **P6** shows three absorption bands at 250 nm, 291 nm and 365 nm. Compounds **P7** · 2MeCN and **P8** exhibit only one absorption band at 345 nm and 284 nm, respectively.

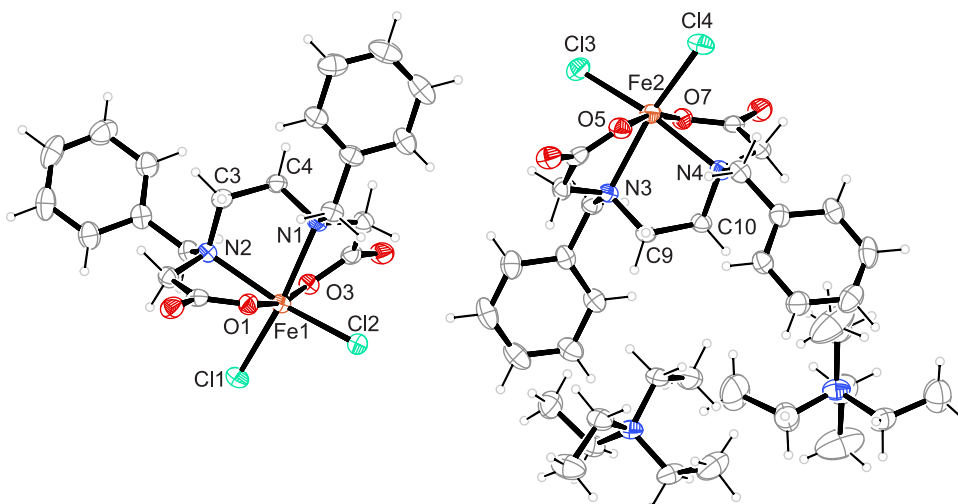
**P5** crystallizes in the triclinic space group  $P\bar{1}$  and compound **P6** in the monoclinic space group  $P2_1/n$ . Their primitive cells contain four and eight formula units, respectively. In both cases the asymmetric units contain two formula units with two independent complex anions together with their respective cations. The molecular structures are displayed in

Figure 2.8 (**P5**) and 2.9 (**P5**) with their relevant distances and angles in the caption. The central metals in **P5** are sixfold coordinated by two deprotonated molecules of quinaldic acid and two chlorido ligands in *cis* position. The qu ligands coordinate *via* five-membered chelate rings and with their carboxylato moieties in *trans* position. The same coordination behavior is seen in the molecular structure of **P6** where the central metal is sixfold coordinated by one deprotonated Bn<sub>2</sub>edda ligand and two chlorido ligands in *cis* position. Both coordination polyhedra can be best described as distorted octahedra.

The mean Fe–Cl distances are 2.3022(9) Å in **P5** and 2.309(1) Å in **P6**. The carboxylato functions coordinate with a mean distance of 1.955 Å in **P5** and 1.987 Å in **P6**, average Fe–N distances are 2.287 Å (**P5**) and 2.257 Å (**P6**). The Cl–Fe–Cl angle in **P5** is with 95° approximately 5° smaller than in **P6**. While the qu ligands in **P5** are less rigid due to the absence of an ethylene bridge as in Bn<sub>2</sub>edda, the octahedral coordination is slightly less distorted compared to **P6**.



**Figure 2.8:** Ortep plot of (NBnMe<sub>3</sub>)[FeCl<sub>2</sub>(qu)<sub>2</sub>] in crystals of **P5**. The thermal ellipsoids are drawn at 50% probability. For clarity, hydrogen atoms are not depicted. Interatomic distances (Å) and bond angles (°). The standard deviation of the last decimal is given in parentheses: Fe1–O1 1.953(2), Fe1–O3 1.955(2), Fe1–N2 2.273(3), Fe1–N1 2.295(2), Fe1–Cl1 2.2907(9), Fe1–Cl2 2.3137(9), Fe2–O5 1.952(2), Fe2–O7 1.958(2), Fe2–N3 2.296(3), Fe2–N4 2.283(2), Fe2–Cl3 2.3214(9), Fe2–Cl4 2.2924(9); O1–Fe1–N1 76.52(9), O2–Fe1–N2 76.30(9), Cl1–Fe1–Cl2 96.45(3), Cl1–Fe1–N1 91.03(6), Cl1–Fe1–O1 96.77(7), Cl2–Fe1–O2 96.17(7), N2–Fe1–Cl2 88.25(7), O1–Fe1–Cl2 93.60(7), O2–Fe1–Cl2 97.25(7), N1–Fe1–Cl2 168.28(6), N2–Fe1–Cl1 171.61(7), O1–Fe1–O3 162.05(9), N2–Fe1–N1 85.47(9), O5–Fe2–N3 75.36(9), O7–Fe2–N4 75.79(9), Cl4–Fe2–Cl3 94.81(3), O5–Fe2–Cl3 101.26(7), O7–Fe2–Cl3 91.81(7), N3–Fe2–Cl3 87.80(7), O5–Fe2–Cl4 95.15(7), O7–Fe2–Cl4 100.59(7), N4–Fe2–Cl4 90.31(7), N4–Fe2–Cl3 167.29(7), Cl4–Fe2–N3 170.50(7), O5–Fe2–O7 158.60(9), N4–Fe2–N3 89.03(9).



**Figure 2.9:** Ortep plot of  $(\text{NEt}_4)[\text{Fe}(\text{Bn}_2\text{edda})\text{Cl}_2]$  in crystals of **P6**. The thermal ellipsoids are drawn at 50% probability. Interatomic distances ( $\text{\AA}$ ) and bond angles ( $^\circ$ ). The standard deviation of the last decimal is given in parentheses: Fe1–O1 1.997(3), Fe1–O3 1.986(3), Fe1–N1 2.255(3), Fe1–N2 2.253(3), Fe1–Cl1 2.311(1), Fe1–Cl2 2.307(1), Fe2–O5 1.989(3), Fe2–O7 1.976(3), Fe2–N3 2.260(3), Fe2–N4 2.258(3), Fe2–Cl3 2.319(1), Fe2–Cl4 2.299(1); O1–Fe1–N2 75.8(1), O3–Fe1–N1 76.1(1), O1–Fe1–N1 92.7(1), N2–Fe1–N1 80.0(1), O3–Fe1–Cl2 97.15(8), O1–Fe1–Cl2 91.33(8), N1–Fe1–Cl2 90.97(8), O3–Fe1–Cl1 91.78(8), O1–Fe1–Cl1 97.78(8), N2–Fe1–Cl1 91.85(8), Cl2–Fe1–Cl1 99.72(4), O1–Fe1–O3 166.0(1), O7–Fe2–O5 166.0(1), O7–Fe2–N4 76.2(1), O5–Fe2–N4 94.2(1), O7–Fe2–N3 92.4(1), O5–Fe2–N3 75.8(1), N4–Fe2–N3 80.0(1), O7–Fe2–Cl4 98.50(8), O5–Fe2–Cl4 91.53(8), N4–Fe2–Cl4 90.38(8), O7–Fe2–Cl3 89.19(8), O5–Fe2–Cl3 98.33(8), N3–Fe2–Cl3 91.04(8), Cl4–Fe2–Cl3 101.57(4), O5–Fe2–O7 166.0(1).

**P7** · 2MeCN crystallizes in the monoclinic space group  $P2_1/c$  with two formula units in the unit cell. The asymmetric unit of **P7** · 2MeCN consists of half a molecule, one triethylammonium cation and one acetonitrile. The binuclear, inversion-symmetric, dianionic complex is built up by two equivalent iron(III) central atoms. The molecular structure of **P7** · 2MeCN is shown in Figure 2.10 with all relevant distances and angles in the respective caption. Each iron center is sixfold coordinated by one chlorido and one heida ligand whereby the two ethoxy moieties act as bridging ligands between the two metal ions. The resulting coordination polyhedron is best described as distorted octahedron.

The mean Fe–Cl and Fe1–O<sub>carb.</sub> distances are slightly longer than in **P5** and **P6**. The reverse counts for the Fe1–N1 distance in **P7** · 2MeCN which is approximately 0.05  $\text{\AA}$  shorter than the comparable distances in the other complexes. Due to the inversion symmetry, the chlorido ligands are in *trans* position to each other.

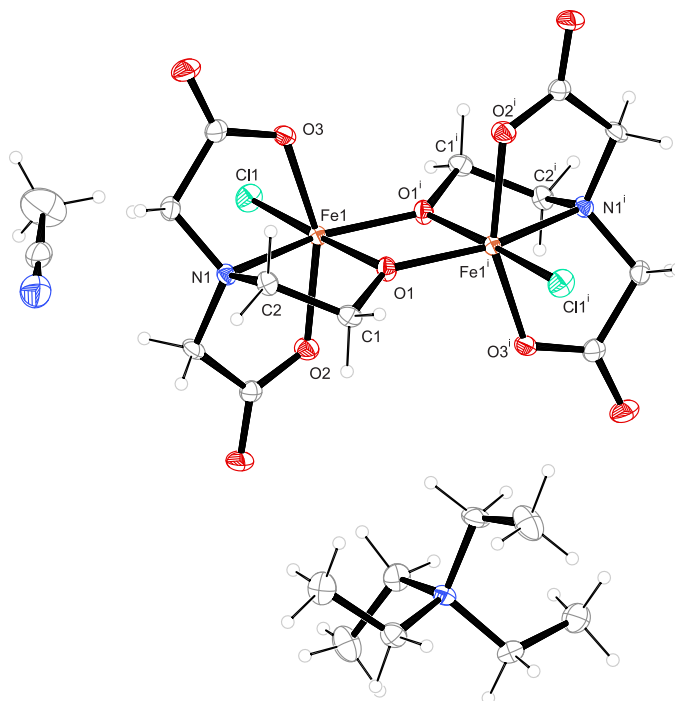


**Figure 2.10:** Ortep plot of the inversion-symmetric compound  $(\text{NEt}_4)_2[\text{Fe}_2\text{Cl}_2(\mu\text{-heida})_2] \cdot 2\text{MeCN}$  in crystals of **P7** · 2MeCN. The thermal ellipsoids are drawn at 50% probability. For clarity, the symmetry generated acetonitrile and tetraethylammonium cation are omitted. Interatomic distances (Å) and bond angles (°). The standard deviation of the last decimal is given in parentheses: Fe1–O1 1.927(2), Fe1–O1<sup>i</sup> 2.050(2), Fe1–O2 1.991(2), Fe1–O3 1.994(2), Fe1–N1 2.217(2), Fe1–Cl1 2.3437(7), O1–Fe1–O1<sup>i</sup> 74.96(8), Fe1–O1–Fe1 105.05(7), O1<sup>i</sup>–Fe1–N1 154.19(8), O2–Fe1–N1 78.71(7), O3–Fe1–N1 76.67(7), O1–Fe1–N1 79.33(7), O1–Fe1–Cl1 100.05(5), O2–Fe1–Cl1 91.05(6), O3–Fe1–Cl1 89.49(5), O1<sup>i</sup>–Fe1–Cl1 174.72(5), N1–Fe1–Cl1 105.72(6), O1–Fe1–O2 102.61(7), O1–Fe1–O3 102.34(7), O2–Fe1–O3 154.56(7), O2–Fe1–O1<sup>i</sup> 88.41(7), O3–Fe1–O1<sup>i</sup> 93.25(7). Symmetry code: <sup>i</sup> 1–*x*, 1–*y*, 1–*z*.

#### 2.2.4 Synthesis of $[\text{Fe}_2\text{Cl}_2(\text{Hbpmea})_2(\mu\text{-O})]\text{Cl}_2 \cdot 2\text{MeCN}$ (**P9** · 2MeCN)

The brown oil of Hbpmea was stirred with sodium bicarbonate in water to obtain the respective sodium salt. Afterwards, the colorless solid was directly treated with a solution of iron(III) chloride in acetonitrile to obtain **P9** · 2MeCN. The substance is stable for at least four months in the reaction solution under nitrogen atmosphere at 5°C. Removing the solvent results in turbidity of the crystalline product within a few hours due to the loss of co-crystallized solvent. **P9** · 2MeCN was characterized by elemental analysis, single-crystal X-ray diffraction, IR and UV-Vis spectroscopy.

A solution of **P9** · 2MeCN in acetonitrile shows UV-Vis absorption bands at 342 nm and 432 nm.

**P9** · 2MeCN crystallizes in the triclinic space group  $P\bar{1}$  with one formula unit in the primitive cell. The asymmetric unit includes half a complex cation, one chloride counterion and one molecule acetonitrile. The molecular structure of **P9** · 2MeCN is shown in Figure 2.11 with distances and angles in the respective caption. Due to inversion symmetry, the binuclear complex consists of two equivalent iron(III) central metals which

are bridged by an oxido ligand. In addition, each central metal is sixfold coordinated by one chlorido ligand and one tetradentate Hbpmea *via* three five-membered chelate rings. The chlorido ligands are in *trans* position to each other. The coordination polyhedron is a distorted octahedron. The Fe1–N1 distance of the ligand’s central nitrogen atom is circa 0.08 Å longer than the Fe1–N distances of the pyridyl moieties. Two symmetric equivalent, classical hydrogen bonds between the chloride ions and the non-deprotonated ligands are found. Distances and angles regarding the hydrogen bond are given in Table 2.

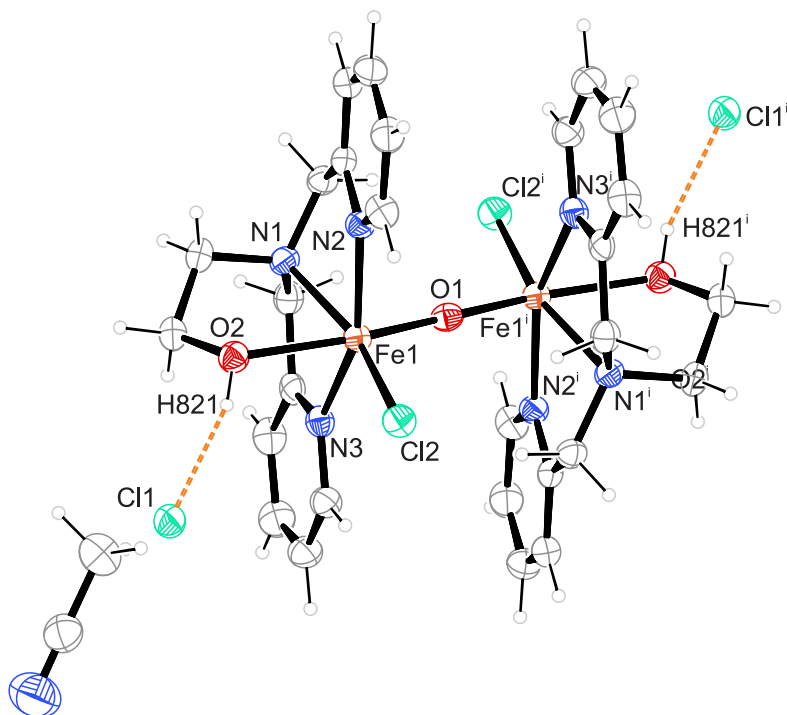


**Figure 2.11:** Ortep plot of  $[\text{Fe}_2\text{Cl}_2(\text{Hbpmea})_2(\mu\text{-O})]\text{Cl}_2 \cdot 2\text{MeCN}$  in crystals of **P9** · 2MeCN. For clarity, the symmetry generated acetonitrile is omitted. The thermal ellipsoids are drawn at 50% probability. Interatomic distances (Å) and bond angles ( $^\circ$ ). The standard deviation of the last decimal is given in parentheses: Fe1–O1 1.7929(4), Fe1–O2 2.204(2), Fe1–N1 2.194(3), Fe1–N2 2.126(3), Fe1–N3 2.112(3), Fe1–Cl2 2.2982(9); O1–Fe1–O2 167.35(6), O1–Fe1–N1 91.81(7), O1–Fe1–N2 93.08(7), O1–Fe1–N3 90.41(7), N2–Fe1–N1 76.8(1), N3–Fe1–N1 78.9(1), N3–Fe1–N2 155.5(1), N1–Fe1–O2 76.73(9), N2–Fe1–O2 89.51(9), N3–Fe1–O2 82.23(9), O1–Fe1–Cl2 104.73(3), O2–Fe1–Cl2 86.95(7), N1–Fe1–Cl2 163.38(8), N2–Fe1–Cl2 100.30(8), N3–Fe1–Cl2 102.28(8). Symmetry code:  $i$  1– $x$ , 1– $y$ , – $z$ .

**Table 2:** Distances and angles of hydrogen bonds in **P9** · 2MeCN. The standard deviation of the last decimal is given in parentheses.

D–H···A	$d(\text{D–H})/\text{\AA}$	$d(\text{H}\cdots\text{A})/\text{\AA}$	$d(\text{D}\cdots\text{A})/\text{\AA}$	$\angle(\text{D–H}\cdots\text{A})/^\circ$
O2–H821···Cl1	0.83(4)	2.17(4)	2.968(3)	161(4)

### 2.2.5 Synthesis of the salen precursor compounds (P10-P12)

[FeCl(salen)] (**P10**), [FeCl(*t*Bu<sub>2</sub>salen)] (**P11**) and [FeCl(*t*Bu<sub>4</sub>salen)] (**P12**) were synthesized according to literature procedures by adding the ligand together with triethylamine to an ethanolic solution of iron(III) chloride. The compounds are thermally stable and air-stable and were characterized by elemental analysis, IR and UV-Vis spectroscopy.<sup>[68,69]</sup> Acetonitrile solutions of the substances show absorption bands below 330 nm in all UV-Vis spectra. For each compound one absorption band in the visible region is observed. These bands are found at at 468 nm (**P10**), 482 nm (**P11**) and 502 nm (**P12**) .

### 2.2.6 Synthesis of [Fe(bipzpy)X<sub>3</sub>] (X = Cl, Br) (P13 and P14)

[Fe(bipzpy)Cl<sub>3</sub>] (**P13**) and [Fe(bipzpy)Br<sub>3</sub>] (**P14**) were prepared according to Gong *et al.* by adding bipzpy to a THF solution of the respective iron(III) halogenide.<sup>[70]</sup> While compound **P13** is thermally stable and air-stable, **P14** shows moisture sensitivity over longer time periods and needs to be stored under inert conditions. The compounds were characterized by elemental analysis, single-crystal X-ray diffraction, IR and UV-Vis spectroscopy. The crystal structure of **P13** was already described by In-Iam but with one additional methanol. However, the herein described solvent-free compound was used for the further discussion with related compounds.<sup>[71]</sup>

The UV-Vis-spectroscopic analysis of **P13** in acetonitrile shows absorption maxima at 304 nm and 359 nm. Beside many absorption bands below 310 nm, the UV-Vis spectrum of **P14** in acetonitrile exhibits two absorption bands at 390 nm and 468 nm.

**P13** crystallizes in the monoclinic space group  $P2_1/c$  and **P14** crystallizes in  $C2/c$ . Both substances exhibit four formula units in the unit cell. While **P13** exhibits one complex molecule in the asymmetric unit, **P14** contains only half a molecule due to a twofold axis through the Br-Fe-Br axis. Their molecular structures with the corresponding relevant distances and angles are depicted in Figures 2.12 and 2.13. In both neutral molecules, the central metals are meridionally coordinated by one tridentate bipzpy ligand *via* two five-membered chelate rings and three halogenido ligands. Due to the small bite angle of bipzpy, the coordination polyhedra are best described as strongly distorted octahedron. The N-Fe-N angles between the opposing nitrogen atoms of bipzpy and the iron center differ more than 30° from the 180° value of an ideal octahedron. The angles between the halogenido ligands are close to 90° in both molecules. A comparison of the distances between central metal and halogenido ligands reveals that in both cases the ligand, which is co-planar with bipzpy, is closer to the central metal than those which are axially coordinated. In the case of **P13** the equatorial chlorido ligand is approximately 0.10 Å closer to Fe1, in the case of the bromido ligand in **P14**, it is even 0.16 Å.

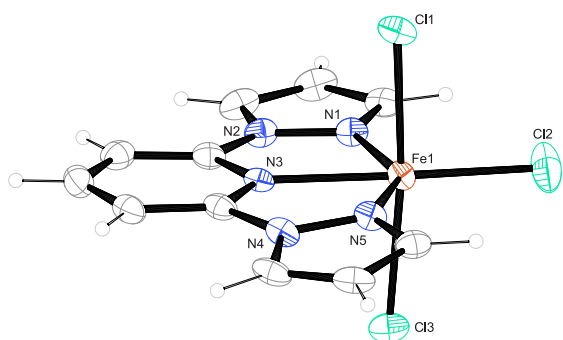


**Figure 2.12:** Ortep plot of  $[\text{Fe}(\text{bipzpy})\text{Cl}_3]$  in crystals of **P13**. The thermal ellipsoids are drawn at 50% probability. Interatomic distances ( $\text{\AA}$ ) and bond angles ( $^\circ$ ). The standard deviation of the last decimal is given in parentheses: Fe1–Cl1 2.346(1), Fe1–Cl2 2.252(1), Fe1–Cl3 2.357(1), Fe1–N1 2.110(3), Fe1–N3 2.145(3), Fe1–N5 2.131(3); N1–Fe1–N5 146.7(1), N1–Fe1–N3 73.1(1), N5–Fe1–N3 73.6(1), N1–Fe1–Cl1 91.38(9), N3–Fe1–Cl1 88.92(9), N5–Fe1–Cl1 85.38(9), N1–Fe1–Cl2 96.6(1), N3–Fe1–Cl2 169.6(1), N5–Fe1–Cl2 116.7(1), N1–Fe1–Cl3 94.46(9), N3–Fe1–Cl3 84.55(9), N5–Fe1–Cl3 85.01(9), Cl1–Fe1–Cl3 169.59(4), Cl2–Fe1–Cl1 93.54(5), Cl2–Fe1–Cl3 94.33(5).

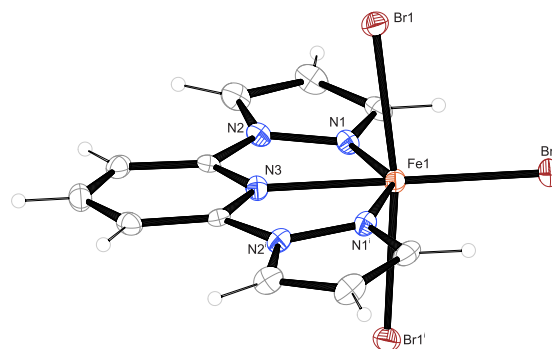


**Figure 2.13:** Ortep plot of  $[\text{Fe}(\text{bipzpy})\text{Br}_3]$  in crystals of **P14**. The thermal ellipsoids are drawn at 50% probability. Interatomic distances ( $\text{\AA}$ ) and bond angles ( $^\circ$ ). The standard deviation of the last decimal is given in parentheses: Fe1–Br1 2.5359(4), Fe1–Br2 2.3737(8), Fe1–N1 2.121(3), Fe1–N3 2.126(4); N1–Fe1–N1<sup>i</sup> 147.5(2), N1–Fe1–N3 73.77(8), N1–Fe1–Br1 106.23(8), N1<sup>i</sup>–Fe1–Br2 90.16(8), N1–Fe1–Br2 87.12(8), N3–Fe1–Br2 85.12(2), Br1–Fe1–Br2 94.88(2), Br1–Fe1–Br1<sup>i</sup> 170.24(3). Symmetry code: <sup>i</sup>  $-x, +y, 1/2-z$ .

### 2.2.7 Synthesis of $[\text{FeCl}_3(\text{Me}_3\text{tacn})]$ (**P15**)

$[\text{FeCl}_3(\text{Me}_3\text{tacn})]$  (**P15**) was prepared following the procedure of Chaudhuri *et al.* by reacting  $\text{Me}_3\text{tacn}$  with iron(III) chloride hexahydrate in methanol. The thermally stable and air-stable product was characterized by elemental analysis, IR and UV-Vis spectroscopy.<sup>[72]</sup>

In accordance with its color, solutions of **P15** in acetonitrile show a strong absorption at 392 nm which reaches in the visible region of the UV-Vis spectrum.

### 2.2.8 Synthesis of $[\text{FeCl}_2(\text{tpya})](\text{ClO}_4)$ (**P16**)

**P16** was synthesized by the reaction of tris(2-pyridylmethyl)amine with iron(III) chloride and sodium perchlorate in acetone. The thermally stable and air-stable substance can be stored without special conditions for several weeks. **P16** was characterized by elemental analysis, single-crystal X-ray diffraction, IR and UV-Vis spectroscopy.

In accordance with the pale yellow solution of **P16** in acetonitrile, the UV-Vis spectrum features only absorption bands in the UV region at 280 nm and 374 nm.

**P16** crystallizes in the chiral orthorhombic space group  $P2_12_12_1$  [Flack parameter = 0.005(11)] with four formula units in the primitive cell and one formula unit per asymmetric unit. The molecular structure with relevant distances and angles is shown in Figure 2.14. The iron center is sixfold coordinated by the tetradentate tpya ligand *via* three five-membered chelate rings and two chlorido ligands in *cis* position. The resulting coordination polyhedron can be best described as a slightly distorted octahedron. The Fe1–Cl1 distance is circa 0.05 Å longer than Fe1–Cl2. Due to the relatively small steric demand of the tetradentate tpya, the Cl1–Fe1–Cl2 angle is widened to over 90°.

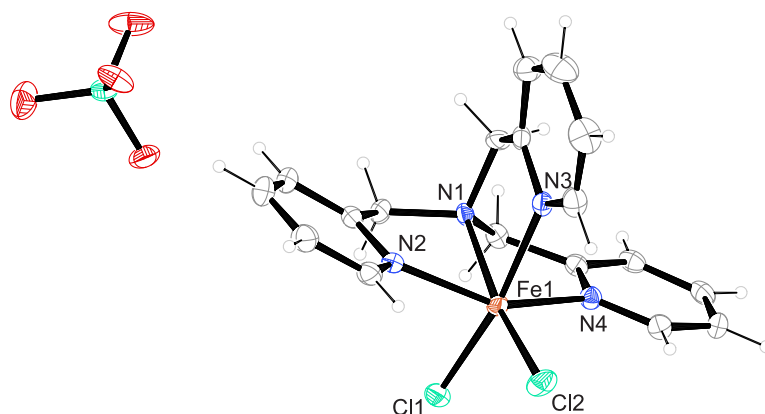


**Figure 2.14:** Ortep plot of  $[\text{FeCl}_2(\text{tpya})](\text{ClO}_4)$  in crystals of **P16**. The thermal ellipsoids are drawn at 50% probability. Interatomic distances (Å) and bond angles ( $^\circ$ ). The standard deviation of the last decimal is given in parentheses: Fe1–N1 2.207(3), Fe1–N2 2.146(3), Fe1–N3 2.203(3), Fe1–N4 2.119(3), Fe1–Cl1 2.288(1), Fe1–Cl2 2.240(1); N2–Fe1–N1 76.5(1), N3–Fe1–N1 78.7(1), N4–Fe1–N1 75.5(1), N1–Fe1–Cl2 170.66(8), N2–Fe1–Cl2 103.90(9), N3–Fe1–Cl2 92.08(8), N4–Fe1–Cl2 102.87(9), N1–Fe1–Cl1 91.33(8), N2–Fe1–Cl1 93.11(8), N3–Fe1–Cl1 169.46(8), N4–Fe1–Cl1 92.70(9), Cl2–Fe1–Cl1 97.96(4).

## 2.3 Nitrito compounds with O-Donor co-ligands

### 2.3.1 Synthesis of nitrito complexes with perfluoropinacolate (**1a-M** (M = Al, Sc, Cr, Fe, Ga, In, Tl, Bi) and **1b**)

Substances with the general formula  $(\text{HNEt}_3)_2[\text{M}^{\text{III}}(\text{fpin})_2(\text{NO}_2)]$  (**1a-M** with M = Al, Sc, Cr, Fe, Ga, In, Tl, Bi) were prepared by adding perfluoropinacol, triethylamine and silver nitrite to a solution of the respective metal chlorides (trifluoroacetate in the case of Tl) in methanol. Alternatively, **1a-Fe** can be synthesized by adding silver nitrite to a methanolic solution of **P1**. Crystals of **1a-Al**, **1a-Sc**, **1a-Cr**, **1a-Fe** and **1a-Ga** are stable under inert conditions at room temperature for more than half a year. However, **1a-In**, **1a-Tl** and **1a-Bi** cannot be stored longer than a week at 5°C under inert atmosphere. After that time, the crystals decay and turn black.

$(\text{PPN})_2[\text{Fe}_2(\text{fpin})_2(\text{NO}_2-\kappa^2\text{O}, \text{O}')_2(\mu\text{-OMe})_2]$  (**1b**) was prepared by adding perfluoropinacol and triethylamine to a methanolic solution of  $(\text{PPN})_2[\text{Fe}(\text{NO}_2)_4]$  which was *in-situ* synthesized according to the procedure published by Liaw *et al.*<sup>[73]</sup> **1b** is thermally stable, and air-sensitive but can be stored for at least three years at 5°C under an inert atmosphere. All **1a-M** substances and **1b** were characterized by single-crystal X-ray diffraction, elemental analysis, IR and UV-Vis spectroscopy.

Since the most obtained **1a-M** compounds are colorless, methanolic solutions show only absorptions in the UV region below 330 nm. Only the solution of **1a-Cr** in methanol shows an absorption at 585 nm. The yellow color of **1a-Bi** arises from a strong absorption at 357 nm, that spreads into the visible part of the spectrum. Although crystals of **1a-Fe** appear yellow, methanolic solutions of this compound only show absorption bands at 243 nm and 326 nm. The UV-Vis spectrum of **1b** in methanol exhibits absorption maxima at 225 nm and 320 nm.

Since the perfluoropinacolato ligands show many vibrational bands within the fingerprint region of the IR spectra, in most cases it was not possible to assign all nitrite-related bands. In most cases, the allocation was either performed by comparison with literature values or, if possible, due to the shifted bands of the  $^{15}\text{NO}_2^-$ -enriched substances.<sup>[74-78]</sup> Because there is no comparative data for **1a-Sc**, **1a-Ga** and **1a-Bi**, only the vibrational bands are given that could be reliably assigned due to the isotope-induced shift. Due to the small amount of **1a-Cr- $\kappa^2\text{O}, \text{O}'$**  in the crystal structure, no nitrite-related vibrations were found in the spectrum for the chelating nitrito ligand. Table 3 shows the identifiable nitrite-related vibrational bands of the **1a-M** substances. In the case of **1b**, only the bending vibration at  $823\text{cm}^{-1}$  could be assigned since a synthesis with  $\text{Ag}^{15}\text{NO}_2$  was not feasible.

**Table 3:** Identifiable IR vibrations of the nitrito ligands in the **1a-M** substances with the values of the respective vibrations in the  $^{15}\text{NO}_2^-$ -enriched substances.

Compound	vibration	$\tilde{\nu}(^{14}\text{NO}_2^-)/\text{cm}^{-1}$	$\tilde{\nu}(^{15}\text{NO}_2^-)/\text{cm}^{-1}$
<b>1a-Al</b>	$\delta$	858	853
	$\nu(\text{N}=\text{O})$	1510	1482
<b>1a-Sc</b>	$\delta$	857	851
<b>1a-Cr-<math>\kappa^2O</math></b>	$\delta$	837	–
	$\nu(\text{N}-\text{O})$	1039	–
<b>1a-Ga</b>	$\delta$	841	840
	$\nu(\text{N}-\text{O})$	1010	980
	$\nu(\text{N}=\text{O})$	1519	1492
<b>1a-In</b>	$\delta$	843	–
	$\nu_s$	1208	–
<b>1a-Tl</b>	$\delta$	846	841
	$\nu_s$	1209	1186
<b>1a-Bi</b>	$\delta$	813	805
	$\nu(\text{N}=\text{O})$	1375	1351

During the structure solution it became obvious that the crystal structures of **1a-Sc**, **1a-Cr- $\kappa^2O, O'$** , **1a-Fe** and **1a-In** are isotypic. All those structures share the same monoclinic space group ( $P2_1/c$ ) with four formula units in the unit cell. The respective asymmetric units consist of one complex anion with two triethylammonium cations. In Figure 2.15,  $(\text{HNEt}_3)_2[\text{Fe}(\text{fpin})_2(\text{NO}_2-\kappa^2O, O')]$  (**1a-Fe**) is depicted representative for **1a-Sc** and **1a-In**. Distances and angles of all three crystal structures are found in the caption. The central metals in the mononuclear compounds are sixfold coordinated by two bidentate perfluoropinacolato ligands *via* five-membered chelate rings and one chelating nitrito ligand. While in the case of **1a-Sc** and **1a-In** the M–O1 distances are rather similar to the M–O2 distances ( $\Delta \leq 0.01 \text{ \AA}$ ), the chelation in **1a-Cr- $\kappa^2O, O'$**  and **1a-Fe** is more asymmetric with deviations of circa  $0.02 \text{ \AA}$  and  $0.04 \text{ \AA}$ , respectively. Furthermore, all named isotypic structures share the same hydrogen-bond pattern. Therefore, the observed arrangements of two cations and one anion can be formulated as electroneutral 'molecules' that and interact only *via* weak C–H $\cdots$ F interactions in the solid. Beside two classical N–H $\cdots$ O<sub>fpin</sub> hydrogen bonds between the cations and the two opposing coordinated oxygen atoms O4 and O5 of the perfluoropinacolato ligands, further non-classical, very weak, C–H $\cdots$ F and slightly stronger C–H $\cdots$ O<sub>nitrite</sub> hydrogen bonds are found within the  $(\text{HNEt}_3)_2[\text{M}(\text{fpin})_2(\text{NO}_2-\kappa^2O, O')]$  entities. Relevant distances and angles related to the hydrogen bonds are listed in Table 4.

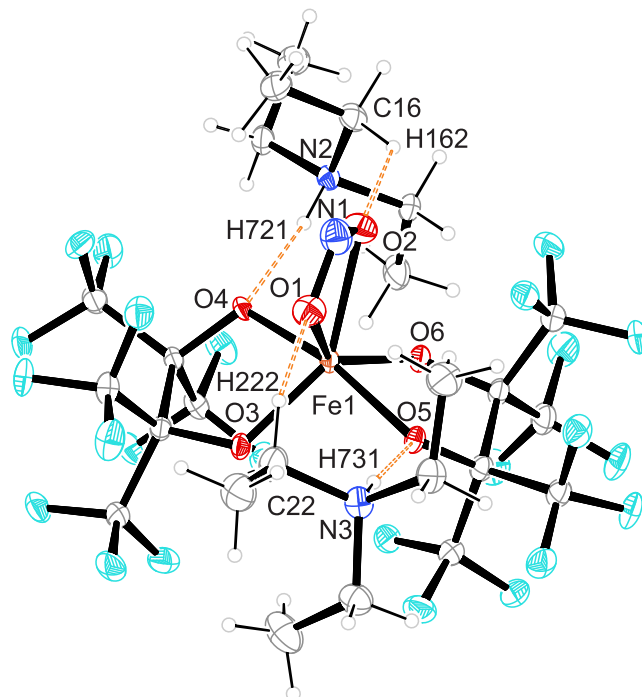


**Figure 2.15:** Ortep plot of  $(\text{HNEt}_3)_2[\text{Fe}(\text{fpin})_2(\text{NO}_2\text{-}\kappa^2\text{O},\text{O}')] in crystals of **1a-Fe** representative for **1a-Sc** and **1a-In**. The thermal ellipsoids are drawn at 50% probability. Interatomic distances ( $\text{\AA}$ ) and bond angles ( $^\circ$ ). The standard deviation of the last decimal is given in parentheses: Fe1–O1 2.197(2), Fe1–O2 2.158(2), Fe1–O3 1.934(1), Fe1–O4 2.015(2), Fe1–O5 1.999(2), Fe1–O6 1.928(2), O1–N1 1.257(3), N1–O2 1.252(3); O3–Fe1–O4 80.58(7), O6–Fe1–O5 81.01(7), O2–Fe1–O1 56.56(7), O3–Fe1–O5 93.46(7), O6–Fe1–O4 90.96(7), O6–Fe1–O3 125.99(7), O5–Fe1–O4 164.58(7), O6–Fe1–O2 93.88(7), O3–Fe1–O1 90.71(7), O2–N1–O1 110.6(2).$

Sc1–O1 2.258(1), Sc1–O2 2.245(1), Sc1–O3 2.013(1), Sc1–O4 2.084(1), Sc1–O5 2.101(1), Sc1–O6 2.018(1), N1–O1 1.264(2), N1–O2 1.267(2); O3–Sc1 O1 140.09(5), O3–Sc1 O2 96.16(5), O3–Sc1 O4 77.04(4), O3–Sc1 O5 92.24(4), O3–Sc1 O6 124.46(5), O4–Sc1 O1 88.15(5), O4–Sc1 O2 111.99(5), O4–Sc1 O5 159.63(4), O5–Sc1 O1 110.61(5), O5–Sc1 O2 86.09(4), O6–Sc1 O1 93.22(5), O6–Sc1 O2 135.91(5), O6–Sc1 O4 94.83(4), O6–Sc1 O5 76.83(4), O1–N1–O2 111.3(1).

In1–O1 2.293(2), In1–O2 2.280(2), In1–O3 2.080(2), In1–O4 2.150(2), In1–O5 2.140(2), In1–O6 2.076(2), N1–O1 1.258(4), N1–O2 1.261(4); O3–In1–O1 92.68(8), O3–In1–O2 135.97(8), O3–In1–O4 78.21(8), O3–In1–O5 94.07(8), O4–In1–O1 109.68(8), O4–In1–O2 86.37(8), O5–In1–O1 87.78(8), O5–In1–O2 110.59(8), O5–In1–O4 161.03(8), O6–In1–O1 140.14(8), O6–In1–O2 95.76(8), O6–In1–O3 125.29(8), O6–In1–O4 91.48(8), O6–In1–O5 78.76(8), O1–N1–O2 111.7(2).

In **1a-Cr** two different isomers of the complex anion are found disordered. However, the  $\kappa^2\text{O},\text{O}'$  isomers make up only 20% of the occupation which leads to a high standard deviation compared to the other structures. Figure 2.16 shows the molecular structure of the  $\kappa\text{O}$  isomer in crystals of **1a-Cr**, the co-crystallized  $\kappa^2\text{O},\text{O}'$  isomer is depicted in Figure 2.17. The N1–O1 and N1–O2 bond lengths differ less within the chelating isomer (0.06  $\text{\AA}$ ) than in the  $\kappa\text{O}$  isomer (0.10  $\text{\AA}$ ). As one might expect, the mean Cr–O<sub>fpin</sub> distances for the six-coordinated compound are larger than those of the five-coordinated substances. In addition, the perfluoropinacolato ligands are coordinated in a different way within the first named isomer, reasons for that are discussed in Section 3.6. Regarding the hydrogen bond situation, the chelating isomer shows the same pattern as the previously described ferrate(III), scandate(III) and indate(III). In the case of **1a-Cr** with the monodentate

bound nitrito ligand, a different hydrogen bond behavior is observed. Beside the two classical N–H···O hydrogen bonds, two weaker non-classical C–H···O bonds are found. The latter, are observed between two different methylene hydrogens of the triethylammonium cation with the coordinating oxygen atom O1a of the nitrito ligand and the O3a atom of the fpin ligand as acceptors. Distances and angles of the hydrogen bonds are listed in Table 4.

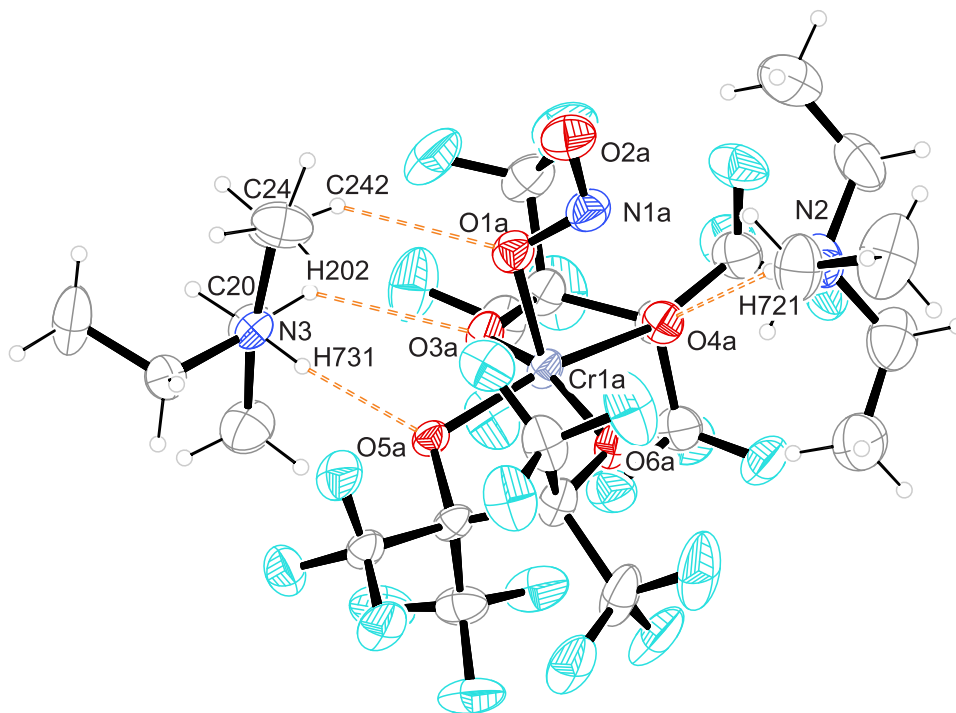


**Figure 2.16:** Ortep plot of  $(\text{HNEt}_3)_2[\text{Cr}(\text{fpin})_2(\text{NO}_2\text{-}\kappa\text{O})]$  in crystals of **1a-Cr**. The thermal ellipsoids are drawn at 50% probability. Interatomic distances (Å) and bond angles ( $^\circ$ ). The standard deviation of the last decimal is given in parentheses: Cr1a–O1a 1.906(2), Cr1a–O3a 1.917(4), Cr1a–O4a 1.946(3), Cr1a–O5a 1.962(3), Cr1a–O6a 1.910(4), N1a–O1a 1.307(7), N1a–O2a 1.207(6); O1a–Cr1a–O3a 97.6(2), O1a–Cr1a–O4a 98.3(1), O1a–Cr1a–O5a 92.5(1), O1a–Cr1a–O6a 103.3(2), O3a–Cr1a–O4a 83.0(1), O3a–Cr1a–O5a 95.3(2), O4a–Cr1a–O5a 169.3(1), O6a–Cr1a–O3a 159.1(2), O6a–Cr1a–O4a 95.3(2), O6a–Cr1a–O5a 82.6(1), O2a–N1a–O1a 114.4(5).

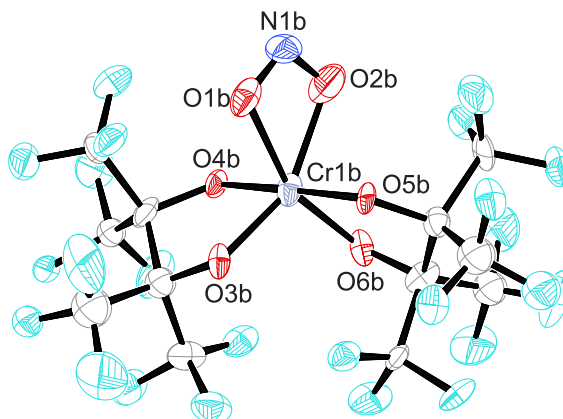


**Figure 2.17:** Ortep plot of  $(\text{HNEt}_3)_2[\text{Cr}(\text{fpin})_2(\text{NO}_2-\kappa^2\text{O},\text{O}')]$  in crystals of **1a-Cr**. The thermal ellipsoids are drawn at 50% probability. Interatomic distances (Å) and bond angles ( $^\circ$ ). The standard deviation of the last decimal is given in parentheses: Cr1b–O1b 2.06(1), Cr1b–O2b 2.08(3), Cr1b–O3b 1.90(2), Cr1b–O4b 1.78(1), Cr1b–O5b 1.97(1), Cr1b–O6b 1.90(2), N1b–O1b 1.27(2), N1b–O2b 1.33(3); O3b–Cr1b–O1b 97.6(6), O3b–Cr1b–O2b 155.7(8), O3b–Cr1b–O4b 81.0(5), O3b–Cr1b–O5b 99.8(6), O3b–Cr1b–O6b 104.3(7), O4b–Cr1b–O1b 93.1(5), O4b–Cr1b–O2b 87.6(8), O5b–Cr1b–O1b 89.5(4), O5b–Cr1b–O2b 92.6(8), O5b–Cr1b–O4b 177.2(5), O6b–Cr1b–O1b 157.4(6), O6b–Cr1b–O2b 98.2(8), O6b–Cr1b–O4b 96.1(6), O6b–Cr1b–O5b 81.1(5), O1b–N1b–O2b 109(2).

Beside **1a-Cr- $\kappa\text{O}$** , both compounds **1a-Al** and **1a-Ga** show nitrito ligands in the *E*-nitrito- $\kappa\text{O}$  binding mode. In Figure 2.18,  $(\text{HNEt}_3)_2[\text{Al}(\text{fpin})_2(\text{NO}_2-\kappa^2\text{O},\text{O}')] (\mathbf{1a-Al})$  is depicted. **1a-Ga** crystallizes isotypic and is therefore not shown. The distances and angles for both structures are found in the caption. In both substances the nitrito ligand is disordered in two directions in a ratio of circa 2:1 which is why only the most populated isomers are compared in the following part. Just as in the chromate, the N1–O2 bond lengths within the nitrito ligands are smaller than the N1–O1 distances. The respective differences are 0.10 Å in the case of **1a-Al** and 0.09 Å in the case of **1a-Ga**. Beside very weak non-classical C–H $\cdots$ F interactions, the classical N–H $\cdots$ O<sub>fpin</sub> hydrogen bonds between triethylammonium cations and the coordinating oxygen atoms O4 and O5 of the fpin ligand are found. Again, the arrangement of cations and anion forms a neutral 'molecule'. Distances and angles related to the hydrogen bonds are listed in Table 4.

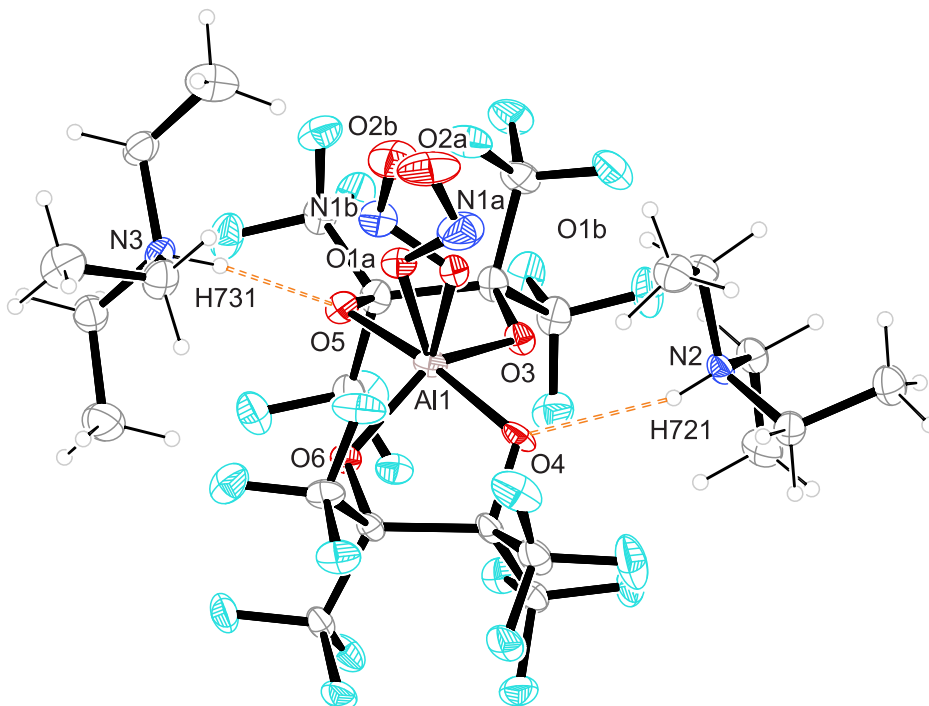


**Figure 2.18:** Ortep plot of  $(\text{HNEt}_3)_2[\text{Al}(\text{fpin})_2(\text{NO}_2\text{-}\kappa\text{O})]$  in crystals of **1a-Al**. The thermal ellipsoids are drawn at 50% probability. Interatomic distances (Å) and bond angles ( $^\circ$ ). The standard deviation of the last decimal is given in parentheses: Al1–O1a 1.834(5), Al1–O1b 1.821(8), Al1–O3 1.802(2), Al1–O6 1.806(2), Al1–O4 1.872(2), Al1–O5 1.885(2), O1a–N1a 1.306(7), O1b–N1b 1.31(1), N1a–O2a 1.206(8), N1b–O2b 1.21(1); O3–Al1–O1a 106.0(2), O3–Al1–O1a 106.0(2), O3–Al1–O1b 119.5(2), O3–Al1–O4 85.44(9), O3–Al1–O5 90.33(9), O3–Al1–O6 136.57(9), O4–Al1–O1a 104.1(2), O4–Al1–O1b 84.2(3), O4–Al1–O5 169.97(9), O5–Al1–O1a 85.9(2), O5–Al1–O1b 105.7(3), O6–Al1–O1a 116.7(2), O6–Al1–O1b 103.2(3), O6–Al1–O4 91.6(9), O6–Al1–O5 85.2(9), O1a–N1a–O2a 114.1(7), O1b–N1b–O2b 113.3(1).

Ga1–O1a 1.906(5), Ga1–O1b 1.881(9), Ga1–O3 1.877(2), Ga1–O4 1.955(2), Ga1–O5 1.967(2), Ga1–O6 1.880(2), N1a–O1a 1.301(7), N1a–O2a 1.211(8), N1b–O1b 1.30(1), N1b–O2b 1.24(1); O3–Ga1–O1a 106.5(2), O3–Ga1–O1b 121.6(2), O3–Ga1–O4 84.63(8), O3–Ga1–O5 91.04(8), O3–Ga1–O6 134.45(8), O4–Ga1–O1a 104.6(2), O4–Ga1–O1b 85.1(3), O4–Ga1–O5 169.37(8), O1b–Ga1–O5 105.4(3), O1a–Ga1–O5 86.0(2), O6–Ga1–O1a 118.2(2), O6–Ga1–O1b 103.2(2), O6–Ga1–O4 92.04(8), O6–Ga1–O5 84.05(8), O2a–N1a–O1a 113.9(6), O2b–N1b–O1b 113.3(1).

Despite the fact that the thallium complex **1a-Tl** is composed like all other mononuclear examples in this row, and its appearance with a chelating nitrito ligand reminds of the compounds **1a-M** ( $M = \text{Sc}, \text{Fe}, \text{In}$ ) the structures are not isotypic. Beside different cell parameters, this becomes obvious when the hydrogen bonds are examined in more detail. While both triethylammonium cations in **1a-M** ( $M = \text{Sc}, \text{Fe}, \text{In}$ ) stabilize the structure by forming non-classical hydrogen bonds towards the nitrito ligand, it is only one of the both cations in **1a-Tl**. The other cation forms a  $\text{C-H}\cdots\text{O}_{\text{fpin}}$  interaction between one methylene H and the coordinating O6 atom of one fpin ligand. However, the two  $\text{N-H}\cdots\text{O}_{\text{fpin}}$  hydrogen bonds which are found in almost every structure of the **1a-M** series are also present in **1a-Tl**. Further information regarding the hydrogen bonds are given in Table 4. The N–O distances within the chelating nitrito ligand are almost equal as in **1a-Sc** and **1a-In**.

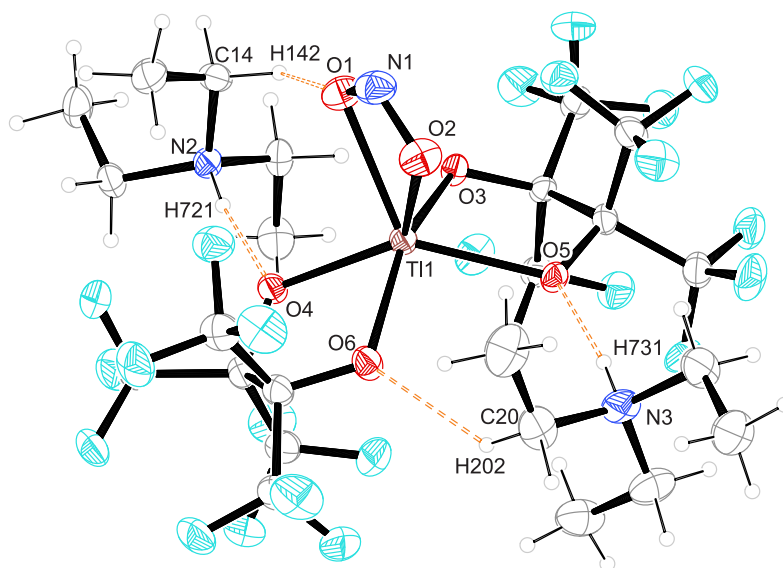


**Figure 2.19:** Ortep plot of  $(\text{HNEt}_3)_2[\text{Tl}(\text{fpin})_2(\text{NO}_2-\kappa^2\text{O},\text{O}')] ]$  in crystals of **1a-Tl**. The thermal ellipsoids are drawn at 50% probability. Interatomic distances ( $\text{\AA}$ ) and bond angles ( $^\circ$ ). The standard deviation of the last decimal is given in parentheses: Tl1–O1 2.383(3), Tl1–O2 2.387(3), Tl1–O3 2.149(2), Tl1–O4 2.249(2), Tl1–O5 2.255(2), Tl1–O6 2.149(2), N1–O1 1.251(4), N1–O2 1.255(4); O3–Tl1–O1 122.3(1), O3–Tl1–O2 90.5(1), O3–Tl1–O4 76.14(9), O3–Tl1–O5 92.31(9), O3–Tl1–O6 152.3(1), O4–Tl1–O1 93.9(1), O4–Tl1–O2 128.5(1), O4–Tl1–O5 137.98(9), O5–Tl1–O1 125.27(9), O5–Tl1–O2 91.2(1), O6–Tl1–O1 83.97(9), O6–Tl1–O2 114.8(1), O6–Tl1–O4 94.84(9), O6–Tl1–O5 76.84(9), O1–N1–O2 113.5(3).

The structure within the  $(\text{HNEt}_3)_2[\text{M}^{\text{III}}(\text{fpin})_2(\text{NO}_2)]$  series that deviates the most is found with the bismuth complex. As the only example this compound crystallizes in the monoclinic space group  $P2_1/n$ . The primitive cell contains four formula units and the asymmetric unit consists of one complex anion with two triethylammonium cations. The molecular structure of  $(\text{HNEt}_3)_2[\text{Bi}(\text{fpin})_2(\text{NO}_2-\kappa\text{O})]$  (**1a-Bi**) is shown in Figure 2.20 with distances and angles in the caption. As in the other complexes with monodentate bound nitrito ligands, the N1–O2 distance is shorter (0.05  $\text{\AA}$ ) than the N1–O1 distance. The nitrito ligand is bound in its  $E-\kappa\text{O}$  binding mode, but in contrast to **1a-Al** and **1a-Ga** it is not disordered and strongly tilted towards one of two cations. This results in a different hydrogen-bond situation compared to the other mononuclear fpin-complexes. While one of the two cations forms a classical hydrogen bond towards the coordinating O4 atom of one fpin ligand, the other triethylammonium cation forms a second classical hydrogen bond with O1 of the nitrito ligand as acceptor. Further information regarding the hydrogen bonds are given in Table 4.

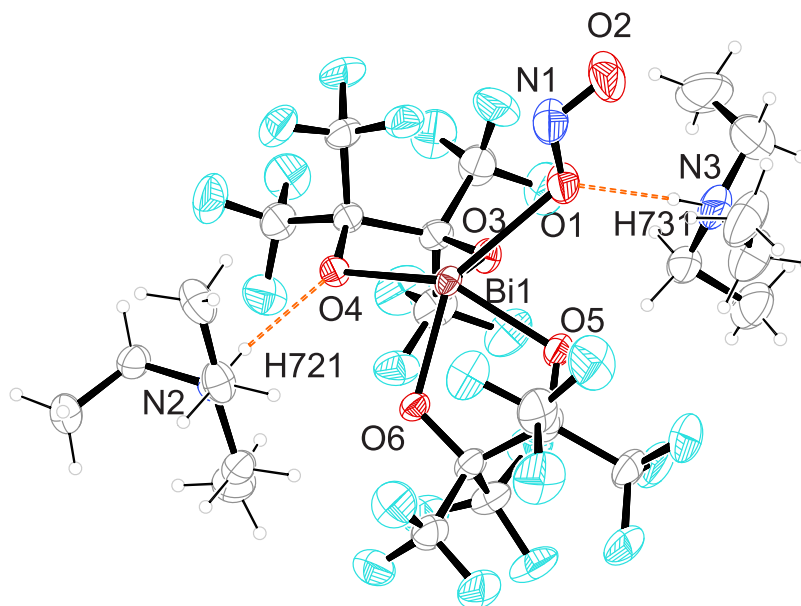


**Figure 2.20:** Ortep plot of  $(\text{HNEt}_3)_2[\text{Bi}(\text{fpin})_2(\text{NO}_2\text{-}\kappa O)]$  in crystals of **1a-Bi**. The thermal ellipsoids are drawn at 50% probability. Only one position of the disordered N3 triethylammonium ion is depicted. Interatomic distances ( $\text{\AA}$ ) and bond angles ( $^\circ$ ). The standard deviation of the last decimal is given in parentheses: Bi1–O1 2.562(2), Bi1–O3 2.128(2), Bi1–O4 2.383(2), Bi1–O5 2.203(2), Bi1–O6 2.201(2), N1–O1 1.272(3), N1–O2 1.221(3); O3–Bi1–O1 74.39(7), O3–Bi1–O4 71.47(6), O3–Bi1–O5 86.34(7), O3–Bi1–O6 102.73(6), O4–Bi1–O1 128.42(6), O5–Bi1–O4 140.35(6), O5–Bi1–O1 72.30(7), O6–Bi1–O1 145.46(6), O6–Bi1–O4 80.07(6), O6–Bi1–O5 73.17(6), O2–N1–O1 114.3(2).

## Results

**Table 4:** Distances and angles of hydrogen bonds in **1a-M**. The standard deviation of the last decimal is given in parentheses.

Compound	D–H···A	$d(\text{D–H})/\text{\AA}$	$d(\text{H}\cdots\text{A})/\text{\AA}$	$d(\text{D}\cdots\text{A})/\text{\AA}$	$\angle(\text{D–H}\cdots\text{A})/^\circ$
<b>1a-Sc</b>	N2–H721···O4	0.83(2)	2.20(2)	3.013(2)	166(2)
	N3–H731···O5	0.84(2)	2.06(2)	2.888(2)	174(2)
	C22–H222···O1	0.99	2.29	3.076(2)	135.3
	C16–H161···O2	0.99	2.33	3.067(2)	130.7
<b>1a-Cr-<math>\kappa^2O,O'</math></b>	N2–H721···O4B	0.81(3)	2.10(4)	2.903(1)	165(3)
	N3–H731···O5B	0.84(3)	2.09(3)	2.871(9)	155(3)
	C22–H222···O1	0.99	2.53	3.09(3)	115.6
	C16–H161···O2	0.99	1.81	2.715(1)	150.3
<b>1a-Fe</b>	N2–H721···O4	0.89(3)	2.16(3)	3.020(3)	164(2)
	N3–H731···O5	0.90(3)	1.97(3)	2.872(3)	175(2)
	C22–H222···O1	0.99	2.33	3.038(3)	127.7
	C16–H161···O2	0.99	2.32	3.031(3)	128.0
<b>1a-In</b>	N2–H721···O4	0.88(4)	2.12(4)	2.974(3)	163(3)
	N3–H731···O5	0.75(4)	2.10(4)	2.853(3)	177(4)
	C22–H222···O1	0.99	2.34	3.082(4)	131.5
	C16–H161···O2	0.99	2.31	3.113(4)	137.8
<b>1a-Al</b>	N2–H721···O4	0.78(3)	2.22(3)	2.958(3)	161(3)
	N3–H731···O5	0.91(3)	1.97(4)	2.872(3)	173(3)
<b>1a-Ga</b>	N2–H721···O4	0.88(3)	2.08(3)	2.930(3)	161(3)
	N3–H731···O5	0.84(3)	2.01(3)	2.850(3)	174(3)
<b>1a-Cr-<math>\kappa O</math></b>	N2–H721···O4A	0.81(3)	2.22(4)	3.004(4)	162(3)
	N3–H731···O5A	0.84(3)	2.03(3)	2.867(3)	172(3)
	C24–H242···O1a	0.99	2.54	3.269(4)	130.5
	C20–H202···O3A	0.99	2.46	3.224(5)	133.4
<b>1a-Tl</b>	N2–H721···O4	0.84(4)	2.02(5)	2.847(4)	169(4)
	N3–H731···O5	0.88(4)	1.97(4)	2.843(4)	172(4)
	C14–H142···O1	0.99	2.52	3.248(5)	130.3
<b>1a-Bi</b>	N2–H721···O4	0.90(3)	2.01(3)	2.854(3)	156(3)
	N3–H731···O1	0.76(4)	2.01(4)	2.769(3)	177(4)

**1b** crystallizes in the monoclinic space group  $P2_1/c$  with two formula units in the unit cell. The asymmetric unit contains half a complex anion and one PPN cation. Each central metal in the inversion symmetric, binuclear compound **1b** is sixfold coordinated by one chelating nitrito ligand, two bridging methoxido ligands and one perfluoropinacolate that coordinates *via* a five-membered chelate ring. The coordination environment of **1b** is comparable to that of **1a-Fe** and can best be described as a strongly distorted octahedron. The molecular structure of **1b** is depicted in Figure 2.21 with the most relevant distances and angles in the caption. The mean Fe–O<sub>fpin</sub> distance is 1.935 Å.

Despite the similarity to **1a-Fe** with regard to the coordination environment of the central metals, some differences are observed with regard to the nitrito ligand. While in **1a-Fe** the difference between Fe1–O1 and Fe1–O2 is 0.04 Å, it is 0.09 Å in **1b**. The N1–O2 distance in **1b** is 0.02 Å smaller compared to N1–O1. The O1–N1–O2 angle is slightly larger than in **1a-Fe** which corresponds with the slightly more asymmetric coordination of the nitrito ligand. Therefore, the nitrito ligand seems not to be an ideal chelating nitrito ligand but has tendencies to be a *Z*-nitrito- $\kappa O$  ligand.

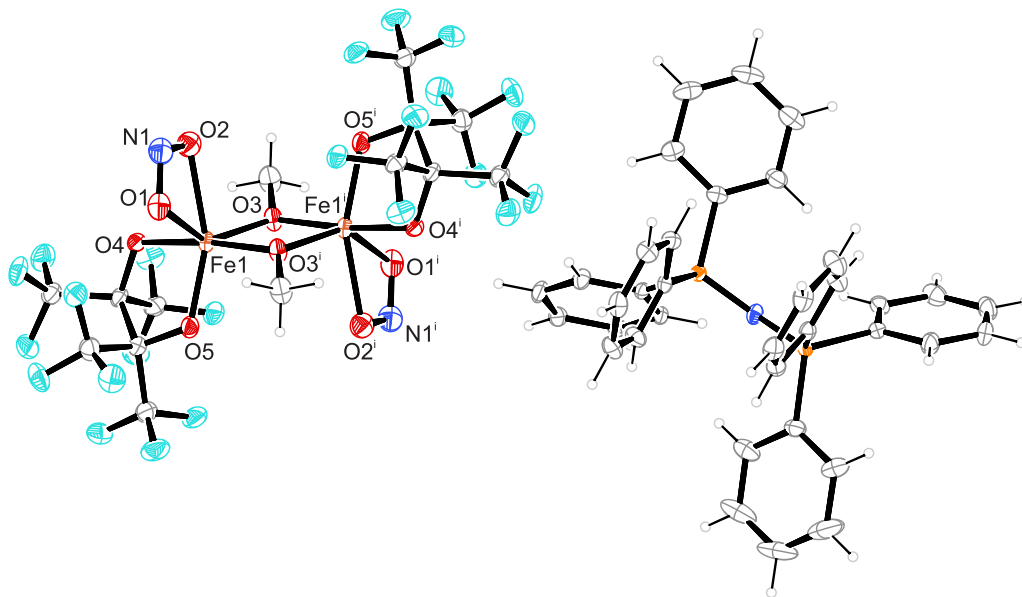


**Figure 2.21:** Ortep plot of  $(\text{PPN})_2[\text{Fe}_2(\text{fpin})_2(\text{NO}_2\text{-}\kappa^2\text{O},\text{O}')_2(\mu\text{-OMe})_2]$  in crystals of **1b**. The thermal ellipsoids are drawn at 50% probability. For clarity, the second, symmetry generated PPN cation is omitted. Interatomic distances (Å) and bond angles ( $^\circ$ ). The standard deviation of the last decimal is given in parentheses: Fe–O1 2.127(1), Fe–O2 2.219(2), Fe–O3 1.957(2), Fe–O3<sup>i</sup> 1.986(2), Fe–O4 1.937(2), Fe–O5 1.933(2), N1–O1 1.274(3), N1–O2 1.254(3); O1–Fe1–O2 57.35(6), O3–Fe1–O3<sup>i</sup> 76.40(6), O4–Fe1–O5 81.78(6), Fe–O3–Fe<sup>i</sup> 103.61(7), O2–N1–O1 111.3(2). Symmetry code: <sup>i</sup>  $-x, 2-y, 1-z$ .

The steric demand of the perfluoropinacolato ligand leads to markedly distorted coordination polyhedra. Published results show that the coordination numbers four and five are preferred, and only a few examples for coordination numbers of six or higher are found for the late transition metals.<sup>[79–83]</sup> In terms of Alvarez’s Continuous Shape Measurements (CShM), the coordination polyhedra are more or less distorted variants of a trigonal prism (TPR-6) or an octahedron (OC-6).<sup>[84]</sup> Figure 2.22 shows the so-called Bailar path which connects an ideal octahedron and an ideal trigonal prism via the rotation of two opposite triangles as the only distortion. The obtained CShMOC-6 and CShMTPR-6 values lie apart from the Bailar path thus indicating an additional type of distortion.<sup>[84]</sup> While **1a-Al**, **1a-Cr- $\kappa O$**  and **1a-Ga** show only slightly distorted square pyramidal coordination, the distortion in the compounds containing chelating nitrito ligands is pronounced. While the coordination polyhedron **1a-Tl** is better described as a trigonal bipyramid, it is more an octahedron in the case of **1a-Cr- $\kappa^2 O, O'$** . The three isostructural compounds **1a-Sc**, **1a-Fe** and **1a-In** and the binuclear **1b** are inbetween those two coordination figures.

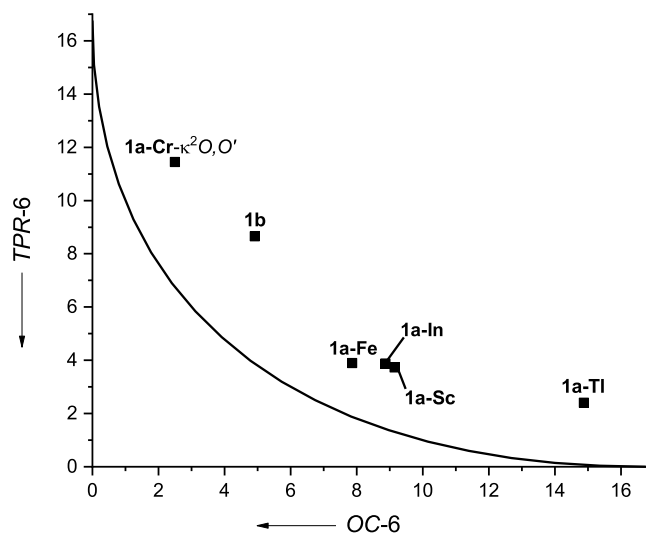


**Figure 2.22:** CShM calculations of the hexacoordinated anions in **1a-M** ( $M = \text{Sc}, \text{Cr}, \text{Fe}, \text{In}, \text{Tl}$ ) and **1b** (black squares); the solid line marks the Bailar path.<sup>[84]</sup> Ideal OC-6 at (0, 16.737), ideal TPR-6 at (16.737, 0).

### 2.3.2 Synthesis of nitritoiron complexes with bisphosphane oxides (2-4)

The nitrito complexes with bisphosphane oxide as auxiliary ligands of the general formula  $[\text{FeL}_2(\text{NO}_2)_2](\text{ClO}_4)$  ( $L = \text{dppe}(\text{O})_2$  (**2** · MeCN),  $\text{dppp}(\text{O})_2$  (**3** · 2MeCN),  $\text{dppf}(\text{O})_2$  (**4** · 3MeCN)) were obtained by dissolving the respective chlorido complexes **P2-P4** in acetonitrile and adding a stoichiometric amount of silver nitrite (**3** · 2MeCN and **4** · 3MeCN). In the case of **2** · MeCN, a slight surplus of silver nitrite was used. The dried powders of **2** · MeCN and **3** · 2MeCN are thermally stable and air-stable. **4** · 3MeCN decomposes quickly after the removal of the crystals from the mother liquor by the loss of co-crystallized solvent which is observed by outgasing in paraffin oil and therefore has to be kept in the reaction solution at  $-25^\circ\text{C}$ . If stored at room temperature without solvent, crystals of **4** · 3MeCN turn opaque after a few hours. The substances were characterized by single-crystal X-ray diffraction, elemental analysis, IR and UV-Vis spectroscopy.

Acetonitrile solutions of all compounds show absorption bands below 300 nm. In the case of **3** · 2MeCN an additional absorption band appears at 358 nm (**3** · 2MeCN). **4** · 3MeCN shows absorptions at 306 nm and 435 nm.

The IR vibrational bands of the nitrito ligands in all bisphosphane oxide compounds **2-4** were allocated by comparison with the IR spectra of corresponding precursor compounds **P2-P4**. The three observable vibration bands for each compound are depicted in Table 5.

**Table 5:** IR vibrations of the nitrito ligands in compounds **2-4** verified by comparison with their respective precursor compounds **P2-P4**.

compound	vibration	$\tilde{\nu}(\text{NO}_2^-)/\text{cm}^{-1}$
	$\delta$	809
<b>2</b> · MeCN	$\nu(\text{N-O})$	985
	$\nu(\text{N=O})$	1472
	$\delta$	805
<b>3</b> · 2MeCN	$\nu(\text{N-O})$	981
	$\nu(\text{N=O})$	1469
	$\delta$	818
<b>4</b> · 3MeCN	$\nu(\text{N-O})$	1006
	$\nu(\text{N=O})$	1460

All isolated nitrito complexes with bisphosphane oxide ligands crystallize in different monoclinic space groups with four formula units in the unit cell. The space groups are  $P2_1/c$  (**2** · MeCN),  $P2_1/n$  (**3** · 2MeCN) and  $C2/c$  (**4** · 3MeCN). The asymmetric cells of **3** · 2MeCN and **4** · 3MeCN consist of one complex cation, one perchlorate anion and two (**3** · 2MeCN) or three (**4** · 3MeCN) acetonitrile. In the case of **2** · MeCN, two independent halves of the complex cation together with one perchlorate anion and one acetonitrile are found in the asymmetric unit cell. In every structure, the perchlorate counter-ion is more or less disordered. The molecular structures of the compounds **2-4** with all relevant distances and angles in the captions are depicted in Figure 2.23, Figure 2.24 and Figure 2.25, respectively.

Each central metal in **2** · MeCN, **3** · 2MeCN and **4** · 3MeCN is sixfold coordinated by two chelating bisphosphane oxide ligands in equatorial position. The axial positions are occupied by two *E*-nitrito- $\kappa\text{O}$  ligands. The resulting coordination polyhedra are nearly perfect octahedra. The bisphosphane oxide ligands coordinate *via* a seven-membered chelate ring in **2** · MeCN and an eight-membered chelate ring in **3** · 2MeCN. The nitrito ligands in **2** · MeCN and **4** · 3MeCN point in opposite directions while those ligands in **3** · 2MeCN face in the same direction. The mean Fe–O distances between the central metal and phosphane oxide ligands are 1.991 Å in **2** · MeCN, 1.997 Å in **3** · 2MeCN and 1.992 Å in **4** · 3MeCN. All O–Fe–O angles in the three complexes are nearly 90°. The average Fe–O<sub>nitrite</sub> distances are around 2.0 Å and the O–N–O angles in all complexes do not differ much from 114°. Within the nitrito ligands the distance between the nitrogen atom and the non-bound oxygen atom is shorter than the distance to the coordinated oxygen atom. The mean differences are 0.104 Å in **2** · MeCN, 0.111 Å in **3** · 2MeCN and 0.08 Å in **4** · 3MeCN.

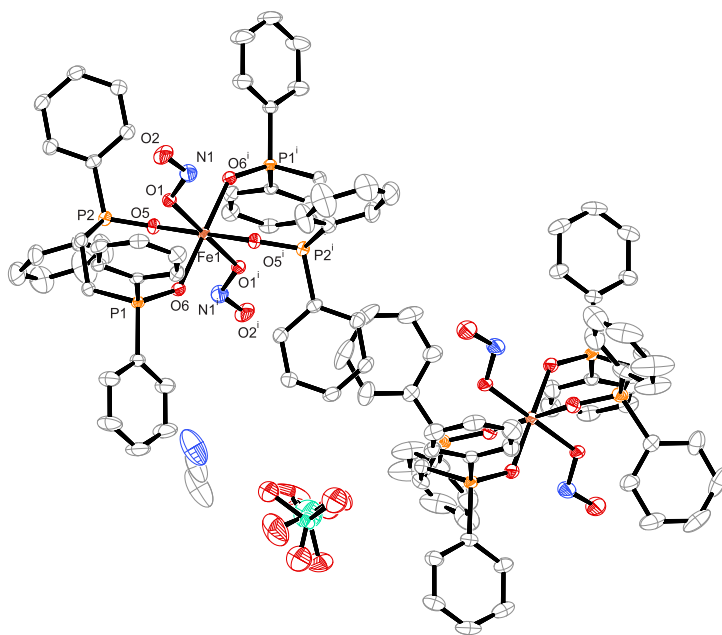


**Figure 2.23:** Ortep plot of  $[\text{Fe}(\text{dppe}(\text{O})_2)_2(\text{NO}_2\text{-}\kappa\text{O})_2](\text{ClO}_4) \cdot \text{MeCN}$  in crystals of **2** · MeCN. The thermal ellipsoids are drawn at 50% probability. For clarity, hydrogen atoms are not depicted. Interatomic distances (Å) and bond angles ( $^\circ$ ). The standard deviation of the last decimal is given in parentheses: Fe1–O1 1.994(1), Fe1–O5 2.001(2), Fe1–O6 2.005(2), N1–O1 1.309(3), N1–O2 1.205(3); O1<sup>i</sup>–Fe1–O6 90.21(7), O1–Fe1–O5 93.28(7), O1<sup>i</sup>–Fe1–O5 86.72(7), O1–Fe1–O6 89.79(7), O5<sup>i</sup>–Fe1–O6 89.93(7), O5–Fe1–O6 90.07(7), O2–N1–O1 113.6(2). Symmetry code: <sup>i</sup>  $-x, 1-y, 1-z$ .

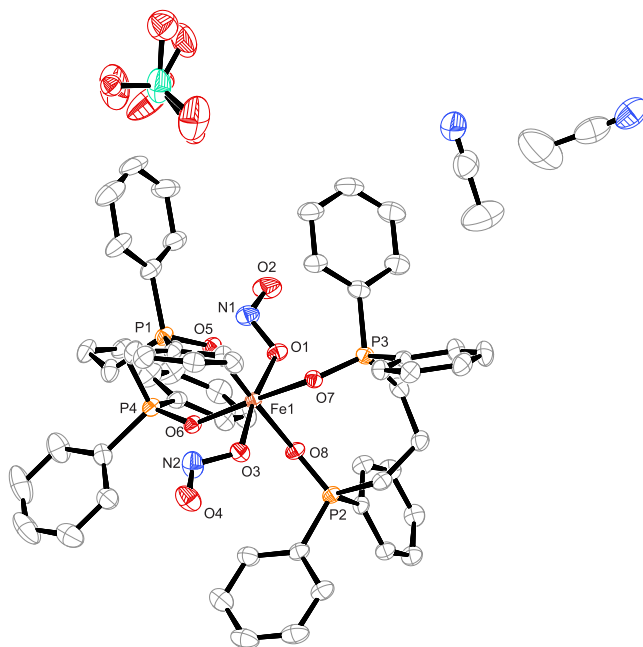


**Figure 2.24:** Ortep plot of  $[\text{Fe}(\text{dppp}(\text{O})_2)_2(\text{NO}_2\text{-}\kappa\text{O})_2](\text{ClO}_4) \cdot 2\text{MeCN}$  in crystals of **3** · 2MeCN. The thermal ellipsoids are drawn at 50% probability. For clarity, hydrogen atoms are not depicted. Interatomic distances (Å) and bond angles ( $^\circ$ ). The standard deviation of the last decimal is given in parentheses: Fe1–O1 2.015(2), Fe1–O3 2.004(2), Fe1–O6 1.981(2), Fe1–O5 2.000(2), Fe1–O7 1.989(2), Fe1–O8 2.017(2), N1–O1 1.315(3), N1–O2 1.204(3), N2–O4 1.199(4), N2–O3 1.310(3); O7–Fe1–O8 91.44(8), O6–Fe1–O5 90.66(8), O7–Fe1–O5 88.35(8), O6–Fe1–O8 89.83(8), O6–Fe1–O7 175.19(9), O5–Fe1–O8 176.65(8), O3–Fe1–O7 89.72(8), O3–Fe1–O8 86.20(8), O1–Fe1–O7 83.59(8), O1–Fe1–O8 88.74(8), O3–Fe1–O1 171.50(9), O2–N1–O1 114.1(3), O4–N2–O3 115.1(3).

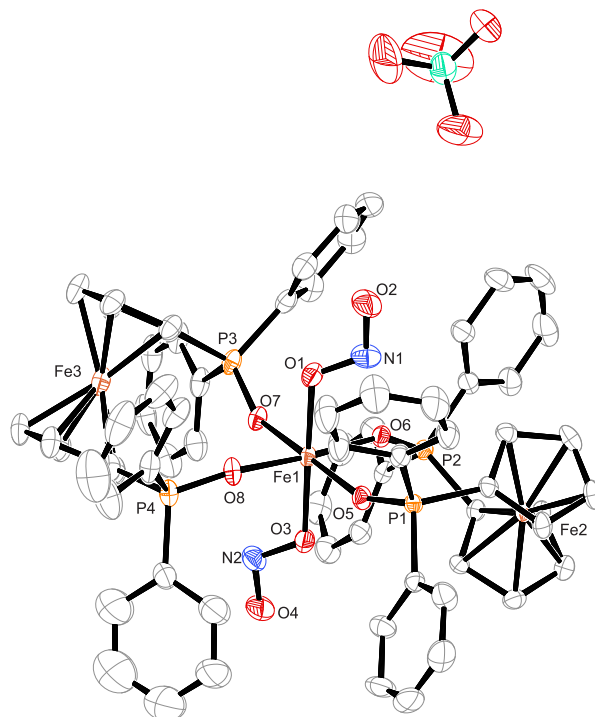


**Figure 2.25:** Ortep plot of  $[\text{Fe}(\text{dppf}(\text{O})_2)_2(\text{NO}_2\text{-}\kappa\text{O})_2](\text{ClO}_4) \cdot 3\text{MeCN}$  in crystals of  $4 \cdot 3\text{MeCN}$ . The thermal ellipsoids are drawn at 50% probability. For clarity, hydrogen atoms and co-crystallized solvent molecules are not depicted. Interatomic distances ( $\text{\AA}$ ) and bond angles ( $^\circ$ ). The standard deviation of the last decimal is given in parentheses: Fe1–O1 2.008(3), Fe1–O3 2.019(3), Fe1–O5 2.001(3), Fe1–O6 1.972(3), Fe1–O7 1.999(3), Fe1–O8 1.995(3), N1–O1 1.282(5), N1–O2 1.212(5), N2–O3 1.306(5), N2–O4 1.220(5); O6–Fe1–O8 176.6(1), O6–Fe1–O7 87.2(1), O8–Fe1–O7 91.2(1), O6–Fe1–O5 89.9(1), O8–Fe1–O5 92.0(1), O7–Fe1–O5 175.7(1), O6–Fe1–O1 91.4(1), O8–Fe1–O1 85.6(1), O7–Fe1–O1 90.4(1), O5–Fe1–O1 92.7(1), O6–Fe1–O3 89.9(1), O8–Fe1–O3 93.2(1), O7–Fe1–O3 92.6(1), O5–Fe1–O3 84.4(1), O1–Fe1–O3 176.8(1), O2–N1–O1 114.0(4), O4–N2–O3 112.6(4).

## 2.4 Nitrito compounds with N,O-Donor co-ligands

### 2.4.1 Synthesis of nitritoiron complexes with aminocarboxylato ligands (5-8)

The nitrito complexes with aminocarboxylato co-ligands **5** · 2MeCN, **6** and **8** were prepared by adding stoichiometric amounts of silver nitrite to acetonitrile solutions of the respective precursor compounds. In the case of **7** a surplus of silver nitrite was used. Crystals and solutions of **5** · 2MeCN are not stable against air and higher temperatures. They decompose rapidly after removing them from the mother liquor yielding a yellow amorphous powder. After the synthesis and successful crystallization, the crystals are stable for 2 days only at most and decompose a few minutes after the reaction vessel was opened. Therefore, the characterization of **5** · 2MeCN was only possible by single-crystal X-ray diffraction and no yield was determined. Products **6** and **8** are thermally stable but need to be stored under inert atmosphere to avoid oxidation. Compound **7** is thermally stable and air-stable for several weeks. **6-8** were characterized by single-crystal X-ray diffraction, elemental analysis, IR and UV-Vis spectroscopy.

The UV-Vis-spectroscopic analysis of **6-8** in acetonitrile features absorption bands at 276 nm **6** and 251 nm **7**. **8** exhibits absorption maxima at 256 nm and 300 nm. IR-spectroscopic characterization of the stable compounds showed all nitrite-related vibration modes which were identified by comparison with the associated precursor compound (**P6-P8**). The vibration modes were verified by the isotope-induced shift in the IR spectra of the  $^{15}\text{NO}_2^-$ -enriched substances. A summary of the nitrite-related vibrations is depicted in Table 6.

**Table 6:** IR vibrations of the nitrito ligands in compounds **6-8** with the values of the respective vibrations in the  $^{15}\text{NO}_2^-$ -enriched substances.

Compound	vibration	$\tilde{\nu}(^{14}\text{NO}_2^-)/\text{cm}^{-1}$	$\tilde{\nu}(^{15}\text{NO}_2^-)/\text{cm}^{-1}$
<b>6</b>	$\delta$	814	811
	$\nu(\text{N-O})$	968	954
	$\nu(\text{N=O})$	1462	1446
<b>7</b>	$\delta$	824	823
	$\nu(\text{N-O})$	1146	1122
	$\nu(\text{N=O})$	1381	1355
<b>8</b>	$\delta$	806/863	805/859
	$\nu(\text{N-O})/\nu_{\text{as}}$	1125/1255	1101/1240
	$\nu(\text{N=O})/\nu_{\text{s}}$	1396/1320	1372/1308

**5** · 2MeCN and **6** crystallize in the triclinic space group  $P\bar{1}$ . **7** crystallizes in the orthorhombic space group  $Pbca$  and compound **8** in the monoclinic space group  $P2_1/c$ .

While the unit cell of  $\mathbf{5} \cdot 2\text{MeCN}$  contains two formula units, it has four formula units for the other three substances. The asymmetric unit cells of  $\mathbf{5} \cdot 2\text{MeCN}$  and  $\mathbf{8}$  consist of one formula unit. The asymmetric unit cell of  $\mathbf{7}$  consists of half a formula unit. In the case of  $\mathbf{6}$ , two independent complex molecules are found in the asymmetric unit cell.

The molecular structure of  $\mathbf{5} \cdot 2\text{MeCN}$  reveals that the iron center is sixfold coordinated by two bidentate quinolinecarboxylato ligands *via* five-membered chelate rings. As well as in the precursor compound **P5**, the carboxy moieties coordinate in *trans* position. The remaining coordination sites are occupied by two *E*-nitrito- $\kappa O$  ligands in *cis* position. The resulting coordination polyhedron is an almost non-distorted octahedron. The mono-anionic complex crystallizes with one  $\text{NBnMe}_3^+$  cation and two equivalents of acetonitrile. The nitrito complex is slightly disordered with the corresponding chlorido complex **P1** in a ratio of 22:3. Figure 2.26 shows the molecules in crystals of  $\mathbf{5} \cdot 2\text{MeCN}$  with distances and angles in the caption.

The mean  $\text{Fe}-\text{N}_{\text{carb.}}$  and  $\text{Fe}-\text{O}_{\text{carb.}}$  distance in the iron complex are 2.264 Å and 1.949 Å, respectively. The average distance between the iron center and the coordinated O-atom of the nitrito ligands is 1.964(3) Å. Within the nitrito ligands the average O–N–O angle is 113.4°. The mean difference between the two N–O bonds within the nitrito ligands is 0.109 Å whereby the distance between the nitrogen atom and coordinated O-atom is the longer one in both cases. The two nitrito ligands in  $\mathbf{5} \cdot 2\text{MeCN}$  face in different directions resulting in a close approach of the two nitrogen atoms.

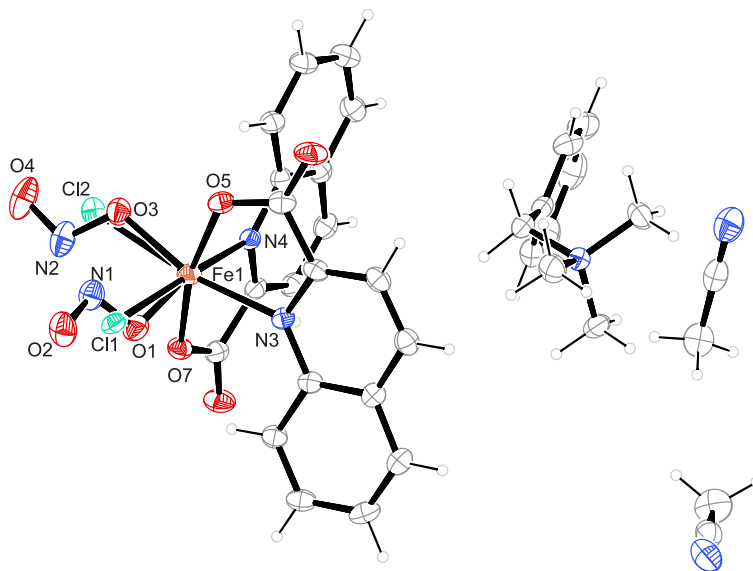


**Figure 2.26:** Ortep plot of  $(\text{NBnMe}_3)[\text{Fe}(\text{NO}_2\text{-}\kappa O)_2(\text{qu})_2] \cdot 2\text{MeCN}$  in crystals of  $\mathbf{5} \cdot 2\text{MeCN}$ . The thermal ellipsoids are drawn at 50% probability. Interatomic distances (Å) and bond angles (°). The standard deviation of the last decimal is given in parentheses: Fe1–O1 1.962(3), Fe1–O3 1.966(3), Fe1–O5 1.947(1), Fe1–O7 1.951(1), Fe1–N3 2.268(2), Fe1–N4 2.259(2), Fe1–Cl1 2.426(8), Fe1–Cl2 2.433(8), N1–O1 1.308(4), N1–O2 1.215(3), N2–O4 1.207(3), N2–O3 1.319(4); O1–Fe1–O3 98.2(1), O1–Fe1–O5 100.83(9), O1–Fe1–O7 87.80(9), O1–Fe1–N3 88.12(9), O3–Fe1–O5 86.77(9), O3–Fe1–O7 102.55(9), O3–Fe1–N4 87.3(1), O5–Fe1–N3 76.29(5), O5–Fe1–N4 94.04(5), O7–Fe1–N3 93.64(5), O7–Fe1–N4 76.72(5), N3–Fe1–N4 90.84(5), O1–N1–O2 114.0(2), O3–N2–O4 112.8(3).

The central metals of both independent molecules in **6** are sixfold coordinated by one tetradentate  $\text{Bn}_2\text{edda}$  ligand *via* three five-membered chelate rings and two *E*-nitrito- $\kappa\text{O}$  ligands creating a similar coordination environment compared to **5** · 2MeCN. The resulting coordination polyhedron can best be described as slightly distorted octahedron. A visualization of the molecules in crystals of **6** is depicted in Figure 2.27 with distances and angles in the caption. The mean Fe–O and Fe–N distances regarding the aminocarboxylato ligand are 1.982 Å and 2.221 Å, respectively. It is notable, that the O7–N4–O8 nitrito ligand is slightly disordered due to a distorted coordination. Therefore the ligand was refined using the PART instruction to separate the two independent positions. A closer look at the two complex molecules in **6** reveals that the nitrito ligands are equally coordinated in both complexes. In contrast to **5** · 2MeCN, the nitrogen atoms of the ligands face in opposite directions. The average O–N–O angle within the nitrito ligands is 114.7° and the mean Fe–O<sub>nitrite</sub> distance is 1.997 Å. As expected, in all nitrito ligands the distance between nitrogen and coordinated oxygen atom is approximately 0.03 Å longer than its distance to the non-coordinating oxygen.

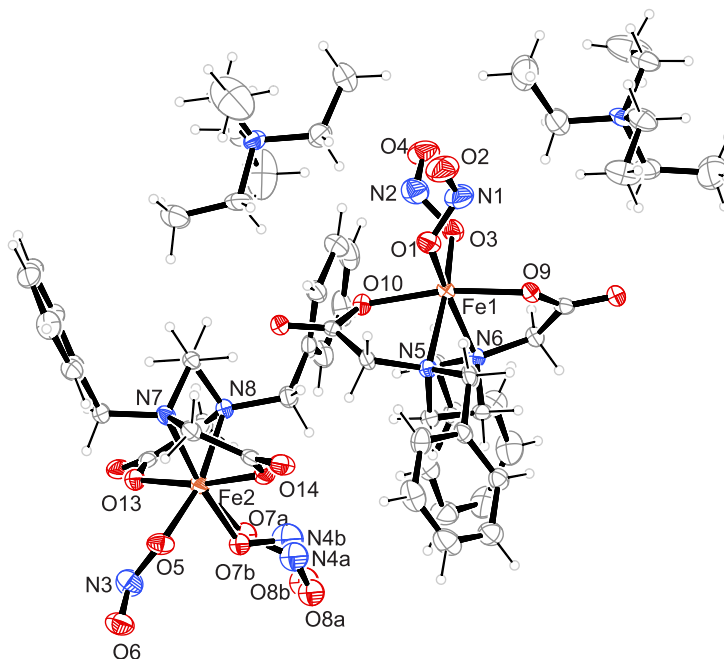


**Figure 2.27:** Ortep plot of  $(\text{NEt}_4)[\text{Fe}(\text{Bn}_2\text{edda})(\text{NO}_2\text{-}\kappa\text{O})_2]$  in crystals of **6**. The thermal ellipsoids are drawn at 50% probability. Interatomic distances (Å) and bond angles (°). The standard deviation of the last decimal is given in parentheses: Fe1–O1 1.982(3), Fe1–O3 2.006(3), Fe1–O9 1.983(3), Fe1–O10 1.988(3), Fe1–N5 2.222(3), Fe1–N6 2.229(4), Fe2–O5 2.012(3), Fe2–O7a 2.050(1), Fe2–O7b 1.936(9), Fe2–O13 1.978(3), Fe2–O14 1.978(3), Fe2–N7 2.213(4), Fe2–N8 2.218(4), N1–O1 1.285(5), N1–O2 1.204(6), N2–O3 1.258(5), N2–O4 1.224(5), N3–O5 1.253(5), N3–O6 1.218(5), N4a–O7a 1.278(2), N4a–O8a 1.207(1), N4b–O7b 1.232(2), N4b–O8b 1.258(1); O1–Fe1–O9 94.5(1), O1–Fe1–O10 92.3(1), O1–Fe1–O3 102.6(1), O1–Fe1–N5 87.8(1), O1–Fe1–N6 166.1(1), O3–Fe1–O9 93.2(1), O2–Fe1–O10 93.6(1), O3–Fe1–N5 166.6(1), O3–Fe1–N6 89.1(1), N5–Fe1–N6 81.7(1), O5–Fe2–O13 95.0(1), O5–Fe2–O14 92.2(1), O5–Fe2–N7 89.0(1), O5–Fe2–N8 167.4(1), O7a–Fe2–O5 102.8(4), O7b–Fe2–O5 92.3(4), O7a–Fe2–O13 88.8(3), O7b–Fe2–O13 93.2(3), O7a–Fe2–O14 96.6(3), O7b–Fe2–O14 93.7(3), O7a–Fe2–N7 167.2(3), O7b–Fe2–N7 171.5(3), O7a–Fe2–N8 87.2(4), O7b–Fe2–N8 98.1(4), N7–Fe2–N8 81.7(1), O1–N1–O2 113.1(5), O3–N2–O4 114.2(4), O5–N3–O6 114.3(4), O7a–N4a–O8a 115(1), O7b–N4b–O8b 117(1).

Figure 2.28 depicts the molecular structure of the inversion-symmetric complex anion in crystals of **7** with distances and angles in the caption. The two equivalent iron centers are each coordinated by one tetradentate heida ligand *via* three five-membered chelate rings and one *Z*- $\kappa O$  binding nitrito ligand. The two central metals are bridged by the two ethoxy moieties of heida. The coordination polyhedra are best described as strongly distorted octahedra. The N1–O2 distance is 0.05 Å shorter than the N1–O1 distance and the O1–N1–O2 angle is 112.5(3)°. The mean Fe1–O<sub>carb.</sub> distance is 1.971 Å and the Fe1–Fe1<sup>i</sup> distance is 3.228 Å.

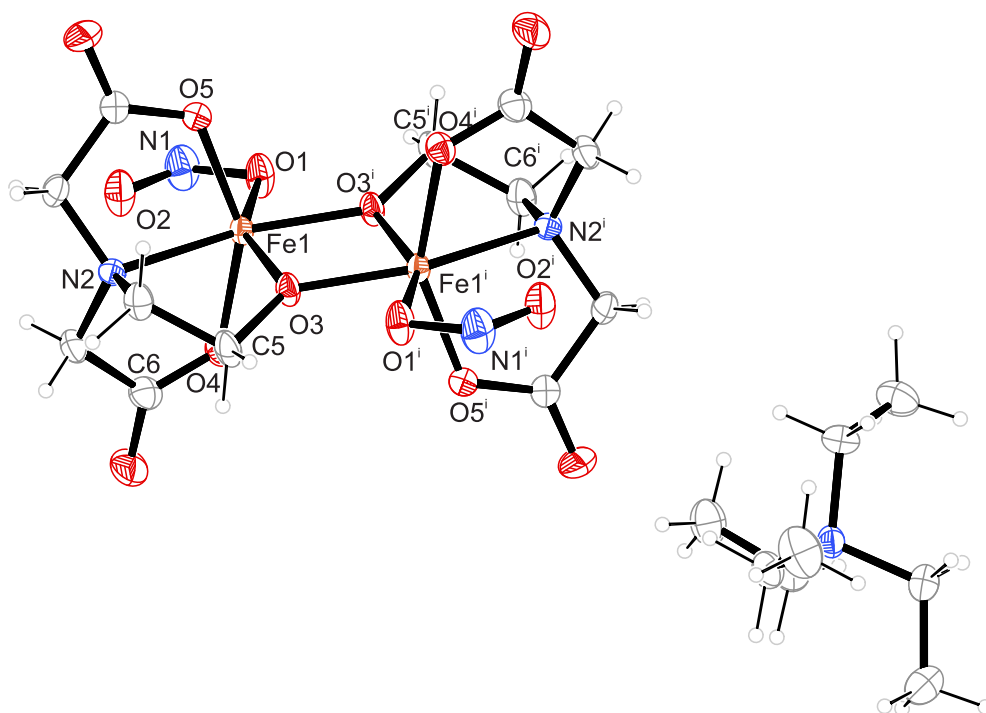


**Figure 2.28:** Ortep plot of  $(\text{NEt}_4)_2[\text{Fe}_2(\mu\text{-heida})_2(\text{NO}_2\text{-}\kappa O)_2]$  in crystals of **7**. For clarity, the second, symmetry generated tetraethylammonium cation is omitted. The thermal ellipsoids are drawn at 50% probability. Interatomic distances (Å) and bond angles (°). The standard deviation of the last decimal is given in parentheses: Fe1–O1 2.115(2), Fe1–O2 2.584(2), Fe1–O3 2.015(2), Fe1–O3<sup>i</sup> 1.966(2), Fe1–O4 1.962(2), Fe1–O5 1.980(2), Fe1–N2 2.267(3), O1–N1 1.289(4), N1–O2 1.243(4), O1–Fe1–N2 128.66(9), O3–Fe1–N2 78.29(9), O3<sup>i</sup>–Fe1–N2 148.91(9), O4–Fe1–N2 77.2(1), O5–Fe1–N2 78.3(1), O3–Fe1–O1 152.25(9), O3<sup>i</sup>–Fe1–O1 82.22(9), O4–Fe1–O1 93.3(1), O5–Fe1–O1 89.5(1), O3–Fe1–O4 100.2(1), O3–Fe1–O5 109.3(1), Fe1–O3–Fe1<sup>i</sup> 108.3(1), O3–Fe1–O3<sup>i</sup> 71.7(1). Symmetry code: <sup>i</sup>  $-x, 1-y, 1-z$ .

The central metal in **8** is coordinated by one trianionic, tetradentate nta ligand *via* three five-membered chelate rings. Furthermore the complex anion exhibits two nitrito ligands in different binding modes, one in the  $\kappa^2 O, O'$  and one in the *Z*- $\kappa O$  binding mode. The coordination polyhedron of the sevenfold coordinated complex can best be described as a distorted pentagonal bipyramid.

In the case of **8**, the difference between the chelating and *Z*- $\kappa O$  isomer is very obvious since both ligands differ much in their binding behavior. The Fe1–O2 distance is with 2.932(2) Å almost 0.9 Å longer than the Fe1–O1 distance. In the case of the nitrito- $\kappa^2 O, O'$  ligand the difference between both Fe–O distances is less than 0.03 Å. The N–O

bond lengths within the chelating nitrito ligand differ by 0.003 Å while they differ by 0.006 Å in the *Z*-nitrito- $\kappa O$  case. Furthermore, the O1–N1–O2 angle of the monodentate binding nitrite is over 3° bigger than the O3–N2–O4 angle in the chelating nitrito ligand. The mean Fe1–O<sub>carb.</sub> is 2.005 Å.

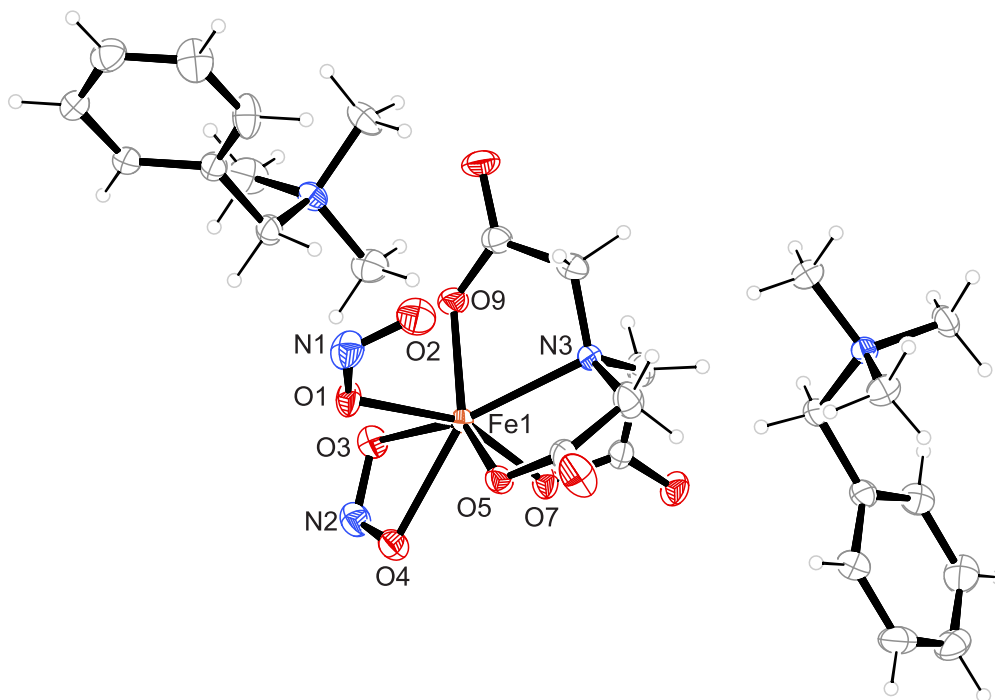


**Figure 2.29:** Ortep plot of  $(\text{NBnMe}_3)_2[\text{Fe}(\text{NO}_2\text{-}\kappa^2\text{O},\text{O}')(\text{NO}_2\text{-}\kappa\text{O})(\text{nta})]$  in crystals of **8**. The thermal ellipsoids are drawn at 50% probability. Interatomic distances (Å) and bond angles (°). The standard deviation of the last decimal is given in parentheses: Fe1–O1 2.068(1), Fe1–O3 2.209(2), Fe1–O4 2.252(2), Fe1–O5 1.980(1), Fe1–O7 2.038(1), Fe1–O9 1.997(2), Fe1–N3 2.271(2), O1–N1 1.294(2), N1–O2 1.230(3), N2–O4 1.264(2), N2–O3 1.267(2); O1–Fe1–O3 81.41(6), O1–Fe1–O4 79.29(6), O1–Fe1–O5 85.55(6), O1–Fe1–O7 156.95(6), O1–Fe1–O8 87.51(6), O1–Fe1–N3 125.92(6), O5–Fe1–N3 77.30(6), O7–Fe1–N3 76.47(6), O9–Fe1–N3 74.12(6), O5–Fe1–O3 138.39(6), O7–Fe1–O3 82.54(6), O9–Fe1–O3 80.25(6), O3–Fe1–N3 140.59(6), O4–Fe1–N3 145.77(6), O3–Fe1–O4 55.91(6), O1–N1–O2 114.9(2), O3–N2–O4 111.5(2).

#### 2.4.2 Synthesis of $[\text{Fe}_4(\mu\text{-bpmea})_2(\text{Z-NO}_2\text{-}\kappa\text{O})_2(\text{E-NO}_2\text{-}\kappa\text{O})_4(\mu_3\text{-O})_2] \cdot 2\text{MeCN}$ (**9** · 2MeCN)

**9** · 2MeCN was synthesized by dissolving Hbpmea with iron(III) chloride in acetonitrile, removing the solvent and letting the yellow powder react with a surplus of silver nitrite in acetonitrile. An alternative route to obtain **9** · 2MeCN was by dissolving **P9** · 2MeCN in acetonitrile and adding a surplus of silver nitrite. In the reaction solution, and stored at  $-20^\circ\text{C}$ , the substance is stable for several months. At room temperature under inert atmosphere, the solid product decomposes within a few days when the mother liquor is removed due to the loss of co-crystallized solvent (outgasing). The substance was characterized by single-crystal X-ray diffraction, elemental analysis, IR and UV-Vis spectroscopy.

Methanolic solutions of **9** · 2MeCN exhibit a single UV-Vis absorption band at 338 nm.

Compound **9** · 2MeCN exhibits two *Z*-nitrito- $\kappa O$  and four *E*-nitrito- $\kappa O$  ligands. Therefore, at least six different nitrite-related IR vibration bands are observed in the IR spectrum which were identified by comparison with the IR spectrum of **P9** · 2MeCN (Table 7).

**Table 7:** IR vibrations of the nitrito ligands in compounds **9** · 2MeCN.

ligand	vibration	$\tilde{\nu}({}^{14}\text{NO}_2^-)/\text{cm}^{-1}$
	$\delta$	814
<i>E</i> - $\kappa O$	$\nu(\text{N-O})$	968
	$\nu(\text{N=O})$	1464
	$\delta$	863
<i>Z</i> - $\kappa O$	$\nu(\text{N-O})$	-
	$\nu(\text{N=O})$	1343

The tetranuclear iron complex **9** · 2MeCN crystallizes in the monoclinic space group  $P2_1/c$  with two formula units in the unit cell. The asymmetric cell contains half a complex molecule and one acetonitrile. Due to inversion-symmetry **9** exhibits only two different types of iron centers which were bridged by one deprotonated ethoxido moiety of the bpmea ligand between Fe1 and Fe2 and one threefold bridging oxido ligand between Fe1, Fe2 and Fe1<sup>i</sup>. Fe1 is sixfold coordinated by two nitrito ligands – one *Z*- and one *E*-nitrito- $\kappa O$  ligand – and the three bridging ligands. Fe2 is sixfold coordinated by the deprotonated bpmea ligand *via* three five-membered chelate rings with bridging ethoxy function, the  $\mu^3$ -oxido ligand and one *E*-nitrito- $\kappa O$  ligand. The coordination polyhedra of both central metals can best be described as distorted octahedra. The formation of the bridging oxido ligand is discussed in more detail in Section 3.4. The molecular structure of **9** · 2MeCN with distances and angles in the captions is depicted in Figure 2.30.

The mean Fe2–N<sub>bpmea</sub> distance is 2.166 Å and the average Fe–O length within the whole complex is 2.003 Å. The O–N–O angles in the *E*-nitrito- $\kappa O$  ligands are around 114° which is approximately 3° above the angle of the *Z*-nitrito- $\kappa^2 O$  ligands. In the latter case, the intramolecular N–O distances differ only by 0.03 Å while the difference is 0.09 Å within the *E*-nitrito- $\kappa O$  ligands.

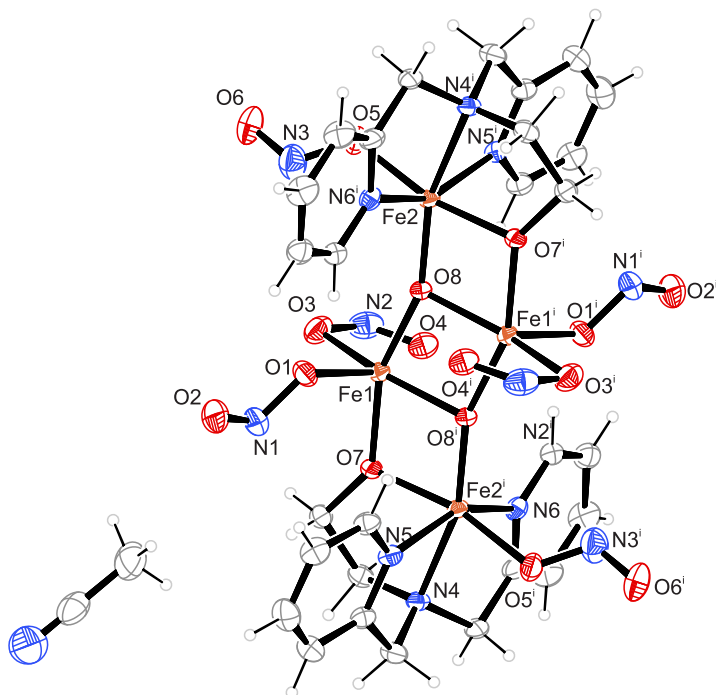


**Figure 2.30:** Ortep plot of  $[\text{Fe}_4(\mu\text{-bpmea})_2(\text{Z-NO}_2\text{-}\kappa\text{O})_2(\text{E-NO}_2\text{-}\kappa\text{O})_4(\mu_3\text{-O})_2] \cdot 2\text{MeCN}$  in crystals of **9** · 2MeCN. For clarity, the second, symmetry generated acetonitrile is omitted. The thermal ellipsoids are drawn at 50% probability. Interatomic distances (Å) and bond angles ( $^\circ$ ). The standard deviation of the last decimal is given in parentheses: Fe1–O1 1.956(3), Fe1–O3 2.095(3), Fe1–O4 2.225(3), Fe1–O7 1.972(2), Fe1–O8 1.901(2), Fe1–O8<sup>i</sup> 2.010(2), Fe2–O5 2.003(3), Fe2<sup>i</sup>–O7 2.003(2), Fe2–O8 1.853(2), Fe2<sup>i</sup>–N4 2.212(3), Fe2<sup>i</sup>–N5 2.149(3), Fe2<sup>i</sup>–N6 2.138(3), N1–O1 1.314(4), N1–O2 1.194(4), N2–O4 1.245(4), N2–O3 1.278(5), N3–O6 1.220(4), N3–O5 1.278(4); O1–Fe1–O3 95.5(1), O1–Fe1–O4 153.0(1), O1–Fe1–O7 99.0(1), O1–Fe1–O8 93.2(1), O1–Fe1–O8<sup>i</sup> 110.1(1), O3–Fe1–O4 57.6(1), O3–Fe1–O7 94.3(1), O3–Fe1–O8 101.2(1), O3–Fe1–O8<sup>i</sup> 153.9(1), O4–Fe1–O7 86.9(1), O4–Fe1–O8 89.8(1), O4–Fe1–O8<sup>i</sup> 97.0(1), O7–Fe1–O8 159.3(1), O8–Fe1–O8<sup>i</sup> 82.5(1), O5–Fe2–O7<sup>i</sup> 167.5(1), O5–Fe2–O8 109.5(1), O5–Fe2–N4<sup>i</sup> 90.7(1), O5–Fe2–N5<sup>i</sup> 83.7(1), O5–Fe2–N6<sup>i</sup> 90.3(1), O7–Fe1–O8<sup>i</sup> 77.6(1), O7<sup>i</sup>–Fe2–O8 80.5(1), O7<sup>i</sup>–Fe2–N4<sup>i</sup> 79.5(1), O7<sup>i</sup>–Fe2–N5<sup>i</sup> 86.6(1), O7<sup>i</sup>–Fe2–N6<sup>i</sup> 94.8(1), O8–Fe2–N4<sup>i</sup> 159.8(1), O8–Fe2–N5<sup>i</sup> 103.7(1), O8–Fe2–N6<sup>i</sup> 102.6(1), N4<sup>i</sup>–Fe2–N6<sup>i</sup> 76.5(1), N4<sup>i</sup>–Fe2–N5<sup>i</sup> 77.9(1), N5<sup>i</sup>–Fe2–N6<sup>i</sup> 153.6(1), Fe2–O8–Fe1 159.2(1), Fe2–O8–Fe1<sup>i</sup> 102.9(1), Fe1–O8–Fe1<sup>i</sup> 97.5(1), Fe1–O7–Fe2<sup>i</sup> 99.0(1), O1–N1–O2 114.3(3), O3–N2–O4 111.3(3), O5–N3–O6 113.9(4). Symmetry code: <sup>i</sup> 1–x, 1–y, 1–z.

The four bridging ligands between the iron centers create a planar  $\text{Fe}_4\text{O}_4$ -framework comprising of three diamond-shaped moieties (Figure 2.31). The middle part is made of the two equivalent central metals Fe1 and Fe1<sup>i</sup> and the  $\mu_3$ -oxido ligands O8. The two outer  $\text{Fe}_2\text{O}_2$  moieties are made of Fe1, Fe2<sup>i</sup>, O8 and the oxygen atom O7 of the bridging ethoxy moiety. Both outer rhomboids are equivalent due to the inversion center.

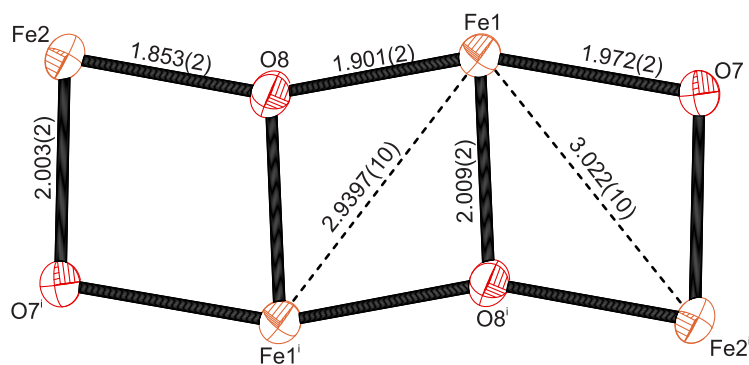


**Figure 2.31:** Ortep plot of the  $\text{Fe}_4\text{O}_4$  core in crystals of **9** · 2MeCN. The thermal ellipsoids are drawn at 50% probability. Interatomic distances are given in Å with the standard deviation of the last decimal in parentheses. Symmetry code:  $^i 1-x, 1-y, 1-z$ .

### 2.4.3 Synthesis of nitritoiron complexes with salen and its derivatives (10-12)

$[\{\text{Fe}(\text{NO}_2\text{-}\kappa\text{O})(\text{salen})\}_2] \cdot 2\text{MeCN}$  (**10** · 2MeCN),  $[\text{Fe}(\text{NO}_2\text{-}\kappa^2\text{O}, \text{O}')(\text{tBu}_2\text{salen})]$  (**11**) and  $[\text{Fe}(\text{NO}_2\text{-}\kappa^2\text{O}, \text{O}')(\text{tBu}_4\text{salen})]$  (**12**) were prepared by adding a surplus of silver nitrite to a solution of the respective precursor compounds in acetonitrile. The crystalline substances are stable against air and higher temperatures. The products were characterized by single-crystal X-ray diffraction, elemental analysis, IR and UV-Vis spectroscopy.

UV-Vis spectra of **10** · 2MeCN, **11** and **12** in acetonitrile feature absorption bands in the UV region below 330 nm and each one shows intensive absorption in the visible region at 502 nm (**10** · 2MeCN), 527 nm (**11**) and 551 nm (**12**).

The IR-spectroscopic analysis of the substances exhibits nitrite-related vibration modes. Their identification was done by comparison with the respective precursor compounds. In addition, the IR bands were verified by the isotope-induced shift of the  $^{15}\text{NO}_2^-$ -enriched substances. In the case of **11** and **12** it was not possible to identify the  $\nu_s$  vibration. The nitrite-related IR bands of both compounds are given in Table 8.

**Table 8:** IR vibrations of the nitrito ligands in compounds **10** · 2MeCN, **11** and **12** with the values of the respective vibrations in the  $^{15}\text{NO}_2^-$ -enriched substances.

compound	vibration	$\tilde{\nu}(^{14}\text{NO}_2^-)/\text{cm}^{-1}$	$\tilde{\nu}(^{15}\text{NO}_2^-)/\text{cm}^{-1}$
<b>10</b> · 2MeCN	$\delta$	811	802
	$\nu(\text{N-O})$	1028	1013
	$\nu(\text{N=O})$	1440	1414
<b>11</b>	$\delta$	868	862
	$\nu_{\text{as}}$	1209	1183
<b>12</b>	$\delta$	866	863
	$\nu_{\text{as}}$	1211	1184

The single-crystal X-ray structure analysis reveals that all nitrito complexes with salen

co-ligands crystallize in the monoclinic space group  $P2_1/n$ . The primitive cells contain two formula units in the case of **10** · 2MeCN and four formula units in the case of **11** and **12**. The respective asymmetric unit cell of **10** · 2MeCN consists of a monomer unit of  $[\{\text{Fe}(\text{NO}_2\text{-}\kappa\text{O})(\text{salen})\}_2]$  and one acetonitrile. In **11** and **12**, the asymmetric units consist of one complex molecule. The molecular structures with distances and angles in the captions are depicted in Figures 2.32, 2.33 and 2.34.

The central metal in **10** · 2MeCN is sixfold coordinated by one unsubstituted salen ligand and one *E*-nitrito- $\kappa\text{O}$  ligand. The remaining coordination site opposing the nitrito ligand is occupied by a bridging alkoxide function of a second  $\{\text{Fe}(\text{NO}_2\text{-}\kappa\text{O})(\text{salen})\}$  unit creating a centrosymmetric, dimeric complex. The resulting coordination spheres can best be described as slightly distorted octahedra. The central metals in **11** and **12** are sixfold coordinated each by one substituted salen and one chelating nitrito ligand. The coordination polyhedra can be described as in-between octahedra and trigonal bipyramids. In all complexes, the salen ligands bind *via* two six-membered and one five-membered chelate rings to the iron center. The Fe–O<sub>nitrite</sub> distances within **11** and **12** differ by circa 0.03 Å and 0.05 Å respectively, while the N–O distances differ by less than 0.01 Å in both cases. The most striking difference between the salen-based ligands lies in their steric demand. This becomes obvious when the coordination behavior of the unsubstituted ligand is compared to that of the complexes with *t*Bu<sub>2</sub>salen and *t*Bu<sub>4</sub>salen. While in the case of the unsubstituted salen ligand, N2, N3, O3 and O4 are almost co-planar and one of the phenol moieties is tilted, the steric demand of the *tert*-butyl groups in **11** and **12** forces the chelate ligands in a non-coplanar arrangement which does not allow the formation of a dimer like in **10** · 2MeCN. Despite that the *tert*-butyl moieties have a great influence on the molecular structure, the torsion within the chelator's ethylenediamine backbone remains almost unaltered with N2–C1–C2–N3 48.2(2)° in **10** · 2MeCN and N2–C8–C9–N3 49.8(2)° in **12**. However, the torsion angle N2–C8–C9–N3 in **11** differs with 42.65° by more than 6° compared to the other mononuclear compound. Average Fe–N distances are 2.107(1) Å in **10** · 2MeCN, 2.096(2) Å in **11** and 2.101(1) Å in **12**. The mean Fe–O distance between central metal and salen ligand are 1.947 Å 1.876 Å and 1.883 Å in **10** · 2MeCN, **11** and **12**, respectively.

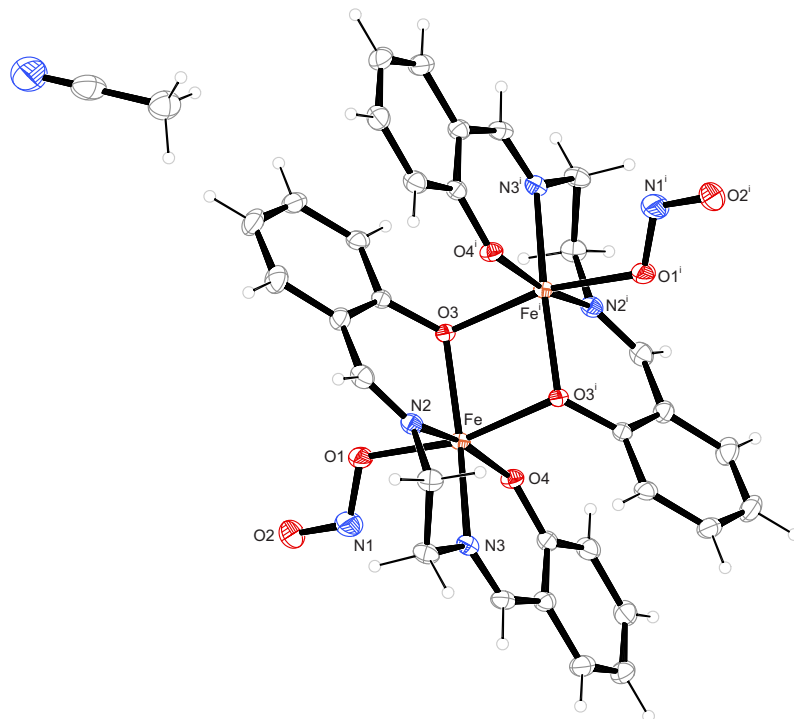


**Figure 2.32:** Ortep plot of  $[\{\text{Fe}(\text{NO}_2\text{-}\kappa\text{O})(\text{salen})\}_2] \cdot 2\text{MeCN}$  in crystals of **10** · 2MeCN. The thermal ellipsoids are drawn at 50% probability. For clarity, the second, symmetry generated acetonitrile is omitted. Interatomic distances (Å) and bond angles ( $^\circ$ ). The standard deviation of the last decimal is given in parentheses: Fe–O1 2.023(1), Fe–O3 2.005(1), Fe–O3<sup>i</sup> 2.118(1), Fe1–O4 1.890(1), Fe–N2 2.110(1), Fe–N3 2.104(1), N1–O2 1.207(2), N1–O1 1.293(3); O4–Fe–O3 109.54(5), N3–Fe–N2 77.24(5), O4–Fe–N3 88.43(5), O3–Fe–N2 84.36(5), O4–Fe–O1 94.31(5), O3–Fe–O1 88.76(5), O1–Fe–N3 95.94(5), O1–Fe–N2 91.24(5), O3–Fe1–O3<sup>i</sup> 77.68(5), Fe–O3–Fe<sup>i</sup> 102.31(5), O2–N1–O1 115.7(1). Symmetry code: <sup>i</sup>  $-x, 1-y, 1-z$ .

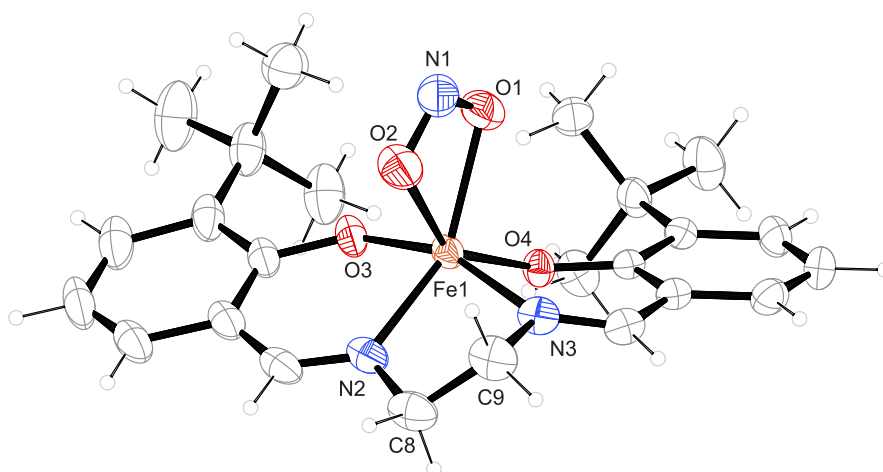


**Figure 2.33:** Ortep plot of  $[\text{Fe}(\text{NO}_2\text{-}\kappa^2\text{O}, \text{O}')(\text{tBu}_2\text{salen})]$  in crystals of **11**. The thermal ellipsoids are drawn at 50% probability. Interatomic distances (Å) and bond angles ( $^\circ$ ). The standard deviation of the last decimal is given in parentheses: Fe1–O1 2.149(1), Fe1–O2 2.184(2), Fe1–O3 1.871(1), Fe1–O4 1.891(1), Fe1–N2 2.111(2), Fe1–N3 2.087(2), N1–O1 1.261(3), N1–O2 1.254(3); O1–Fe1–O2 57.23(6), O1–Fe1–O3 96.87(6), O1–Fe1–O4 90.92(6), O1–Fe1–N2 142.49(6), O1–Fe1–N3 103.13(6), O2–Fe1–O3 100.11(6), O2–Fe1–O4 145.62(5), O2–Fe1–N2 85.39(6), O2–Fe1–N3 89.39(6), O3–Fe1–O4 95.97(5), O3–Fe1–N2 85.95(6), O3–Fe1–N3 159.93(6), O4–Fe1–N2 126.12(6), O4–Fe1–N3 85.54(5), N3–Fe1–N2 77.17(6), O2–N1–O1 111.2(2).

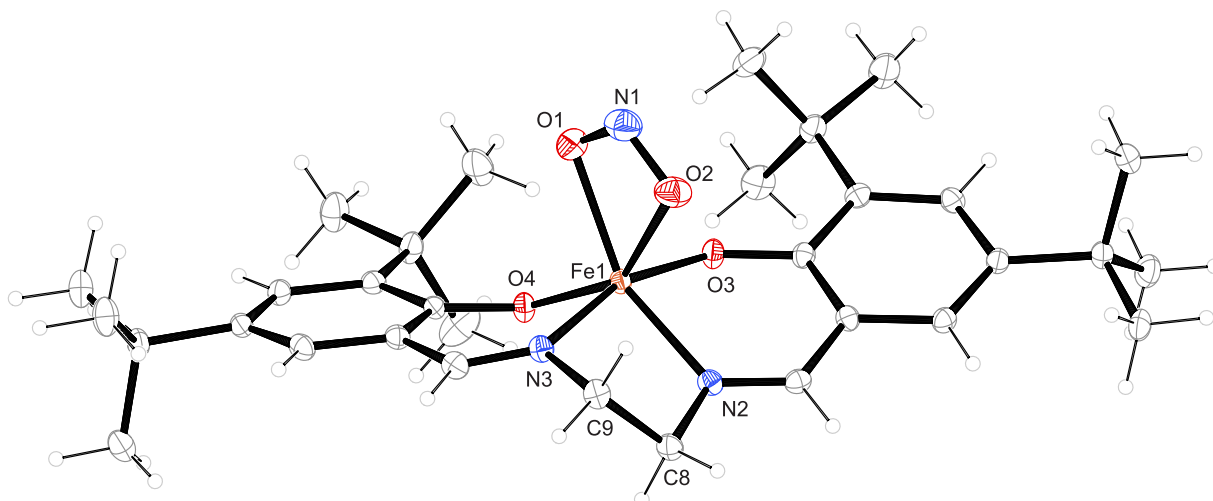


**Figure 2.34:** Ortep plot of  $[\text{Fe}(\text{NO}_2\text{-}\kappa^2\text{O},\text{O}')(\text{tBu}_4\text{salen})]$  in crystals of **12**. The thermal ellipsoids are drawn at 50% probability. Interatomic distances (Å) and bond angles ( $^\circ$ ). The standard deviation of the last decimal is given in parentheses: Fe1–O1 2.143(1), Fe1–O2 2.199(1), Fe1–O3 1.883(1), Fe1–O4 1.882(1), Fe1–N2 2.104(1), Fe1–N3 2.098(1), N1–O2 1.264(2), N1–O2 1.261(2); O1–Fe1–O4 91.54(5), O1–Fe1–O3 97.36(5), O1–Fe1–N3 99.28(5), O1–Fe1–N2 144.42(6), O2–Fe1–O4 146.96(5), O2–Fe1–O3 96.10(5), O2–Fe1–N3 88.21(5), O2–Fe1–N2 86.97(5), N2–Fe1–O3 86.19(5), N2–Fe1–O4 122.96(5), N3–Fe1–O3 162.46(5), N3–Fe1–O4 85.82(5), N3–Fe1–N2 77.04(5), O4–Fe1–O3 99.28(5), O1–Fe1–O2 57.46(5), O2–N1–O1 111.5(2).

## 2.5 Nitrito compounds with N-Donor co-ligands

### 2.5.1 Synthesis of $[\text{Fe}(\text{bipzpy})\text{X}_2(\text{NO}_2\text{-}\kappa^2\text{O},\text{O}')]\cdot\text{MeCN}$ ( $\text{X} = \text{Cl}, \text{Br}$ ) (**13** · MeCN and **14** · MeCN)

Substances with the general formula  $[\text{Fe}(\text{bipzpy})\text{X}_2(\text{NO}_2)]$  ( $\text{X} = \text{Cl}, \text{Br}$ ) were prepared by dissolving the respective precursor compounds **P13** and **P14** in acetonitrile at  $-20^\circ\text{C}$  and adding silver nitrite. The addition of more than one equiv silver nitrite leads first to the formation of the corresponding nitrate complex and then to the precipitation of an undefinable brown powder. Both substances are not air-stable but can be stored for several weeks under inert conditions at room temperature. Due to the small yield, **13** · MeCN was characterized only by single-crystal X-ray diffraction and IR spectroscopy. The slightly higher yield of **14** allowed a full characterization by single-crystal X-ray diffraction, elemental analysis, IR and UV-Vis spectroscopy.

The UV-Vis spectrum of **14** in acetonitrile shows several absorption bands below 304 nm and two absorption bands in the visible region at 395 nm and 468 nm.

The IR bands of the nitrito ligands were allocated by comparison with the IR spectra of the corresponding precursor compounds **P13** and **P14**. The observable vibration bands for each compound are depicted in Table 9.

**Table 9:** IR vibrations of the nitrito ligands in compounds **13** · MeCN and **14** · MeCN verified by comparison with their respective precursor compounds **P13** and **P14**.

compound	vibration	$\tilde{\nu}(\text{NO}_2^-)/\text{cm}^{-1}$
<b>13</b> · MeCN	$\delta$	870
	$\nu_{\text{as}}$	1182
<b>14</b> · MeCN	$\delta$	869
	$\nu_{\text{as}}$	1212
	$\nu_{\text{s}}$	1284

The neutral compounds **13** · MeCN and **14** · MeCN crystallize in the monoclinic space group  $P2_1/c$  each with four formula units in the primitive cell. Their asymmetric units consist of one complex molecule with one acetonitrile. The central metals are sevenfold coordinated resulting in a distorted pentagonal-bipyramidal coordination polyhedron. The molecular structures of both complex molecules are depicted in Figures 2.35 and 2.36 with distances and angles in the respective captions. The equatorial positions are occupied by one tridentate bipzpy *via* two five-membered chelate rings and a nitrito- $\kappa^2\text{O},\text{O}'$  ligand. The two halogenido ligands are located on the remaining axial positions. Mean Fe–N distances are 2.174 Å in both complexes and as well as in the precursor compound, the Fe–N4 distance across the nitrito ligand is the longest of the three Fe–N bonds. The average Fe–X distance is 2.318 Å in **13** · MeCN and 2.487 Å (**13** · MeCN). Both chelating nitrito

ligands possess almost identical N–O distances and an O–N–O angle of approximately  $110^\circ$ . The mean Fe–O distances are 2.161 Å in both complexes.

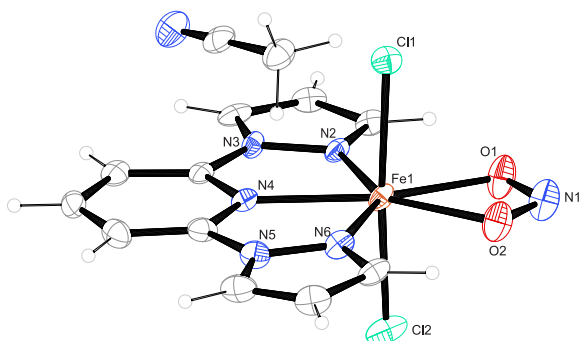


**Figure 2.35:** Ortep plot of  $[\text{Fe}(\text{bipzpy})\text{Cl}_2(\text{NO}_2\text{-}\kappa^2\text{O},\text{O}')]\cdot\text{MeCN}$  in crystals of **13** · MeCN. The thermal ellipsoids are drawn at 50% probability. Interatomic distances (Å) and bond angles ( $^\circ$ ). The standard deviation of the last decimal is given in parentheses: Fe1–O1 2.175(3), Fe1–O2 2.146(3), Fe1–N2 2.167(3), Fe1–N4 2.192(4), Fe1–N6 2.164(4), Fe1–Cl1 2.319(1), Fe1–Cl2 2.317(1), N1–O1 1.262(5), N1–O2 1.269(5), O1–Fe1–N2 81.3(1), O2–Fe1–N6 78.1(1), N2–Fe1–N4 71.4(1), N6–Fe1–N4 71.4(1), O2–Fe1–O1 57.9(1), O1–Fe1–N4 152.6(1), O1–Fe1–Cl1 88.5(1), O2–Fe1–Cl1 89.3(1), N2–Fe1–Cl1 88.5(1), N4–Fe1–Cl1 93.1(1), N6–Fe1–Cl1 93.0(1), O1–Fe1–Cl2 86.0(1), O2–Fe1–Cl2 89.2(1), N2–Fe1–Cl2 89.0(1), N4–Fe1–Cl2 91.0(1), N6–Fe1–Cl2 92.1(1), Cl2–Fe1–Cl1 174.27(6), O1–N1–O2 111.4(4).

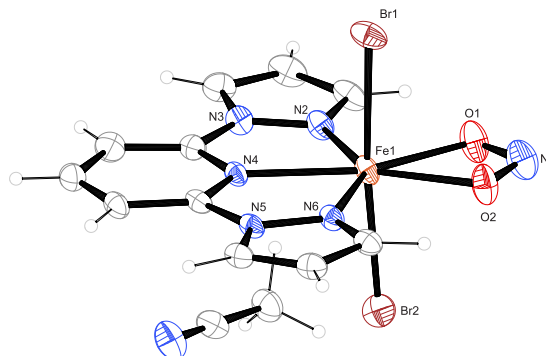


**Figure 2.36:** Ortep plot of  $[\text{Fe}(\text{bipzpy})\text{Br}_2(\text{NO}_2\text{-}\kappa^2\text{O},\text{O}')]\cdot\text{MeCN}$  in crystals of **14** · MeCN. The thermal ellipsoids are drawn at 50% probability. Interatomic distances (Å) and bond angles ( $^\circ$ ). The standard deviation of the last decimal is given in parentheses: Fe1–O1 2.145(3), Fe1–O2 2.178(4), Fe1–N2 2.168(4), Fe1–N4 2.197(4), Fe1–N6 2.158(4), Fe1–Br1 2.4749(9), Fe1–Br2 2.4985(9), N1–O1 1.264(6), N1–O2 1.265(5); O1–Fe1–N2 78.2(1), O2–Fe1–N6 81.2(1), N2–Fe1–N4 71.4(1), N6–Fe1–N4 71.5(1), O1–Fe1–O2 57.6(1), O1–Fe1–Br1 89.2(1), O2–Fe1–Br1 85.6(1), N2–Fe1–Br1 92.1(1), N4–Fe1–Br1 91.3(1), N6–Fe1–Br1 88.9(1), O1–Fe1–Br2 88.9(1), O2–Fe1–Br2 87.6(1), N2–Fe1–Br2 94.4(1), N4–Fe1–Br2 93.7(1), N6–Fe1–Br2 87.8(1), Br1–Fe1–Br2 172.83(3), O1–N1–O2 111.0(4).

### 2.5.2 Synthesis of nitrito complexes with Me<sub>3</sub>tacn (**15a** · 0.5DCM and **15b** · 2DCM)

$[\text{Fe}(\text{Me}_3\text{tacn})(\text{NO})(\text{NO}_2\text{-}\kappa\text{O})_2](\text{NO}_3)\cdot 0.5\text{DCM}$  (**15a** · 0.5DCM) was synthesized by dissolving **P15** in dichloromethane and adding a surplus of silver nitrite. Between many crystals of **15b** · 2DCM a few orange platelets of **15a** · 0.5DCM were found. The amount of **15a** · 0.5DCM can be multiplied by replacing the nitrogen atmosphere with nitric oxide. Due to its high air- and temperature-sensitivity, no determination of the yield and no characterization *via* elemental analysis was possible. However, the compound was characterized by single-crystal X-ray diffraction, IR and UV-Vis spectroscopy.

Solvent-free crystals of  $[\text{Fe}_2(\text{Me}_3\text{tacn})_2(\text{NO}_2\text{-}\kappa\text{O})_4(\mu\text{-O})]$  (**15b**) are obtained if the reaction is performed in acetonitrile. **15b** is only slightly sensitive to oxidation and higher temperatures. **15b** · 2DCM decomposes quickly after the removal of the mother liquor due to the loss of co-crystallized dichloromethane. Therefore, **15b** was characterized by elemental analysis, single-crystal X-ray diffraction, IR and UV-Vis spectroscopy and **15b** · 2DCM only by single-crystal X-ray diffraction.

In the case of **15a** · 0.5DCM the UV-Vis spectrum was directly measured from the reac-

tion solution (dichloromethane) whereby absorption bands at 251 nm, 302 nm and 395 nm are observed. **15b** in acetonitrile exhibits absorption bands at 284 nm and 360 nm.

The IR spectra of both compounds showed all three observable vibration modes of the nitrito ligands. Since **15a** · 0.5DCM possesses a nitrosyl ligand, the corresponding intense stretching vibration is observed at  $1887\text{cm}^{-1}$ . When the reaction solution of **15a** · 0.5DCM is dried completely and an IR spectrum of the crude substance is recorded, a second nitrosyl vibration is observed at  $1767\text{cm}^{-1}$ . When the reaction solution is stirred for several days, an IR spectrum of the dried powder shows that just the  $\{\text{FeNO}\}^7$ -related vibrational band is left. However, it was not possible to obtain crystals from this substance. The nitrosyl- and nitrite-related IR bands of **15a** · 0.5DCM and **15b** · 2DCM were verified by comparison with the IR spectra of the  $^{15}\text{NO}_2^-$ -enriched substance *via* isotope-induced shift. Table 10 depicts the wavenumbers of all nitrite-related IR bands and their respective vibration modes.

**Table 10:** IR vibrations of the nitrito ligands in compounds **15a** · 0.5DCM and **15b** · 2DCM. In the case of **15b** · 2DCM the values were verified by comparison with the vibrations in the  $^{15}\text{NO}_2^-$ -enriched substance.

compound	vibration	$\tilde{\nu}(^{14}\text{NO}_2^-)/\text{cm}^{-1}$	$\tilde{\nu}(^{15}\text{NO}_2^-)/\text{cm}^{-1}$
<b>15a</b> · 0.5DCM	$\delta$	812	802
	$\nu(\text{N-O})$	987	976
	$\nu(\text{N=O})$	1440	1413
	$\nu(\text{nitrosyl})$	1887	1840
<b>15b</b>	$\delta$	811	805
	$\nu(\text{N-O})$	1051	1024
	$\nu(\text{N=O})$	1439	1414

To lighten the reaction pathway that leads to the formation of the  $\mu$ -O ligand, further IR-spectroscopic investigations were performed. First of all, the reaction was traced by *in-situ* IR spectroscopy. Figure 2.37 shows the time-resolved spectrum directly after addition of the silver nitrite. At first a vibrational band at  $1880\text{cm}^{-1}$  – which is found in the isolated  $\{\text{FeNO}\}^6$  **15a** · 0.5DCM – grows directly after addition of the nitrite source, reaches a maximum and then decreases for the rest of the investigated time period. Almost simultaneously with the start of this decrease, a second vibrational band at around  $1750\text{cm}^{-1}$  arises and stabilizes its height after a few minutes. Since an evolution of nitrous oxide in this reaction is conceivable, additional gas-phase IR spectroscopy was performed. Here, the samples were taken from the gas-phase above the reaction solution over a time period of 150 min. In consensus with the previously described *in-situ* spectrum, the evolution of nitric oxide started delayed after approximately one hour after addition of the silver nitrite. The resulting spectrum (Figure 2.38) shows a constant growth of

two vibrational bands at  $2236\text{ cm}^{-1}$  and  $2211\text{ cm}^{-1}$  which are characteristic for nitrous oxide.<sup>[85,86]</sup> In addition, the evolution of brown  $\text{NO}_2$  gas is observed, if the reaction vessel is opened after the addition of silver nitrite.

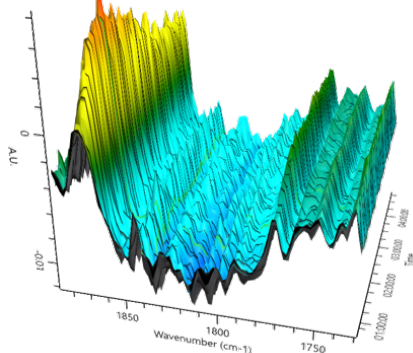


**Figure 2.37:** Time-resolved *in-situ* IR spectrum of the reaction of **P15** with silver nitrite.

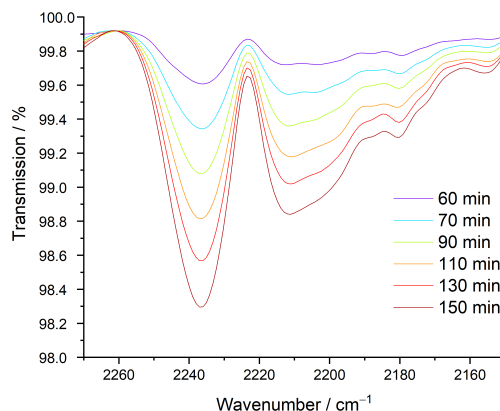


**Figure 2.38:** Evolution of nitrous oxide during the reaction of **P15** with silver nitrite at room temperature. Samples were collected from the gas-phase above the solution after a reaction time of 60 min.

The  $\{\text{FeNO}\}_6$  complex **15a** · 0.5DCM crystallizes in the triclinic space group  $P\bar{1}$ . The primitive cell contains two formula units and the asymmetric unit consists of two crystallographically independent complex molecules, two nitrate counter ions and one molecule of co-crystallized dichloromethane. Both sixfold coordinated iron complexes are composed of one facial binding  $\text{Me}_3\text{tacn}$  ligand, two *Z*-nitrito- $\kappa\text{O}$  ligands and one nitrosyl ligand. The coordination polyhedron can best be described as a slightly distorted octahedron. The structure of **15a** · 0.5DCM is illustrated in Figure 2.39 with all relevant distances and angles in the caption. The non-binding oxygen atoms of the two nitrito ligands point towards the nitrosyl ligand. The average distance between those oxygen atoms and the central metal is  $3.044\text{ \AA}$ . The mean distance from Fe to the coordinated oxygen atoms is  $1.937(2)\text{ \AA}$  and all intramolecular O–N–O angles within the nitrito ligands are around  $117^\circ$ . The average Fe– $\text{N}_{\text{Me}_3\text{tacn}}$  distance is  $2.038\text{ \AA}$  whereby the Fe–N bond opposing the nitrosyl ligand is circa  $0.01\text{ \AA}$  longer than the other two bonds. In both cases the Fe–N–O angle within the nitrosyliron unit is, with around  $173^\circ$ , nearly linear.

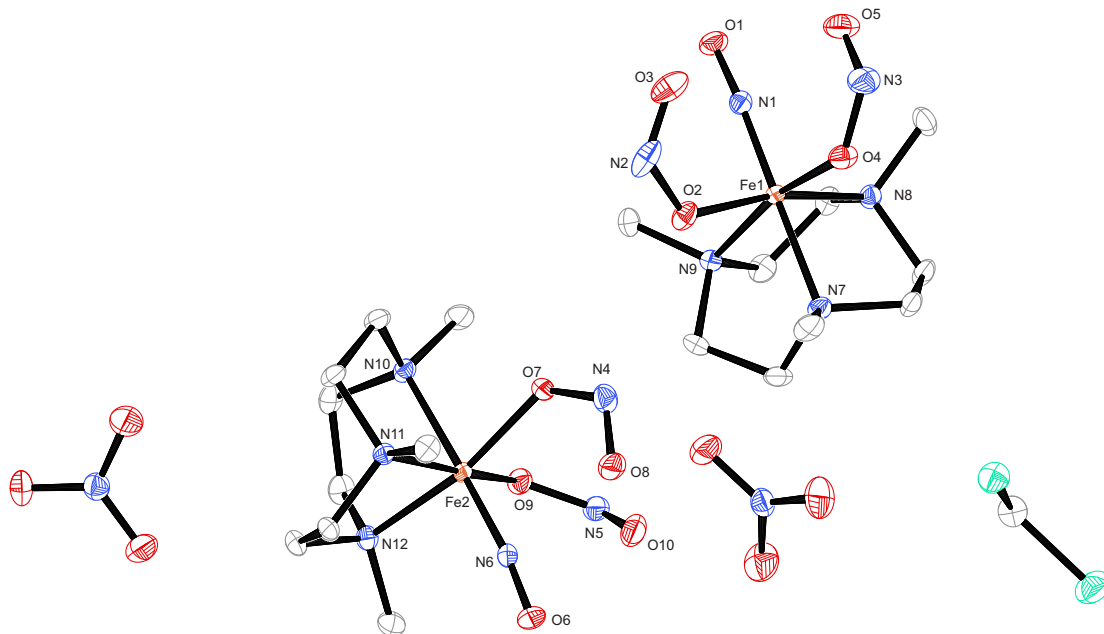


**Figure 2.39:** Ortep plot of  $[\text{Fe}(\text{Me}_3\text{tacn})(\text{NO})(\text{NO}_2\text{-}\kappa\text{O})_2](\text{NO}_3) \cdot 0.5\text{DCM}$  in crystals of **15a** · 0.5MeCN. The thermal ellipsoids are drawn at 50% probability. For clarity, the hydrogen atoms are not depicted. Interatomic distances (Å) and bond angles (°). The standard deviation of the last decimal is given in parentheses: Fe1–O2 1.934(2), Fe1–O4 1.935(2), Fe1–N1 1.662(2), Fe1–N7 2.045(2), Fe1–N8 2.034(2), Fe1–N9 2.033(2), N1–O1 1.144(2), N2–O2 1.311(2), N2–O3 1.212(3), N3–O5 1.215(3), N3–O4 1.306(2), Fe2–O7 1.935(1), Fe2–O9 1.943(2), Fe2–N6 1.659(2), Fe2–N10 2.049(2), Fe2–N11 2.037(2), Fe2–N12 2.030(2), N6–O6 1.148(2), N4–O7 1.307(2), N4–O8 1.215(2), N5–O9 1.312(2), N5–O10 1.211(3); N1–Fe1–O2 95.66(8), N1–Fe1–O4 98.55(7), N1–Fe1–N7 178.51(8), N1–Fe1–N8 93.50(8), N1–Fe1–N9 94.57(8), O2–Fe1–N7 85.60(7), O2–Fe1–N8 168.80(7), O2–Fe1–N9 87.58(7), O4–Fe1–N7 82.24(7), O4–Fe1–N8 95.58(7), O4–Fe1–N9 166.77(7), O2–Fe1–O4 89.43(7), N6–Fe2–O7 98.62(7), N6–Fe2–O9 95.08(7), N6–Fe2–N10 178.60(8), N6–Fe2–N11 94.25(8), N6–Fe2–N12 94.11(8), O7–Fe2–N10 82.46(7), O7–Fe2–N11 95.39(7), O7–Fe2–N12 167.17(7), O9–Fe2–N10 85.80(7), O9–Fe2–N11 168.82(7), O9–Fe2–N12 87.96(7), O7–Fe2–O9 89.28(6), O1–N1–Fe1 173.24(2), O6–N6–Fe2 172.69(2), O2–N2–O3 116.4(2), O4–N3–O5 116.7(2), O7–N4–O8 117.0(2), O9–N5–O10 116.6(2), Fe1–N1–O1 173.2(2), Fe2–N6–O6 172.7(2).

While crystals of **15b** exhibit heavily disordered  $\text{Me}_3\text{tacn}$  ligands, the molecular structure of **15b** · 2DCM shows no such disorder and much better quality factors. Therefore, only the crystal structure of **15b** · 2DCM is discussed. The neutral, inversion symmetric, binuclear complex crystallizes in the monoclinic space group  $P2_1/n$  with two formula units in the primitiv cell. The asymmetric unit consists of half a complex molecule and half a dichloromethane. Each central metal is sixfold coordinated by one facially binding  $\text{Me}_3\text{tacn}$  ligand, two  $E$ -nitrito- $\kappa\text{O}$  ligands and one bridging oxido ligand. The resulting coordination polyhedron can be described as a slightly distorted octahedron. The molecular structure of **15b** · 2DCM is depicted in Figure 2.39 with distances and angles in the caption.

The mean Fe–N distance is 2.253 Å and the nitrito ligands coordinate with an average distance of 2.023 Å to the central metal. Both nitrito ligands are twisted in opposite directions resulting in the nearest possible conformation of the nitrito ligands nitrogen atoms. The mean intramolecular distances in within the  $\text{NO}_2^-$  ligands differ by 0.08 Å whereby the distance between the nitrogen and the non-coordinated oxygen-atom is the

shorter one. Due to the inversion symmetry in the binuclear complex, the Fe1–O5–Fe1<sup>i</sup> is exactly 180°.

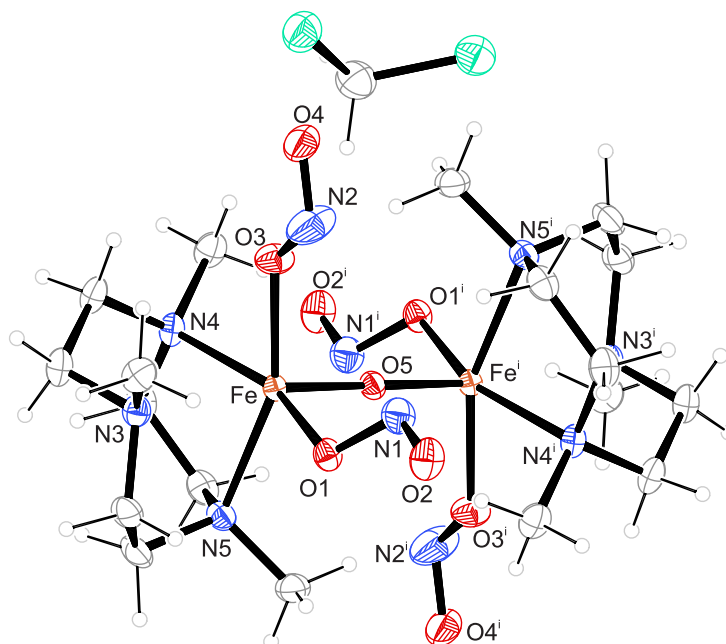


**Figure 2.40:** Ortep plot of  $[\text{Fe}_2(\text{Me}_3\text{tacn})_2(\text{NO}_2\text{-}\kappa\text{O})_4(\mu\text{-O})] \cdot 2\text{DCM}$  in crystals of **15b** · 2DCM. For clarity, the second, symmetry generated chloroform molecule is omitted. The thermal ellipsoids are drawn at 50% probability. Interatomic distances (Å) and bond angles (°). The standard deviation of the last decimal is given in parentheses: Fe1–O1 2.033(1), Fe1–O3 2.013(1), Fe1–O5 1.8068(3), Fe1–N3 2.340(2), Fe1–N4 2.214(2), Fe1–N5 2.204(2), N1–O1 1.316(2), N1–O2 1.211(2), N2–O4 1.208(2), N2–O3 1.263(2); O1–Fe1–O5 101.69(4), O1–Fe1–N3 82.50(5), O1–Fe1–N4 159.55(6), O1–Fe1–N5 92.77(6), O1–Fe1–O3 98.91(5), O3–Fe1–O5 102.16(4), O3–Fe1–N3 87.25(6), O3–Fe1–N4 82.77(6), O3–Fe1–N5 158.70(6), N4–Fe1–N3 77.21(6), N5–Fe1–N3 76.64(6), N5–Fe1–N4 80.17(6), O2–N1–O1 113.93(2), O3–N2–O4 116.0(2). Symmetry code: <sup>i</sup> 1–*x*, 1–*y*, 1–*z*.

### 2.5.3 Synthesis of $[\text{Fe}_2(\text{NO}_2\text{-}\kappa\text{O})_2(\text{tpya})_2(\mu\text{-O})](\text{ClO}_4)_2 \cdot 2\text{C}_3\text{H}_6\text{O}$ (**16a** · $2\text{C}_3\text{H}_6\text{O}$ ) and $[(\text{NO}_2\text{-}\kappa\text{O})(\text{tpya})\text{Fe}(\mu\text{-O})\text{Fe}(\text{NO}_2\text{-}\kappa^2\text{O},\text{O}')(\text{tpya})](\text{ClO}_4)_2 \cdot 3\text{C}_3\text{H}_6\text{O}$ (**16b** · $3\text{C}_3\text{H}_6\text{O}$ )

Both substances were obtained by adding silver nitrite to a solution of **P16** in acetone. After crystallization, a mixture of red, grown-together needles and orange, block-like crystals were obtained. The crystalline products are neither thermally stable nor air-stable but can be stored for several weeks at 5°C in the mother liquor under inert atmosphere. The solid mixture was characterized by single-crystal X-ray diffraction, elemental analysis, IR and UV-Vis spectroscopy.

The UV-Vis-spectroscopic analysis of a solution of **16** in dichloromethane shows three absorption bands at 315 nm, 362 nm and 495 nm.

The IR vibrations of the chelating nitrito ligand in **16b** ·  $3\text{C}_3\text{H}_6\text{O}$  were partly superimposed by other vibrations, also due to the smaller amount of the chelating isomer, their intensities were decreased to those of the monodentate ligand. Therefore, it was not possible to determine the vibration bands of the nitrito- $\kappa^2\text{O},\text{O}'$  ligand. The observ-

able vibration modes were identified by comparison with the IR spectrum of **P16** and verified the isotope-induced shift of the  $^{15}\text{NO}_2^-$ -enriched substances. Table 11 shows the wavenumbers of the nitrite-related IR bands and their respective vibration modes.

**Table 11:** IR vibrations of the nitrito- $\kappa O$  ligands in **16** with the values of the respective vibrations in the  $^{15}\text{NO}_2^-$ -enriched substances. The IR band of the symmetric stretching vibration of the chelating nitrito ligand was not found in the spectrum.

binding mode	vibration	$\tilde{\nu}(^{14}\text{NO}_2^-)/\text{cm}^{-1}$	$\tilde{\nu}(^{15}\text{NO}_2^-)/\text{cm}^{-1}$
	$\delta$	818	815
$\kappa O$	$\nu(\text{N}-\text{O})$	1020	998
	$\nu(\text{N}=\text{O})$	1471	1463

The isolated crystals differ in their habitus and could be separated by visual inspection with an optical microscope. **16a**  $\cdot 2\text{C}_3\text{H}_6\text{O}$  crystallizes in the orthorhombic space group  $Fdd2$  with eight formula units in the primitive cell. The respective asymmetric unit consists of half a complex cation, one perchlorate anion and two acetone.

The two sixfold coordinated iron centers in the inversion symmetric complex are bridged by one oxido ligand. Furthermore, each central metal is coordinated by one facially binding, tetradentate tpya ligand *via* three five-membered chelate rings and one *E*-nitrito- $\kappa O$  ligand. **16b**  $\cdot 3\text{C}_3\text{H}_6\text{O}$  crystallizes in the triclinic space group  $P\bar{1}$  with two formula units in the primitive cell. The asymmetric cell contains a full complex molecule, two perchlorate anions and three equivalents of co-crystallized acetone. As well as in **16a**  $\cdot 2\text{C}_3\text{H}_6\text{O}$ , the iron atoms in the binuclear complex are bridged by one oxido ligand. The remaining coordination sites are occupied by one tpya ligand. Instead of two *E*- $\kappa O$ -nitrito ligands as in **16a**  $\cdot 2\text{C}_3\text{H}_6\text{O}$ , **16b** exhibits one chelating nitrito ligand and one *E*-nitrito- $\kappa O$  ligand. According to this, **16a** and **16b** can be considered isomers. Fe1 in **16b** is sixfold coordinated and Fe2 is sevenfold coordinated. The resulting coordination polyhedra are best described as distorted octahedra and pentagonal-bipyramids, respectively. It is notable that every *E*-nitrito- $\kappa O$  ligand is opposed by a pyridyl moiety while the chelating nitrite binds opposed to a the bridging nitrogen atom of a tpya ligand. The molecular structures of both isomers are depicted in Figure 2.41 and 2.42 with distances and angles in the caption.

The average Fe–N distance are 2.181 Å and 2.198 Å in **16a**  $\cdot 2\text{C}_3\text{H}_6\text{O}$  and **16b**  $\cdot 3\text{C}_3\text{H}_6\text{O}$ , respectively. As in the precursor compound **P16**, the distance between central metal and bridging, tertiary nitrogen atom of the tpya ligand marks the longest Fe–N bond. The Fe1–O3–Fe1<sup>1</sup> angle in **16a** is with 163.7(4)° more bent than in its isomer **16b** where the Fe1–O5–Fe2 angle is 175.11(11)°. The Fe– $\mu\text{O}$  distances in both complexes are almost equal. All O–N–O angles are around 114°. The N–O distances within the chelating nitrito ligand in **16b**  $\cdot 3\text{C}_3\text{H}_6\text{O}$  differ only by 0.012 Å which implies nearly ideal delocalization of the double bond.

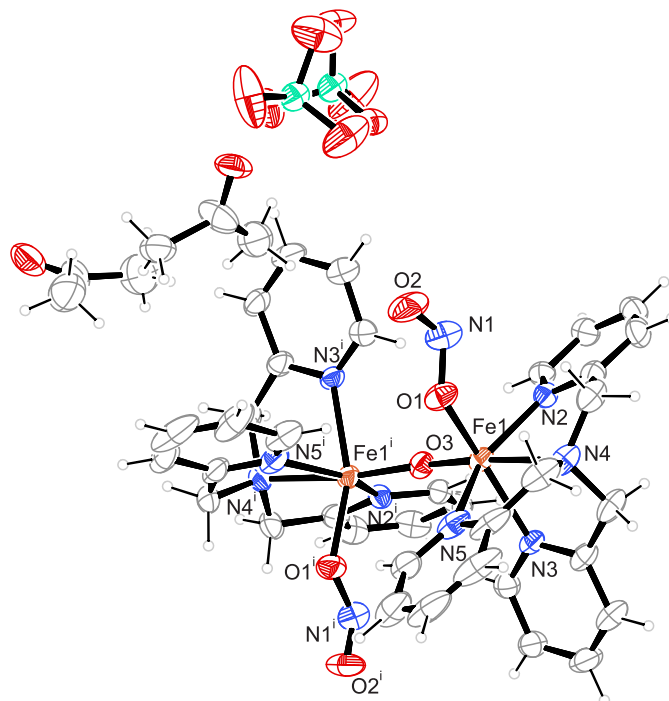


**Figure 2.41:** Ortep plot of  $[\text{Fe}_2(\text{NO}_2\text{-}\kappa\text{O})_2(\text{tpya})_2(\mu\text{-O})](\text{ClO}_4)_2 \cdot 2\text{C}_3\text{H}_6\text{O}$  in crystals of **16a** ·  $2\text{C}_3\text{H}_6\text{O}$ . For clarity, the second, symmetry generated perchlorate anion is omitted. The thermal ellipsoids are drawn at 50% probability. Interatomic distances (Å) and bond angles (°). The standard deviation of the last decimal is given in parentheses: Fe1–O1 2.008(5), Fe1–O3 1.798(1), Fe1–N2 2.132(5), Fe1–N3 2.165(5), Fe1–N4 2.253(5), Fe1–N5 2.173(6), N1–O1 1.302(8), N1–O2 1.197(9); N4–Fe1–N2 75.5(2), N4–Fe1–N3 77.78(2), N4–Fe1–N5 76.2(2), N4–Fe1–N1 87.8(2), O3–Fe1–O1 100.1(2), O3–Fe1–N2 101.8(2), O3–Fe1–N3 95.0(2), O1–Fe1–N2 95.3(2), O1–Fe1–N3 159.9(2), O1–Fe1–N5 82.4(2), O1–N1–O2 114.5(7). Symmetry code: <sup>i</sup> 1–*x*, 1–*y*, +*z*.

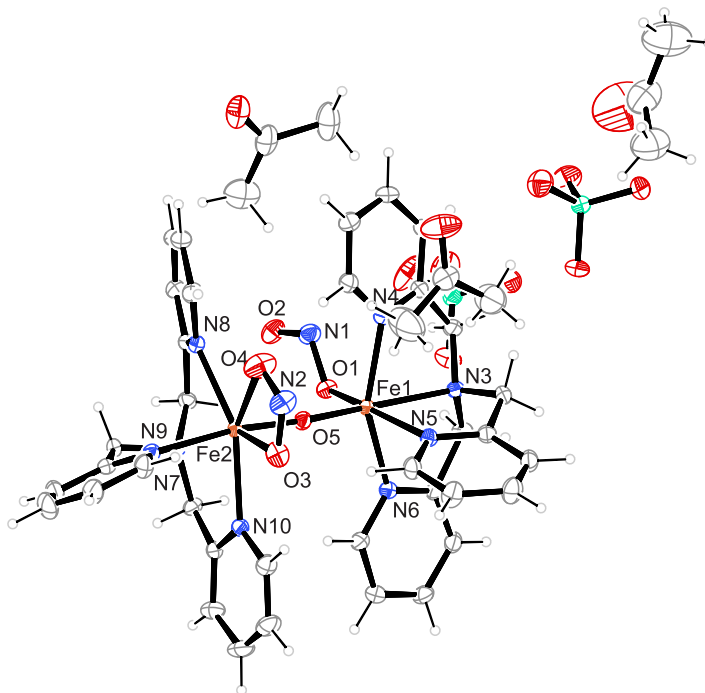


**Figure 2.42:** Ortep plot of  $[(\text{NO}_2\text{-}\kappa\text{O})(\text{tpya})\text{Fe}(\mu\text{-O})\text{Fe}(\text{NO}_2\text{-}\kappa^2\text{O},\text{O}')(\text{tpya})](\text{ClO}_4)_2 \cdot 3\text{C}_3\text{H}_6\text{O}$  in crystals of **16b** ·  $3\text{C}_3\text{H}_6\text{O}$ . The thermal ellipsoids are drawn at 50% probability. Interatomic distances (Å) and bond angles ( $^\circ$ ). The standard deviation of the last decimal is given in parentheses: Fe1–O1 2.023(2), Fe1–O5 1.798(2), Fe1–N3 2.269(2), Fe1–N4 2.114(2), Fe1–N5 2.162(2), Fe1–N6 2.150(2), Fe2–O3 2.237(2), Fe2–O4 2.246(2), Fe2–O5 1.801(2), Fe2–N7 2.220(2), Fe2–N8 2.228(2), Fe2–N9 2.210(2), Fe2–N10 2.230(2), N1–O1 1.328(3), N1–O2 1.202(3), N2–O3 1.264(3), N2–O4 1.252(3); O1–Fe1–N3 88.89(8), O5–Fe1–N3 170.67(8), N4–Fe1–N3 75.34(8), N5–Fe1–N3 77.09(8), N6–Fe1–N3 76.37(8), O1–Fe1–O5 100.17(8), O1–Fe1–N4 91.01(8), O1–Fe1–N5 162.78(8), O1–Fe1–N6 84.31(8), N7–Fe2–O4 96.38(8), N7–Fe2–N9 77.88(8), N7–Fe2–N8 72.32(8), N7–Fe2–O3 151.78(8), N7–Fe2–N10 76.15(8), O5–Fe2–O3 97.31(8), O5–Fe2–O4 96.14(9), N8–Fe2–O4 76.74(8), N10–Fe2–O3 79.02(8), O3–Fe2–O4 54.53(8), O2–N1–O1 113.9(2), O4–N2–O3 109.4(2).

#### 2.5.4 Synthesis of $[\text{Fe}_2\text{Cl}_2(\text{NO}_2\text{-}\kappa^2\text{O},\text{O}')_2(\text{py})_4(\mu\text{-O})] \cdot \text{py}$ (**17** · py)

**17** · py was prepared by adding silver nitrite to a solution of iron(III) chloride in pyridine at  $-20^\circ\text{C}$ . The substance is highly sensitive to temperatures above  $-20^\circ\text{C}$  and oxidation and decays within a few minutes under the loss of pyridine. Therefore, a further purification of the product was not feasible and only single-crystal X-ray diffraction and IR spectroscopy were used for characterization.

The IR spectrum of **17** · py showed the three nitrite-related vibrations at  $1302\text{cm}^{-1}$  ( $\nu_s$ ),  $1232\text{cm}^{-1}$  ( $\nu_{as}$ ) and  $856\text{cm}^{-1}$  ( $\delta$ ).

**17** · py crystallized in the monoclinic space group  $C2/c$  with four formula units in the unit cell. The asymmetric unit contains half a complex molecule and half a pyridine. The central metals in the neutral, binuclear, inversion-symmetric complex are bridged by one oxido ligand. The remaining coordination sites are occupied by one chlorido ligand, two opposing pyridine ligands and one chelating nitrito ligand. The resulting polyhedron is best described by a strongly distorted octahedron. The molecular structure of **17** · py is depicted in Figure 2.43 with distances and angles in the caption. The average Fe–N

distance is 2.169 Å. The difference between the two Fe–O<sub>nitrite</sub> coordination bonds is 0.09 Å. The intramolecular N–O distances within the nitrito ligand differ by circa 0.01 Å. The co-crystallized pyridine acts as acceptor for a long, non-classical hydrogen bond outgoing from C6–H6. Further details regarding the hydrogen bond are listed in Table 12.

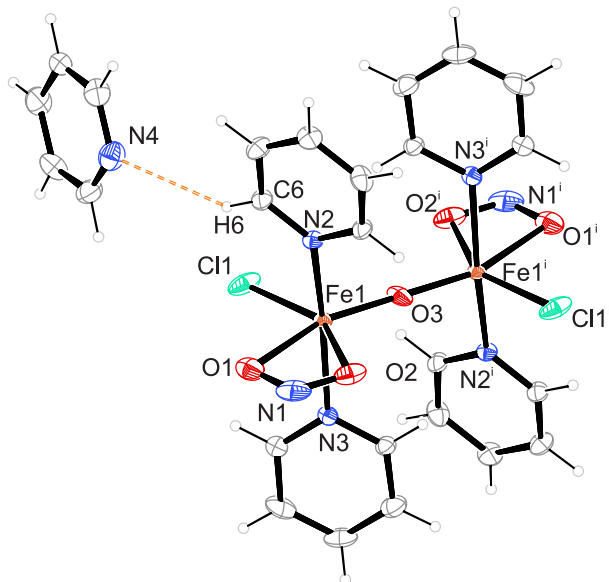


**Figure 2.43:** Ortep plot of  $[\text{Fe}_2\text{Cl}_2(\text{NO}_2\text{-}\kappa^2\text{O}, \text{O}')_2(\text{py})_4(\mu\text{-O})] \cdot \text{py}$  in crystals of **17** · **py**. The thermal ellipsoids are drawn at 50% probability. For clarity, the second, symmetry-generated pyridine is omitted. Interatomic distances (Å) and bond angles ( $^\circ$ ). The standard deviation of the last decimal is given in parentheses: Fe1–O1 2.239(3), Fe1–O2 2.154(3), Fe1–O3 1.7734(6), Fe1–N2 2.170(3), Fe1–N3 2.167(3), Fe1–Cl1 2.275(1), N1–O1 1.268(6), N1–O2 1.260(5); O1–Fe1–Cl1 92.8(1), O3–Fe1–O2 101.0(1), O3–Fe1–Cl1 109.18(4), N2–Fe1–O1 84.0(1), N2–Fe1–O2 83.6(1), N2–Fe1–O3 95.19(9), N2–Fe1–Cl1 95.15(9), N3–Fe1–O1 82.7(1), N3–Fe1–O2 81.8(1), N3–Fe1–O3 93.8(1), N3–Fe1–Cl1 94.2(1), N3–Fe1–N2 164.1(1), O2–Fe1–O1 57.0(1), Fe1–O3–Fe1<sup>i</sup> 180.00(4), O2–N1–O1 112.2(4). Symmetry code: <sup>i</sup>  $1/2-x, 3/2-y, 1-z$ .

**Table 12:** Distances and angles of hydrogen bonds in **17** · **py**. The standard deviation of the last decimal is given in parentheses. Values without standard deviation refer to hydrogen atoms which were calculated on idealized positions, riding on their parent atoms.

D–H···A	$d(\text{D–H})/\text{Å}$	$d(\text{H} \cdots \text{A})/\text{Å}$	$d(\text{D} \cdots \text{A})/\text{Å}$	$\angle(\text{D–H} \cdots \text{A})/^\circ$
C6–H6···N4	0.95	265	3.432(7)	139.6

## 2.6 Computer-chemical calculations

### 2.6.1 Validation of the computer-chemical results *via* structural optimization

To determine the best computer-chemical method for the following scan calculations, structural optimization was used as indicator for the quality of the calculations. Since the focus is mainly set on the nitrite’s binding modes, the results of the structural optimizations needed to reproduce the experimentally determined  $M-O_{\text{nitrite}}$  distances. Starting geometries were taken directly from the crystal structures derived from single-crystal X-ray diffraction. Technical information regarding the calculations are listed in Section 5.2.7. The following tables sum up the comparison between different calculation methods and the experimental data. In the case of the two anionic complexes **1a-M** ( $M = \text{Al, Sc, Cr, Fe, Ga, In, Tl}$ ) and **7**, the respective anions were not part of the structural optimization since the presence of those parts would lead to a much higher calculation time for the following scan calculations. However, in the case of **1a-Sc** and **1a-Fe**, the results of calculations (BP86 functional with CPCM) including the cations are shown (Tables 13 and 15).

In almost every optimization calculation regarding the anions in **1a-M** with  $M = \text{Al, Sc, Cr, Fe, Ga, In, Tl}$ ), the poorest agreement with the experimental data was obtained when the gga functional BP86 was utilized together with the solvation model. A slight improvement is observed, if the CPCM instruction is omitted from the calculations but the results are usually still the second worst. The meta-gga functional TPSS was demonstrated as an improvement compared to the BP86. The generally best results with a were obtained when the hybrid-functional TPSSh was applied.

Only two exceptions were found in the **1a-M** series. The chromate complex containing the monodentate bound nitrito ligand exhibits an excellent concordance in all performed calculations and shows, in general, a  $\Delta_{\text{mean}}$  below  $0.01 \text{ \AA}$ . The chelating isomer of **1a-Cr** also shows a different behavior compared to the other complexes in **1a-M** since the smallest mean deviation is obtained by the BP86 functional without the solvation model followed by the meta-gga functional TPSS. Furthermore, the otherwise best choice, the TPSSh functional, shares the greatest deviation with the BP86 calculation including CPCM. The by far worst agreements between X-ray data and calculated values are found the calculations regarding **1a-Tl**. Not only that the mean deviation of the BP86 is worse without CPCM than with CPCM, the  $\Delta_{\text{mean}}$  is still over  $0.066 \text{ \AA}$  even if the hybrid-functional is used.

Including the two cations in the calculations led to a wuch better agreement between calculated values and X-ray data in the case of the scandium compound. In fact, a deviation of less than  $0.01 \text{ \AA}$  let it surpass the otherwise best results of the calculations with the hybrid-functional TPSSh. However, no significant improvement is observed in the case of **1a-Fe**. The obtained  $\Delta_{\text{mean}}$  is, indeed, slightly better than the both BP86 calculations

without the anion but still worse than the results from the TPSS and TPSSh functionals.

**Table 13:** Comparison of the experimental data and calculated values of the complex anions in **1a-Al** and **1a-Sc**. Shown values are the shorter M–O ( $d$ ) and the longer M–O' ( $d'$ ) distances between central metal and coordinating nitrito ligands of the X-ray results and various functional/def2-TZVP calculations. All distances are given in Å.  $\Delta_{\text{mean}} = [\text{abs}(d_{\text{exp.}} - d_{\text{calc.}}) + \text{abs}(d'_{\text{exp.}} - d'_{\text{calc.}})]/2$ .

	<b>1a-Al</b>		<b>1a-Sc</b>		
	M–O ( $d$ )	$\Delta_{\text{mean}}$	M–O ( $d$ )	M–O' ( $d'$ )	$\Delta_{\text{mean}}$
X-ray	1.834	-	2.245	2.258	-
BP86(CPCM)	1.877	0.043	2.302	2.311	0.055
BP86	1.858	0.024	2.294	2.299	0.045
TPSS	1.856	0.022	2.289	2.294	0.040
TPSSh	1.850	0.016	2.283	2.287	0.033
BP86(CPCM)-2cat	-	-	2.268	2.276	0.008

**Table 14:** Comparison of the experimental data and calculated values of the complex anions in **1a-Cr**. Shown values are the shorter M–O ( $d$ ) and the longer M–O' ( $d'$ ) distances between central metal and coordinating nitrito ligands of the X-ray results and various functional/def2-TZVP calculations. All distances are given in Å.  $\Delta_{\text{mean}} = [\text{abs}(d_{\text{exp.}} - d_{\text{calc.}}) + \text{abs}(d'_{\text{exp.}} - d'_{\text{calc.}})]/2$ .

	<b>1a-Cr-<math>\kappa O</math></b>		<b>1a-Cr-<math>\kappa^2 O, O'</math></b>		
	M–O ( $d$ )	$\Delta_{\text{mean}}$	M–O ( $d$ )	M–O' ( $d'$ )	$\Delta_{\text{mean}}$
X-ray	1.906	-	2.063	2.081	-
BP86(CPCM)	1.906	0.000	2.120	2.130	0.053
BP86	1.902	0.004	2.108	2.111	0.037
TPSS	1.907	0.001	2.114	2.114	0.042
TPSSh	1.914	0.008	2.125	2.125	0.053

**Table 15:** Comparison of the experimental data and calculated values of the complex anions in **1a-Fe** and **1a-Ga**. Shown values are the shorter M–O ( $d$ ) and the longer M–O' ( $d'$ ) distances between central metal and coordinating nitrito ligands of the X-ray results and various functional/def2-TZVP calculations. All distances are given in Å.  $\Delta_{\text{mean}} = [\text{abs}(d_{\text{exp.}} - d_{\text{calc.}}) + \text{abs}(d'_{\text{exp.}} - d'_{\text{calc.}})]/2$ .

	<b>1a-Fe</b>			<b>1a-Ga</b>	
	M–O ( $d$ )	M–O' ( $d'$ )	$\Delta_{\text{mean}}$	M–O ( $d$ )	$\Delta_{\text{mean}}$
X-ray	2.158	2.197	-	1.906	-
BP86(CPCM)	2.256	2.280	0.090	1.964	0.058
BP86	2.246	2.264	0.077	1.944	0.038
TPSS	2.221	2.233	0.050	1.936	0.030
TPSSh	2.206	2.219	0.035	1.928	0.022
BP86(CPCM)-2cat	2.194	2.306	0.073	-	-

**Table 16:** Comparison of the experimental data and calculated values of the complex anions in **1a-In** and **1a-Tl**. Shown values are the shorter M–O ( $d$ ) and the longer M–O' ( $d'$ ) distances between central metal and coordinating nitrito ligands of the X-ray results and various functional/def2-TZVP calculations. All distances are given in Å.  $\Delta_{\text{mean}} = [\text{abs}(d_{\text{exp.}} - d_{\text{calc.}}) + \text{abs}(d'_{\text{exp.}} - d'_{\text{calc.}})]/2$ .

	<b>1a-In</b>			<b>1a-Tl</b>		
	M–O ( $d$ )	M–O' ( $d'$ )	$\Delta_{\text{mean}}$	M–O ( $d$ )	M–O' ( $d'$ )	$\Delta_{\text{mean}}$
X-ray	2.280	2.293	-	2.383	2.387	-
BP86(CPCM)	2.369	2.375	0.085	2.475	2.538	0.121
BP86	2.367	2.372	0.083	2.506	2.524	0.130
TPSS	2.342	2.347	0.058	2.463	2.495	0.094
TPSSh	2.327	2.330	0.042	2.432	2.470	0.066

In the calculations of **7** (Table 17), the best agreement with the experimental data is not obtained with the hybrid functional TPSSh but with TPSS. Here, the mean deviation is 0.008 Å smaller in the case of the latter. In agreement with the results of **1a-Fe**, the greatest deviation is obtained by the gga density functional BP86 including the CPCM solvation model. A slightly better agreement is achieved when this model is excluded. However, the Fe–O distances from the X-ray structure are much better reproduced than the Fe–O' distances.

**Table 17:** Comparison of the experimental data and calculated values of the complex anion in **7**. Shown values are the shorter M–O ( $d$ ) and the longer M–O' ( $d'$ ) distances between central metal and coordinating nitrito ligands of the X-ray results and various functional/def2-TZVP calculations. All distances are given in Å.  $\Delta_{\text{mean}} = [\text{abs}(d_{\text{exp.}} - d_{\text{calc.}}) + \text{abs}(d'_{\text{exp.}} - d'_{\text{calc.}})]/2$ .

	<b>7</b>		
	M–O ( $d$ )	M–O' ( $d'$ )	$\Delta_{\text{mean}}$
X-ray	2.115	2.584	-
BP86(CPCM)	2.187	2.685	0.086
BP86	2.163	2.684	0.074
TPSS	2.157	2.622	0.040
TPSSh	2.126	2.669	0.048

**11** and **12** show the same behavior in the different optimization calculations. In the case of the BP86 functional, the mean deviation improves by 0.039 Å (**11**) and 0.041 Å (**12**) when the CPCM is not included. With regard to the other functionals (TPSS and TPSSh), the calculated values improve by taking the HF exchange into account. Thus, TPSSh exhibits a 0.008 Å (**11**) and 0.016 Å (**12**) lower mean deviation than the pure density TPSS functional.

**Table 18:** Comparison of the experimental data and calculated values of compounds **11** and **12**. Shown values are the shorter M–O ( $d$ ) and the longer M–O' ( $d'$ ) distances between central metal and coordinating nitrito ligands of the X-ray results and various functional/def2-TZVP calculations. All distances are given in Å.  $\Delta_{\text{mean}} = [\text{abs}(d_{\text{exp.}} - d_{\text{calc.}}) + \text{abs}(d'_{\text{exp.}} - d'_{\text{calc.}})]/2$ .

	<b>11</b>			<b>12</b>		
	M–O ( $d$ )	M–O' ( $d'$ )	$\Delta_{\text{mean}}$	M–O ( $d$ )	M–O' ( $d'$ )	$\Delta_{\text{mean}}$
X-ray	2.150	2.184	-	2.143	2.200	-
BP86(CPCM)	2.226	2.296	0.094	2.229	2.298	0.092
BP86	2.181	2.264	0.055	2.182	2.264	0.051
TPSS	2.156	2.239	0.031	2.158	2.237	0.026
TPSSh	2.137	2.218	0.023	2.141	2.218	0.010

Just like in the previous cases, the calculations on **13** and **14** show the best agreement with the experimental results if the TPSSh hybrid functional is applied, followed by slightly worse results of the TPSS functional. Contrary to **1a-Fe**, **7**, **11** and **12**, the calculated Fe–O<sub>nitrite</sub> distances are already in relatively good agreement using the pure density functional BP86 excluding CPCM. Again, the solvation model results in a deterioration of the concordance with the experimental values leading to over 0.05 Å more mean deviation compared to the calculation without this model.

**Table 19:** Comparison of the experimental data and calculated values of compounds **13** and **14**. Shown values are the shorter M–O ( $d$ ) and the longer M–O' ( $d'$ ) distances between central metal and coordinating nitrito ligands of the X-ray results and various functional/def2-TZVP calculations. All distances are given in Å.  $\Delta_{\text{mean}} = [\text{abs}(d_{\text{exp.}} - d_{\text{calc.}}) + \text{abs}(d'_{\text{exp.}} - d'_{\text{calc.}})]/2$ .

	<b>13</b>			<b>14</b>		
	M–O ( $d$ )	M–O' ( $d'$ )	$\Delta_{\text{mean}}$	M–O ( $d$ )	M–O' ( $d'$ )	$\Delta_{\text{mean}}$
X-ray	2.146	2.175	-	2.145	2.178	-
BP86(CPCM)	2.258	2.263	0.100	2.249	2.261	0.094
BP86	2.201	2.204	0.042	2.201	2.206	0.043
TPSS	2.187	2.192	0.029	2.191	2.196	0.033
TPSSh	2.180	2.182	0.021	2.155	2.160	0.012

### 2.6.2 Spin density distribution in **1a-Fe** and **1a-Cr**

Since **1a-Fe** and **1a-Cr** exhibit only partially filled d orbitals, the substances allowed investigation of the influence of varying filled d orbitals on the binding behavior of the nitrito ligand. A useful methodology is to visualize the spin density of coordination compounds by plotting it as an isodensity surface according to Ruiz *et al.*<sup>[87]</sup> The center of the paramagnetic, high-spin d<sup>5</sup> complex **1a-Fe** exhibits five  $\alpha$ -spin electrons that are evenly distributed in the five d orbitals. As a result, the spin-density distribution on the center of the ferric compound appears more or less spherical (Figure 2.44). Deviations from the

normally spherical shape can be traced back to the delocalization of the central metal's spin density into the ligand orbitals.<sup>[87]</sup> Symmetry allowed  $\sigma$ -interactions between the central metal's  $e_g$  orbitals and the p orbitals of the nitrite's coordinating O-atoms resulting in the delocalization of  $\alpha$ -spin density into the ligand orbitals. No spin density is found in the nodal plane between metal and ligand which serves as a graphical representation of the frontier MO's antibonding character and the consequent mainly ionic interaction between iron(III) and the nitrito ligand. In the case of the fpin ligand, additional  $\pi$ -antibonding is found resulting in the oddly shaped  $\alpha$ -spin densities. In accordance with the results of Ruiz *et al.* no signs of spin-polarization are found since the orbital interactions are symmetry allowed.<sup>[87]</sup>

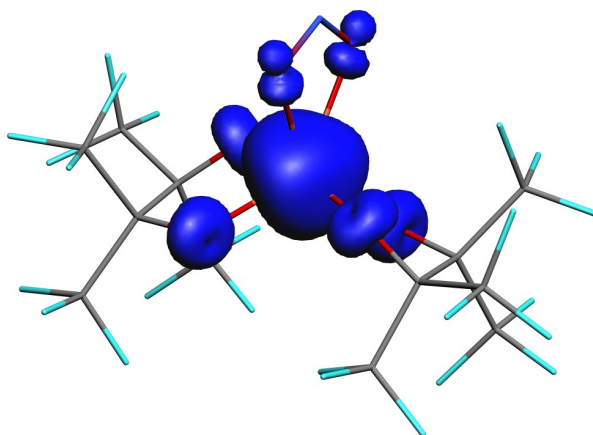


**Figure 2.44:** Spin population in **1a-Fe**. ( $0.01 a_0^{-3}$  surface; blue:  $\alpha$ -spin excess, yellow:  $\beta$ -spin excess).

In the case of **1a-Cr**, only the  $d_{xy}$ ,  $d_{yz}$ ,  $d_{xz}$  orbitals are occupied with each one  $\alpha$ -spins and the  $d_{x^2-y^2}$  and  $d_{z^2}$  orbitals remain empty. The resulting spin density distribution has the shape of a cube with six deep holes on its faces (Figure 2.45 and 2.46). In contrast to the spin delocalization in **1a-Fe**, spin polarization is found in **1a-Cr** resulting in observable  $\beta$ -spin density concentrated on the coordinating O-atom of the nitrito ligand. According to Ruiz *et al.*, the spin polarization in the binding orbital of the coordinating atom is a result of the missing  $\alpha$ -spin density at the coordination site that shows the non-binding character of the orbital interaction.<sup>[87]</sup> Again, no spin density is found in the nodal planes between metal and ligand.

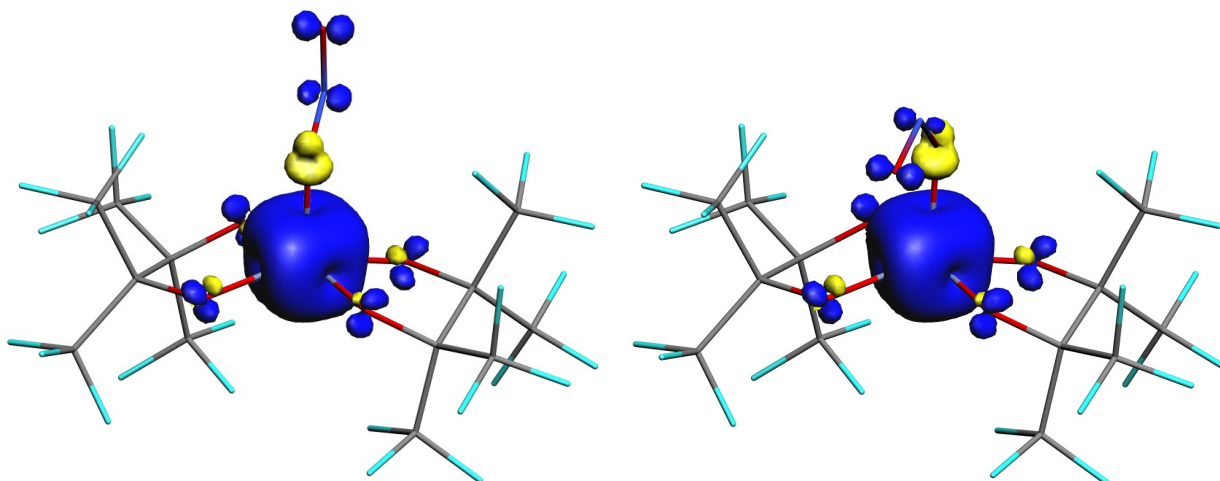


**Figure 2.45:** Spin population in **1a-Cr- $\kappa O$** . (0.01  $a_0^{-3}$  surface; blue:  $\alpha$ -spin excess, yellow:  $\beta$ -spin excess).

**Figure 2.46:** Spin population in **1a-Cr- $\kappa^2 O, O'$** . (0.01  $a_0^{-3}$  surface; blue:  $\alpha$ -spin excess, yellow:  $\beta$ -spin excess).

### 2.6.3 Quantum-chemical scan calculations

The scan calculation on the dianionic complex **1a-Fe** was performed with the GGA functional BP86 and the meta-GGA functional TPSS. For comparison purposes, in the case of **1a-Fe** the Conductor-like Polarizable Continuum Model (CPCM) was applied in a second calculation with the BP86 functional. The scan graphs (Figure 2.47) show that the most stable isomer is represented by the isolated  $\kappa^2 O, O'$  binding mode in each calculation. The three deepest potential pots appear at the same Fe–O1–N angles. While the general appearance of the TPSS graph is very similar to that of the BP86 functional, the curve of the BP86(CPCM) calculation exhibits a much smoother shape. This becomes obvious if the  $Z$ - $\kappa O$  isomer is viewed in more detail. In all calculations it appears as a shoulder beside the minimum of the chelating isomer but becomes less prominent from TPSS over BP86 to BP86(CPCM). The same applies for the side-on binding mode. While it appears as a shallow potential pot in the TPSS calculation and is still visible as a shoulder in the BP86 case, it vanishes completely if CPCM is included. In the BP86(CPCM) scan, the  $E$ -nitrito- $\kappa O$  isomer appears to be  $4.1 \text{ kJ mol}^{-1}$  less stable than the chelating isomer which is slightly above the TPSS curve ( $3.8 \text{ kJ mol}^{-1}$ ) followed by  $1.4 \text{ kJ mol}^{-1}$  in the case of BP86. A much bigger difference is found if the relative energies of the  $\kappa N$  binding mode are viewed. Here, the energy obtained from the BP86(CPCM) calculation is only  $0.2 \text{ kJ mol}^{-1}$  above that of the chelating isomer, and is  $3.7 \text{ kJ mol}^{-1}$  and  $9.8 \text{ kJ mol}^{-1}$  for BP86 without the solvation model and TPSS, respectively. The needed energy for the  $\kappa^2 O, O'$  to  $E$ - $\kappa O$  isomerization is calculated to be  $28.7 \text{ kJ mol}^{-1}$  in the case of BP86(CPCM),  $22.1 \text{ kJ mol}^{-1}$  with TPSS and  $20.1 \text{ kJ mol}^{-1}$  using the BP86 functional.  $17.0 \text{ kJ mol}^{-1}$  are needed to overcome the  $E$ - $\kappa O \rightarrow \kappa N$  barrier according to the BP86(CPCM) calculation and  $14.0 \text{ kJ mol}^{-1}$  if only BP86 is applied. In the case of the TPSS calculation this barrier is interrupted by the local minimum of the side-on binding

mode ( $14.5 \text{ kJ mol}^{-1}$ ) which is separated by two small energy barriers of  $0.8 \text{ kJ mol}^{-1}$  and  $0.9 \text{ kJ mol}^{-1}$  from the potential pots of the  $E-\kappa O$  and the  $\kappa N$  isomers, respectively. The scan graph of **1a-Sc** (Figure 2.48) shows a different appearance from all other scan graphs. The energies of the TPSS scan are in parantheses behind the value of the BP86 scan. The global minimum is represented by the chelating isomer which was also isolated in the single-crystal X-ray analysis. The slight shift of the minimum depending on the used functional is most likely a result of the scan increment of  $10^\circ$ . In contrast to all other scan graphs in the **1a-M** series, the scan of **1a-Sc** shows no local minimum for the nitrito- $\kappa N$  isomer but this binding mode is represented by the highest maximum of the graph at  $35.0 \text{ kJ mol}^{-1}$  ( $38.1 \text{ kJ mol}^{-1}$ ). The only other clear minimum is found with the  $\kappa^2 N, O$  isomer which has a relative energy of  $5.4 \text{ kJ mol}^{-1}$  ( $6.6 \text{ kJ mol}^{-1}$ ) above the chelating binding mode. The  $E$ -nitrito- $\kappa O$  isomer is found as a shoulder in the BP86 ( $11.8 \text{ kJ mol}^{-1}$ ) which is slightly more pronounced in the TPSS scan ( $12.4 \text{ kJ mol}^{-1}$ ). In the latter, it appears as a minimum separated by two small energy barriers from the  $\kappa^2 N, O$  ( $1.4 \text{ kJ mol}^{-1}$ ) and the chelating isomer ( $7.9 \text{ kJ mol}^{-1}$ ). According to the BP86 scan, an energy of  $18.6 \text{ kJ mol}^{-1}$  has to be applied for the  $\kappa^2 O, O' \rightarrow \kappa^2 N, O$  isomerization.

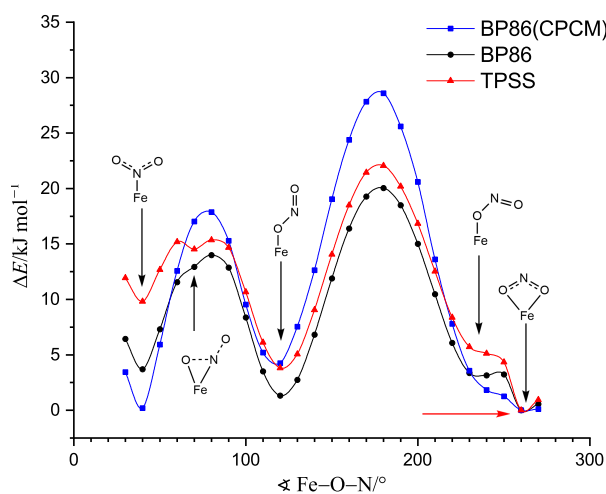


**Figure 2.47:** Comparison of the scan graphs calculated with the functionals TPSS (red curve), BP86 without solvation model (black curve) and including CPCM (blue curve) for the dianionic complex in **1a-Fe**. The red arrow marks the position of the X-ray structure analysis results.

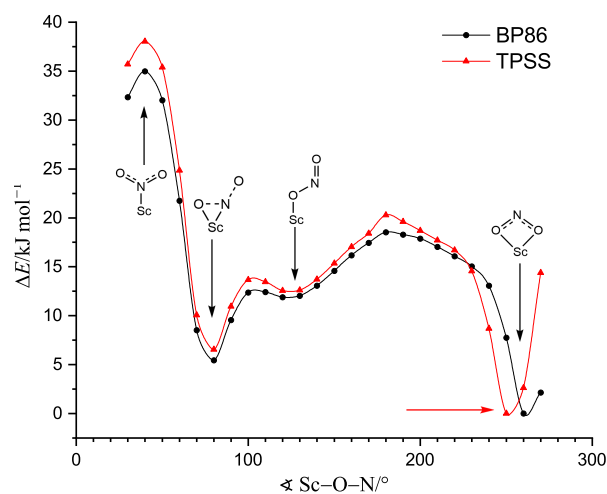


**Figure 2.48:** Comparison of the scan graphs calculated with the functionals TPSS (red curve) and BP86 without solvation model (black curve) for the dianionic complex in **1a-Sc**. The red arrow marks the position of the X-ray structure analysis results.

The scan curves of **1a-Cr** (Figure 2.49) show some differences compared to all other obtained scan graphs. Although the  $E-\kappa O$  and the  $\kappa^2 O, O'$  isomer were isolated in the structure of **1a-Cr**, the former is not found as the deepest potential pot although is the main isolated isomer. Furthermore, both functionals give different relative energies for the isomers and since the graphs are referenced to the most stable isomer, a different

description had to be formulated.

The global minimum of the BP86 scan curve is represented by the  $\kappa N$  isomer. The  $E$ - $\kappa O$ ,  $Z$ - $\kappa O$  and  $\kappa^2 O, O'$  binding modes are  $13.6 \text{ kJ mol}^{-1}$ ,  $14.5 \text{ kJ mol}^{-1}$  and  $6.6 \text{ kJ mol}^{-1}$ , respectively. The side-on isomer ( $12.3 \text{ kJ mol}^{-1}$ ) appears as a shoulder between the minima of N-bound and  $E$ - $\kappa O$  binding mode. According to the BP86 scan, the rotation barriers of the  $\kappa^2 O, O' \rightarrow Z$ - $\kappa O \rightarrow E$ - $\kappa O \rightarrow \kappa N$  pathway are  $13.6 \text{ kJ mol}^{-1}$ ,  $44.8 \text{ kJ mol}^{-1}$  and  $12.1 \text{ kJ mol}^{-1}$ .

In the TPSS scan curve, the most stable isomer is represented by the  $\kappa^2 O, O'$  binding mode. The relative energies of the other isomers are  $11.9 \text{ kJ mol}^{-1}$  ( $Z$ - $\kappa O$ ),  $10.8 \text{ kJ mol}^{-1}$  ( $E$ - $\kappa O$ ),  $8.4 \text{ kJ mol}^{-1}$  ( $\kappa^2 N, O$ ) and  $3.8 \text{ kJ mol}^{-1}$  ( $\kappa N$ ). The chelating isomer is separated by an energy barrier of  $24.0 \text{ kJ mol}^{-1}$  from the  $Z$ - $\kappa O$  binding mode; further  $36.0 \text{ kJ mol}^{-1}$  has to be applied to overcome the barrier towards the  $E$ - $\kappa O$ . The potential pot of the side-on binding mode is separated by two smaller rotation barriers of  $14.6 \text{ kJ mol}^{-1}$  and  $7.3 \text{ kJ mol}^{-1}$  from the  $E$ - $\kappa O$  binding mode and the  $\kappa N$  isomer, respectively.

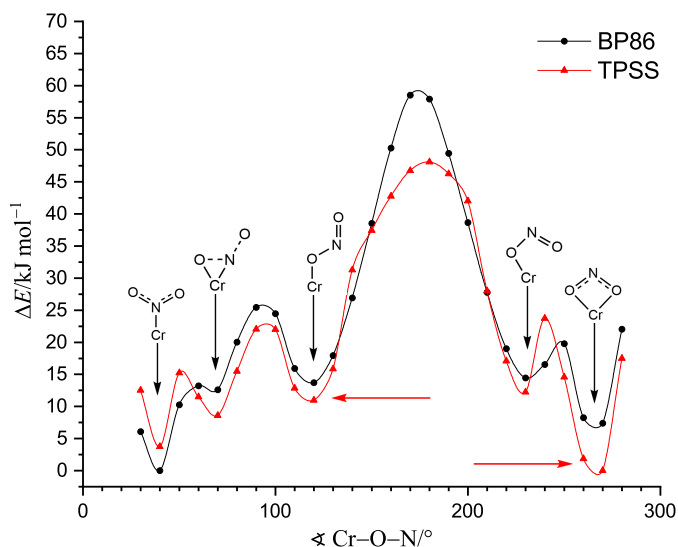


**Figure 2.49:** Comparison of the scan graphs calculated with the functionals TPSS (red curve) and BP86 without solvation model (black curve) for the dianionic complex in **1a-Cr**. The red arrow marks the position of the X-ray structure analysis results.

Figures 2.50 to 2.53 depict the scan graphs of the anions in **1a-M** with group 13 elements calculated with BP86 and TPSS as functionals. Beside two slightly more pronounced potential pots in the TPSS scans in the case of **1a-Al** and **1a-Ga**, no great differences are found between the scans from both functionals. Therefore, only the BP86 scans will be compared. The graphs of **1a-Al** and **1a-Ga** show that the  $E$ - $\kappa O$  binding mode marks the most stable isomer, followed by the  $Z$ - $\kappa O$  binding mode (**1a-Al**:  $8.7 \text{ kJ mol}^{-1}$  and **1a-Ga**:  $0.8 \text{ kJ mol}^{-1}$ ) and the nitrito- $\kappa N$  isomer (**1a-Al**:  $28.7 \text{ kJ mol}^{-1}$  and **1a-Ga**:

11.8 kJ mol<sup>-1</sup>). A minimum representing the  $\kappa^2O,O'$  isomer is not observed in the case of the gallate but it appears as a shoulder in the aluminate. To overcome the  $E-\kappa O \rightarrow Z-\kappa^2O$  isomerization barrier, 29.1 kJ mol<sup>-1</sup> are needed in the case of the aluminate and 41.3 kJ mol<sup>-1</sup> in the case of the gallate. The  $E-\kappa O \rightarrow \kappa N$  are 44.0 kJ mol<sup>-1</sup> and 42.7 kJ mol<sup>-1</sup> for **1a-Al** and **1a-Ga**, respectively.

**1a-In** and **1a-Tl** show a very similar energy curve which shows the global minima at the position of the chelating isomer without signs of a  $Z-\kappa O$  binding mode. The two other minima on the scan graph represent the  $\kappa N$  isomer and the  $E-\kappa O$  isomer. The former is 29.5 kJ mol<sup>-1</sup> and 23.5 kJ mol<sup>-1</sup> less stable than the chelating isomer in the case of **1a-In** and **1a-Tl**, respectively. The energies of the monodentate O-binding isomer are 23.0 kJ mol<sup>-1</sup> for the indate and 34.3 kJ mol<sup>-1</sup> for the thallate. The heights of the two rotation barriers between the isomers in the  $\kappa^2O,O' \rightarrow E-\kappa O \rightarrow \kappa N$  pathway are 60.0 kJ mol<sup>-1</sup> and 24.6 kJ mol<sup>-1</sup> in the case of **1a-In** and 71.6 kJ mol<sup>-1</sup> and 20.0 kJ mol<sup>-1</sup> in the case of **1a-Tl**.

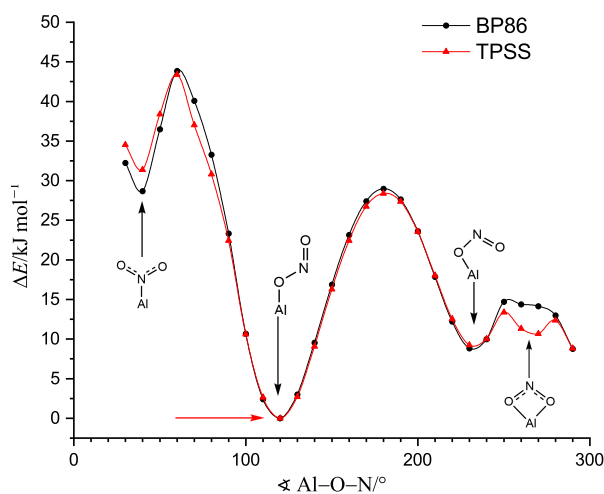


**Figure 2.50:** Comparison of the scan graphs calculated with the functionals TPSS (red curve) and BP86 without solvation model (black curve) for the dianionic complex in **1a-Al**. The red arrow marks the position of the X-ray structure analysis results.

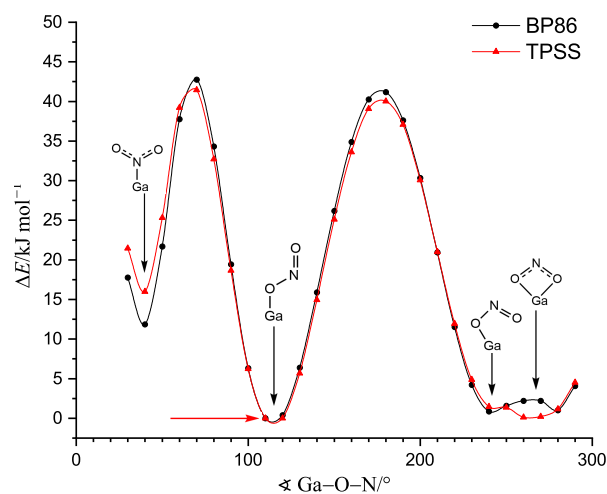


**Figure 2.51:** Comparison of the scan graphs calculated with the functionals TPSS (red curve) and BP86 without solvation model (black curve) for the dianionic complex in **1a-Ga**. The red arrow marks the position of the X-ray structure analysis results.

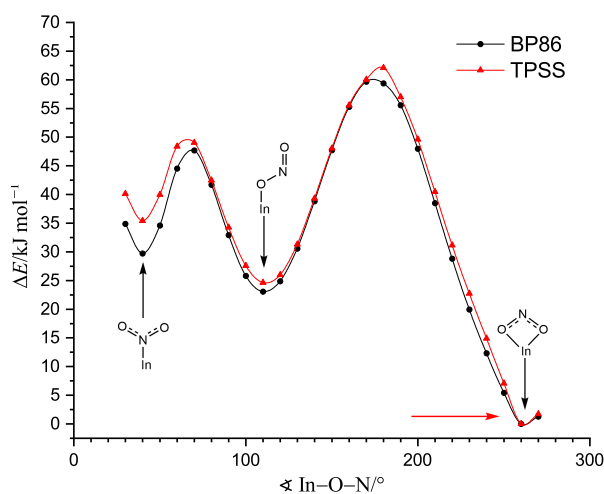


**Figure 2.52:** Comparison of the scan graphs calculated with the functionals TPSS (red curve) and BP86 without solvation model (black curve) for the dianionic complex in **1a-In**. The red arrow marks the position of the X-ray structure analysis results.

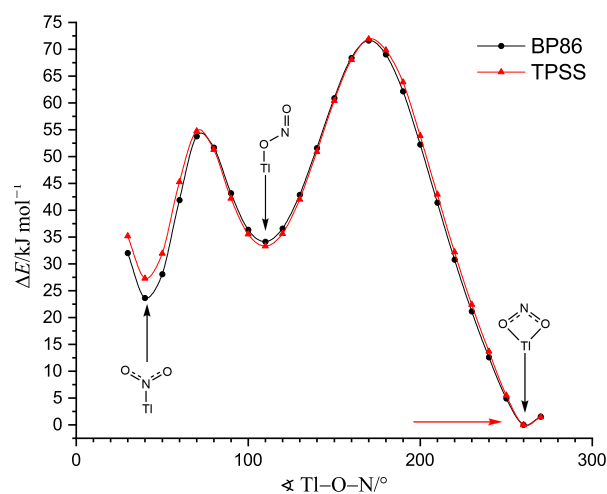


**Figure 2.53:** Comparison of the scan graphs calculated with the functionals TPSS (red curve) and BP86 without solvation model (black curve) for the dianionic complex in **1a-Tl**. The red arrow marks the position of the X-ray structure analysis results.

In contrast to the **1a-M** complexes, the nitrite in **7**, **11** and **12** is surrounded by an asymmetric ligand environment. In Figure 2.54, the various investigated end positions of the nitrito ligand in scans of **7** and **11**, when the Fe–O–N angle reaches 180°, are shown. In the case of **7**, the non-coordinating oxygen atom points either towards the carboxylate function's CH<sub>2</sub> moieties or in the direction of the bridging ethoxy function. In **11** and

**12** it is the ethylenediamine bridge or the *tert*-butyl moieties of the salen ligand. Due to this, the scan calculations were performed by rotating either over O1 (Fe–O1–N angle) or O2 (Fe–O2–N angle) of the FeNO<sub>2</sub> unit to investigate the rotation direction's influence on the scan graphs.

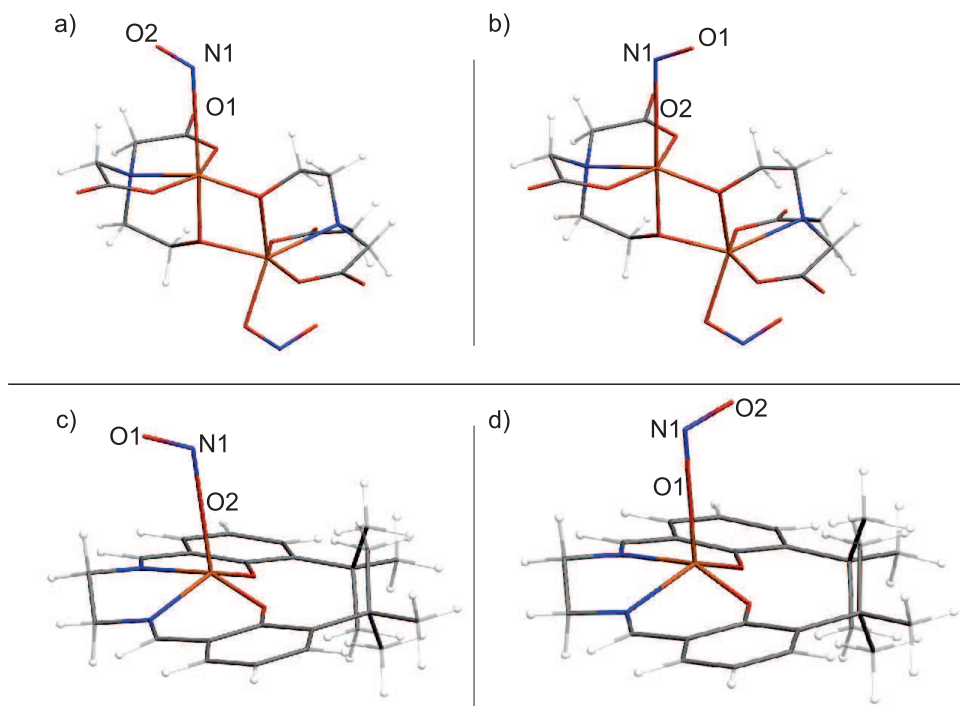


**Figure 2.54:** Two possible arrangements of the nitrito ligand in the compounds **7** (a and b) and **11** (c and d) when the Fe–O–N angle reaches 180°.

The scan calculation of the binuclear complex anion in **7** was very time consuming and therefore only the BP86 calculation was performed. In the case of the Fe–O1–N scan, the binding mode which is found in the X-ray structure (*Z*- $\kappa O$ ) represents the absolute minimum of the scan graph (Figure 2.55 black curve). Other minima on the curve are assigned to the *E*- $\kappa O$  (12.7 kJ mol<sup>-1</sup>),  $\kappa^2 N, O$  (2.8 kJ mol<sup>-1</sup>) and  $\kappa N$  (3.5 kJ mol<sup>-1</sup>) isomers. An additional, special isomer (*E*- $\kappa O^*$ ) is found at an Fe–O1–N angle of 160° which is a result of a C–H···N<sub>nitrite</sub> hydrogen-bond is 12.7 kJ mol<sup>-1</sup> above the most stable isomer of that scan curve. According to the calculation, an energy of 24.0 kJ mol<sup>-1</sup> has to be supplied to trigger an isomerization from the *Z*- $\kappa O$  isomer to the hydrogen-bond isomer *E*- $\kappa O^*$ . Between the two different *E*-nitrito- $\kappa O$  isomers, a rotation barrier with a height of 4.1 kJ mol<sup>-1</sup> is found. For the *E*-nitrito- $\kappa O$  →  $\kappa^2 N, O$  isomerization 5.8 kJ mol<sup>-1</sup> are needed.

The Fe–O2–N scan (Figure 2.55 red curve) showed no minimum at the *Z*-nitrito- $\kappa O$  but did for the chelating isomer. The former appears as a shoulder 15.8 kJ mol<sup>-1</sup> above the most stable isomer of this calculation. The two other potential pots can be assigned to the  $\kappa N$  and the *E*- $\kappa O$  isomer which are 2.0 kJ mol<sup>-1</sup> and 6.9 kJ mol<sup>-1</sup> less stable than the chelating isomer, respectively. The side-on binding (3.1 kJ mol<sup>-1</sup>) appears as a shoul-

der between those to binding modes. Approximately  $2.0 \text{ kJ mol}^{-1}$  have to be supplied to overcome the energy barrier in the case of the  $E-\kappa O \rightarrow \kappa N$  isomerization, while it is  $23.8 \text{ kJ mol}^{-1}$  in the case of the  $\rightarrow \kappa^2 O, O' \rightarrow E-\kappa O$  isomerization.

As in the previous case, in the scan calculation of **11**, the nitrito ligand had to be spun in different directions. The graphs resulting from the Fe–O1–N and the Fe–O2–N scan are depicted in Figure 2.56. Both scan graphs show their absolute minimum at the isolated  $\kappa^2 O, O'$  isomer (the deviation of  $10^\circ$  is most probably a result of the  $10^\circ$  scan step). They share an almost congruent pathway up to the  $E-\kappa O$  isomer which is circa  $20.5 \text{ kJ mol}^{-1}$  less stable than the chelating isomer. The respective rotation barrier is  $34.8 \text{ kJ mol}^{-1}$  high. However, the pathway from the  $E-\kappa O$  ( $130^\circ$ ) towards the  $\kappa N$  ( $30^\circ$ ) isomer differs. While the Fe–O1–N scan exhibits a clear minimum for the  $\kappa N$  binding mode ( $16.1 \text{ kJ mol}^{-1}$ ) and does not show signs of a side-on binding mode, the Fe–O1–N scan gives the  $\kappa N$  binding mode as the maximum of a rotation barrier after a potential pot which is assigned to the  $\kappa^2 N, O$  isomer ( $18.9 \text{ kJ mol}^{-1}$ ). The energy needed for the  $E-\kappa O \rightarrow \kappa^2 N, O$  isomerization in the Fe–O2–N scan is  $7.1 \text{ kJ mol}^{-1}$  and  $11.1 \text{ kJ mol}^{-1}$  for the  $\kappa O \rightarrow \kappa N$  isomerization in the Fe–O1–N calculation.

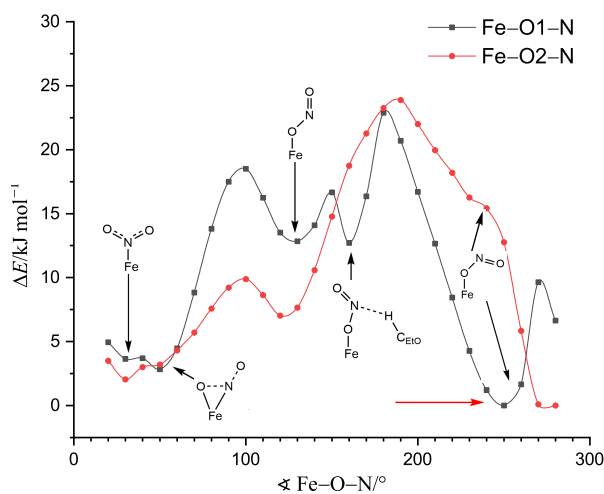


**Figure 2.55:** Comparison of the energy curves obtained from the BP86 calculation by changing the Fe–O1–N (black line) or the Fe–O2–N angle of one  $\text{FeNO}_2$  unit in the complex anion of **7**. The red arrow marks the position of the X-ray structure analysis results.

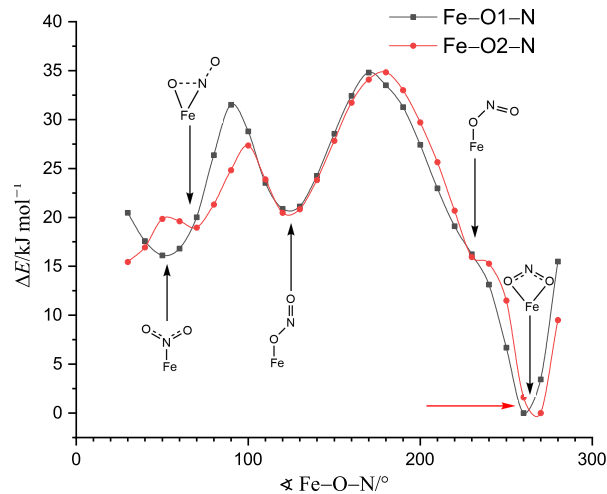


**Figure 2.56:** Comparison of the energy curves obtained from the BP86 calculation by changing the Fe–O1–N (black line) or the Fe–O2–N angle of the  $\text{FeNO}_2$  unit in **11**. The red arrow marks the position of the X-ray structure analysis results.

Since the additional *tert*-butyl group in **12** multiplied the calculation run time, in **12** only the Fe–O2–N scan was performed using BP86 as the functional. As a result, an energy curve was obtained which is nearly congruent with that of **11** (Figure 2.57).

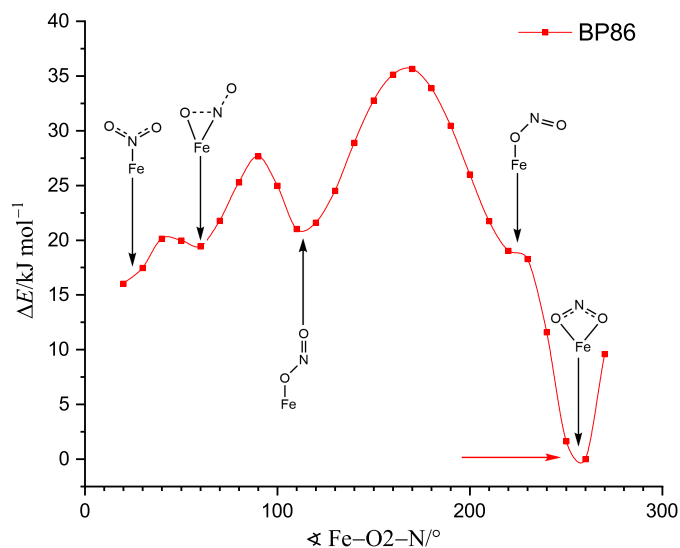


**Figure 2.57:** Energy curve obtained from the BP86 calculation by changing the Fe–O2–N angle of the FeNO<sub>2</sub> unit in **12**. The red arrow marks the position of the X-ray structure analysis results.

The scan graphs of **13** and **14** are almost congruent for both the TPSS and BP86 calculations (Figures 2.58 and 2.59). Just as in the scan of **1a-Fe**, it does not matter in which direction the nitrito ligand is rotated due to the mirror plane within the molecule. The only difference regarding the shape of energy curves is found in the shoulder of the  $Z$ - $\kappa O$  binding mode which is slightly more pronounced in the case of the TPSS scan of **13** otherwise the scan graphs show a more or less parallel development. Therefore in the following the results of **13** are described in more detail and the energies for **14** are listed in brackets after the respective values of **13**. In all cases, the absolute minima of the graphs belong to the isolated chelating isomer. Within the BP86 scan, the  $E$ - $\kappa O$  isomer is 30.2 kJ mol<sup>-1</sup> (29.6 kJ mol<sup>-1</sup>) less stable than the  $\kappa^2 O, O'$  isomer while it is 34.0 kJ mol<sup>-1</sup> (33.3 kJ mol<sup>-1</sup>) in the TPSS scan curve. Both compounds do not exhibit energetic minima for the  $\kappa N$  isomer but show two clearly defined valleys for both possible  $\kappa^2 N, O$  isomers which are 10.4 kJ mol<sup>-1</sup> (11.7 kJ mol<sup>-1</sup>) less stable than the chelating isomer. The cited side-on minima are separated by an energy barrier – which also represents the N-bound isomer – with an height of 14.6 kJ mol<sup>-1</sup> (13.8 kJ mol<sup>-1</sup>) in the case of BP86 and 18.2 kJ mol<sup>-1</sup> (17.7 kJ mol<sup>-1</sup>) in the case of TPSS. An energy of 40.7 kJ mol<sup>-1</sup> (40.3 kJ mol<sup>-1</sup>) is needed to overcome the  $\kappa^2 O, O' \rightarrow E$ - $\kappa O$  rotation barrier according to the BP86 scan curve and 43.6 kJ mol<sup>-1</sup> (42.7 kJ mol<sup>-1</sup>) according to the TPSS calculation. The sharp rotation barrier for the  $E$ - $\kappa O \rightarrow \kappa^2 N, O$  has a height of 11.9 kJ mol<sup>-1</sup> (BP86) and 11.5 kJ mol<sup>-1</sup> (TPSS) in both **13** and **14**, respectively.

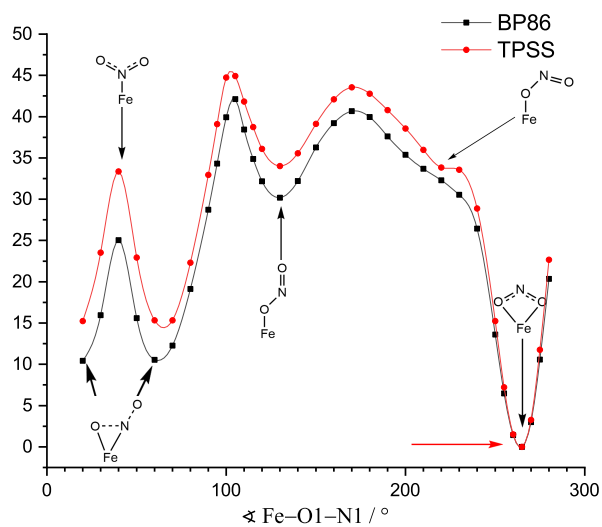


**Figure 2.58:** Comparison of the scan graphs calculated with the pure density functionals TPSS (red curve) and BP86 (black curve) for compound **13**. The red arrow marks the position of the X-ray structure analysis results.

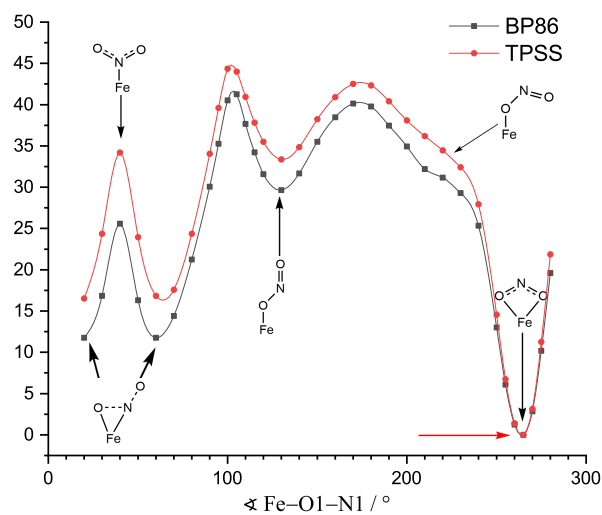


**Figure 2.59:** Comparison of the scan graphs calculated with the pure density functionals TPSS (red curve) and BP86 (black curve) for compound **14**. The red arrow marks the position of the X-ray structure analysis results.

## 2.7 Photoinduced linkage isomerism experiments

For photoinduced linkage isomerism experiments **1a-Fe**, **2** · MeCN, **6**, **7**, **8** and **15b** were chosen. The wavelengths for the irradiation experiments were selected by determining the solid state UV-Vis absorption of the samples in KBr pellets. As light sources LEDs with well-defined energies were utilized. The linkage isomerism was monitored by IR spectroscopy on the irradiated specimens in KBr. Various spectra were generated by subtraction of the GS spectrum of the substance at measurement temperature prior to irradiation from the IR spectra of the irradiated samples.

### 2.7.1 Photoirradiation on 1a-Fe

The only solid state UV-Vis absorption of **1a-Fe** appears at 325 nm. The first sample was cooled down to 10 K and irradiated for 5 min with light of wavelengths of 365 nm and 405 nm. Since both wavelengths provided almost similar results over three irradiation cycles and the sample already showed signs of decomposition, a second sample was prepared. Here, the substance was cooled down to 100 K and was irradiated with light of a wavelength of 365 nm for 170 min. The respective difference spectrum is found in Figure 2.60. The IR spectra of the irradiated sample show a major decrease of the vibrational bands at  $870\text{ cm}^{-1}$ ,  $935\text{ cm}^{-1}$ ,  $1104\text{ cm}^{-1}$  and in the range of  $1224\text{ cm}^{-1}$ – $1262\text{ cm}^{-1}$ . Simultaneous new IR bands appear at  $965\text{ cm}^{-1}$ ,  $1196\text{ cm}^{-1}$ ,  $1219\text{ cm}^{-1}$ ,  $1313\text{ cm}^{-1}$  and  $1343\text{ cm}^{-1}$ . Other increasing and decreasing IR bands originate, most probably, a rearrangement of the co-ligands. Furthermore, a single band at  $1808\text{ cm}^{-1}$  arises as the irradiation starts, indicating the formation of a nitrosyl ligand. After approximately 30 min, a second, smaller nitrosyl-related band at  $1742\text{ cm}^{-1}$  appears.

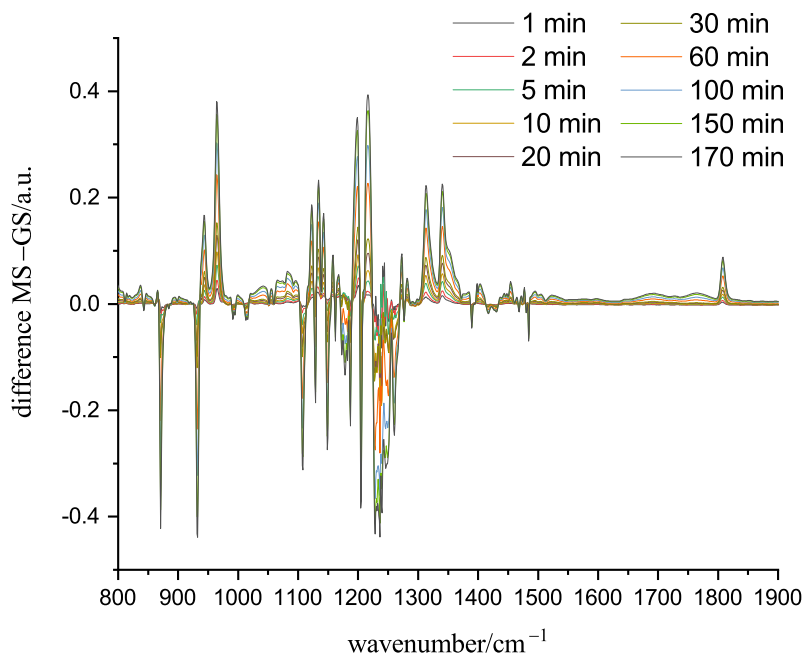


**Figure 2.60:** Difference IR spectra of the photoirradiation experiment of **1a-Fe** at 100 K with light of a wavelength of 365 nm over a time period of 170 min.

Increasing the temperature to room temperature leads to a slow decrease of the previously emerged vibrational bands which are fully gone by reaching a temperature of 230 K. Only the two bands at  $961\text{ cm}^{-1}$  and  $1742\text{ cm}^{-1}$  remain after reaching room temperature indicating a partial decomposition of the sample.

### 2.7.2 Photoirradiation on **2** · MeCN

The solid state UV-Vis spectrum of compound **2** · MeCN in KBr reveals absorption bands at 350 nm and 450 nm. Figure 2.61 shows the difference spectra of a sample which was cooled down to 10 K and irradiated with light of various wavelengths. The maximal effect is obtained with blue light of 470 nm. Further irradiation with light of 780 nm and 590 nm results in the formation of an IR band at  $1726\text{ cm}^{-1}$  indicating the decomposition of the nitrito complex. The difference spectrum shows mainly the decrease of three vibrational bands at  $816\text{ cm}^{-1}$ ,  $990\text{ cm}^{-1}$  and  $1474\text{ cm}^{-1}$  while two bands at  $1323\text{ cm}^{-1}$  and  $1378\text{ cm}^{-1}$  increase. Three almost undetectable IR bands at  $874\text{ cm}^{-1}$ ,  $940\text{ cm}^{-1}$  and  $1237\text{ cm}^{-1}$  vanish during the experiment and do not return. A closer look at the IR spectrum of the irradiated sample reveals that the irradiation with light of the wavelengths of 405 nm and 590 nm triggers a partial depopulation of the MS back to the GS. A visualization of the most important areas in the IR spectrum is depicted in Figure 2.62.

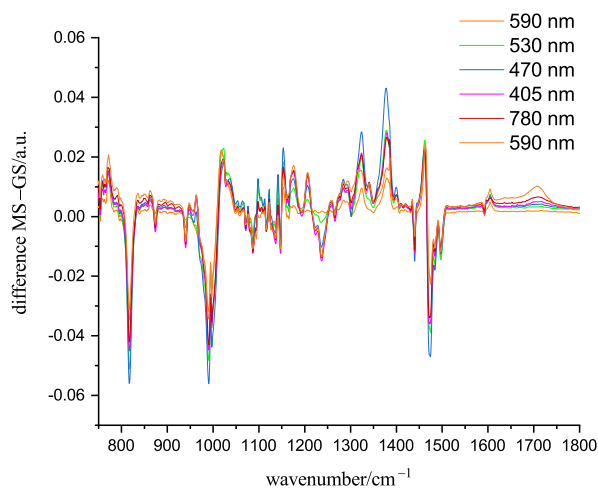


**Figure 2.61:** Difference IR spectra of the photoirradiation experiment of  $\mathbf{2} \cdot \text{MeCN}$  at 10 K with light of various wavelengths and irradiation times of each 5 min.

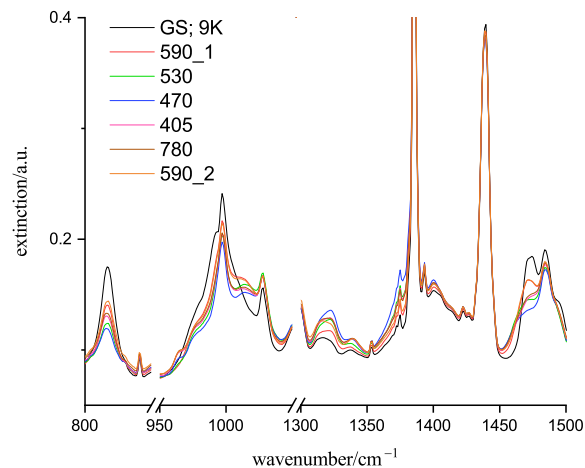


**Figure 2.62:** Depopulation of the MS state of  $\mathbf{2} \cdot \text{MeCN}$  at 10 K by irradiation with light of various wavelengths.

Increasing the temperature leads to a relaxation back to the GS between 50 K and 100 K. However, thawing the sample is accompanied by the formation of an IR band at  $1706 \text{ cm}^{-1}$  which shifts to  $1726 \text{ cm}^{-1}$  until a temperature of 230 K is reached. This behavior is depicted in Figure 2.63.

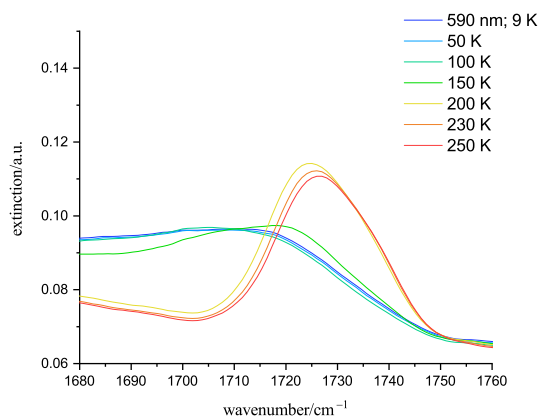


**Figure 2.63:** Evolution and shift of the nitrosyl-related vibrational band by increasing the temperature of the irradiated sample of  $\mathbf{2} \cdot \text{MeCN}$ .

### 2.7.3 Photoirradiation on **7**

**7** in KBr shows solid-state UV-Vis absorptions at 590 nm and 470 nm. For the experiment, a sample of **7** was cooled down to 10 K and irradiated with light of the wavelengths of 625 nm, 590 nm, 530 nm and 470 nm. In the case of the first two wavelengths, no detectable change in the IR spectrum is observed. However, with the 530 nm laser, major changes in the IR spectrum are detectable which reach almost a conversion rate of 100% when a 470 nm laser was utilized. The corresponding difference spectra and a comparison of the GS spectrum at 10 K with those of the irradiated samples are depicted in Figure 2.64 and 2.65, respectively. The difference spectrum shows a clear decrease of the vibrational bands at  $830\text{ cm}^{-1}$ ,  $1154\text{ cm}^{-1}$  and around  $1380\text{ cm}^{-1}$  which were previously assigned to the *Z*-nitrito- $\kappa O$  ligand. Simultaneously, an increase of bands at  $813\text{ cm}^{-1}$ , from  $1054\text{ cm}^{-1}$ – $1077\text{ cm}^{-1}$  and from  $1442\text{ cm}^{-1}$ – $1464\text{ cm}^{-1}$  is observed. Irradiation on the MS at 10 K with light of wavelengths of 405 nm and 530 nm results in a partial, destruction-free depopulation of the MS back to the GS.

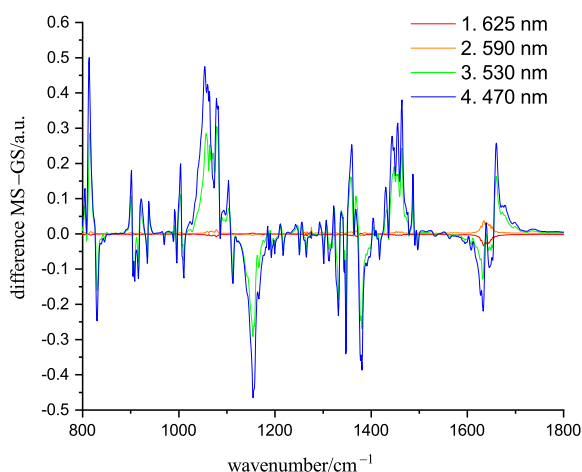


**Figure 2.64:** Difference IR spectra of the photoirradiation experiment of **7** at 10 K with light of various wavelengths and irradiation times of each 5 min.

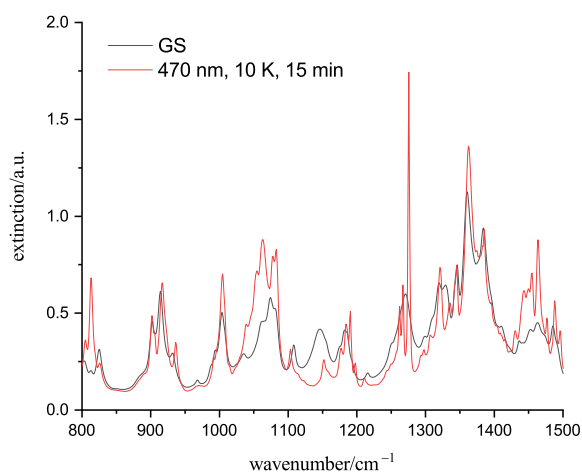


**Figure 2.65:** Comparison of the IR spectra of **7** at 10 K before (GS, black line) and after irradiation with light of the wavelength of 470 nm over a time period of 15 min (MS, red line).

Increasing the irradiated sample's temperature results in a full relaxation back to the GS between 60 K and 70 K. This behavior is depicted in Figure 2.66.

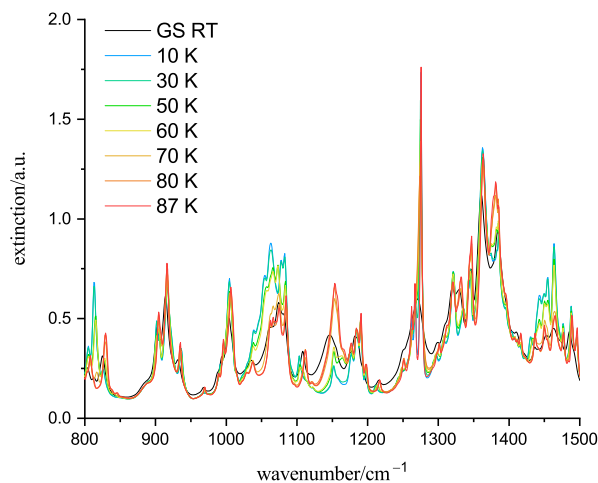


**Figure 2.66:** IR spectra compound **7** while increasing the temperature after irradiation at 10 K with light of a wavelength of 470 nm for 15 min.

#### 2.7.4 Photoirradiation on **15b**

The solid state UV-Vis spectrum of **15b** in KBr shows absorption bands at 290 nm, 320 nm, 375 nm and 520 nm. For the experiment the sample was cooled down to 10 K and irradiated successively with light of the wavelengths of 505 nm, 470 nm, 405 nm and again 505 nm for each 5 min. Here, a decrease of IR bands at  $818\text{ cm}^{-1}$ ,  $1031\text{ cm}^{-1}$ – $1080\text{ cm}^{-1}$ ,  $1273\text{ cm}^{-1}$  and  $1434\text{ cm}^{-1}$ – $1465\text{ cm}^{-1}$  is observed. Simultaneously, an increase of an IR band at  $1325\text{ cm}^{-1}$  and a double band from  $1340$ – $1355\text{ cm}^{-1}$  occurs. However, the irradiation with a wavelength of 405 nm is accompanied by the rise of vibrational bands at  $1660\text{ cm}^{-1}$  and  $1731\text{ cm}^{-1}$  which is a sign for the photolytic decomposition of the sample. Irradiation on the MS at 10 K with light of a wavelength of 590 nm leads to a depopulation of that state by reversing the previously described changes. The IR bands which arose from the decomposition with 405 nm light remain unaltered. The difference spectra relative to the substance's ground state at 10 K is depicted in Figure 2.67.

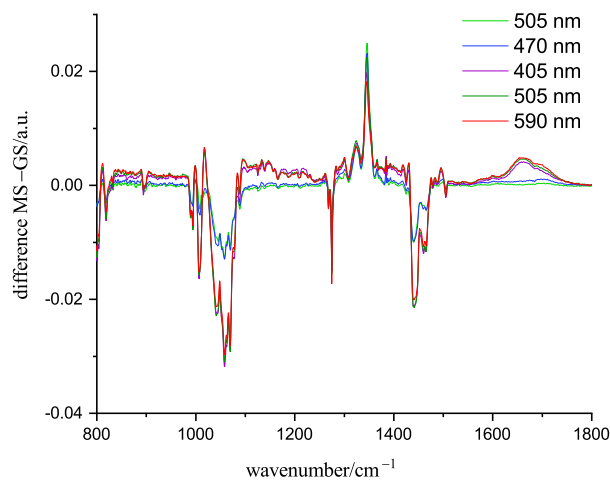


**Figure 2.67:** Difference IR spectra of the photoirradiation experiment of **15b** at 10 K with light of various wavelengths and irradiation times of each 5 min.

Following those results, a second sample was irradiated at 10 K only with light of 526 nm and 590 nm which resulted in the described changes above without signs of decomposition. The IR vibration at  $1660\text{ cm}^{-1}$  was already present before the measurement which indicates a slightly decomposed sample but the intensity of this band had not been increased after the measurement showing that no further decomposition occurred. A subsequent irradiation with a wavelength of 590 nm resulted in a slow but almost complete depopulation of the MS (Figure 2.68). Increasing the temperature over 50 K after irradiation with 526 nm results in a relaxation back to the ground state that is completed above circa 90 K. The temperature dependent relaxation is depicted in Figure 2.69.

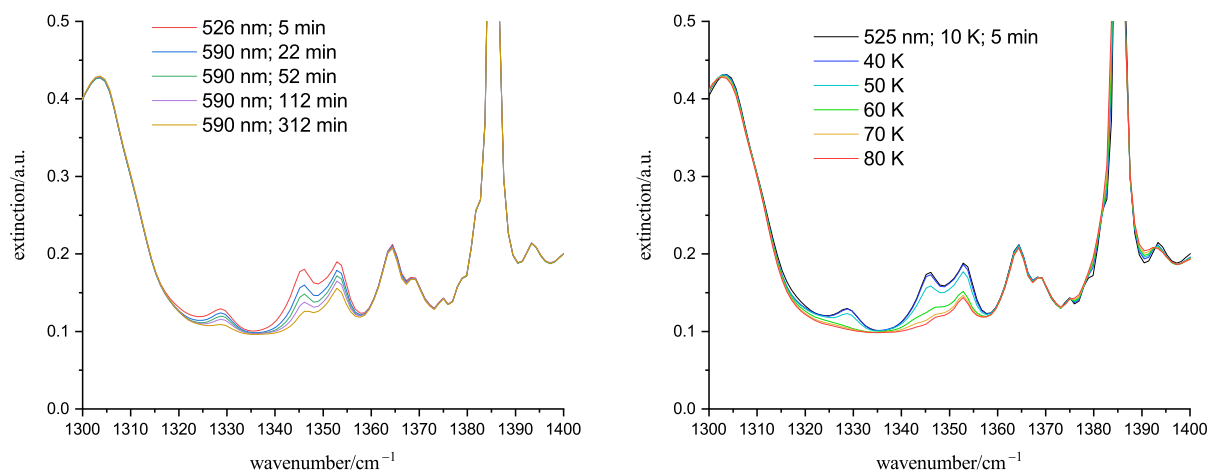


**Figure 2.68:** Depopulation of the MS state of **15b** at 10 K by irradiation with light of a wavelength of 590 nm over a time period of 312 min.

**Figure 2.69:** IR spectra compound **15b** while increasing the temperature after irradiation at 10 K with light of a wavelength of 525 nm for 5 min.

### 2.7.5 Photoirradiation on **6** and **8**

The solid state UV-Vis spectrum of **6** in KBr showed absorption bands at 300 nm, 350 nm and 500 nm. **8** exhibits absorptions at 300 nm, 340 nm, 400 nm and 470 nm. Both substances show irreversible changes during the experiment. Irradiation with light of wavelengths of 405 nm and 470 nm lead to a rise of a vibrational band at  $2343\text{ cm}^{-1}$ . Simultaneously, a decrease of the IR vibrations of the carboxylate functions around  $1650\text{ cm}^{-1}$  appears.<sup>[88]</sup> In addition, **6** features a new IR vibration at  $2230\text{ cm}^{-1}$ . Increasing the temperature leads to the rise of a shoulder at  $1724\text{ cm}^{-1}$  and a decrease of the bands around  $830\text{ cm}^{-1}$  ( $\delta_{\text{NO}_2^-}$ ) and  $2343\text{ cm}^{-1}$ . The rising bands relating the decomposition products for compounds **6** and **8** are depicted in Figures 2.70 and 2.71. The final IR spectrum of both substances after reaching room temperature has drastically changed compared to the starting spectra, indicating a complete destruction of the sample during the experiment.

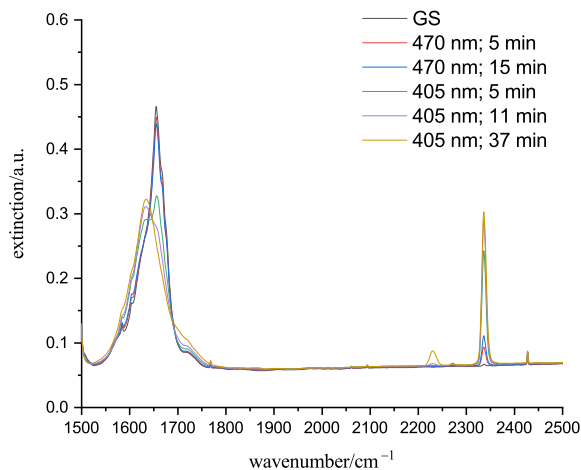


**Figure 2.70:** Rising  $\text{N}_2\text{O}$  and  $\text{CO}_2$ -related IR band in the photoirradiation experiment of **6**.<sup>[85,86,88]</sup>

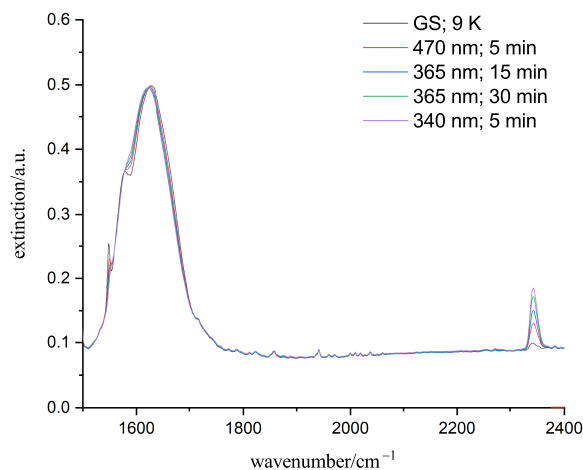


**Figure 2.71:** Rising  $\text{CO}_2$ -related IR band in the photoirradiation experiment of **8**.<sup>[88]</sup>

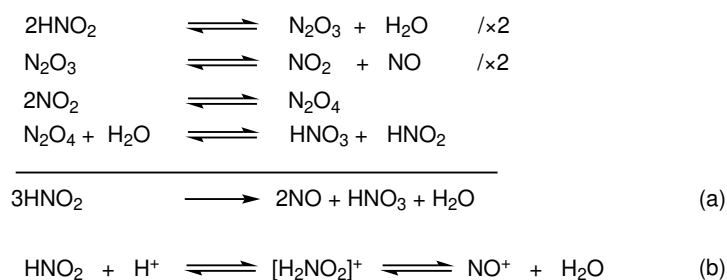
### 3 Discussion

#### 3.1 Tactics for the successful synthesis of novel nitritoiron complexes

##### 3.1.1 Selection of solvents, ligands and oxidation state of the central metal

As mentioned in Section 1.2, the number of known non-heme nitritoiron complexes is rather low. This is remarkable, especially since iron is one of the best-investigated central metals in coordination chemistry, and nitrite, as one of the main actors in nature's nitrogen cycle, can be seen as an essential substance for life on earth. Due to this, the first step is to develop a reliable and reproducible scheme for the synthesis of novel nitritoiron complexes by defining suitable reaction conditions.

A reason for the low number of the desired complexes is most likely the fact that no iron nitrites such as  $\text{Fe}(\text{NO}_2)_2$  or  $\text{Fe}(\text{NO}_2)_3$  are known. Attempts to synthesize these compounds starting from the corresponding chlorides in aqueous solution yield only undefined mixtures of iron oxides, nitrate and in the evolution of nitrous gases.<sup>[89,90]</sup> Due to this, pure iron nitrites cannot be used as starting materials for the syntheses. Furthermore, the chemistry of nitrite and its corresponding acid – nitrous acid ( $\text{pK}_a = 3.29$ ) – is dominated mainly by a complex redox chemistry.<sup>[17]</sup> Already in slightly acidic environment, nitrite is able to disproportionate in nitric oxide and nitrate. The corresponding reaction equation is depicted in Scheme 3 (a).<sup>[17,91,92]</sup> This decomposition occurs already at room temperature and is the reason why pure nitrous acid is not storable under standard conditions. In the presence of strong acids (Scheme 3 (b)),  $\text{NO}^+$  is generated by double protonation of the nitrite and successive elimination of water.<sup>[17]</sup> To minimize the risk of a proton-triggered decomposition of the nitrito ligands, aprotic solvents as acetonitrile, dichloromethane, pyridine and acetone were utilized for the syntheses. In the case of **1a-Fe** and **1b**, methanol was used for the synthesis but nitrite was added to the reaction solutions only after the addition of triethylamine to adjust the pH value. However, even in aprotic solvents, the combination of nitrites and Lewis-acidic salts  $\text{MCl}_3$  ( $\text{M} = \text{Fe}, \text{Al}, \text{In}$ ) is able to release  $\text{NO}^+$ . These mixtures are known as nitrosating-agents and find an application in organic syntheses.<sup>[18,93–95]</sup>



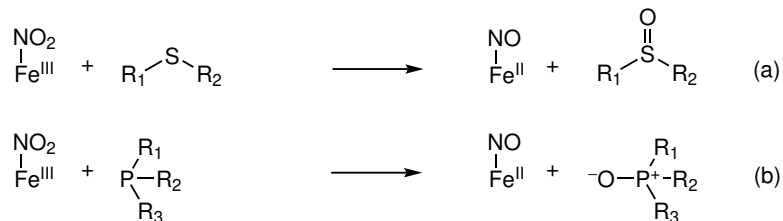
**Scheme 3:** Decomposition of nitrite in slightly (a) and strongly (b) acidic environment.<sup>[17]</sup>

In addition, iron(II) and its complexes tend to react directly with nitrite and lead to the formation of nitric oxide or nitrosyl complexes. Only few examples of non-heme nitritoiron complexes with iron(II) as the central metal were isolated and structurally characterized in the literature and many of them are unstable at elevated temperatures. Scheme 4 depicts the literature-known decomposition of nitrite in aqueous solution in the presence of iron(II).<sup>[96,97]</sup> Many preliminary experiments showed that water is optional in this reaction equation and even in aprotic solvents the formation of nitric oxide, nitrate and nitrosyliron complexes is documented if iron(II) is involved.<sup>[98]</sup> Therefore, only iron(III) was used as the central metal for the syntheses to minimize the chance of unwanted side reactions and to obtain stable compounds for further applications.



**Scheme 4:** Decomposition of nitrite in presence of iron(II).

The probably most important factor for a traceable synthesis of novel nitritoiron complexes is the choice of suitable ligands. Several common ligand classes proved to be unusable due to the possibility of side reactions with nitrite. It is notable that nitric oxide, which is required for some of the depicted reactions, can be generated by the above described mechanisms. As already described in Section 1.1 in Scheme 1, primary and secondary amines as well as substances with amide bridges are not considered as suitable co-ligands due to the possibility of forming *N*-nitrosamines, *N*-nitrosamides and carbenium ions. Thiols, thioethers and phosphanes react with nitrite and its complexes by taking one of the ligand's oxygen atoms (oxygen-atom transfer) by forming sulfoxides and phosphane oxides, respectively. Although this reaction is unwelcome if nitrito complexes are to be synthesized, it is commonly used to synthesize novel nitrosyl complexes by reductive nitrosylation (Scheme 5).<sup>[19,73,91,92,99–101]</sup>



**Scheme 5:** Reaction of thiols, thioethers and phosphanes with nitrite.<sup>[19,73,91,92,99–101]</sup>

It is notable that nitritoiron complexes with thiolato ligands and phosphanes are known but rather rare.<sup>[73,102,103]</sup> In most cases their formation is associated with the previously named side reactions resulting in a decreased yield or the presence of nitrosyl ligands.<sup>[73,100]</sup> Even if some of the described reactions are unlikely in aprotic environment, the named



solvents which has a highly positive effect on the reaction time and yield. Nitrite salts with organic cations like  $\text{PPN}^+$  and  $\text{NBnMe}_3^+$ , which are often used in the literature, have the drawback that, in most cases, all reaction products are soluble in the utilized solvents resulting either in an incomplete exchange of the ligands or provoke difficult purification procedures.<sup>[39]</sup>

## 3.2 Synthesis of the precursor compounds

### 3.2.1 Halogenidoiron(III) complexes known to literature

**P10-P12** and **P15** were prepared exactly as in literature procedures.<sup>[68,69,72]</sup> **P4** is known in literature but was obtained by an alternative synthesis route similar to the other phosphaneoxide compounds.<sup>[65,66]</sup> However, the syntheses of **P2**, **P3**, **P8** and **P16** needed some adjustments since the corresponding counter ions of the literature syntheses were entailed with some problems. In the case of the cationic complexes **P2**, **P3** and **P16**, the original counter ions are  $[\text{FeCl}_4]^-$ .<sup>[65,67,112]</sup> The presence of this complex anion is not preferred since the following reaction with silver nitrite would lead to an exchange of the "wrong" chlorido ligands. Therefore, the substances were prepared by adding sodium perchlorate to a solution of ferric chloride and the ligands in acetonitrile. This method was successfully applied in the syntheses of compounds **P2-P4** and **P16**. The presence of perchlorate was either demonstrated by IR spectroscopy or by single-crystal X-ray crystallography. While attempts to gain crystals of the highly soluble compounds **P2** and **P3** did not succeed and the structure of **P4** is already known in literature, **P16** was successfully crystallized and characterized by single-crystal X-ray analysis.<sup>[65,66]</sup> A literature-known synthesis of **P16** includes the use of explosive  $\text{tpya} \cdot 3\text{HClO}_4$ . Furthermore, the described substance contains  $[\text{Fe}_2\text{Cl}_2(\text{tpya})_2(\mu\text{-O})]^{2-}$  which represents a decomposition product from the reaction with atmospheric oxygen or water.<sup>[113]</sup> The herein described synthesis yielded the pure compound in nearly quantitative yield *via* a safer synthesis route. Furthermore, it was possible to determine the crystal structure without the corresponding decomposition product and with better quality factors than in the other published structures with  $[\text{FeCl}_4]^-$  and chloride as the counter ions.<sup>[112,114]</sup>

Initially the complex anion in **P8** was synthesized and crystallized according to the literature-known procedure.<sup>[67]</sup> However, the following metathesis reaction with  $\text{AgNO}_2$  led only to a heavily disordered nitritoiron complex. Therefore the synthesis of **P8** was reproduced with  $\text{NBnMe}_3^+$  instead of  $\text{NEt}_4^+$ . An additional single-crystal X-ray analysis revealed a successful synthesis with the desired cation but a heavily disordered  $[\text{FeCl}_2(\text{nta})]^{2-}$  in the precursor compound. Therefore, this structure is not depicted in this thesis.

The crystal structure of the complex molecule in **P13** is already described with 1 equiv of methanol of crystallization by In-Iam.<sup>[71]</sup> However, re-crystallization of **P13** from acetonitrile/diethyl ether yielded the solvent-free compound which allowed the further use

of the substance without carryover of a protic solvent. With regards to the determined bond distances and angles within the molecule, no major differences are found compared to In-Iam's structure.<sup>[71]</sup>

### 3.2.2 Novel halogenidoiron(III) complexes

Since complexes with the chosen ligands are not always known to literature, several new halogenidoiron(III) complexes were synthesized for this thesis in order to use them as precursors for the following ligand-exchange reactions. As a result, the five novel chloridoiron complexes **P1**, **P5**, **P6**, **P7** · 2MeCN and **P9** · 2MeCN and one bromido complex (**P14**) have been successfully synthesized.

Since perfluoropinacol is known to form complexes with coordination numbers smaller than six, **P1** is thought to act as precursor for a mononitritoiron complex.<sup>[83,97,115]</sup> As well as most literature-known fivefold coordinated perfluoropinacolatoiron compounds, the coordination polyhedron can be described as square pyramidal.<sup>[97,116,117]</sup>

For the synthesis of the chloridoiron(III) complexes with aminocarboxylates, qu and nta were already considered suitable ligands since they match to the previously defined restrictions. However, the N-substituted derivatives of other commonly used aminocarboxylato ligands like edda and ida had to be synthesized first. Since the molecular structure of the complex molecule in **P8** is already described in the literature and the anion is heavily disordered, the result of the single-crystal X-ray diffraction is not depicted in this thesis.<sup>[67]</sup> Subsequently, three novel chloridoiron(III) complexes with aminocarboxylate as co-ligand were obtained.

**P9** · 2MeCN was obtained accidentally by trying to obtain [Fe(bpmea)Cl<sub>2</sub>] which is already known in the literature.<sup>[118]</sup> The synthesis led to an oxido bridged binuclear chlorido iron(III) complex which met the requirements as well. The  $\mu$ -oxido ligand is most probably a result of remaining water after the *in-situ* synthesis of Na(bpmea). Similar complexes to **P9** are known in literature but the used ligands are only the ether derivatives of bpmea. All these compounds are built exactly like **P9** and exhibit comparable distances and angles within the molecule.<sup>[118-122]</sup>

A comparison of the molecular structures of **P13** and **P14** show many similarities and the presence of three halogenido ligands would theoretically allow the synthesis of trinitritoiron complexes.

Beside their ability to act as precursor compounds for novel nitritoiron complexes, the synthesized chlorido complexes herein can be regarded as, presumably, useful for other applications. In synthetic organic chemistry chloridoiron complexes are already utilized as catalysts for alkylation of aromatic grignard reagents and the formation of disulfides from thiols and dithiols. Furthermore they can be used as tools to oxidize H<sub>2</sub>S to elemental sulfur under mild conditions and for the controlled polymerization of conjugated dienes. Further advantages of the chloridoiron complexes as catalysts are their low toxicity, envi-

ronmental sustainability, cheap and easy synthesis as well as their high stability against oxygen and moisture.<sup>[67,70,123]</sup>

### 3.3 Synthesis and characterization of novel nitrito complexes

#### 3.3.1 Nitrito complexes with perfluoropinacol as co-ligand

With perfluoropinacolate as co-ligand, nine novel nitrito complexes were synthesized. While all mononuclear complexes were obtained by the same synthesis method, the binuclear complex **1b** was synthesized in a different way. Here, the synthesis starts from the literature-known iron(II) precursor compound  $(\text{PPN})_2[\text{Fe}(\text{NO}_2)_4]$ . During the reaction time, the remaining silver chloride acts as oxidizing agent and turns dark gray as a result of being reduced to elemental silver. Due to this, the iron(II) was oxidized to iron(III). The eight mononuclear complexes with the general formula  $(\text{HNEt}_3)_2[\text{M}^{\text{III}}(\text{fpin})_2(\text{NO}_2)]$  **1a-M** ( $\text{M} = \text{Al}, \text{Sc}, \text{Cr}, \text{Fe}, \text{Ga}, \text{In}, \text{Tl}, \text{Bi}$ ) were isolated. Beside the relatively rare examples of a nitritochromium(III) and two nitritoiron(III) complexes, it was possible to isolate the first described nitrito complex with scandium(III) as the central metal. **1a-Ga** marks the first structurally characterized nitritogallium(III) complex. In the case of **1a-Bi** the obtained substance is, at least, the first nitritobismuth(III) complex.<sup>[37]</sup> While **1a-In** and **1a-Tl** are the second structurally described examples for nitrito complexes with these elements, **1a-Al** is the third structurally resolved example.<sup>[76–78,124]</sup> It is notable, that it was possible to synthesize a homologous row of nitrito complexes with every stable group 13 metal.

With regard to the scan calculations, the **1a-M** ( $\text{M} = \text{Al}, \text{Sc}, \text{Cr}, \text{Fe}, \text{Ga}, \text{In}, \text{Tl}$ ) series can be seen as a simple model system for the following scan calculations since only one switchable ligand is present. It also allows the investigation of the different central metals' influence on the scan curve. Compared to the mononuclear iron complex **1a-Fe** the coordination of the nitrito ligands in **1b** is slightly more asymmetric. However a definite distinction between the chelating and *Z*-nitrito- $\kappa\text{O}$  binding mode is not trivial. It is shown that the scan calculations performed can be used as tool to distinguish between these two nitrite binding modes. The scan calculations with the complexes of the **1a-M** series are discussed in Section 3.7.

Unfortunately, except for **1a-Cr** and **1a-Fe** all compounds from this series are colorless which does not allow the excitation with laser light in PLI experiments. At least the first two substances named exhibit a visible color and can be considered suitable for further irradiation experiments. The results of the PLI measurement of **1a-Fe** are discussed in Section 3.8.2.

### 3.3.2 Nitritoiron complexes with bisphosphane oxides as co-ligand

The bisphosphane oxide complexes were all synthesized *via* their respective precursor compounds. Due to their good stability, at least **2** · MeCN and **3** · 2MeCN are regarded as very suitable for PLI experiments. In contrast to perfluoropinacolate, the coordinating bisphosphane oxides allow the presence of more than one additional ligand in the complexes. **2** · MeCN, **3** · 2MeCN and **4** · 3MeCN each exhibit two *E*-nitrito- $\kappa O$  ligands which are located in the axial positions while the bidentate co-ligands occupy the equatorial coordination sites. This is in contrast to the literature-known structure of the  $[\text{FeCl}_2(\text{dppe}(\text{O})_2)_2]^+$  cation where the chlorido ligands are in *cis* position to each other. Since it was not possible to crystallize the corresponding precursor **P2**, it is unclear if the complex cation rearranges during the metathesis reaction or if the chlorido complex is already in this conformation.<sup>[65]</sup> In **P4**, the chlorido ligands are already in *trans* position just like the nitrito ligands in **4** · 3MeCN. It is notable that **3** · 2MeCN exhibits a remarkably big 7-membered chelate ring which is found only in rare cases.<sup>[125]</sup> However, no explanation is found as to why the nitrito ligands in **2** · MeCN and **4** · 3MeCN face different directions while the ligands in **3** · 2MeCN face in the same direction.

With regard to possible photocrystallographic PLI measurements, Hatcher *et al.* determined that the cell volume of a unit cell must not change more than 2% with the linkage isomerism to prevent irreversible damages of the crystalline substance.<sup>[47]</sup> So-called "reaction cavities" have a positive influence on the crystalline substance's stability as well as the conversion rates during the switching process since they allow the PLI active ligand to rotate more freely without having an impact on the whole crystal lattice.<sup>[47,56]</sup> In the case of the synthesized complexes, the bulky phenyl moieties of the bisphosphane oxides create such pockets for the two nitrito ligands. Furthermore, they do not interact strongly with the nitrito ligands which facilitates the switching process. The spatial distance between the two nitrito ligands prevents them from interfering with each other sterically.

Due to the good stability and the promising structural properties, **2** · MeCN and **3** · 2MeCN can be considered candidates for PLI experiments. The results of the measurements will be discussed in Section 3.8.3 in further detail.

### 3.3.3 Nitritoiron complexes with aminocarboxylato co-ligands

With the aminocarboxylato precursor complexes **P5-P8** it was possible to synthesize four novel nitritoiron complexes. Unfortunately, the, probably, best known aminocarboxylates, the amino acids, were unsuitable due to their primary and secondary amine moieties. Preliminary experiments with N-protected amino acids did not yield the isolation of nitrito complexes. The lower stability of **5** · 2MeCN can, most probably, be assigned to the co-crystallized acetonitrile molecules which are absent in the complexes **6-8**. Furthermore, **5** can be obtained only with  $\text{NBnMe}_3^+$  as counter ion. It is notable that the crystals of **5** · 2MeCN were obtained only as mixture of the nitrito complex with the chlorido

complex in a ratio of 22:3. Attempts to crystallize the pure compound did not succeed. Nonetheless, the structure is included in this thesis for the purpose of comparison with the other aminocarboxylato compounds.

The four complexes obtained include all three possible non-bridging O-bound isomers of nitrito ligands. **6** exhibits the same ligand environment as **5** and both complexes exhibit *E*-nitrito- $\kappa O$  ligands. The binuclear complex **7** exhibits one *Z*-nitrito- $\kappa O$  ligand on each central metal. The nta complex **8** shows a clearly chelating nitrito ligand and one in its *Z*- $\kappa O$  binding mode. The variety of different binding modes is most probably a result of the various sterical demands of the co-ligands.

**6-8** are of great interest in terms of possible linkage isomerism. The PLI experiments on the substances mentioned are discussed in Section 3.8. Due to its instability and impurity, a further use of **5** · 2MeCN in PLI experiments is inconvenient. Furthermore, it is notable that the isolated substances mark the first examples of nitritoiron complexes with aminocarboxylato co-ligands.

### 3.3.4 $[\text{Fe}_4(\mu\text{-bpmea})_2(\text{Z-NO}_2\text{-}\kappa\text{O})_2(\text{E-NO}_2\text{-}\kappa\text{O})_4(\mu_3\text{-O})_2] \cdot 2\text{MeCN}$ (**9** · 2MeCN)

**9** · 2MeCN represents the first known structurally characterized, tetranuclear nitritoiron complex. In addition, with four *E*-nitrito- $\kappa O$  and two *Z*-nitrito- $\kappa O$ , the substance exhibits two different binding modes of nitrite. While the oxido bridges from the synthesis with **P9** · 2MeCN have, most probably, their origin in the used precursor, in the case of the alternative synthesis they are a product of the decomposition of nitrite. This behavior is discussed in more detail in Section 3.4. Using less silver nitrite for the synthesis did only yield the quantitative precipitation of brown, amorphous powder regardless of the crystallization technique. Due to the very small yield and low stability against oxygen and higher temperatures, the substance cannot be used in further PLI experiments.

### 3.3.5 Nitritoiron complexes with salen and its derivatives

In the late 1980s, Settin tried to synthesize a nitritoiron complex with salen as co-ligand by letting  $[\{\text{Fe}(\text{salen})\}_2(\mu\text{-O})]$  react with  $\text{N}_2\text{O}_3$  in dichloromethane. But further analysis showed that the resulting black solid was a mixture of the nitrate, nitrito and  $\mu$ -oxido species. Later, Ankers *et al.* tried to synthesize "[Fe(NO<sub>2</sub>)(salen)]" from the reaction of [FeCl(salen)] (**P10**) with various nitrite salts in various solvents. Their research showed an almost quantitative evolution of nitric oxide with formation of  $[\{\text{Fe}(\text{salen})\}_2(\mu\text{-O})]$  and nitrate. The desired nitrito complex had never been observed by the authors.<sup>[126]</sup> Reasons for the unsuccessful synthesis in previous publications could be the relatively long crystallization time.

While **10** · 2MeCN was obtained containing only the dimer of [Fe(NO<sub>2</sub>- $\kappa O$ )(salen)], it was possible to synthesize mononuclear nitritoiron complexes by choice, if the substituted salen ligands H<sub>2</sub>*t*Bu<sub>2</sub>salen and H<sub>2</sub>*t*Bu<sub>4</sub>salen were used. Already, the steric demand of

two *tert*-butyl groups in *ortho* position to the coordinating alkoxide moieties is enough to result in a torsion of the ligand and hinders the molecule of forming dimers. Two additional *tert*-butyl moieties in *para* position to the coordinating alkoxide groups have no further influence on the nitrito complexes structure. Instead of filling the coordination site opposite to the nitrito ligand by the formation of a dimeric complex, the distortion triggered by the bulky *tert*-butyl moieties creates more space for the nitrito ligand which is then able to coordinate in its chelating binding mode. It is notable, that the synthesized complexes act exactly like literature-known nitrate complex which can either be found in its dimeric form with a nitrate- $\kappa O$  ligand or as monomer containing a chelating nitrate- $\kappa^2 O, O'$  ligand.<sup>[127,128]</sup>

A closer look at the UV-Vis spectra of the dissolved substances in acetonitrile shows a clear red shift of the absorption band around 500 nm with progressing substitution of *tert*-butyl groups. As already mentioned in Section 1.3, either  $d \rightarrow d$  transitions or an MLCT charge transfer between metal and switching ligand are a requirement for good photoinduced linkage isomerism.<sup>[47,54]</sup> However, the MLCTs referred to in the literature are assigned mostly to a  $M(d) \rightarrow \pi^*(L)$  transition of nitrosyl complexes. Since O-coordinating nitrite is a pure  $\sigma$ -donor ligand with no  $\pi$ -acidity, an MLCT from the central metal to the nitrite cannot alter the bonding situation as it is the case in nitrosyl complexes. That the iron(III)-nitrite interaction is mainly of ionic nature is also nicely shown in the spin-density plot of **1a-Fe** (Figure 2.44).

According to literature, the transition observed in compounds **10-12** arose from a salen-to-iron charge transfer (LMCT) and not from the ligand's inner  $\pi$ -system.<sup>[129]</sup> This implies that the transition has a direct influence on the central metal's oxidation state at least for the duration of the excitation.<sup>[130]</sup> However, no studies were found in the literature which discuss the influence of a "co-ligand"-to-metal charge transfer on a switchable ligand. It is feasible that the altered charge of the central metal influences the ionic bond between iron and nitrite. Since the LMCT absorption band's position changes with varying substitution of the salen ligand, the Fe-nitrite-salen complexes could represent a wavelength-tuneable system. Further advantages are the high stability of the solid substances and the good yield. Nonetheless, a slight drawback of the synthesized examples are their extreme dark color which prevents the irradiated light from a deep penetration into the substance. This, and the promising results of the scan calculations on compounds **11** and **12** (Section 3.7.4) make the substances interesting candidates but the corresponding PLI experiments are pending as of date.

### 3.3.6 Nitritoiron complexes with bipzpy

A closer look at the nitritoiron(III) complexes synthesized with purely N-donating auxiliary ligands reveals a different reaction behavior compared to the complexes containing O- and N,O-donating co-ligands. Except for the bipzpy-containing compounds **13** · MeCN and **14** · MeCN, all other complexes with pure nitrogen-donor ligands exhibit oxido bridges. This topic will be discussed in more detail in Section 3.4.

Attempts to remove the remaining two halogenido ligands in **13** and **14** did not succeed. When more than two equiv of silver nitrite are added to the reaction solutions or the temperature exceeds  $-20^{\circ}\text{C}$ , only formation of the nitrate compound  $[\text{Fe}(\text{bipzpy})\text{X}_2(\text{NO}_3-\kappa^2\text{O},\text{O}')] (X = \text{Cl}, \text{Br})$  is observed. A comparison with the molecular structures of **P13** and **P14** reveals that in both cases the strongest bound halogenido ligand is exchanged with nitrite. However, the very small yields of the syntheses limit the use in further PLI experiments until a better synthesis route is found. The isostructural, seven-fold coordinated, pentagonal bipyramidal complexes possess a relatively small number of atoms per molecule and only one switchable nitrito ligand. Therefore, both compounds show almost ideal conditions for quantum-chemical scan calculations. In addition, the effect of different halogenido ligands on the scan graph can be examined.

## 3.4 Nitritoiron complexes containing oxido bridges

While the reactions with bipzpy as co-ligand already had to be performed at low temperatures to avoid unintended side reactions, it is unavoidable to obtain complexes without oxido bridges when  $\text{Me}_3\text{tacn}$ ,  $\text{bpmea}$ ,  $\text{tpya}$  and pyridine are used as ligands. It is notable, that the formation of oxido bridges is observed only when more than three nitrogen donor atoms are present in the ligand. Co-ligands that possess less than three nitrogen donor atoms do not show such reaction behavior. It is assumed that the strong Lewis acidity of iron(III) is the driving factor behind this effect. Unfortunately, the poor data situation due to the lack of examples does not allow a detailed discussion.

Although paths from nitrito complexes to the formation of binuclear, oxido bridged complexes are already described in the literature, no investigation of these reactions *via in-situ* infrared spectroscopy has been done until now.<sup>[101,131,132]</sup> Most publications start from nitritoiron(III) complexes that are reductively nitrosylated via OAT either by  $\text{PPh}_3$  or thio-compounds. As a result, the emerging nitrosyl complexes can be described as  $\{\text{FeNO}\}^7$  compounds according to the Enemark-Feltham notation.<sup>[131,132]</sup> In a further step, two equivalents of the  $\{\text{FeNO}\}^7$  complex react with each other forming nitrous oxide.<sup>[131-133]</sup> While in similar, literature-known reactions in acidic aqueous solutions the resulting oxido ligand is sometimes protonated and dissociates as a water molecule, in aprotic solvents, the formation of bridging oxido ligands is observed.<sup>[101,131,132,134]</sup>

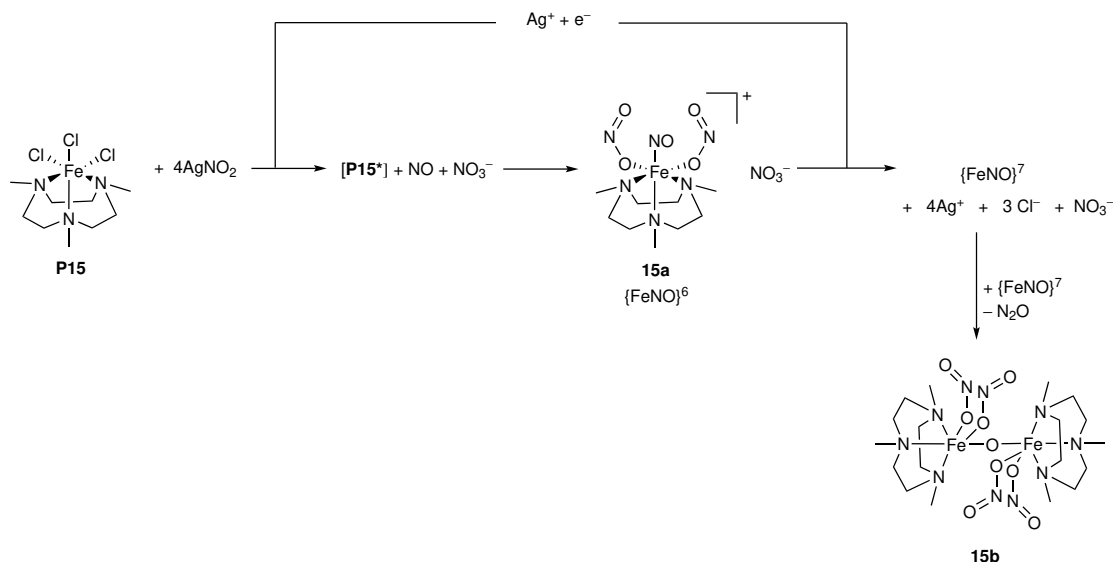
While the formation of the oxido bridge is too fast to keep track of in the case of **9** · 2MeCN, **16a** · 2C<sub>3</sub>H<sub>6</sub>O, **16b** · 3C<sub>3</sub>H<sub>6</sub>O and **17** · py, the reaction of **P15** with silver nitrite allowed the isolation of the intermediate {FeNO}<sup>6</sup> complex (**15a** · 0.5DCM) and a detailed examination by IR spectroscopic means. It is notable that the isolated compound is a rare example of an octahedrally coordinated {FeNO}<sup>6</sup> species.<sup>[135,136]</sup>

Since the yield of **15a** · 0.5DCM can be raised up by performing the reaction in the presence of nitric oxide, the involvement of this gas in the formation is assumed. The observed NO stretching vibration is in agreement with the literature-known complex [Fe(tacn)(NO)(NO<sub>2</sub>-κO)(NO<sub>2</sub>-κN)](ClO<sub>4</sub>) which has been synthesized by Wieghard *et al.* by letting [FeCl<sub>3</sub>(tacn)] react with NaNO<sub>2</sub> in 0.1M hydrochloric acid. Here, the stretching vibration of the linear NO ligand is observed at 1885 cm<sup>-1</sup>.<sup>[99,100,135,137-139]</sup> The vibrational band at 1767 cm<sup>-1</sup> which is observed if the reaction solution is dried *in vacuo* is in accordance with literature data of comparable {FeNO}<sup>7</sup> compounds.<sup>[97,136,139-142]</sup> The formation of elemental silver out of the remaining silver chloride was not observed.

The following *in-situ* IR experiment shows clearly that **15a** forms before the {FeNO}<sup>7</sup> compound. The IR vibration of the latter starts to grow after approximately one hour, directly when the intensity decrease of the vibrational band of **15a** begins. The vibration's intensity reaches a plateau which indicates that the {FeNO}<sup>7</sup> does not enrich in the solution but reacts further. Examination on the gas-phase above the reaction solution showed the emergence of nitric oxide almost directly after addition of the silver nitrite which was detected by the formation of brown nitrogen dioxide after opening the reaction vessel. An IR spectroscopic examination of the gas-phase showed NO-related vibrational bands that appear one hour after the silver nitrite was added. This is in agreement with the observation of the {FeNO}<sup>7</sup> complex in the *in-situ* IR spectrum. A similar behavior was already described by Franz and Lippard in an *in-situ* IR experiment but instead of the formation of a bridging oxido ligand, the corresponding complex eliminates nitrogen dioxide in another mechanism.<sup>[107]</sup>

If all information is taken into account, a proposed reaction equation can be formulated (Scheme 7). Immediately after the addition of silver nitrite to the precursor complex, the ligand exchange starts forming the unknown intermediate compound **P15\***. Furthermore, a part of the nitrite anions decompose under the formation of nitrate and nitric oxide. The instability of nitrite in presence of iron(III) complexes with many N-donor ligands is already described for various porphyrinate systems.<sup>[143]</sup> The latter is able to react with **P15\*** resulting in the formation of the isolated {FeNO}<sup>6</sup> compound **15a** · 0.5DCM. In the next step, **15a** is reduced to the spectroscopically observed {FeNO}<sup>7</sup>. Unfortunately, it was not possible to clarify the location of the one electron during the formation of the {FeNO}<sup>6</sup> species. It is assumed, however, that the silver chloride, which is present during the whole reaction, could act as a mediator for the involved oxidation and reduction. Two equivalents of that compound are now able to eliminate nitrous oxide under the formation

of the oxido bridged final product **15b**. The reaction described herein shares some similarities with the cytochrome  $cd_1$  NiR described in Section 1.1 like the preceding formation of  $\{\text{FeNO}\}^6$  before  $\{\text{FeNO}\}^7$ .<sup>[24]</sup>



**Scheme 7:** Presumed reaction mechanism for the formation of the oxido bridge in compound **15b** according to the isolated substances and additional IR spectroscopic examination.

In the case of **16a** · 2C<sub>3</sub>H<sub>6</sub>O and **16b** · 3C<sub>3</sub>H<sub>6</sub>O, not only the formation of an bridging oxido ligand is observed but also two different isomers are found which can be formulated as [Fe<sub>2</sub>(NO<sub>2</sub>-κO)<sub>2</sub>(tpya)<sub>2</sub>(μ-O)](ClO<sub>4</sub>)<sub>2</sub> · 2C<sub>3</sub>H<sub>6</sub>O (**16a** · 2C<sub>3</sub>H<sub>6</sub>O) and [(NO<sub>2</sub>-κO)(tpya)Fe(μ-O)Fe(NO<sub>2</sub>-κ<sup>2</sup>O, O')](tpya)](ClO<sub>4</sub>)<sub>2</sub> · 3C<sub>3</sub>H<sub>6</sub>O (**16b** · 3C<sub>3</sub>H<sub>6</sub>O). The different arrangement of one tpya ligand in **16b** results into an increase of space for the nitrito ligand which allows the formation of a nitrito-κ<sup>2</sup>O, O' ligand due to a decreased steric hindrance. The previously described reaction scheme can also be used as a possible explanation for the occurrence of the two isomers of **16**. The precursor **P16** exhibits two chlorido ligands that can be exchanged with nitrite. However, the initially desired [Fe(NO<sub>2</sub>)<sub>2</sub>(tpya)](ClO<sub>4</sub>) (**16\***) is not observed since it reacts very quickly under formation of an bridging oxido ligand. According to Scheme 7, this would include the formation of an  $\{\text{FeNO}\}^7$  species that reacts in a subsequent reaction with a second molecule of its kind under the formation of nitrous oxide. Depending on which of the two nitrito ligands in a theoretical **16\*** is converted into a nitrosyl, the opposing nitrogen atom of the tpya ligand is either a part of the pyridyl moiety (**16<sup>†</sup>**) or the tertiary amine nitrogen (**16<sup>‡</sup>**). The two isomeric nitrosyliron complexes are able to react in the three different combinations **16<sup>†</sup>**/**16<sup>†</sup>**, **16<sup>†</sup>**/**16<sup>‡</sup>** and **16<sup>‡</sup>**/**16<sup>‡</sup>**. Two of those three possible isomers of **16** are isolated with **16a** · 2C<sub>3</sub>H<sub>6</sub>O and **16b** · 3C<sub>3</sub>H<sub>6</sub>O. The third isomer, which would contain two chelating nitrito ligands, was not observed in this thesis.

**17** · py is the only compound in this thesis which was obtained by simply dissolving iron(III) chloride in a solvent and adding silver nitrite. When iron(III) chloride is dis-

solved in pyridine, yellow crystals of the literature-known substance  $[\text{FeCl}_3(\text{py})_3] \cdot \text{py}$  can be isolated.<sup>[144]</sup> This compound can be seen as a precursor complex for the synthesis of **17** · py and verifies the above mentioned effect that three or more N-donating ligands on the formation of oxido bridges. Attempts to characterize the bromide analogue to **17** failed since the dark-brown crystals obtained decompose after a few seconds when either exposed to room temperature or by removing the pyridine environment.

While the instability towards higher temperatures did not allow the PLI experiments on the substances **15a** · 0.5DCM, **16a** · 2C<sub>3</sub>H<sub>6</sub>O, **16b** · 2C<sub>3</sub>H<sub>6</sub>O and **17** · py, the solvent free compound **15b** exhibits superior stability and was, therefore, chosen for further measurements. The results of the irradiation experiment will be discussed in Section 3.8.5.

### 3.5 Observed binding modes and absence of nitrito- $\kappa N$ in the case of the nitritoiron(III) complexes

Without exception, all nitrito complexes synthesized in this thesis contain O-bound nitrito ligands which was confirmed by single-crystal X-ray diffraction and by IR spectroscopy. The obtained distances and angles as well as the IR vibrations of the nitrito ligands are in consensus with literature-known data for nitritoiron complexes and can, therefore, be regarded as reliable for the discussion.<sup>[39,89,99–101,103,131,132,135,140,145–150]</sup>

As already mentioned in Section 1.2, most of the structurally characterized nitritoiron complexes exhibit N-bound nitrito ligands.<sup>[37,41]</sup> According to the literature, kinetic, thermodynamic and steric effects as well as ligand-ligand interactions and the electronic structure of the central metal are the main influencing factors for the formation of various binding modes.<sup>[38,39]</sup>

The synthesized substances show that various coordination environments (pure O-donor, pure N-donor or mixed N,O-donor ligands) do not seem to have an influence on which kind of O-binding mode the nitrite binds. This becomes obvious if the binding modes of **1a-Fe**, **1b** and **2-4** are compared to their coordination environment. The complexes named exhibit ligands that provide four oxygens to the coordination sphere of each central metal but all possible O-binding modes of the nitrito ligand are found. Accordingly, steric effects and the resulting vacant space for the nitrito ligands are more decisive for the formation of the different O-binding modes. This applies also for the mixed N,O-donor and pure N-donor co-ligands where all possible, non-bridging, O-bound binding modes are observed.

A closer look at the literature-known nitritoiron complexes shows that the synthesis method seems to play an important role in obtaining the certain isomers. Complexes which are synthesized with NaNO<sub>2</sub> and (NBu<sub>4</sub>)NO<sub>2</sub> as the nitrite source exhibit, in almost every case, N-bound nitrito ligands.<sup>[96,103,131,132,135,145–150]</sup> Only three exceptions are found for these nitrite salts.<sup>[99,101]</sup> An additional exemption in the case of (Bu<sub>4</sub>N)NO<sub>2</sub> is explained by a special hydrogen-bonding situation.<sup>[39]</sup> Furthermore, all nitritoiron com-

plexes obtained from alternative synthesis routes such as the introduction of nitrogen dioxide, adding an excess of nitric oxide or the synthesis in basic aqueous solution exhibit all nitrito- $\kappa N$  ligands.<sup>[75,110,147,151,152]</sup> (PPN)NO<sub>2</sub> as the nitrite source forms mainly iron complexes with O-bound nitrito ligands.<sup>[100,140,153]</sup> Only one exception is described in the literature, however. In this case a very unique coordination environment is found since a nitrito ligand is accompanied by one nitrosyl and one phosphane co-ligand.<sup>[73]</sup>

Without exception, every nitritoiron compound synthesized *via* the AgNO<sub>2</sub> route exhibits O-bound nitrito ligands which is in agreement with the results of this thesis.<sup>[89,100]</sup> Accordingly, the synthesis with AgNO<sub>2</sub> shows a high selectivity for the formation of O-bound nitrito complexes with iron. Other central metals such as cobalt, ruthenium, palladium and platinum are not as selective as iron with the formation of O-bound nitrito ligands by reaction with AgNO<sub>2</sub> and form nitrito- $\kappa N$  complexes, as well.<sup>[154–158]</sup>

### 3.6 Binding modes in (HNEt<sub>3</sub>)<sub>2</sub>[M<sup>III</sup>(fpin)<sub>2</sub>(NO<sub>2</sub>)] (1a-M with M = Al, Sc, Cr, Fe, Ga, In, Tl, Bi)

In their review about nitrito complexes Hitchman and Rowbottom worked out various factors that influence the nitrito ligand's binding mode. *Inter alia* the authors described the central metals 'electronic structure' as one of these factors. However, their assumptions were based only on nitrito complexes with late transition metals.<sup>[38]</sup> Until now, almost 40 years later, the number of known nitrito complexes with early transition metals and p-block elements is still rather low. The **1a-M** series synthesized in this thesis allows, for the first time, a detailed investigation of the nitrito ligand's binding behavior in complexes with those elements.

Taking a look at the synthesized complexes with spherical charge distributions, an influence of the central metals radii becomes obvious. In the case of **1a-Sc** and all group 13 metal complexes, the spherical charge distribution is achieved by a closed-shell electron distribution. As shown in the spin density plot of **1a-Fe** (Figure 2.44) the high-spin-d<sup>5</sup> metal center also exhibits a more or less spherical charge distribution.<sup>[87]</sup> If the synthesized complexes of these elements are now compared, a connection between their size and the binding mode of the nitrito ligands is found. For this comparison, the crystal radii according to Shannon and Prewitt's compilation of fluoride- and oxide-based radii are used.<sup>[159]</sup> A list of the central metals' crystal radii and their d electron configuration together with the observed binding modes is found in Table 20. According to this, the threshold of the radius-implied switch from the monodentate *E*- $\kappa O$  binding to a chelating nitrito ligand in the present (HNEt<sub>3</sub>)<sub>2</sub>[M<sup>III</sup>(fpin)<sub>2</sub>(NO<sub>2</sub>)] system seems to be between 0.76 Å (Ga<sup>3+</sup>) and 0.79 Å (Fe<sup>3+</sup>). If the central metal's radius is above the value of iron, only chelating nitrito ligands are observed.

**Table 20:** Shannon’s crystal radii of penta- and hexacoordinated trivalent metal ions with their respective d electron configuration and the observed binding mode in complexes of the type  $[M^{III}(\text{fpin})_2(\text{NO}_2)]^{2-}$ . In the case of five-coordinated  $\text{Cr}^{3+}$  no value for the ionic radius is given in the literature.<sup>[159]</sup>

	$\text{Al}^{3+}$	$\text{Sc}^{3+}$	$\text{Cr}^{3+}$	$\text{Fe}^{3+}$	$\text{Ga}^{3+}$	$\text{In}^{3+}$	$\text{Tl}^{3+}$
binding mode $\text{NO}_2^-$	$\kappa O$	$\kappa^2 O, O'$	$\kappa O /$ $\kappa^2 O, O'$	$\kappa^2 O, O'$	$\kappa O$	$\kappa^2 O, O'$	$\kappa^2 O, O'$
d electron configuration	–	$3d^0$	$3d^3$	$3d^5$	$3d^{10}$	$4d^{10}$	$5d^{10}$
$r(\text{CN}5)/\text{\AA}$	0.62	–	–	0.72	0.69	–	–
$r(\text{CN}6)/\text{\AA}$	0.68	0.89	0.76	0.79	0.76	0.94	1.03

A similar result is also observed by looking at the only other literature-known nitrito complexes of group 13 elements. In the  $[M(\text{NO}_2)_2(\text{pc})]^-$  system ( $M = \text{Al}^{3+}, \text{In}^{3+}, \text{Tl}^{3+}$ ; pc = the phthalocyaninat dianion) the aluminium complex exhibits monodentate bound nitrite while the ligands are in their chelating form in the case of indium and thallium.<sup>[76–78]</sup> It has to be noted, that the influence of the central metal’s ionic radius is already described for a row of homoleptic nitrito complexes containing various lanthanoid(III) ions and yttrium(III) as central metal.<sup>[160]</sup> However, **1a-Cr** shows that a prediction of the nitrites binding mode cannot be done by using only the ionic radii of the central metal since, according to Shannon, the crystal radius of chromium(III) with CN 6 has the same value as for gallium(III) but both  $E\text{-}\kappa O$  and the chelating binding mode are found. However, if the spin density distribution is plotted (Figures 2.45 and 2.46), it is obvious that no spherical charge distribution is found in the case of chromium(III). Instead, the spin density appears as a cube with six holes on its faces. The nitrito ligand coordinates in one of those holes which is in contrast to the other investigated cases. Therefore, the plotting of spin densities according to Alvarez *et al.* can be considered a useful tool to visualize the central metal’s influence on the nitrito ligands binding mode when partially filled d orbitals are present.<sup>[87]</sup> Taking a look at the literature, in fact more than 90% of the known nitrito complexes with chromium(III) exhibit  $E\text{-nitrito-}\kappa O$  ligands.<sup>[37]</sup> This is an indication, that in the case of chromium(III), monodentate binding modes are more stabilized. This topic will be discussed in further detail in Section 3.7.3 where it is also shown that the main impact of the non-spherical charge distribution is seen in the scan graph of **1a-Cr**.

As can be seen in the molecular structure, **1a-Bi** shows a very different coordination behavior compared to the other complexes in the **1a-M** series. The explanation for this is the filled  $6s^2$  orbital in bismuth(III) which acts as a stereochemically active valence-shell lone pair. This orbital is heavily p-polarized to fulfill its steric needs. Bulging out trans to the two fpin ligands, it occupies almost half of the coordination sphere (Figure 3.72) resulting in a ‘buckling’ of the nitrito ligand in the direction of one triethylammonium cation. The same behavior is already observed in literature for the  $[\text{SbF}_4]^-$  anion where the

central atom and ligands together create a  $C_{2v}$ -symmetric anion instead of an tetrahedral molecule due to the steric demand of the filled and p-polarized 5s orbital.<sup>[161,162]</sup> Attempts to synthesize **1a-Sb** did not succeed since the smaller radius of the central metalloid did not allow the presence of a further ligand in addition to the two perfluoropinacolato ligands.

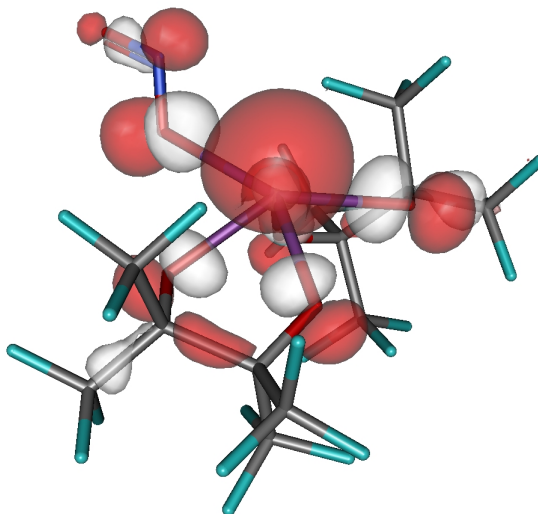


**Figure 3.72:** Visualization of the stereochemically active valence-shell lone pair (HOMO) in **1a-Bi** calculated using mp2/def2-tzvpp with cpcm.<sup>[163]</sup> Isovalue 0.04.

## 3.7 Quantum-chemical calculations

To choose suitable complexes for the quantum-chemical calculations, two eligibility criteria were applied. First of all, the maximal number of nitrito ligands per central metal should be one to obtain a, preferably, simple system without interference by other simultaneous switching ligands in the same molecule. Second, to avoid excessively long calculation times, preferably small mononuclear nitrito complexes were chosen for the calculations. Therefore, the choice fell upon **1a-M** ( $M = \text{Al, Sc, Cr, Fe, Ga, In, Tl}$ ), **11**, **12**, **13**, **14** and **7**. The latter is an exception as it is the only binuclear complex, and was chosen due to good results in the PLI experiments. The high-spin state of all substances was verified either by Evans-NMR measurements, comparison of the Fe–L distances within the molecules with literature-known values for similar high-spin complexes, or by comparison with the calculated values.

### 3.7.1 Structure optimization

Comparison of the  $M\text{-O}_{\text{nitrite}}$  distances obtained from single-crystal X-ray analysis with those of the optimized geometries calculated with various functionals showed an increasing agreement when HF exchange is included in the calculations. In all cases, except in **1a-Cr** and **7**, the best results were obtained with the TPSSh hybrid functional (10% HF

exchange). However, the runtimes for a whole optimization are approximately one to two weeks per molecule which would result in runtimes up to half a year per scan calculation. Due to this, the TPSSh functional is considered unusable for this application. In addition, including the CPCM solvation model decreases the compliance in every examined case and, therefore, the CPCM instruction is omitted in the scan calculations. Including the two cations to the BP86(CPCM) calculation improved the accordance enormously in the case of the scandium complex but did not show any improvements for the iron compound. However, the cation were omitted in every case since they only increase each optimization step's runtime which is not preferred for the following scan calculations. Although the TPSS functional showed generally better results, all followed scans were performed with both TPSS and BP86 to investigate possible differences and similarities within the resulting energy curves depending on the used functional.

### 3.7.2 Scan calculations I: general statements and methodology

Although scan calculations for nitrosyl complexes are described in the literature for the prediction of the stabilities of different isomers, this method is not described for nitrito complexes.<sup>[164–167]</sup> Only calculations for individual isomers and transition states are found but no energy pathways obtained from relaxed surface scans.<sup>[168]</sup> Therefore, the actual appearance of those graphs was still unknown. In the following, some general statements are formulated that can be derived from the obtained scan graphs.

Regarding the different functionals, TPSS and BP86 show their energetic minima at the same Fe–O–N angles and both calculation methods show at least shoulders for the less pronounced isomers. However, the potential pot of the side-on binding mode is slightly more pronounced in TPSS scan curves. In most cases, the TPSS scan curve runs almost parallel to the BP86 curve. In the case of the anionic complexes **1a-M**, the calculated energies show almost no differences except for the  $\kappa N$  minimum where greater discrepancies are found since the BP86 scan always gives a smaller value. Due to this, to obtain a maximal comparability of different scan graphs it is advised to use the same functional if more scan graphs are compared. Therefore, in the following section only the BP86 scans are compared with each other. Future photocrystallographic studies could be helpful to compare the distances and angles of MS with the results of the scan calculations. This would allow to discover which functional fits better. However, statements – except for the structural optimization of the isolated isomer – to verify the superiority of one of the two functionals cannot be given in this work. With respect to the calculations' runtimes no severe differences between TPSS and BP86 are found.

In contrast to the calculation with CPCM, the relative positions of the minima to each other remains the same. Only with regard to the relative energies of the rotation barriers

and the depth of the various isomers' potential pots, slight differences are found. The scan curves of **1a-Fe** showed that the CPCM should not be included in the scan calculations since it results in a "smoothing" of the energy curve. This is accompanied by an information loss since fewer isomers with less pronounced potential pots or shoulders in the curves, like the side-on binding mode in **1a-Fe**, do not appear in the resulting energy pathway.

An advantage of the relaxed surface scans is that they allow the ligand during rotation to elaborate the energetically preferred position. This also is important if the scan curves of **11** and **12** are discussed. With these, the Fe–O2–N angle was scanned from 20° to 170° but after reaching an angle of 100°, the nitrito ligand rotates sideways and follows the pathway of the Fe–O1–N scan which results in a final arrangement in which the non-coordinating O-atom of nitrite faces in the direction of the *tert*-butyl groups.

All scan graphs share the similarity that all minima can be clearly assigned to the possible binding modes of nitrite and all absolute minima are represented by the corresponding binding mode which is found in the isolated molecules. In some cases, when no minimum is found for a binding mode – in most cases the side-on binding – shoulders appear on the graph. Beside the determination of the stability of different binding modes, the scan method's second advantage is that it can be regarded as a tool to distinguish between the  $\kappa^2O,O'$  and *Z*-nitrito- $\kappa O$  isomers. As can be seen in almost every calculation, both isomers appear at separated positions either as critical or stationary points on the scan curve.

An important factor regarding the calculations is the symmetry of the nitrito ligand's environment. If the environment is symmetric, as is found in the more or less  $C_2$ -symmetric complexes **1a-M**, **13** and **14**, it does not matter if the Fe–O1–N angle or the Fe–O2–N is scanned. The resulting energy curves will be congruent in both cases.

In contrast, asymmetric environments, as found in compounds **7**, **11** and **12**, lead to different pathways depending on the rotation of the nitrito ligand. As seen in the scan graphs of **7** and **11** (Figure 2.56 and 2.55), the Fe–O1–N rotation gives a divergent energy curve as the Fe–O2–N rotation. This is a result of varying intramolecular interactions between co-ligands. Beside steric effects, mainly hydrogen bonds are able to change the shape of the scan curve. This effect is seen in the scan graph of the anion in **7**. Here, an additional minimum between potential pot of the *E*- $\kappa O$  isomer and the rotation barrier in direction of the *E*- $\kappa O$  is found in the Fe–O1–N scan. This stabilized binding mode arises from a stabilizing C–H...N<sub>nitrite</sub> hydrogen-bond. Due to this, the scan curve directly shows that hydrogen bonds must not be forgotten in the prediction of possible isomers during experiments that try to excite various MS. However, this should not be considered as drawback since the presence of hydrogen bonds is known to be an important factor in

the formation of different isomers in nitrito complexes.<sup>[39]</sup> Neither in the symmetric nor in the asymmetric case the rotation direction ( $30^\circ \rightarrow 170^\circ$  or  $170^\circ \rightarrow 30^\circ$ ) affects the scan graphs appearance.

Regarding steric effects, the scan curves of **11** and **12** directly showed, that only the close environment of the scanned ligand determines the graphs appearance. The Fe–O2–N scan curves of both substances are congruent which shows that the distant *tert*-butyl moieties in the case of **12** do not influence the scan graph. This gives the opportunity for 'cutting off' distant functional groups that do not interact with the nitrito ligand to reduce the calculations runtime without influencing the scans outcome. Also, possible orbital interactions should be taken into account, but, unfortunately, scan calculations containing plotted orbitals are not possible at the moment due to the available computational resources.

Overall, it can be said that all substances investigated are of great interest for linkage isomerism experiments since the various isomers appear as clear defined minima on the energy hypercurve and are separated by surmountable energy barriers. These barriers are, in general, higher than those between various nitrosyl isomers.<sup>[164-167]</sup> This allows a "latching" of the nitrito ligand in the energetic minima of different stable or metastable isomers. However, the scan calculations give insight only into the relative stabilities of the various isomers and possible isomerizations of the nitrito ligand. Statements regarding the stability against a photolytic cleavage of the ligands cannot be made from these calculations. A closer comparison between the results of the scan calculations and the results of the PLI experiments were possible in the case of the substances **1a-Fe** and **7**. This will be discussed in Section 3.8.

### 3.7.3 Scan calculations II: scan graphs of the **1a-M** (M = Al, Sc, Cr, Fe, Ga, In, Tl) series

At first, its necessary to distinguish between the scan graphs of the anions with a spherical charge distribution ( $\text{Al}^{3+}$ ,  $\text{Fe}^{3+}$ ,  $\text{Ga}^{3+}$ ,  $\text{In}^{3+}$ ,  $\text{Tl}^{3+}$ ) and that with a non-spherical charge distribution due to partially filled d orbitals ( $\text{Cr}^{3+}$ ). Due to its special scan graph, **1a-Sc** has to be discussed separately.

The scan curves from **1a-Fe** and the four group 13 metal complexes show, in general, a very 'smooth' development with a decreasing number of minima and shoulders that can be assigned to different MS. In every case the isolated isomer also represents the most stable one in the scan curves. Furthermore, by comparing the graphs with each other, it becomes obvious that the chelating isomer is more and more stabilized in comparison to the other isomers with increasing atomic numbers (ionic radii) of the central metal as same is observed when the  $E-\kappa O$  is compared to the  $\kappa N$  binding mode. While the former is the most stable isomer in the case of **1a-Al** and the latter the least stable, their energy

difference shrinks until the the N-bound binding mode becomes more stable in **1a-Tl**. **1a-Sc** shows a rather different scan graph (Figure 2.48) compared to the other examples in the **1a-M** row. In contrast to all the other graphs, the scandium compound shows no minima for the  $\kappa N$  and  $E-\kappa O$  isomers. According to literature, the coordination number five is highly unfavored by scandium compounds since its coordination behavior is mainly driven by its relatively large ionic radius compared to other trivalent 3d transition metals. This becomes obvious when already published scandium complexes are viewed since CN 6 and over are preferred.<sup>[169–171]</sup> However, scandium(III) is still smaller than indium(III) and thallium(III) but the latter two do not exhibit such conspicuous scan curves.<sup>[159]</sup> In contrast to the two named p-block elements, scandium(III) exhibits a close shell [Ar] configuration and no  $d^{10}$  configuration which means that the scandium-nitrite interaction should be mainly of an ionic nature. This may indicate that d orbitals play an important role in the appearance of the scan graph since covalent interactions become possible. According to Ruiz *et al.* spin delocalization can be considered a sign of covalence and therefore the metal-ligand bond, at least in the case of **1a-Fe**, exhibits a partial covalent character.<sup>[87]</sup> However, this statement needs to be investigated further by additional calculations on the various complexes. Here, electrostatic potential (ESP) maps of the nitrito ligand could be useful to evaluate the electron density of the binding sites. Furthermore, QTAIM calculations would be helpful to look at the bond-critical points to show if there are differences in the covalency of the metal-nitrite bondings between the investigated complexes.

An explanation for the high rotation barriers in **1a-Cr** is found by looking at the spin density distributions (Figures 2.45 and 2.46). The nitrito ligand in **1a-Cr** is 'trapped' in a hole of spin density due to the unfilled  $dx^2-y^2$  and  $dz^2$  orbitals, resulting in much higher energies needed for the isomerization. Also, a visualization of the scan calculation shows that the isomerization from chelating to monodentate bound nitrite includes a rearrangement of the perfluoropinacolato ligands since the  $O_{\text{fpin}}$  atoms tend to coordinate in the spin density holes. It is notable that in the case of the chromium compound the general shape of the TPSS and the BP86 are, indeed, very similar as in the other calculations, but the isomer stabilities switch their order depending on the functional used. Since the minima involved all belong to not-isolated MS, only the results of photocrystallographic measurements would give answers to the question of which functional depicts reality. Therefore, no definite statement can be made at the moment about which functional fits the best.

### 3.7.4 Scan calculations III: scan graphs of nitritoiron complexes

Since all investigated nitritoiron complexes are in the high-spin state and were calculated with the same functionals, it is possible to compare the respective scan curves with each other. As observed in the already described scan graphs, all minima can be assigned to

possible binding modes of the nitrito ligand. In all cases, the never structurally observed  $\kappa^2N,O$  isomer appears either as a shoulder (**1a-Fe**, **7** and the Fe–O2–N1 scan of **11** and **12**) or as defined minima on the energy curve (**13** and **14**).

In the case of **7**, the scan method is applied on a binuclear complex. For technical reasons, only one of the two nitrito ligands is rotated. The actual switching process, however, remains unknown until photocrystallographic measurements are made. But the scan graph can give some important information regarding stable isomers of **7**. It has to be noted that the X-ray structure of the anion in **7** already exhibits a *Z*-nitrito- $\kappa O$  ligand which non-coordinating O-atom shows in the direction of the bridging moiety of heida. Accordingly, the Fe–O1–N scan should be regarded, at least in the area from 180° to 280°, as the most probable pathway since it reflects results of the X-ray structure analysis.

Furthermore, the calculations show that the saturation of the coordination sphere seem to have a great influence on the relative heights of the minima. A lowering of the coordination number, compared to the isolated structure leads, in general, to higher relative energies of the isomers. In the case of **1a-Fe**, the two sterically demanding perfluoropinacolato ligands allow a fivefold as well as a sixfold coordination of the iron center. Therefore, the isomer's relative minimum energies on the curve are closer to each other. The same is found in the case of **7**, where an *Z*-nitrito- $\kappa O$  ligand coordinates to an already fivefold-coordinated central metal. **11** and **12** reach a coordination number of only 6 with a chelating nitrito ligand. This is also supported by the structure of **10** · 2MeCN, where the {Fe(NO<sub>2</sub>)(salen)} units need to form dimers to complete their coordination spheres. Furthermore, preliminary scan calculations on **10** showed a dissociation of the monomers when a chelating coordination of the nitrito ligand is enforced. Accordingly, the scan graphs of the mononuclear salen complexes show their absolute minimum at the crystallized  $\kappa^2O,O'$  isomer. The other two monodentate isomers (*E*- $\kappa O$  and  $\kappa N$ ) are almost 15 kJ mol<sup>-1</sup> less stable than the chelating isomer. In addition, the side-on binding mode appears as a small minimum beside the  $\kappa N$  isomer. Both minima are separated from each other by a tiny rotation barrier. This behavior is even more pronounced for the bipzpy complexes **13** and **14**. Here, the  $\kappa N$  isomer appears not as a local minimum but, instead, two minima appear which can be assigned to the side-on binding mode. This is also interesting since this isomer has never been observed in substance and is predicted only as an intermediate towards various MS in isomerism experiments. Accordingly, **13** and **14** were able to form the [Fe(bipzpy)X<sub>2</sub>(NO<sub>2</sub>- $\kappa^2N,O$ )] (X = Cl, Br) isomer, at least as an MS in PLI experiments. While the coordination number of the isolated isomers is seven, an isomerization to the  $\kappa N$  and *E*- $\kappa O$  binding modes would lead to a decrease to CN = 6. Accordingly, the side-on binding mode contributes more to the filling of the coordination sphere.

**13** and **14** allow one to examine the influence of different halogenido ligands on the isomer stability and the rotation barriers of the nitrito ligand – with the result, that both graphs

are almost congruent since the halogenido ligands do not interact with the nitrite.

## 3.8 Photoinduced linkage isomerism of selected compounds

### 3.8.1 Requirements for the tested substances and PLI of nitritoiron complexes

A few criteria were formulated before some of the synthesized substances were chosen for the PLI experiments. First of all, the compounds should exhibit UV-Vis absorption bands to determine suitable wavelengths for irradiation. Second, the yield has to be good enough to synthesize manageable amounts of substance for the experiments. Since the PLI measurements were performed in Nancy, France, and had to be sent *via* mail, a good stability against heat was advantageous. According to these criteria, the substances **1a-Fe**, **2** · MeCN, **6-8** and **15b** were determined to be promising candidates for the PLI experiments. Since the number of possible measurements was limited, the compounds **1b** and **3** · 2MeCN were not chosen due to their similarity to compounds **1a-Fe** and **2** · MeCN, respectively. Due to their colorlessness, all other compounds of the **1a-M** series, except **1a-Cr**, are not suitable for these experiments but, unfortunately, it was not possible to isolate manageable amounts of the chromium complex.

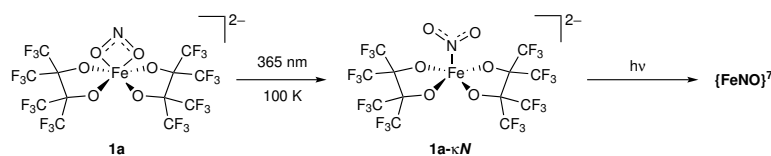
While the number of examined nitrosyliron complexes which undergo PLI is quite high, only one example for a PLI of a nitritoiron complex is found in the literature.<sup>[172]</sup> In this example the nitrito-heme complex possesses an additional nitrosyl *trans* position to the nitrito ligand which switches simultaneously during the irradiation experiment. This constellation does not allow one to gather information about the effect of the irradiation on the nitrito ligands itself.<sup>[127,172-175]</sup> PLI experiments on pure nitritoiron complexes are nonexistent in the literature. Hence, the performed PLI experiments in this work are, at least, the first with non-heme nitritoiron complexes. This allows for new insight into the formation of various linkage isomers and shows that nitritoiron compounds could be promising for possible future applications such as for data storage or as optical switches. Since the PLI effect of the tested substances is traced by IR spectroscopy, the previously performed IR experiments with the <sup>15</sup>NO<sub>2</sub>-enriched substances helped for a better identification of the nitrite-related bands.

### 3.8.2 PLI of **1a-Fe**

The PLI experiment of **1a-Fe** reveals that irradiation with UV light of 365 nm at 100 K leads to a partial switching of the nitrito ligand. The main decreasing bands are assigned to the chelating nitrito ligand in the anionic complex. Simultaneously increasing bands comply with literature-known values for nitrito-κN ligands.<sup>[74,176]</sup> Furthermore, the switching is accompanied by a partial decomposition of the sample, indicated by the formation of a nitrosyl stretching vibration at 1808 cm<sup>-1</sup>. In comparison to literature-known nitrosyliron complexes this band can be assigned to a {FeNO}<sup>6</sup> species.<sup>[100,136-139]</sup> This

kind of photoinduced cleavage of nitrite is described in the literature as a method for the synthesis of  $\{\text{FeNO}\}^6$  systems.<sup>[99]</sup> The vibrational band at  $1742\text{ cm}^{-1}$  which appears after 30 min matches exactly to Monsch's  $(\text{HNEt}_3)_2[\text{Fe}(\text{fpin})_2\text{NO}]$  ( $\{\text{FeNO}\}^7$ ).<sup>[97]</sup> It is conceivable that the delayed growth of the second nitrosyl band is the result of a subsequent reduction process of the previously formed  $\{\text{FeNO}\}^6$  complex. After increasing the temperature back to room temperature, only the  $\{\text{FeNO}\}^7$ -related vibrational band remains, indicating that the  $\{\text{FeNO}\}^6$  decays by losing its nitrosyl ligand. No evidence for other reaction products, such as nitrate, were found in the IR vibrations. The location of the split-ff oxygen is hard to determine without a suitable substrate and in the literature this topic was not further discussed.<sup>[99]</sup> Therefore, the exact decomposition mechanism of **1a-Fe** remains unclear. Scheme 8 depicts the proposed mechanism in the described PLI experiment.

To investigate the isomerization pathway more experiments are needed. Here, the addition of  $\text{PPh}_3$  to the sample would help to catch the nitrite's dissociated oxygen atom and prevent the substance from undergoing unfavorable side reactions during the irradiation process.<sup>[99]</sup> Also, for a better comprehension of the whole mechanism, an additional PLI experiment with the  $^{15}\text{NO}_2$ -enriched substance would be helpful since the isotopic-induced shift allows a better identification of NO and nitrite-related vibrational bands. Unfortunately, the decay of the sample makes a further photocrystallographic examination impossible.

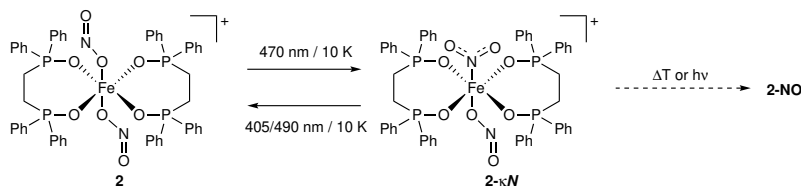


**Scheme 8:** PLI of the nitrito ligand in **1a-Fe** according to IR spectroscopic investigations after irradiation of a sample with light of a wavelength of 365 nm at 100 K. Destruction of the sample occurs by photolytic cleavage of the nitrito ligand.

If the results of the measurement are compared with the scan graph, the nitrito- $\kappa\text{N}$  complex is, indeed, found to be a metastable isomer. No vibrations of the nitrito- $\kappa\text{O}$  isomer are observed in the IR spectra, which implies that this isomer is either not accessible or other irradiation conditions have to be investigated. However, the scan calculation is not able to predict the photolytic cleavage of the nitrito ligand. For this, an additional calculation method has to be found.

### 3.8.3 PLI of **2** · MeCN

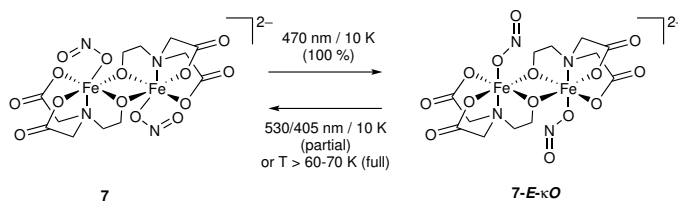
The decreasing bands during the irradiation of **2** · MeCN at 10 K with blue light of 470 nm for 10 min can be clearly assigned to the *E*-nitrito- $\kappa O$  ligands while the simultaneously increasing bands at  $1323\text{ cm}^{-1}$  and  $1378\text{ cm}^{-1}$  match the literature-known values for nitrito- $\kappa N$  ligands.<sup>[74,176]</sup> The generated MS can be partially depopulated by irradiation with light of wavelengths of 405 nm and 490 nm without the destruction of the sample. However, since the vibrational bands of the O-bound nitrito ligand do not disappear completely the conversion rate is determined to be lower than 100% since the nitrite-related bands do not vanish completely. Further irradiation with wavelengths of 780 nm and 590 nm lead to the photolytic cleavage of the nitrito ligand with formation of a nitrosyl complex which is reflected by the vibrational band at  $1727\text{ cm}^{-1}$ . In contrast to **1a-Fe**, the vibrational bands are not assignable to a  $\{\text{FeNO}\}^6$  species but comply with values of known  $\{\text{FeNO}\}^7$  compounds.<sup>[99,100,136–139]</sup> This implies an additional reduction of the compound during the decomposition process. The critical temperature is determined to be between 50 K and 100 K. A proposed reaction equation for the PLI is found in Scheme 9.



**Scheme 9:** PLI of the nitrito ligand in **2** · MeCN according to IR spectroscopic investigations after irradiation of a sample with light of the wavelength of 470 nm at 10 K. Partial depopulation of the MS is obtained by irradiation with light of the wavelengths of 405 nm or 490 nm. Increasing the temperature or longer irradiation times lead to the destruction of substance with formation of the nitrosyl complex **2-NO**.

### 3.8.4 PLI of **7**

Irradiation of **7** at 10 K with light of 470 nm leads to significant PLI with a conversion rate of nearly 100%. Vibrational bands that were previously assigned to the *Z*-nitrito- $\kappa O$  ligands vanish completely while bands appear that can be definitely assigned to the *E*-nitrito- $\kappa O$  binding mode. The MS can be partially depopulated by irradiation with light of the wavelengths of 405 nm and 530 nm without decay of the sample.  $T_{\text{crit.}}$  of **7** is between 60 K and 70 K. No signs of decomposition are observed when the temperature is increased back to RT. A reaction equation of the PLI is depicted in Scheme 10.



**Scheme 10:** PLI of the nitrito ligand in **7** according to IR spectroscopic investigations after irradiation of a sample with light of the wavelength of 470 nm at 10 K. Depopulation of the MS is obtained by irradiation with light of the wavelengths of 405 nm or 530 nm or by increasing the temperature.

A comparison of the results of the PLI experiment with the scan graph of **7** shows that the obtained MS is represented by a local minimum on the energy hypersurface. Vibrational bands that were assigned to the  $\kappa N$  isomer – which is also observed as a local minimum in the scan calculation – have not been observed during the experiment which implies a direct isomerization from *Z*-nitrito- $\kappa O$  to *E*-nitrito- $\kappa O$  binding mode. This and the result of **1a-Fe**, show that the scan calculations are indeed a useful tool to predict possible products of the photoinduced isomerizations since the spectroscopically observed MS appear as local minima in the energy curves. However, without a crystal structure of the observed MS it is not possible to say if it is the classical *E*-nitrito- $\kappa O$  isomer or the hydrogen-bond stabilized one.

Furthermore, the substance here presented is the first nitritoiron complex that shows a conversion rate of 100%.<sup>[172]</sup> The critical temperature of the substance is relatively low compared to other PLI-active substances with comparably high conversion rates.<sup>[46,47]</sup> Photo-crystallographic investigations on **7** are planned and will give a more detailed insight in the isomerization process. But due to its already shown characteristics such as its high stability against heat and oxygen, its high conversion rate and ability to return destruction-free to its GS, compound **7** can be considered a very promising candidate for further applications.

### 3.8.5 PLI of **15b**

Irradiation of **15b** at 10 K with light of various wavelengths lead to an isomerization of the nitrito ligands. Here, the decreasing bands were previously allocated to the *E*- $\kappa O$  ligands and the newly emerging bands comply with literature values of nitrito- $\kappa N$  ligands.<sup>[74,176]</sup> The vibrational band at  $1273\text{ cm}^{-1}$  could not be assigned clearly but is probably from a contamination that contains a nitrito- $\kappa^2 O, O'$  isomer. While the irradiation with light of 505 nm and 470 nm triggers a partial, destruction-free isomerization, additional irradiation with light of a wavelength of 405 nm leads to a photolytic cleavage of the nitrito ligands, resulting in the rise of a broad vibrational band at  $1660\text{ cm}^{-1}$  which most probably originates from a nitrosyl ligand.<sup>[99,100,136–139]</sup> The following irradiation with light of the wavelengths of 505 nm and 590 nm does not increase the vibrational band assigned to the decomposition product.

A second sample was cooled down to 10 K and irradiated only with light of wavelengths of 526 nm-565 nm. The vibrational band at  $1649\text{ cm}^{-1}$  was already present prior to the irradiation and did not change during the experiment. The previously described MS is obtained without signs of decomposition but the conversion rate was, by far, lower than in **7**. Additionally, the MS can be depopulated almost completely by irradiation with 590 nm. Increasing the temperature above 50 K leads to a gradual relaxation back into the GS which is completed at 90 K ( $T_{\text{crit.}}$ ), which indicates a thermally reversible behavior of the substance. Since the experiment does not allow the determination of which nitrito ligands switched during the experiment, no proposed reaction equation is given. At least a part of the four  $E\text{-}\kappa O$  ligands switch to the nitrito- $\kappa N$  binding mode. Now, since the requirements for a destruction-free PLI of **15b** are known, photo-crystallographic experiments need to be done to get a more detailed insight into the isomerization of the four nitrito ligands.

### 3.8.6 PLI of **6** and **8**

The PLI measurements on compounds **6** and **8** can be regarded as unsuccessful since both substances show many irreversible changes which indicate the destruction of the samples. The vibrational band at  $2343\text{ cm}^{-1}$  which appears in both sample's IR spectra, is clearly assignable to the asymmetric stretching vibration of  $\text{CO}_2$  which hints at a decarboxylation of the aminocarboxylato ligands.<sup>[88]</sup> This statement is also supported by a shift of the carboxy groups C=O vibrational band. During the irradiation of **6** the arising band at  $2230\text{ cm}^{-1}$  signals the additional decomposition of the nitrito ligands under the formation of nitrous oxide.<sup>[85,86]</sup> Furthermore, the nitric oxide-related band at around  $1720\text{ cm}^{-1}$ , which appears after increasing the temperature, shows a second possible decomposition pathway of the nitrito ligands.<sup>[99,100,136-139]</sup>

## 4 Summary and outlook

Since only few nitritoiron complexes are known in the literature, the first part of this thesis was to define factors that allow reproducible syntheses of these compounds. It became apparent that it was very helpful to use iron(III) as the central metal in combination with aprotic solvents for the syntheses. Furthermore, the high reactivity of nitrite towards various common ligand classes required a limitation of ligands used. Accordingly, the utilized ligands were categorized as alkoxides, phosphane oxides, aminocarboxylates and tertiary amines. As the synthesis method of choice, the ligand metathesis with silver nitrite was applied. This method required the synthesis of various halogenidoiron complexes containing the previously mentioned ligand classes. While seven chlorido complexes were prepared according to literature-known procedures, eight novel precursor complexes – seven with chloride and one with bromide – were synthesized and characterized by elemental analysis, IR and UV-Vis spectroscopy. The novel compounds were additionally characterized by single-crystal X-ray diffraction. Beside their use as precursor compounds for the synthesis of novel nitritoiron complexes, the halogenido complexes synthesized herein can be regarded as possible catalysts for the alkylation of grignard reagents, controlled polymerization or the formation of disulfides from thiols and dithiols in synthetic organic chemistry.

Reactions of the halogenido complexes with silver nitrite yielded 20 novel nitritoiron compounds which doubled the number of literature-known, structurally characterized iron complexes with O-bound nitrito ligands.<sup>[37,41]</sup> Apart from the ferric compounds, this synthesis method was successfully applied to synthesize seven nitrito complexes with other trivalent central metals. All nitrito compounds which were obtained in manageable yield were fully characterized by single-crystal X-ray diffraction, elemental analysis as well as IR and UV-Vis spectroscopy.

It is striking that not a single nitritoiron complex with an N-bound nitrito ligand was obtained from the syntheses. A comparison with the already known nitritoiron complexes showed a strong influence of the utilized synthesis method and used nitrite sources on the formation of the N-isomers. While every literature-known nitritoiron compound synthesized by the metathesis reaction with silver nitrite exhibits O-bound nitrito ligands, by far the most nitrito- $\kappa N$  compounds known to the literature were synthesized by reactions with sodium nitrite or by alternative synthesis methods. This high selectivity, however, was found only in the case of iron.

With perfluoropinacolate as co-ligand, it was possible to synthesize a row of eight mononuclear complexes all of which exhibit the same general formula  $(\text{HNEt}_3)_2[\text{M}^{\text{III}}(\text{fpin})_2(\text{NO}_2)]$  ( $\text{M} = \text{Al}, \text{Sc}, \text{Cr}, \text{Fe}, \text{Ga}, \text{In}, \text{Tl}, \text{Bi}$ ). Beside the already rare examples of non-heme nitritoiron and nitritochromium complexes, it was possible to isolate the first structurally characterized nitrito complexes with scandium, gallium and bismuth(III). In the case of indium and thallium, the complexes obtained were the second structurally described



**9** · 2MeCN represents the first known tetranuclear nitritoiron complex but due to its instability and low yield it was not regarded as suitable candidate for PLI experiments. The nitritoiron complexes with salen-based co-ligands **10-12** are of great interest for further investigation. Varying substitution on the salen ligand leads to a shift of the LMCT transition bands in the UV-Vis spectra. No studies have been found in which the influence of "co-ligand"-to-metal charge transfer bands on the switching ligand are examined, but since the LMCT changes the central metal's oxidation state for the duration of the excitation, a secondary effect on the switching ligand would be possible. The system described herein could represent a wavelength-tuneable system for a closer examination of this topic. Further advantages are the high stability of the solid substances and their good yield. Accordingly, future work should focus on photoirradiation experiments of these compounds.

When more than three nitrogen-donor ligands were present in the precursor complexes, the metathesis reactions had to be performed at very low temperatures (**13** and **14**) or they led directly to the formation of oxido-bridged, binuclear iron complexes. While this reaction was too fast to keep track of in the case of **9**, **16** and **17**, the reaction of **P15** with silver nitrite allowed the isolation of the intermediate  $\{\text{FeNO}\}^6$  complex **15a** · 0.5DCM beside **15b** which marks the end product of this reaction. Further investigations with *in-situ* and gas-phase IR spectroscopy showed that the reaction pathway shares some similarities with the reaction mechanism of the cytochrome  $cd_1$  NiR of *P. aeruginosa*. This pathway also served as an explanation for the occurrence of two different isolated isomers of **16**. Photoirradiation experiments on **15b** showed that the compound shows PLI activity and isomerizes from  $E-\kappa O$  to the nitrito- $\kappa N$  binding mode. Although the PLI occurred without decomposition if the right conditions were found, the conversion rate was not as high as in the case of **7**. Summing up, the results of the photoirradiation experiments were the first examples for PLI of nitritoiron complexes without other switching ligands. In addition, the 100% conversion rate of **7** proved that those compounds are interesting for further applications such as ultrafast optical switches or as data storage devices. Therefore, another aim for the future should be the synthesis of more nitritoiron complexes that may exhibit a higher  $T_{\text{crit.}}$  than **7** to allow the population of MS at higher temperatures.

Beside their use in PLI experiments, the synthesized nitritoiron complexes can be regarded as precursor compounds for the synthesis of otherwise not accessible novel nitrosyliron complexes. Reactions which turn nitrite into nitric oxide and can occur either by oxygen-atom-transfer, photoirradiation or by acidification of solutions of the dissolved compounds.<sup>[99]</sup> However, since nitrosyliron complexes were not the main topic of this work, the syntheses described should be a matter of future work.

The second part of this thesis dealt with the ambidentate properties of nitrite and isomer stability. For this, five suitable nitritoiron complexes and the  $(\text{HNEt}_3)_2[\text{M}^{\text{III}}(\text{fpin})_2(\text{NO}_2)]$

(M = Al, Sc, Cr, Fe, Ga, In, Tl) series were chosen as model systems to develop a quantum-chemical method for the identification of meta stable isomers. The synthesized bismuth complex was due to its stereochemically active valence-shell lone pair hardly comparable to the other complexes in this series. After working out fitting functionals, a method was developed to calculate an energy hypercurve by rotating the nitrito ligand step by step and determining the respective energies of the structures. As a result, the scan curves showed that it did not matter which functional was utilized, but, for a maximal comparability, only scan graphs which are calculated with the same functional should be compared to each other. Furthermore, it was shown that the ligand environment plays an important role for the calculation of the scan curves. While in a symmetric ligand environment no difference was observed whether the Fe–O1–N or Fe–O2–N angle is changed, it became necessary to perform more scan calculations if an asymmetric co-ligand environment around the nitrite is found. In addition, the scan curves showed that hydrogen bonds and steric interactions between nitrite and co-ligands are able to stabilize certain isomers and alter the appearance of the scan graphs. The respective rotation barriers are surmountable but much higher compared to nitrosyl compounds. This is a perfect condition for PLI since it allows a "latching" of the nitrito ligand in various MS. Beside the prediction of potentially excitable isomers, this method can also be used as a tool to distinguish between similar isomers like the chelating binding mode and the *Z-κO* form of nitrite. Furthermore, the comparison of the six scan graphs obtained from nitrito-iron complexes showed that the saturation of the coordination sphere plays an important role in the relative heights of the isomers' minima. While the calculation of scan graphs proofed already as a useful, there is still some space for improvements such as a more detailed view on possible intramolecular orbital interactions. These improvements should be a matter of future work.

Nonetheless, the scan calculations already showed that it is possible to visualize the stability of different MS and can be used as a simple tool for the prediction of excitable isomers in isomerization experiments. In the case of **1a-Fe** and **7**, a direct comparison between the results of the scan calculations and the result of their photoirradiation experiments was possible. The observed MS was represented by relative minima in both scan curves showing that the scan calculations are, indeed, a suitable method for the prediction of MS isomers linkage isomerism experiments.

The (HNEt<sub>3</sub>)<sub>2</sub>[M<sup>III</sup>(fpin)<sub>2</sub>(NO<sub>2</sub>)] series allowed a special view on the central metal's influence on the nitrito ligand's binding mode. The homologous row from aluminium to thallium, together with the iron, chromium and scandium complex showed clearly that, in the case of spherical charge distribution, the central metal's radius is a significant factor for the formation of various isomers. This statement was further supported by the scan calculations which showed that the chelating binding mode of nitrite becomes more and more stable with the increasing size of the central metal. While all these complexes exhib-

ited more or less similar scan graphs, the scandium compound exhibited a scan curve that deviated strongly from the others. Possible reasons for that are the almost completely ionic nature of the scandium-nitrite bond and its characteristic to prefer coordination numbers greater than six. This could not be finally elucidated in this thesis but future QTAIM calculations may provide answers to this question. With **1a-Cr**, the investigation included a complex that does not exhibit a spherical spin density distribution. It was shown that this has a direct impact on the respective isomerization barriers according to the scan calculations.

## 5 Experimental part

### 5.1 Common working techniques

All reactions, as far as not explicitly described otherwise, were performed under nitrogen atmosphere using standard Schlenk techniques. Syringes and cannulas, used for the dosage of solvents, as well as all reaction vessels were flushed at least three times with nitrogen before usage. All solvents were used as provided by the manufacturer and subsequently dried over a molecular sieve and stored in the original manufacturer's containers under nitrogen or argon atmosphere. If a temperature of  $-20^{\circ}\text{C}$  is mentioned, a sodium chloride/ice mixture (3:1) was used to cool down the solutions. If the layering technique was used for crystallization, the bottom solvent was first frozen with liquid nitrogen before it was layered with the second solvent.

The reaction with gaseous nitric oxide was performed with a special installation which was made up of an inlet for nitric oxide assembled to a Schlenk line. This apparatus allowed the treatment of reaction mixtures with nitric oxide under exclusion of air. In this case, argon instead of nitrogen was used as inert gas. Gaseous nitric oxide was obtained from a compressed gas cylinder, depressurized and led over Ascarite II® for the adsorption of acidic gases.<sup>[177]</sup> To facilitate the introduction of nitric oxide, a slight vacuum was applied to the used Schlenk tubes prior the reaction.

### 5.2 Analytical methods

Analytic Method	Equipment
Crystal selection	Leica MZ12 with polarization filter
Elemental analysis	Elementar vario EL (C, H, N, S content) Elementar vario micro cube (C, H, N, S content)
Infrared spectrometer	Jasco FT/IR-4600 with ATR Diamond Plate
NMR spectroscopy	Jeol Eclipse 270 Joel Eclipse 400 Bruker 400 Bruker 400 TR
Scales	Sartorius ED 124S
UV-Vis spectrometer	Cary 60 UV-Visible-Spectrophotometer
X-ray crystallography	Bruker D8Venture with rotating Mo-Anode, Photon II CCD detector and Kryoflex II cooling unit

### 5.2.1 Elemental analysis

CHNS analyses were done by the Microanalytical Laboratory of the Department of Chemistry, LMU Munich. Interpretation of the data was performed with the internet application JASPER.<sup>[178]</sup> High deviations in the C content in the case of phosphorus containing substances are a result of the phosphorus error.<sup>[179]</sup>

### 5.2.2 IR spectroscopy

Solid samples were recorded by direct application on an ATR diamond plate. All spectra were interpreted using the software Spectra Manager 2.07.00.<sup>[180]</sup> All signals are given in wavenumbers ( $\text{cm}^{-1}$ ). Relative intensities are described as very strong(vs), strong(s), medium(m), weak(w) and very weak(vw).

### 5.2.3 NMR spectroscopy

For NMR spectroscopic analyses, the substances were transferred into NMR tubes and dissolved in deuterated solvents. Chemical shifts  $\delta$  are given in ppm and referred to the signals of the used solvent. All  $^{13}\text{C}$  and  $^{31}\text{P}$  NMR spectra were recorded broad band proton decoupled. The program MestReNova (Version number 12.0.0-20080) was used for the spectra interpretation.<sup>[181]</sup>

### 5.2.4 UV-Vis spectroscopy

UV-Vis spectra of solutions were recorded using sealable quartz glass cuvettes ( $d = 10 \text{ mm}$ ). The spectra were corrected by subtracting the background spectrum of the used solvent and cuvette. Air sensitive samples were prepared by placing the empty cuvette inside a Schlenk tube, flushing it at least three times with inert gas atmosphere and dissolving the substances under inert gas counterflow in the background solvent. Afterwards, the sealed cuvette was transferred to the spectrometer.

### 5.2.5 Single-crystal X-ray diffraction

Crystals for X-ray diffraction were selected using a Leica MZ12 polarization microscope. Suitable crystals were measured at temperatures around 100 K on a Bruker D8 Venture diffractometer using molybdenum- $\text{K}_\alpha$  radiation from a rotating anode followed by the raw data processing with the program Bruker APEX. The structures were solved with direct methods using SHELXT-2014.<sup>[182]</sup> Platon was used for the space groups determination and for the rounding of the standard deviations (1:9-rule rounded).<sup>[183]</sup> The structures were refined by full-matrix least-squares calculations on  $F^2$  using ShelXL.<sup>[184]</sup> Crystal structures were visualized by ORTEP.<sup>[185]</sup> For the creation of package diagrams the programs Mercury and POV-Ray were used.<sup>[186,187]</sup> Further details to the structure measurements are displayed in Section 6.2.

### 5.2.6 PLI experiments

PLI measurements were performed by Prof. Dr. Dominik Schaniel at CRM2, Université de Lorraine. The samples were ground with KBr and then pressed into pellets which were glued with silver paste to a copper sample holder. The temperature was regulated by using an Oxford Optistat V01 with liquid helium. Lasers with different wavelengths and power output were used for the irradiation of the samples. The linkage isomerism was monitored by IR spectroscopy with a Nicolet 5700 FTIR spectrometer in the spectral range from 360–4000  $\text{cm}^{-1}$  and a resolution of 2  $\text{cm}^{-1}$ .

### 5.2.7 Quantum-chemical calculations

All quantum-chemical structure optimizations were performed using the ORCA program system (version 4.2.1).<sup>[188]</sup> Initial geometries for the calculations were taken directly from the data of the single-crystal X-ray analyses. For the calculations the pure density functionals BP86 and TPSS as well as the the hybrid functional TPSSh (10% HF exchange) were used.<sup>[189–193]</sup> The wave functions for the functionals were calculated using the triple zeta basis set def2-TZVP.<sup>[194,195]</sup> In case of the pure density functionals the additional auxiliary basis set def2/J was applied together with the the *multipole-accelerated resolution of identity approximation* (RI) and dispersion correction (D3) to take van-der-Waals interactions into account.<sup>[196–199]</sup> To simulate a crystal lattice, the BP86/def2-TZVP calculations were performed a second time with the Conductor-like Polarizable Continuum Model (CPCM) in which the dielectricity constant is assumed as infinite.<sup>[200]</sup> Chemcraft (Version 1.8 build536b) was used for the visualization and evaluation of the computational results.<sup>[201]</sup> Plotted orbitals were visualized using Avogadro.<sup>[202]</sup>

Subsequent relaxed potential energy surface scans were performed using both the TPSS or BP86 functional. Since Orca is not able to perform scan calculations if the Fe–O1–N1 angle is 180°, the scan calculations were split into three parts which were merged in the same graph. In general, the first calculation was started from a either an Fe–O1–N1 angle of 30° ( $\kappa N$  isomer) followed by the step by step rotation of the nitrito ligand over the *E*-nitrito- $\kappa O$  binding mode to an Fe–O1–N1 angle of 170°. In the second calculation, starting from the chelating binding mode, the Fe–O1–N1 angle was opened until it reached 170° as well. Both scan calculations could also be performed in the opposite direction (170°  $\rightarrow$   $\kappa^2 O, O'$  and 170°  $\rightarrow$   $\kappa N$ ). An additional, optimization was performed with a Fe–O1–N1 angle of 180° to fill the gap between the two curves. In every calculation the angle increment was 10° but if sharp changes near critical points were observed, the region was recalculated by using an angle increment of 5°. In every case the observed minima were verified a second time by an additional structure optimization for the respective isomer. All graphs are referenced to the most stable isomer and the relative energies are given in  $\text{kJ mol}^{-1}$ .

### 5.3 Reagents and solvents

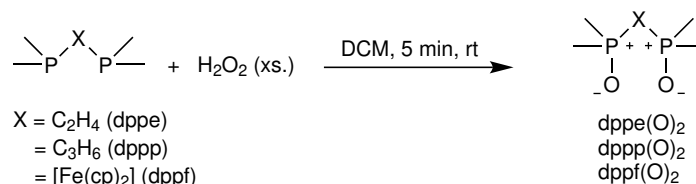
Solvents and reagents	Percentage purity	Manufacturer
2-(aminomethyl)pyridine	99%	Aldrich
acetone	99.5%	Bernd Kraft
acetonitrile	99.9%	Acros
aluminium(III) chloride	99%	Fluka
benzyltrimethylammonium chloride	≥ 98%	Fluka
bismuth(III) chloride	≥ 98%	Aldrich
<i>N,N'</i> -bis(salicylidene)ethylenediamine	98%	Aldrich
bromoacetic acid	97%	Aldrich
<i>N,N'</i> -dibenzylethylenediamine diacetate	≥ 99%	Merck
chromium(III) chloride hexahydrate	98%	Acros
dichloromethane	99.8%	Bernd Kraft
diethyl ether	99.5%	Bernd Kraft
dimethylformamide	≥ 98%	-
1,2-bis(diphenylphosphino)ethane	98%	ABCR
1,1'-bis(diphenylphosphino)ferrocen	97%	Aldrich
1,3-bis(diphenylphosphino)propane	≥ 98%	Honeywell
ethanol	abs.	VWR
ethanolamine	≥ 98%	Aldrich
ethyl acetate	99.9%	Fisher Chemical
ethylenediamine	98%	Sigma Aldrich
gallium(III) chloride	≥ 99.9%	ABCR
<i>n</i> -hexane	95%	Grüssing
hydrogen peroxide (30wt.-%)	≥ 99%	Bernd Kraft
hydrochloric acid	37 wt.-%	Merck
<i>N</i> -(2-hydroxyethyl)iminodiacetic acid	≥ 98%	Aldrich
iron(II) chloride	98%	Aldrich
iron(III) bromide	99%	Grüssig
iron(III) chloride	98%	abcr
iron(III) chloride hexahydrate	≥ 98%	Fluka
indium(III) chloride	≥ 99.9%	Roth
magnesium sulfate	99%	Grüssing
methanol	99.8%	Acros Organics
nitric oxide	99.5%	Air Liquide
perfluoropinacol	97%	FluoroChem
pyridine	99%	AppliChem
pyridine-2-carboxylaldehyde	99%	Aldrich

Solvents and reagents	Percentage purity	Manufacturer
quinaldic acid	98%	Aldrich
scandium(III) chloride hydrate	$\geq 99.9\%$	Alfa
silver nitrite	99%	Aldrich
silver nitrate	99%	VWR
sodium bicarbonate	99%	Brenntag
sodium hydroxide	$\geq 98\%$	Honeywell
sodium nitrite ( $^{15}\text{N}$ )	95%	Sigma Aldrich
sodium perchlorate	98%	abcr
sodium sulfate	99%	Grüssing
sodium triacetoxyborohydride	97%	Aldrich
tetraethylammonium chloride monohydrate	$\geq 98\%$	Merck
tetrahydrofurane	99.5%	Acros Organics
3,5-di- <i>tert</i> -butyl salicylaldehyde	$\geq 98\%$	TCI
3- <i>tert</i> -butyl salicylaldehyde	$\geq 97\%$	BLDpharm
thallium(III) trifluoroacetate	$\geq 95\%$	Alfa Aesar
<i>d</i> -trichloromethane	99.8%	EURISO-top
triethylamine	99%	Riedel de Haen
toluene	$\geq 98\%$	Acros Organics
1,4,7-trimethyl-1,4,7-triazacyclononane	$\geq 98\%$	TCI
trisodium nitritotriacetic acid	$\geq 98\%$	Aldrich
deionized water	de-ionized	house installation

**Table 21:** List of the used solvents and reagents with their corresponding purities and their manufacturers.

## 5.4 Synthesis of the ligands

### 5.4.1 Phosphane oxides



Synthesis according to M. J. Petersson *et al.*, *Chem. Commun.* **2008**, *37*, 4493–4494.

Purification according to C. R. Hilliard *et al.*, *Dalton Trans.* **2012**, *41*, 1742–1754.

#### Starting materials:

dppe/dppp/dppf, hydrogen peroxide (30 wt.-%), dichloromethane, water, magnesium sulfate.

#### Procedure:

The experiment was performed without using Schlenk techniques.

The phosphanes (5 mmol) were dissolved in dichloromethane (200 mL) and shaken together with hydrogen peroxide (30 wt.-%, 25 mL) in a separating funnel for 5 min. The two phases were separated, the organic layer washed with water (2 x 200 mL) and dried over magnesium sulfate. The solvent was removed by rotational evaporation. dppe(O)<sub>2</sub> and dppp(O)<sub>2</sub> were obtained as colorless powders.

In case of dppf(O)<sub>2</sub>, a special step have to be applied since the compound tends to form hydrogen peroxide adducts. Therefore, the crude dppf(O)<sub>2</sub> was dissolved in dichloromethane and stirred for 1 d together with a mole sieve (4 Å) filled tea bag. Complete removal of the solvent under reduced pressure yielded the beige, hydrogen peroxide free product.

**dppe(O)<sub>2</sub>**

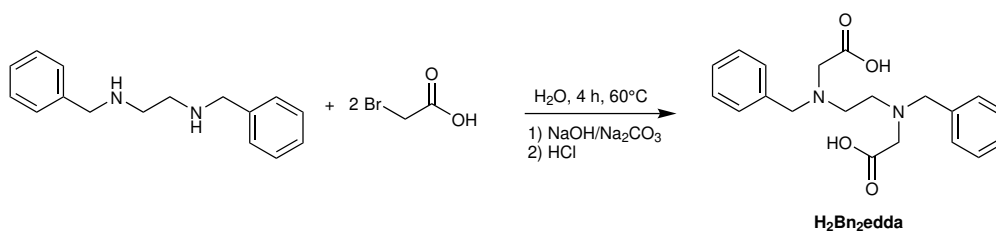
<b>Empirical formula:</b>	C <sub>26</sub> H <sub>24</sub> O <sub>2</sub> P <sub>2</sub> (430.42 g mol <sup>-1</sup> ).
<b>Yield:</b>	2.07 g (4.81 mmol, 96% of th.), colorless powder.
<b><sup>1</sup>H NMR:</b> (400 MHz, CDCl <sub>3</sub> )	δ = 7.71–7.66 (m, 8H), 7.51–7.40 (m, 12H), 2.50 (d, 4H) ppm.
<b><sup>31</sup>P{<sup>1</sup>H} NMR:</b> (162 MHz, CDCl <sub>3</sub> )	δ = 33.71(s) ppm.
<b>Elemental analysis:</b>	found (calcd.): C 72.90% (73.55%), H 5.60% (5.62%), N 0% (0%).
<b>IR:</b> (solid, ATR)	$\tilde{\nu}$ = 1484w, 1437m, 1420w, 1321vw, 1173vs, 1120s, 1103m, 1087m, 1070m, 1028m, 995w, 923vw, 800vw, 762m, 754m, 729vs, 692vs, 655w cm <sup>-1</sup> .

**dppp(O)<sub>2</sub>**

<b>Empirical formula:</b>	C <sub>27</sub> H <sub>26</sub> O <sub>2</sub> P <sub>2</sub> (444.45 g mol <sup>-1</sup> ).
<b>Yield:</b>	1.72 g (3.87 mmol, 94% of th.), colorless powder.
<b><sup>1</sup>H NMR:</b> (400 MHz, CDCl <sub>3</sub> )	δ = 7.72–7.66 (m, 8H), 7.51–7.39 (m, 12H), 2.53–2.46 (m, 4H), 2.07–1.93 (m, 2H) ppm.
<b><sup>31</sup>P{<sup>1</sup>H} NMR:</b> (162 MHz, CDCl <sub>3</sub> )	δ = 32.85(s) ppm.
<b>Elemental analysis:</b>	found (calcd.): C 70.10% (72.97%), H 5.91% (5.90%), N 0% (0%).
<b>IR:</b> (solid, ATR)	$\tilde{\nu}$ = 3054vw, 1662vw, 1590w, 1484w, 1436s, 1405w, 1348w, 1311w, 1245w, 1173vs, 1119vs, 1102s, 1070m, 1027m, 997m, 970w, 932w, 853w, 827m, 736m, 716vs, 692vs, 669vs cm <sup>-1</sup> .

**dppf(O)<sub>2</sub>**

<b>Empirical formula:</b>	C <sub>34</sub> H <sub>28</sub> FeO <sub>2</sub> P <sub>2</sub> (586.39 g mol <sup>-1</sup> ).
<b>Yield:</b>	2.02 g (3.44 mmol, 67% of th.), beige powder.
<b><sup>1</sup>H NMR:</b> (400 MHz, CDCl <sub>3</sub> )	δ = 7.61–7.34 (m, 20H), 4.70 (q, 4H), 4.24 (q, 4H) ppm.
<b><sup>31</sup>P{<sup>1</sup>H} NMR:</b> (162 MHz, CDCl <sub>3</sub> )	δ = 28.61(s) ppm.
<b>Elemental analysis:</b>	found (calcd.): C 69.29% (69.64%), H 4.82% (4.81%) N 0% (0%).
<b>IR:</b> (solid, ATR)	$\tilde{\nu}$ = 3095vw, 1589vw, 1483w, 1435m, 1419w, 1389w, 1370w, 1316w, 1209m, 1189vs, 1179vs, 1167s, 1117m, 1098m, 1075m, 1058w, 1028m, 997w, 869w, 829s, 757s, 722s, 695vs cm <sup>-1</sup> .

5.4.2 H<sub>2</sub>Bn<sub>2</sub>edda

According to modified procedure of S. Ménage *et al.*, *J. Am. Chem. Soc.* **1998**, *120*, 13370–13382.

**Starting materials:**

Bromoacetic acid, sodium bicarbonate, *N,N'*-dibenzylethylenediamine, sodium hydroxide, conc. hydrochloric acid, water.

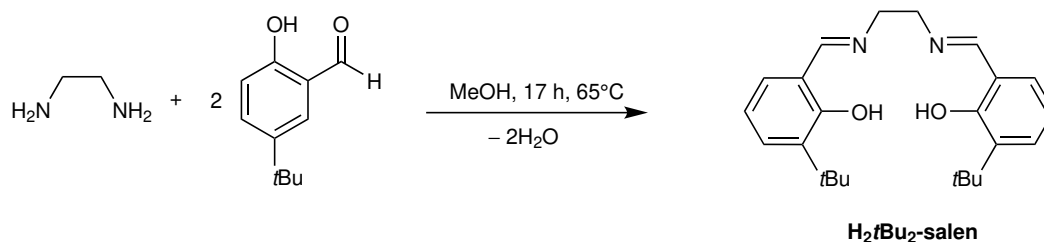
**Procedure:**

The experiment was performed without using Schlenk techniques.

A stirred solution of bromoacetic acid (2.79 g, 20.0 mmol, 2.0 equiv.) in water (6 mL) was cooled down to 0°C followed by portionwise addition of sodium bicarbonate (1.68 g, 20.0 mmol, 2.0 equiv.). *N,N'*-dibenzylethylenediamine (3.60 g, 10.0 mmol, 1.0 equiv.) was dissolved in water (70 mL) and a sodium hydroxide solution (30-wt%, 3 mL) was added subsequently. The two mixtures were merged and stirred under refluxing conditions for 4 h at 60°C. During this time period, the pH-value was checked and, if needed, adjusted to a value between 10 and 11 with the previously mentioned sodium hydroxide solution. The mixture was cooled down to room temperature, acidified with conc. hydrochloric acid to pH-value of 2. The resulting colorless precipitate was filtered off and dried *in vacuo*. For further purification, the crude product was recrystallized from ethanol/water (1:1) yielding a colorless powder.

<b>Empirical formula:</b>	$C_{20}H_{24}N_2O_4$ (356.42 g mol <sup>-1</sup> ).
<b>Yield:</b>	2.79 g (6.53 mmol, 65% of th.), colorless powder.
<b><sup>1</sup>H NMR:</b> (400 MHz, D <sub>2</sub> O)	$\delta = 7.31\text{--}7.17$ (m, 12H), 3.55 (s, 4H), 2.97 (s, 4H), 2.58 (s, 4H) ppm.
<b><sup>13</sup>C{<sup>1</sup>H} NMR:</b> (101 MHz, D <sub>2</sub> O)	$\delta = 178.86$ (s), 137.27 (s), 130.47 (s), 128.47 (s), 128.43 (s), 127.48 (s), 57.58 (s), 57.40 (s), 50.12 (s) ppm.
<b>Elemental analysis:</b>	found (calcd.): C 56.27% (56.30%), H 7.42% (7.51%) N 6.58% (6.57%). (calcd. for $C_{20}H_{24}N_2O_4 \cdot 3.9H_2O$ )
<b>IR:</b> (solid, ATR)	$\tilde{\nu} = 3392w, 2323w, 1739w, 1615vs, 1507m, 1494m, 1461s, 1446m, 1378vs, 1342m, 1322s, 1237s, 1215m, 1070m, 1030m, 972m, 912vs, 862w, 838m, 797m, 745vs, 696vs, 661m$ cm <sup>-1</sup> .

### 5.4.3 H<sub>2</sub>tBu<sub>2</sub>salen



According to T. J. Boyle *et al.*, *Inorg. Chem.* **2018**, *57*, 2402–2415.

#### Starting materials:

3-*tert*-Butylsalicylaldehyde, ethylenediamine, methanol.

#### Procedure:

The experiment was performed without using Schlenk techniques.

3-*tert*-Butylsalicylaldehyde (1.78 g, 10.0 mmol, 2.0 eq) was dissolved in methanol (50 mL). Ethylenediamine (0.30 g, 0.33 mL, 5 mmol, 1.0 eq) was mixed with methanol (50 mL) and added to the first solution. The mixture was stirred for 17 h under refluxing conditions before the precipitating yellow powder was filtered off and dried *in vacuo*.

**Empirical formula:** C<sub>32</sub>H<sub>48</sub>N<sub>2</sub>O<sub>2</sub> (380.53 g mol<sup>-1</sup>).

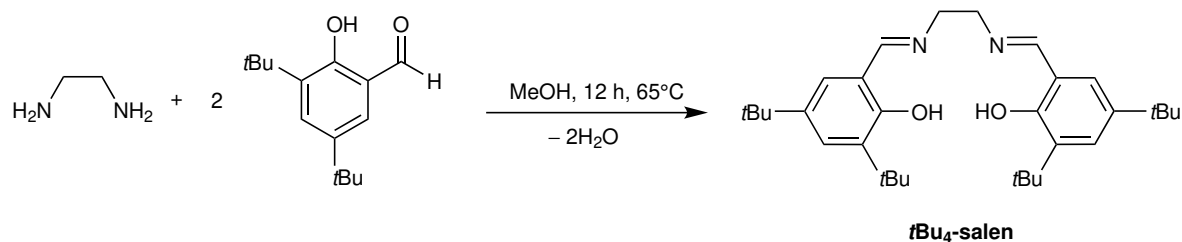
**Yield:** 1.53 g (4.02 mmol, 80% of th.), yellow powder.

**<sup>1</sup>H NMR:** δ = 13.86 (s, 2H), 8.40 (s, 2H), 7.34 (d, 2H), 7.12 (d, 2H), 6.83 (t, 2H), 3.94 (s, 4H), 1.46 (s, 18H) ppm.

**<sup>13</sup>C{<sup>1</sup>H} NMR:** δ = 167.34 (s), 160.50 (s), 137.50 (s), 129.94 (s), 129.64 (s), 118.70 (s), 118.00 (s), 59.67 (s), 34.95 (s), 29.47 (s) ppm.

**Elemental analysis:** found (calcd.): C 75.71% (75.75%), H 8.45% (8.48%) N 7.34% (7.36%).

**IR:** (solid, ATR)  $\tilde{\nu}$  = 2961m, 2865w, 1630vs, 1605s, 1584m, 1496w, 1459s, 1438vs, 1390m, 1359m, 1308m, 1289m, 1268s, 1203s, 1142vs, 1088m, 1037vs, 978m, 845vs, 791m, 746vs, 685m cm<sup>-1</sup>.

5.4.4 H<sub>2</sub>tBu<sub>4</sub>salen


According to T. J. Boyle *et al.*, *Inorg. Chem.* **2018**, *57*, 2402–2415.

**Starting materials:**

3,5-Di-*tert*-butylsalicylaldehyde, ethylenediamine, methanol.

**Procedure:**

The experiment was performed without using Schlenk techniques.

3,5-Di-*tert*-butylsalicylaldehyde (3.75 g, 16.0 mmol, 2.0 eq) was dissolved in methanol (100 mL). Ethylenediamine (0.48 g, 0.53 mL, 8 mmol, 1.0 eq) was mixed with methanol (50 mL) and added to the first solution. The mixture was stirred for 12 h under refluxing conditions before the precipitating yellow powder was filtered off, washed with diethyl ether and dried *in vacuo*.

**Empirical formula:**

C<sub>32</sub>H<sub>48</sub>N<sub>2</sub>O<sub>2</sub> (492.75 g mol<sup>-1</sup>).

**Yield:**

3.34 g (6.78 mmol, 85% of th.), yellow powder.

**<sup>1</sup>H NMR:**

(400 MHz, CDCl<sub>3</sub>)

δ = 13.64 (s, 2H), 8.39 (s, 2H), 7.37 (d, 2H), 7.07 (d, 2H), 3.92 (s, 4H), 1.44 (s, 18H), 1.29 (s, 18H) ppm.

**<sup>13</sup>C{<sup>1</sup>H} NMR:**

(101 MHz, CDCl<sub>3</sub>)

δ = 167.78 (s), 140.21 (s), 136.75 (s), 127.17 (s), 126.20 (s), 117.97 (s), 59.76 (s), 35.17 (s), 34.26 (s), 31.62 (s), 29.58 (s) ppm.

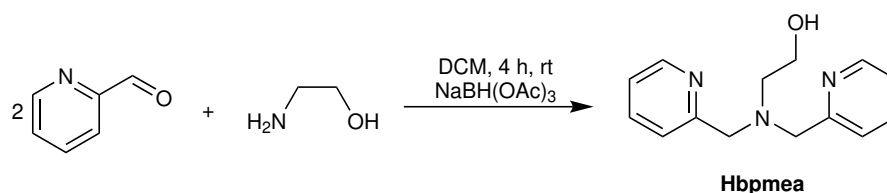
**Elemental analysis:**

found (calcd.): C 78.20% (78.00%), H 9.98% (9.82%)  
N 5.66% (5.69%).

**IR:** (solid, ATR)

$\tilde{\nu}$  = 2995w, 2955m, 2910w, 2868m, 1626vs, 1592m, 1481s, 1465s, 1438s, 1392m, 1361s, 1320w, 1293m, 1269s, 1253s, 1234s, 1212s, 1201s, 1173s, 1132w, 1040s, 973m, 931w, 911vw, 879s, 838s, 830s, 810m, 797m, 773s, 730m, 710m, 662vw cm<sup>-1</sup>.

## 5.4.5 Hbpmea



According to E. C. M. Ording-Wenker *et al.*, *Dalton Trans.* **2015**, *44*, 12196–12209.

**Starting materials:**

Ethanolamine, pyridine-2-carboxaldehyde, sodium triacetoxyborohydride, dichloromethane, sodium bicarbonate, water, sodium sulfate.

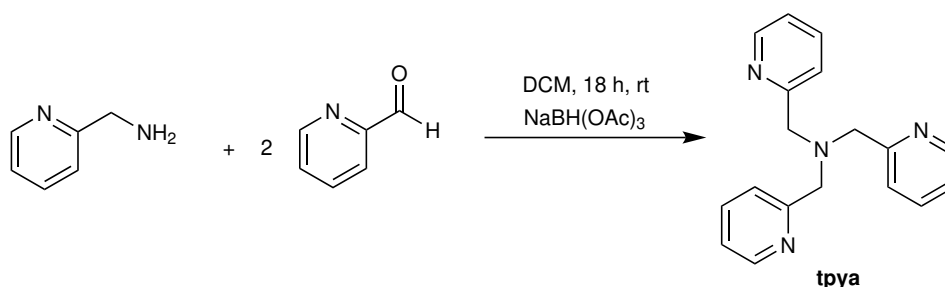
**Procedure:**

The experiment was performed without using Schlenk techniques.

Ethanolamine (0.60 mL, 10.0 mmol, 1.0 equiv.) and pyridine-2-carboxaldehyde (1.90 mL, 20.0 mmol, 2.0 eq) were dissolved in dichloromethane (30 mL) and stirred subsequently. Sodium triacetoxyborohydride (6.09 g, 28.3 mmol, 2.8 equiv.) was added to the solution over a period of 15 min. The solution was stirred for 4 h at room temperature followed by addition of a saturated solution of sodium bicarbonate in water (40 mL). The aqueous phase was extracted two times with dichloromethane (20 mL). The organic phases were fused and dried over sodium sulfate. After the solvent was removed *in vacuo*, the product was obtained as brown oil.

<b>Empirical formula:</b>	C <sub>14</sub> H <sub>17</sub> N <sub>3</sub> O (243.31 g mol <sup>-1</sup> ).
<b>Yield:</b>	2.18 g (8.25 mmol, 83% of th.), brown oil.
<b><sup>1</sup>H NMR:</b> (400 MHz, CDCl <sub>3</sub> )	δ = 8.47 (d, 2H), 7.53 (t <sub>d</sub> , 2H), 7.28 (d, 2H), 7.07 (m, 2H), 5.49 (s, 1H), 3.86 (s, 4H), 3.63 (t, 2H), 2.80 (t, 2H) ppm.
<b><sup>13</sup>C{<sup>1</sup>H} NMR:</b> (101 MHz, CDCl <sub>3</sub> )	δ = 159.32 (s), 149.90 (s), 136.54 (s), 123.07 (s), 122.06 (s), 60.05 (s), 59.71 (s), 56.82 (s) ppm.
<b>Elemental analysis:</b>	found (calcd.): C 64.34% (64.70%), H 6.23% (6.67%), N 15.72% (15.88%). (calcd. for <b>Hbpmea</b> + 0.25DCM)
<b>IR:</b> (solid, ATR)	$\tilde{\nu}$ = 3250vw, 3059vw, 3009vw, 2831w, 1670w, 1590vs, 1569s, 1473s, 1433vs, 1363m, 1305m, 1247m, 1148m, 1047vs, 995s, 893w, 873w, 837w, 809w, 757vs, 708m, 693m cm <sup>-1</sup> .

## 5.4.6 tpya



According to G. J. P. Britovsek *et al.*, *Inorg. Chem.* **2005**, *44*, 8125–8134.

**Starting materials:**

2-(Aminomethyl)pyridine, pyridine-2-carboxylaldehyde, sodium triacetoxyborohydride, sodium bicarbonate, dichloromethane, ethyl acetate, magnesium sulfate.

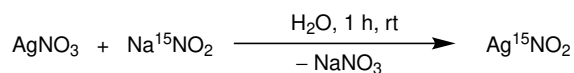
**Procedure:**

The experiment was performed without using Schlenk techniques.

2-(Aminomethyl)pyridine (0.51 mL, 4.95 mmol, 1.0 equiv.) and sodium triacetoxyborohydride (3.12 g, 14.7 mmol, 3.0 equiv.) were suspended in dichloromethane (75 mL). Pyridine-2-carboxylaldehyde (1.0 mL, 10.5 mmol, 2.1 equiv.) was added and the reaction mixture was stirred at room temperature for 18 h.

A saturated solution of sodium bicarbonate in water (150 mL) was added and after another 15 min of stirring, the mixture was extracted with ethyl acetate (3 × 100 mL). The organic phases were merged and dried over magnesium sulfate, followed by the complete evaporation of the solvent under reduced pressure. The residue was washed with *n*-hexane (10 mL) and dried *in vacuo*. For further purification the oily liquid was recrystallized from ethyl acetate. The beige microcrystalline powder was filtered off and dried *in vacuo*.

<b>Empirical formula:</b>	$C_{18}H_{18}N_4$ (290.37 g mol <sup>-1</sup> ).
<b>Yield:</b>	2.47 g (8.50 mmol, 86% of th.), beige powder.
<b><sup>1</sup>H NMR:</b> (400 MHz, CDCl <sub>3</sub> )	$\delta = 8.63$ (d <sub>q</sub> , 3H), 7.80 (t <sub>d</sub> , 3H), 7.71 (d, 3H), 7.32 (t <sub>d</sub> , 3H), 4.59 (s, 6H) ppm.
<b><sup>13</sup>C{<sup>1</sup>H} NMR:</b> (101 MHz, CDCl <sub>3</sub> )	$\delta = 153.39$ (s), 148.22 (s), 138.75 (s), 124.94 (s), 123.81 (s), 57.81 (s) ppm.
<b>Elemental analysis:</b>	found (calcd.): C 41.94% (41.85%), H 3.58% (3.51%), N 10.73% (10.85%).
<b>IR:</b> (solid, ATR)	$\tilde{\nu} = 3015$ vw, 2924vw, 2816vw, 1588m, 1567m, 1473m, 1434m, 1366m, 1311w, 1240w, 1219w, 1154w, 1123w, 1087w, 1046w, 996w, 977m, 959w, 898w, 884w, 838vw, 761vs, 747s, 659vw cm <sup>-1</sup> .

5.4.7 Ag<sup>15</sup>NO<sub>2</sub>

According to S. Kundu *et al.*, *J. Am. Chem. Soc.* **2017**, *139*, 1045–1048.

**Starting materials:**

Silver nitrate, sodium nitrite (<sup>15</sup>N), water.

**Procedure:**

The experiment was performed without using Schlenk techniques.

Silver nitrate (1.70 g, 10.0 mmol, 1.0 equiv.) was dissolved in water (8 mL) and added slowly to an aqueous solution (4 mL) of Na<sup>15</sup>NO<sub>2</sub> (700 mg, 10 mmol, 1 equiv.). The mixture was stirred in the dark for 1 h before the yellow precipitate was filtered off, washed with water (100 mL) and methanol (50 mL) and dried *in vacuo*. The product was obtained as light-sensitive, yellow powder.

**Empirical formula:** AgNO<sub>2</sub> (154.88 g mol<sup>-1</sup>).

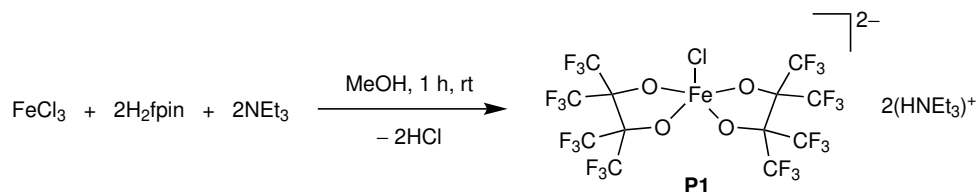
**Yield:** 1.01 g (6.49 mmol, 65% of th.), yellow powder.

**Elemental analysis:** found (calcd.): C 0% (0%), H 0% (0%), N 8.87% (9.69%).

**IR:** (solid, ATR)  $\tilde{\nu} = 1334\text{m}, 1158\text{vs}, 840\text{vs cm}^{-1}$ .

## 5.5 Synthesis of the halogenidoiron(III) precursor compounds

### 5.5.1 $(\text{HNEt}_3)_2[\text{FeCl}(\text{fpin})_2]$ (P1)



#### Starting materials:

Iron(III) chloride,  $\text{H}_2\text{fpin}$ , triethylamine, methanol.

#### Procedure:

Iron(III) chloride (32.4 mg, 0.20 mmol, 1.0 equiv.) was dissolved in methanol (3 mL).  $\text{H}_2\text{fpin}$  (70.0  $\mu\text{L}$ , 134 mg, 0.40 mmol, 2.0 equiv.) and triethylamine (56.0  $\mu\text{L}$ , 0.40 mmol, 2.0 equiv.) were added successively. The mixture was stirred for 1 h at room temperature followed by narrowing the yellow solution until the formation of small crystals was observed. The saturated solution was stored at 5°C for 24 h resulting the growth of big yellow crystals.

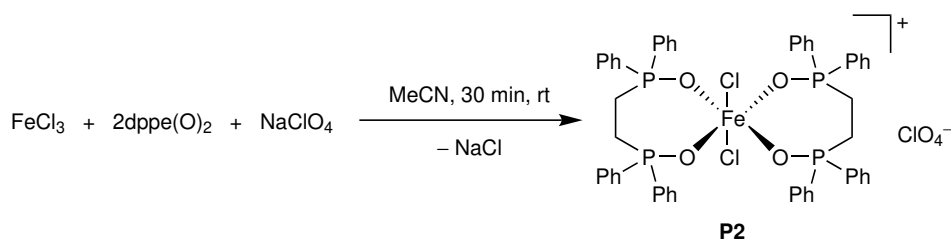
**Empirical formula:**  $\text{C}_{24}\text{H}_{32}\text{ClF}_{24}\text{FeN}_2\text{O}_4$  (959.79 g mol<sup>-1</sup>).

**Yield:** 49.7 mg (0.052 mmol, 26% of th.), yellow crystals.

**Elemental analysis:** found (calcd.): C 28.97% (30.03%), H 3.36% (3.36%), N 3.07% (2.92%).

**IR:** (solid, ATR)  $\tilde{\nu} = 3003\text{vw}, 2950\text{vw}, 2732\text{vw}, 1481\text{m}, 1393\text{w}, 1366\text{w}, 1224\text{vs}, 1202\text{vs}, 1181\text{s}, 1146\text{s}, 1125\text{m}, 1105\text{m}, 1060\text{w}, 1015\text{m}, 989\text{w}, 929\text{s}, 867\text{vs}, 843\text{m}, 813\text{m}, 781\text{m}, 759\text{m}, 741\text{s}, 731\text{m}, 712\text{s}, 677\text{m cm}^{-1}$ .

**UV-Vis:** (solution, MeOH)  $\lambda_{\text{max}} = 248, 332 \text{ nm}$ .

5.5.2  $[\text{FeCl}_2(\text{dppe}(\text{O})_2)_2](\text{ClO}_4)$  (P2)

**Starting materials:**

Iron(III) chloride,  $\text{dppe}(\text{O})_2$ , sodium perchlorate, acetonitrile.

**Procedure:**

Iron(III) chloride (16.2 mg, 0.10 mmol, 1.0 equiv.) and  $\text{dppe}(\text{O})_2$  (86.0 mg, 0.20 mmol, 2.0 equiv.) were dissolved in acetonitrile (10 mL) resulting a yellow solution. Sodium perchlorate (12.2 mg, 0.10 mmol, 1.0 equiv.) was added and the mixture was stirred for 30 min at room temperature before the precipitating sodium chloride was removed by filtration. The product was obtained as yellow powder by evaporating the solvent *in vacuo*.

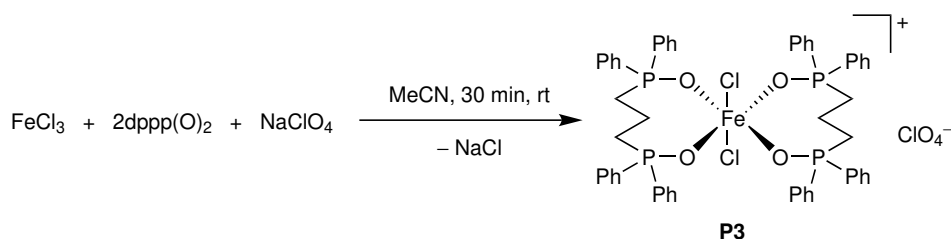
**Empirical formula:**  $\text{C}_{52}\text{H}_{48}\text{Cl}_3\text{FeO}_8\text{P}_4$  (1085.07 g mol<sup>-1</sup>).

**Yield:** quantitative, yellow powder.

**Elemental analysis:** found (calcd.): C 53.64% (57.46%), H 4.17% (4.45%), N 0% (0%).

**IR:** (solid, ATR)  $\tilde{\nu} = 3033\text{vw}, 2360\text{vw}, 1890\text{vw}, 1738\text{w}, 1589\text{w}, 1484\text{vs}, 1437\text{s}, 1336\text{w}, 1320\text{w}, 1283\text{w}, 1205\text{m}, 1165\text{s}, 1129\text{vs}, 1081\text{s}, 1072\text{s}, 1028\text{m}, 924\text{w}, 857\text{w}, 812\text{w}, 750\text{m}, 735\text{vs}, 724\text{s}, 691\text{s}, 673\text{m cm}^{-1}$ .

**UV-Vis:**(solution, MeCN)  $\lambda_{\text{max}} = 310, 361 \text{ nm}$ .

5.5.3 [FeCl<sub>2</sub>(dppp(O)<sub>2</sub>)<sub>2</sub>](ClO<sub>4</sub>) (P3)

**Starting materials:**

Iron(III) chloride, dppp(O)<sub>2</sub>, sodium perchlorate, acetonitrile.

**Procedure:**

Iron(III) chloride (16.2 mg, 0.10 mmol, 1.0 equiv.) and dppp(O)<sub>2</sub> (88.9 mg, 0.20 mmol, 2.0 equiv.) were dissolved in acetonitrile (10 mL) resulting a yellow solution. Sodium perchlorate (12.2 mg, 0.10 mmol, 1.0 equiv.) was added and the mixture was stirred for 30 min at room temperature before precipitating sodium chloride was removed by filtration. The product was obtained as yellow powder by evaporating the solvent *in vacuo*.

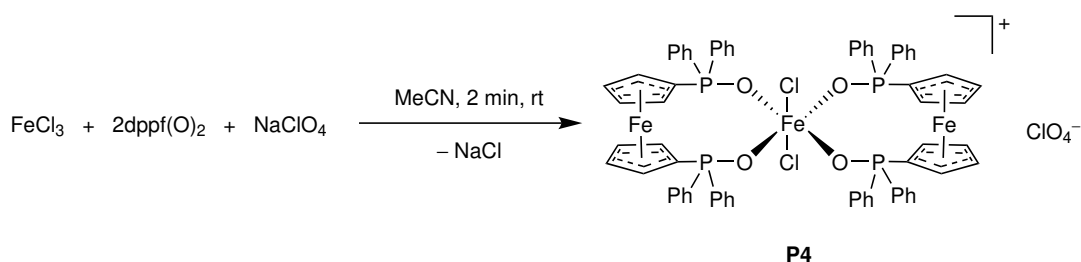
**Empirical formula:** C<sub>54</sub>H<sub>52</sub>Cl<sub>3</sub>FeO<sub>8</sub>P<sub>4</sub> (1115.09 g mol<sup>-1</sup>).

**Yield:** quantitative, yellow powder.

**Elemental analysis:** found (calcd.): C 49.66% (58.17%), H 4.45% (4.70%), N 0% (0%).

**IR:** (solid, ATR)  $\tilde{\nu}$  = 3052w, 2360w, 2318w, 2120w, 2075w, 1828w, 1647w, 1588w, 1485s, 1437s, 1401w, 1337w, 1316w, 1249w, 1180s, 1090vs, 1064vs, 1026s, 997m, 956m, 854w, 815m, 785m, 720s, 694s, 665m cm<sup>-1</sup>.

**UV-Vis:** (solution, MeCN)  $\lambda_{max}$  = 293, 358 nm.

5.5.4 [FeCl<sub>2</sub>(dppf(O)<sub>2</sub>)<sub>2</sub>](ClO<sub>4</sub>) (P4)

**Starting materials:**

Iron(III) chloride, dppf(O)<sub>2</sub>, sodium perchlorate, acetonitrile.

**Procedure:**

Iron(III) chloride (16.2 mg, 0.10 mmol, 1.0 equiv.), dppf(O)<sub>2</sub> (117 mg, 0.20 mmol, 2.0 equiv.) and sodium perchlorate (12.2 mg, 0.10 mmol, 1.0 equiv.) were dissolved in acetonitrile (10 mL) resulting in a green solution which turned dark brown after a few seconds. Immediately after the color change, the precipitating sodium chloride was removed by filtration. The product was obtained as gold-brown crystals by storing at room temperature for a few minutes.

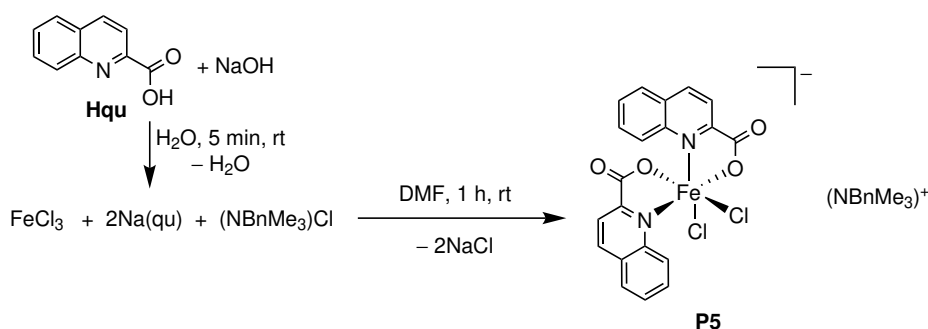
**Empirical formula:** C<sub>68</sub>H<sub>56</sub>Cl<sub>3</sub>Fe<sub>3</sub>O<sub>8</sub>P<sub>4</sub> (1398.97 g mol<sup>-1</sup>).

**Yield:** 18.3 mg (0.013 mmol, 13% of th.), gold-brown crystals.

**Elemental analysis:** found (calcd.): C 56.04% (58.38%), H 3.72% (4.03%), N 0% (0%).

**IR:** (solid, ATR)  $\tilde{\nu}$  = 3613w, 3054w, 2120vw, 1589m, 1483m, 1436s, 1190s, 1146vs, 1089vs, 1028m, 826m, 752m, 725vs, 691vs cm<sup>-1</sup>.

**UV-Vis:** (solution, MeCN)  $\lambda_{max}$  = 357, 459 nm.

5.5.5 (NBnMe<sub>3</sub>)[FeCl<sub>2</sub>(qu)<sub>2</sub>] (P5)

**Starting materials:**

Iron(III) chloride, quinaldic acid, sodium hydroxide, benzyltrimethylammonium chloride, dimethylformamide, acetonitrile.

**Procedure:**

The experiment was performed without using Schlenk techniques.

Quinaldic acid (346 mg, 2.00 mmol, 2.0 equiv.) was dissolved in a 2M aqueous sodium hydroxide solution (2 mL). The solution was stirred for 5 min followed by the complete removal of the solvent under reduced pressure. The colorless solid was suspended with iron(III) chloride (162 mg, 1.00 mmol, 1.0 equiv.) and benzyltrimethylammonium chloride (186 mg, 1.00 mmol, 1.0 equiv.) in dimethylformamide (5 mL). The mixture was stirred for 1 h at room temperature before the solvent was removed *in vacuo*. The resulting yellow solid was dissolved in acetonitrile (100 mL) and the insoluble sodium chloride was removed by filtration. Removing the solvent using the rotary evaporator yielded in the growth of big yellow crystals.

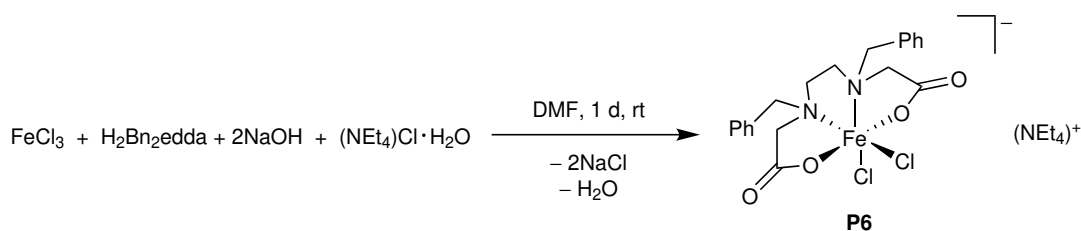
**Empirical formula:** C<sub>30</sub>H<sub>28</sub>Cl<sub>2</sub>FeN<sub>3</sub>O<sub>4</sub> (621.32 g mol<sup>-1</sup>).

**Yield:** 428 mg (0.69 mmol, 69% of th.), yellow crystals.

**Elemental analysis:** found (calcd.): C 57.94% (57.99%), H 4.54% (4.54%), N 6.72% (6.76%).

**IR:** (solid, ATR)  $\tilde{\nu}$  = 3023w, 2922w, 1665vs, 1592m, 1567m, 1508m, 1489m, 1474m, 1457s, 1434m, 1418w, 1374m, 1323vs, 1256m, 1215w, 1168s, 1147s, 1114w, 1026w, 976w, 961w, 926m, 897m, 851m, 807s, 795s, 775s, 722s, 698s cm<sup>-1</sup>.

**UV-Vis:** (solution, MeCN)  $\lambda_{max}$  = 299, 330, 337 nm.

5.5.6 (NEt<sub>4</sub>)[Fe(Bn<sub>2</sub>edda)Cl<sub>2</sub>] (P6)

**Starting materials:**

Iron(III) chloride, H<sub>2</sub>Bn<sub>2</sub>edda, sodium hydroxide, tetraethylammonium chloride monohydrate, dimethylformamide, acetonitrile, diethyl ether.

**Procedure:**

H<sub>2</sub>Bn<sub>2</sub>edda (712 mg, 2.00 mmol, 1.0 equiv.), sodium hydroxide (160 mg, 4.00 mmol, 2.0 equiv.) and tetraethylammonium chloride monohydrate (367 mg, 2.00 mmol, 1.0 equiv.) were dissolved in dimethylformamide (10 mL). Iron(III) chloride (324 mg, 2.00 mmol, 1.0 equiv.) was added and the mixture was stirred for 1 d at room temperature. The colorless precipitate was filtered off and the solvent was removed *in vacuo*. The crude product was obtained as yellow powder. For further purification, the substance was dissolved in acetonitrile and layered with diethyl ether yielding pale yellow crystals.

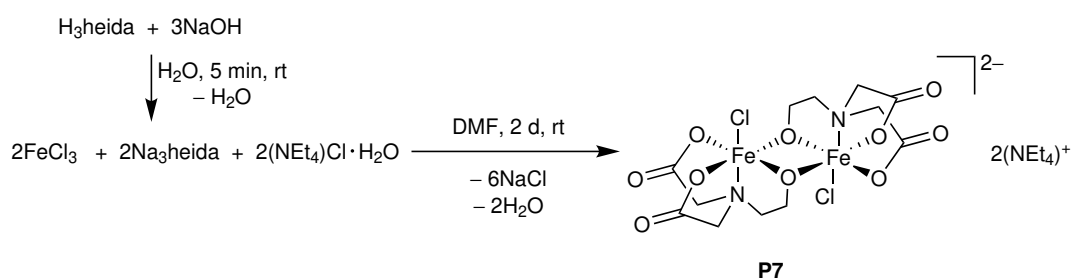
**Empirical formula:** C<sub>28</sub>H<sub>42</sub>Cl<sub>2</sub>FeN<sub>3</sub>O<sub>4</sub> (611.41 g mol<sup>-1</sup>).

**Yield:** 887 mg (1.45 mmol, 73% of th.), yellow powder.

**Elemental analysis:** found (calcd.): C 54.61% (55.01%), H 6.90% (6.92%), N 6.91% (6.87%).

**IR:** (solid, ATR)  $\tilde{\nu} = 2981\text{w}, 2930\text{w}, 1744\text{w}, 1647\text{vs}, 1487\text{m}, 1463\text{m}, 1453\text{m}, 1424\text{w}, 1391\text{m}, 1333\text{m}, 1300\text{s}, 1265\text{w}, 1204\text{w}, 1173\text{m}, 1076\text{m}, 1065\text{m}, 1030\text{w}, 1004\text{m}, 983\text{w}, 971\text{m}, 936\text{w}, 911\text{s}, 844\text{m}, 804\text{w}, 784\text{m}, 754\text{s}, 723\text{m}, 704\text{vs}, 659\text{vw cm}^{-1}$ .

**UV-Vis:** (solution, MeCN)  $\lambda_{\text{max}} = 250, 291, 365 \text{ nm}$ .

5.5.7  $(\text{NEt}_4)_2[\text{Fe}_2\text{Cl}_2(\mu\text{-heida})_2] \cdot 2\text{MeCN}$  (P7 · 2MeCN)

**Starting materials:**

Iron(III) chloride, sodium hydroxide, H<sub>3</sub>heida, water, tetraethylammonium chloride monohydrate, dimethylformamide, acetonitrile.

**Procedure:**

H<sub>3</sub>heida (177 mg, 1.00 mmol, 1.0 equiv.) was dissolved with sodium hydroxide (120 mg, 3.00 mmol, 3.0 equiv.) in water (5 mL). The solution was stirred for 5 min followed by the *in vacuo* removal of the solvent. The colorless solid was suspended with iron(III) chloride (162 mg, 1.00 mmol, 1.0 equiv.) and tetraethylammonium chloride monohydrate (662 mg, 4.00 mmol, 2.0 equiv.) in dimethylformamide (5 mL). The mixture was stirred for 2 d at room temperature before the colorless precipitate was removed by filtration. Diethyl ether was added to the filtrate to obtain a viscous greenish oil which was redissolved in acetonitrile (10 mL). Upon adding diethyl ether, the product precipitated as yellow powder. The substance was washed with diethyl ether and dried *in vacuo*. Recrystallization from acetonitrile/diethyl ether yielded yellow crystals.

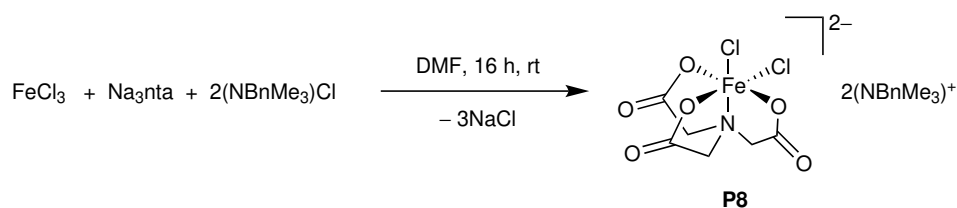
**Empirical formula:** C<sub>32</sub>H<sub>62</sub>Cl<sub>2</sub>Fe<sub>2</sub>N<sub>6</sub>O<sub>10</sub> (873.48 g mol<sup>-1</sup>).

**Yield:** 383 mg (0.44 mmol, 44% of th.), yellow crystals.

**Elemental analysis:** found (calcd.): 43.65% (43.29%), H 7.08% (7.14%), N 8.05% (8.41%).

**IR:** (solid, ATR)  $\tilde{\nu} = 3422\text{m}, 3364\text{m}, 3252\text{m}, 2986\text{m}, 2950\text{m}, 2359\text{w}, 2131\text{vw}, 1633\text{vs}, 1461\text{s}, 1400\text{m}, 1358\text{m}, 1315\text{m}, 1249\text{vw}, 1104\text{w}, 1077\text{m}, 1031\text{s}, 1005\text{s}, 910\text{m}, 834\text{w}, 801\text{s}, 725\text{w}, 664\text{m cm}^{-1}$ .

**UV-Vis:** (solution, MeCN)  $\lambda_{\text{max}} = 345 \text{ nm}$ .

5.5.8 (NBnMe<sub>3</sub>)<sub>2</sub>[FeCl<sub>2</sub>(nta)] (P8)


According to a modified procedure of M. A. Walters *et al.*, *Inorg. Chim. Acta.* **2006**, *359*, 3996–4000.

**Starting materials:**

Iron(III) chloride, trisodium nitrilotriacetic acid, benzyltrimethylammonium chloride, dimethylformamide.

**Procedure:**

The experiment was performed without using Schlenk techniques.

Iron(III) chloride (324 mg, 2.00 mmol, 1.0 equiv.), trisodium nitrilotriacetic acid (514 mg, 2.00 mmol, 1.0 equiv.) and benzyltrimethylammonium chloride (743 mg, 4.00 mmol, 2.0 equiv.) were dissolved in dimethylformamide (6 mL). The mixture was stirred for 16 h at room temperature and the colorless precipitate was removed by filtration. The product was obtained as green-yellow crystals by adding ethyl acetate to the filtrate.

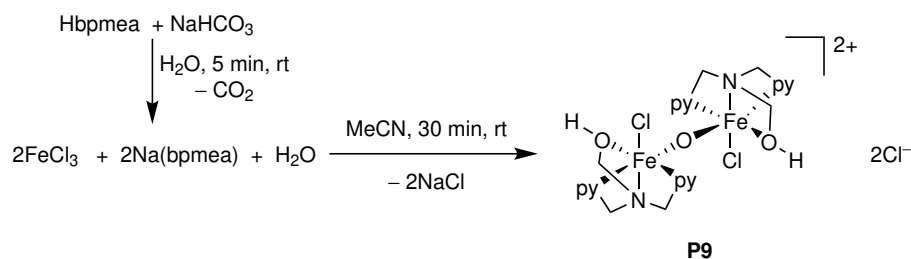
**Empirical formula:** C<sub>26</sub>H<sub>38</sub>Cl<sub>2</sub>FeN<sub>3</sub>O<sub>6</sub> (615.35 g mol<sup>-1</sup>).

**Yield:** 776 mg (1.26 mmol, 63% of th.), green-yellow crystals.

**Elemental analysis:** found (calcd.): C 50.62% (50.75%), H 6.18% (6.22%), N 6.83% (6.83%).

**IR:** (solid, ATR)  $\tilde{\nu} = 3377\text{m}, 3027\text{m}, 2359\text{m}, 2329\text{m}, 1662\text{s}, 1624\text{vs}, 1480\text{m}, 1455\text{m}, 1373\text{s}, 1333\text{m}, 1260\text{w}, 1219\text{m}, 1114\text{w}, 976\text{m}, 906\text{m}, 896\text{m}, 787\text{m}, 729\text{s}, 658\text{m cm}^{-1}$ .

**UV-Vis:** (solution, MeCN)  $\lambda_{\text{max}} = 284 \text{ nm}$ .

5.5.9  $[\text{Fe}_2\text{Cl}_2(\text{Hbpmea})_2(\mu\text{-O})]\text{Cl}_2 \cdot 2\text{MeCN}$  (**P9** · 2MeCN)

**Starting materials:**

Iron(III) chloride, Hbpmea, sodium bicarbonate, water, acetonitrile.

**Procedure:**

Hbpmea (24.3 mg, 0.10 mmol, 1.0 equiv.) and sodium bicarbonate (8.00 mg, 0.10 mmol, 1.0 equiv.) were dissolved in water (2 mL) and stirred for 5 min. The solvent was removed *in vacuo* yielding a colorless powder. A solution of iron(III) chloride (16.2 mg, 0.10 mmol, 1.0 equiv.) in acetonitrile (5 mL) was added and the mixture was stirred for 30 min at room temperature. The colorless precipitate was filtered off yielding an orange solution. **P9** was obtained as big red crystals by concentrating the solution *in vacuo* and storing it for 2 d at 5°C.

**Empirical formula:**  $\text{C}_{32}\text{H}_{40}\text{Cl}_4\text{Fe}_2\text{N}_8\text{O}_3$  (838.23 g mol<sup>-1</sup>)

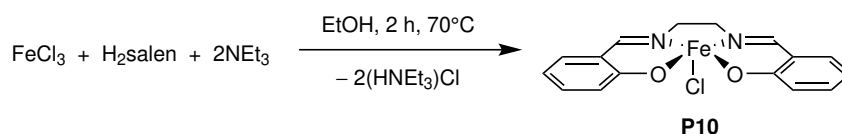
**Yield:** quantitative, red crystals.

**Elemental analysis:** found (calcd.): C 44.27% (44.92%), H 4.67% (4.62%), N 12.44% (11.84%). (calcd. for **P9** · 1.4MeCN)

**IR:** (solid, ATR)  $\tilde{\nu} = 3682\text{vw}, 3377\text{w}, 3284\text{vw}, 2918\text{m}, 2850\text{m}, 2736\text{w}, 2603\text{w}, 2529\text{w}, 2247\text{vw}, 1764\text{vw}, 1605\text{s}, 1572\text{m}, 1480\text{m}, 1444\text{s}, 1351\text{w}, 1323\text{w}, 1291\text{s}, 1150\text{w}, 1024\text{s}, 833\text{s}, 798\text{s}, 763\text{s}, 691\text{w cm}^{-1}$ .

**UV-Vis:** (solution, MeCN)  $\lambda_{\text{max}} = 342, 432 \text{ nm}$ .

## 5.5.10 [FeCl(salen)] (P10)



According to a modified procedure of T. Matsushita *et al.*, *Bull. Chem. Soc. Jpn.* **1982**, *55*, 2581–2587.

**Starting materials:**

Iron(III) chloride, H<sub>2</sub>salen, triethylamine, ethanol.

**Procedure:**

Iron(III) chloride (0.81 g, 5.00 mmol, 1.0 equiv.) and H<sub>2</sub>salen (1.34 g, 5.00 mmol, 1.0 equiv.) were dissolved in ethanol (100 mL). Triethylamine (1.40 mL, 1.01 g, 10.0 mmol, 2.0 eq) was added slowly and the mixture was stirred under refluxing conditions for 2 h at 70°C. Storing the dark purple solution for 2 d at –25°C resulted in a purple precipitate which was filtered off, washed with diethyl ether and dried *in vacuo*. The product was obtained as deep-purple powder.

**Empirical formula:**

C<sub>16</sub>H<sub>14</sub>ClFeN<sub>2</sub>O<sub>2</sub> (357.60 g mol<sup>-1</sup>, ).

**Yield:**

1.43 g (4.00 mmol, 80% of th.), dark purple powder.

**Elemental analysis:**

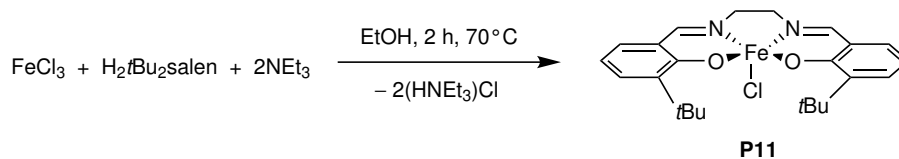
found (calcd.): C 53.73% (53.74%), H 3.87% (3.95%), N 7.82% (7.83%).

**IR:** (solid, ATR)

$\tilde{\nu}$  = 3054vw, 2931vw, 2900vw, 2104vw, 1690m, 1643vs, 1628s, 1596s, 1559m, 1544s, 1473m, 1465m, 1443vs, 1384m, 1326m, 1302m, 1268m, 1244m, 1227w, 1211w, 1195m, 1144m, 1124m, 1088m, 1046m, 1032w, 983m, 970m, 954m, 903m, 889w, 865w, 850w, 795m, 755vs, 669vw, 658vw cm<sup>-1</sup>.

**UV-Vis:** (solution, MeCN)

$\lambda_{max}$  = 301, 310, 468 nm.

5.5.11 [FeCl(*t*Bu<sub>2</sub>salen)] (P11)


According to R. Duan *et al.*, *Macromolecules* **2017**, *50*, 9188–9195.

**Starting materials:**

Iron(III) chloride hexahydrate, H<sub>2</sub>*t*Bu<sub>2</sub>salen, triethylamine, ethanol.

**Procedure:**

Iron(III) chloride (162 mg, 1.00 mmol, 1.0 equiv.) and H<sub>2</sub>*t*Bu<sub>2</sub>salen (381 mg, 1.00 mmol, 1.0 equiv.) were dissolved in ethanol (50 mL). Triethylamine (0.28 mL, 2.00 mmol, 2.0 eq) was added slowly and the mixture was stirred under refluxing conditions for 2 h at 70°C. Storing the dark brown solution for 1 d at –25°C resulted in a black precipitate which was filtered off dried *in vacuo*.

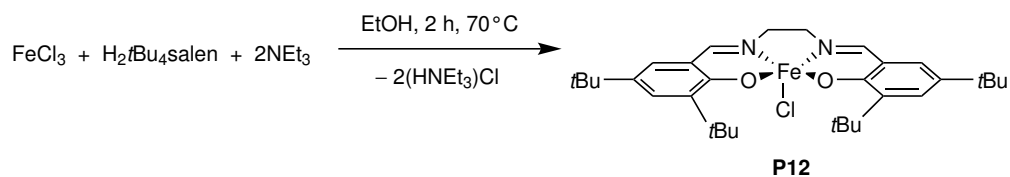
**Empirical formula:** C<sub>24</sub>H<sub>30</sub>ClFeN<sub>2</sub>O<sub>2</sub> (469.81 g mol<sup>-1</sup>, ).

**Yield:** 395 mg (0.84 mmol, 84% of th.), black solid.

**Elemental analysis:** found : C 59.04(59.01%), H 7.66% (7.81%), N 7.18% (7.06%). (calcd. for **11** · 1.2HNEt<sub>3</sub>Cl).

**IR:** (solid, ATR)  $\tilde{\nu}$  = 2952m, 2915m, 1631vs, 1609vs, 1590vs, 1545vs, 1467w, 1438m, 1412m, 1389vs, 1357m, 1332m, 1320m, 1297vs, 1263m, 1231m, 1196s, 1146s, 1089m, 1047s, 984m, 962m, 934m, 869vs, 810m, 780vw, 767vs, 746vs, 689s, 669w cm<sup>-1</sup>.

**UV-Vis:** (solution, MeCN)  $\lambda_{max}$  = 217, 235, 300, 327, 482 nm.

5.5.12 [FeCl(*t*Bu<sub>4</sub>salen)] (P12)


According to R. Duan *et al.*, *Macromolecules* **2017**, *50*, 9188–9195.

**Starting materials:**

Iron(III) chloride hexahydrate, H<sub>2</sub>*t*Bu<sub>4</sub>salen, triethylamine, ethanol.

**Procedure:**

Iron(III) chloride (0.81 g, 5.00 mmol, 1.0 equiv.) and H<sub>2</sub>*t*Bu<sub>4</sub>salen (2.46 g, 5.00 mmol, 1.0 equiv.) were dissolved in ethanol (100 mL). Triethylamine (1.4 mL, 1.01 g, 10.0 mmol, 2.0 eq) was added slowly and the mixture was stirred under refluxing conditions for 2 h at 70°C. Storing the dark brown solution for 1 d at –25°C resulted in a brown precipitate which was filtered off, washed with diethyl ether and dried *in vacuo*. The product was obtained as dark brown powder.

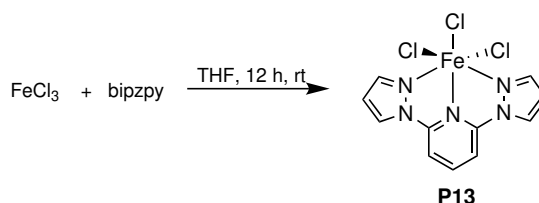
**Empirical formula:** C<sub>32</sub>H<sub>46</sub>ClFeN<sub>2</sub>O<sub>2</sub> (582.03 g mol<sup>-1</sup>, ).

**Yield:** 2.42 g (4.15 mmol, 83% of th.), dark brown solid.

**Elemental analysis:** found (calcd.): 65.99% (66.04%), H 8.10% (7.94%), N 4.90% (4.81%).

**IR:** (solid, ATR)  $\tilde{\nu} = 2999\text{wv}, 2952\text{m}, 2904\text{wv}, 2867\text{wv}, 1630\text{s}, 1608\text{vs}, 1535\text{s}, 1460\text{m}, 1438\text{m}, 1411\text{m}, 1385\text{s}, 1362\text{m}, 1331\text{m}, 1316\text{m}, 1302\text{s}, 1270\text{s}, 1253\text{s}, 1199\text{m}, 1173\text{s}, 1136\text{vw}, 1096\text{vw}, 1045\text{w}, 1024\text{wv}, 974\text{w}, 929\text{w}, 913\text{w}, 888\text{m}, 875\text{w}, 859\text{w}, 838\text{s}, 811\text{m}, 778\text{m}, 750\text{m}, 692\text{vw}, 677\text{vw}, 663\text{vw}, 655\text{vw cm}^{-1}$ .

**UV-Vis:** (solution, MeCN)  $\lambda_{\text{max}} = 221, 244, 273, 502 \text{ nm}$ .

5.5.13 [Fe(bipzpy)Cl<sub>3</sub>] (P13)


According to D. Gong *et al.*, *J. Organomet. Chem.* **2012**, *702*, 10–18.

**Starting materials:**

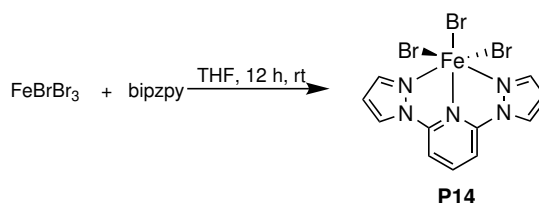
Iron(III) chloride, 2,6-bis(*N*-pyrazolyl)pyridine (bipzpy), tetrahydrofuran.

**Procedure:**

The experiment was performed without using Schlenk techniques.

Iron(III) chloride (81.1 mg, 0.50 mmol, 1.0 equiv.) was dissolved in tetrahydrofuran (10 mL). Then bipzpy (106 mg, 0.50 mmol, 1.0 equiv.) was added slowly and the deep orange solution was stirred for 12 h at room temperature. After addition of diethyl ether, the product precipitated as orange powder, which was washed three times with *n*-hexane (10 mL) and dried *in vacuo*. Recrystallization from acetonitrile/diethyl ether yielded big orange crystals.

<b>Empirical formula:</b>	C <sub>11</sub> H <sub>9</sub> Cl <sub>3</sub> FeN <sub>5</sub> (373.42 g mol <sup>-1</sup> ).
<b>Yield:</b>	302 mg (0.40 mmol, 81% of th.), orange powder.
<b>Elemental analysis:</b>	found (calcd.): C 35.02% (35.38%), H 2.55% (2.43%), N 18.37% (18.75%).
<b>IR:</b> (solid, ATR)	$\tilde{\nu}$ = 3818w, 3133m, 3119m, 3095m, 2113m, 1789w, 1615vs, 1582s, 1528vs, 1494m, 1476vs, 1392vs, 1343vs, 1312s, 1174s, 1062vs, 974vs, 798s, 774vs cm <sup>-1</sup> .
<b>UV-Vis:</b> (solution, MeCN)	$\lambda_{max}$ = 304, 359 nm.

5.5.14 [Fe(bipzpy)Br<sub>3</sub>] (P14)


According to D. Gong *et al.*, *J. Organomet. Chem.* **2012**, *702*, 10–18.

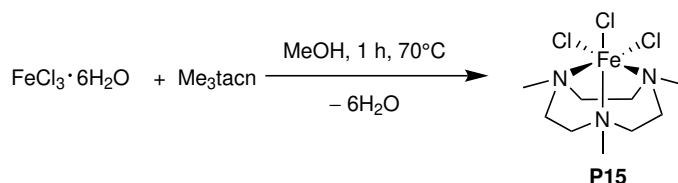
**Starting materials:**

Iron(III) bromide, 2,6-bis(*N*-pyrazolyl)pyridine (bipzpy), tetrahydrofuran.

**Procedure:**

Iron(III) bromide (296 mg, 1.00 mmol, 1.0 equiv.) was dissolved in tetrahydrofuran (20 mL). Then bipzpy (211 mg, 1.00 mmol, 1.0 equiv.) was added slowly and the deep red solution was stirred for 12 h at room temperature. After addition of diethyl ether (50 mL) the product precipitated as dark brown powder, which was washed three times with *n*-hexane (10 mL) and dried *in vacuo*. Big red crystals were obtained by layering a solution of the product in acetonitrile with diethyl ether and letting the solvents slowly evaporate.

<b>Empirical formula:</b>	C <sub>11</sub> H <sub>9</sub> Br <sub>3</sub> FeN <sub>5</sub> (506.79 g mol <sup>-1</sup> ).
<b>Yield:</b>	258 mg (0.51 mmol, 51% of th.), brown powder.
<b>Elemental analysis:</b>	found (calcd.): C 24.71% (24.63%), H 1.62% (1.69%), N 12.74% (13.06%). (calcd. for <b>P14</b> · 0.1FeBr <sub>3</sub> )
<b>IR:</b> (solid, ATR)	$\tilde{\nu}$ = 3106m, 3064m, 3050m, 1619vs, 1589m, 1521s, 1497m, 1480vs, 1397vs, 1346s, 1320s, 1297vw, 1246vw, 1216s, 1178m, 1152w, 1135w, 1077w, 1062vs, 1024m, 976s, 921vw, 912w, 890vw, 862vw, 801s, 771vs, 731w, 675m cm <sup>-1</sup> .
<b>UV-Vis:</b> (solution, MeCN)	$\lambda_{max}$ = 222, 238, 244, 270, 304, 390, 468 nm.

5.5.15 [FeCl<sub>3</sub>(Me<sub>3</sub>tacn)] (P15)


According to P. Chaudhuri *et al.*, *Inorg. Chem.* **1988**, *27*, 1564–1569.

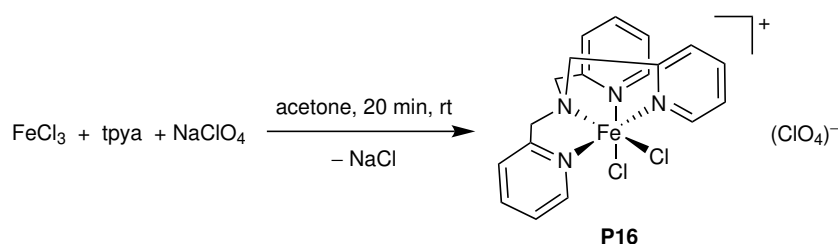
**Starting materials:**

Iron(III) chloride hexahydrate, Me<sub>3</sub>tacn, methanol.

**Procedure:**

Iron(III) chloride hexahydrate (135 mg, 0.50 mmol, 1.0 equiv.) was dissolved in methanol (2 mL) and Me<sub>3</sub>tacn (85.6 mg, 97.0 μL, 0.50 mmol, 1.0 equiv.) was added. The brown suspension was stirred for 1 h at 70°C under refluxing conditions. The supernatant was removed using a syringe, the bright yellow powder was washed with ice cold methanol and was dried *in vacuo*. Crystals of the product were obtained by dissolving the powder in methanol and allow the solvent to evaporate under atmospheric conditions.

<b>Empirical formula:</b>	C <sub>9</sub> H <sub>21</sub> N <sub>3</sub> FeCl <sub>3</sub> (333.48 g mol <sup>-1</sup> ).
<b>Yield:</b>	145.7 mg (0.44 mmol, 88% of th.), yellow powder.
<b>Elemental analysis:</b>	found (calcd.): C 32.26% (32.42%), H 6.10% (6.35%), N 12.38% (12.60%).
<b>IR:</b> (solid, ATR)	$\tilde{\nu} = 3732\text{vw}, 3014\text{w}, 2986\text{w}, 2927\text{m}, 2865\text{m}, 2819\text{w},$ $2159\text{vw}, 1736\text{w}, 1454\text{s}, 1295\text{m}, 1260\text{w}, 1153\text{w}, 1122\text{vw},$ $1061\text{s}, 1000\text{vs}, 893\text{w}, 821\text{vw}, 785\text{m cm}^{-1}.$
<b>UV-Vis:</b> (solution, MeCN)	$\lambda_{\text{max}} = 302, 392 \text{ nm}.$

5.5.16  $[\text{FeCl}_2(\text{tpya})](\text{ClO}_4)$  (P16)

**Starting materials:**

Iron(III) chloride, tpya, sodium perchlorate, acetone.

**Procedure:**

Tpya (29.0 mg, 0.10 mmol, 1.0 equiv.) was added to a solution of iron(III) chloride (16.2 mg, 0.10 mmol, 1.0 equiv.) in acetone (5 mL). Sodium perchlorate (12.2 mg, 0.10 mmol, 1.0 equiv.) was added to the yellow solution and sodium chloride precipitated after a few minutes. The mixture was stirred for 20 min at room temperature before the precipitate was filtered off and the solvent was removed *in vacuo*. For further purification, the yellow powder was dissolved in dichloromethane (5 mL) and layered with toluene (5 mL). The product was obtained as yellow crystals.

**Empirical formula:**  $\text{C}_{18}\text{H}_{18}\text{Cl}_3\text{FeN}_4\text{O}_4$  (516.56 g mol<sup>-1</sup>).

**Yield:** quantitative, yellow crystals.

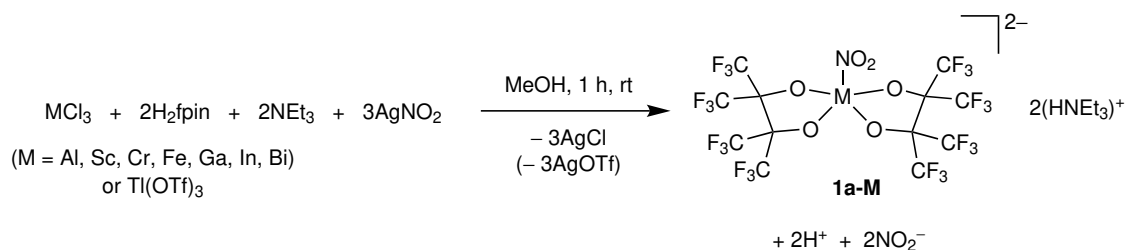
**Elemental analysis:** found (calcd.): C 41.94% (41.85%), H 3.58% (3.51%), N 10.73% (10.85%).

**IR:** (solid, ATR)  $\tilde{\nu} = 1604\text{w}, 1569\text{vw}, 1483\text{vw}, 1436\text{w}, 1319\text{vw}, 1293\text{w}, 1272\text{vw}, 1157\text{vw}, 1080\text{vs}, 1051\text{s}, 1024\text{m}, 999\text{w}, 973\text{w}, 943\text{w}, 914\text{w}, 895\text{w}, 818\text{w}, 780\text{s}, 760\text{s}, 722\text{w cm}^{-1}$ .

**UV-Vis:** (solution, MeCN)  $\lambda_{max} = 280, 374 \text{ nm}$ .

## 5.6 Synthesis of nitrito complexes with O-donor co-ligands

### 5.6.1 $(\text{HNEt}_3)_2[\text{M}(\text{fpin})_2(\text{NO}_2)]$ ( $\text{M} = \text{Al}, \text{Sc}, \text{Cr}, \text{Fe}, \text{Ga}, \text{In}, \text{Tl}, \text{Bi}$ ) (**1a-M**)



#### Starting materials:

$\text{MCl}_3$  ( $\text{M} = \text{Al}, \text{Sc}, \text{Cr}, \text{Fe}, \text{Ga}, \text{In}, \text{Bi}$ ) or thallium triflate,  $\text{H}_2\text{fpin}$ , triethylamine, silver nitrite, methanol.

#### Procedure:

The respective metal salt (0.10 mmol, 1.0 equiv.) was dissolved in methanol (5 mL). Then,  $\text{H}_2\text{fpin}$  (35.0  $\mu\text{L}$ , 66.8 mg, 0.20 mmol, 2.0 equiv.), triethylamine (28.0  $\mu\text{L}$ , 0.2 mmol, 2.0 equiv.) and silver nitrite (46.2 mg, 0.30 mmol, 3.0 equiv.) were added successively. The mixture was stirred for 1 h at room temperature followed by filtration of the precipitating silver chloride. The product was obtained by narrowing the solution and storing it for a week at 5°C. The mother liquid was removed and the obtained crystals were dried *in vacuo*. Used salts, their amounts and crystallization times are given in the table below. Alternatively, **1a-Fe** can be synthesized directly by dissolving **P1** (96.0 mg, 0.1 mmol, 1.0 equiv.) in methanol (5 mL) and adding silver nitrite (15.4 mg, 0.10 mmol, 1.0 equiv.) under vigorous stirring. Further steps are analogue to the previously described procedure.

batch	salt	m/mg
<b>1a-Al</b>	$\text{AlCl}_3$	13.3
<b>1a-Sc</b>	$\text{ScCl}_3 \cdot x\text{H}_2\text{O}$	16.9
<b>1a-Cr</b>	$\text{CrCl}_3 \cdot 6\text{H}_2\text{O}$	26.6
<b>1a-Fe</b>	$\text{FeCl}_3$	16.2
<b>1a-Ga</b>	$\text{GaCl}_3$	17.6
<b>1a-In</b>	$\text{InCl}_3$	22.1
<b>1a-Tl</b>	$\text{Tl}(\text{tfa})_3$	54.3
<b>1a-Bi</b>	$\text{BiCl}_3$	31.5

### 1a-Al

<b>Empirical formula:</b>	$C_{24}H_{32}F_{24}AlN_3O_6$ (941.48 g mol <sup>-1</sup> ).
<b>Yield:</b>	75.3 mg (0.080 mmol, 80% of th.), colorless crystals.
<b>Elemental analysis:</b>	found (calcd.): C 30.52% (30.62%), H 3.14% (3.43%), N 4.41% (4.46%).
<b>IR:</b> (solid, ATR)	$\tilde{\nu} = 3054vw, 2999vw, 2755vw, 1510m, 1483m, 1465w, 1426w, 1394w, 1268m, 1231vs, 1205vs, 1184vs, 1158vs, 1138vs, 1112s, 1073w, 1013s, 991m, 935s, 871s, 854m, 813w, 768m, 752m, 737m, 714s, 687m\text{ cm}^{-1}$ .
<b>UV-Vis:</b> (solution, MeOH)	$\lambda_{max} = 279\text{ nm}$ .

### 1a-Sc

<b>Empirical formula:</b>	$C_{24}H_{32}F_{24}ScN_3O_6$ (959.45 g mol <sup>-1</sup> ).
<b>Yield:</b>	25.0 mg, colorless crystals.
<b>Elemental analysis:</b>	found (calcd.): C 30.09% (30.04%), H 3.43% (3.36%), N 4.34% (4.38%).
<b>IR:</b> (solid, ATR)	$\tilde{\nu} = 2991vw, 1481w, 1396w, 1260m, 1232sh, 1229s, 1203vs, 1180vs, 1147v, 1115m, 1074wv, 1024m, 989w, 929s, 868s, 857m, 842w, 782w, 757w, 740s, 730m, 714s, 677w\text{ cm}^{-1}$ .
<b>UV-Vis:</b> (solution, MeOH)	$\lambda_{max} = 349\text{ nm}$ .

### 1a-Cr

<b>Empirical formula:</b>	$C_{24}H_{32}F_{24}CrN_3O_6$ (966.49 g mol <sup>-1</sup> ).
<b>Yield:</b>	few green crystals.
<b>Elemental analysis:</b>	found (calcd.): C 30.37% (29.83%), H 3.45% (3.34%), N 3.69% (4.35%).
<b>IR:</b> (solid, ATR)	$\tilde{\nu} = 2998vw, 2360vw, 1477w, 1402w, 1355w, 1260m, 1228s, 1207s, 1176vs, 1162w, 1146s, 1115s, 1088s, 1066m, 1039w, 1013w, 985w, 949m, 926m, 868s, 837m, 811vw, 793vw, 755w, 737s, 728m, 714m, 705m\text{ cm}^{-1}$ .
<b>UV-Vis:</b> (solution, MeOH)	$\lambda_{max} = 342, 585\text{ nm}$ .

**1a-Fe**

<b>Empirical formula:</b>	$C_{24}H_{32}F_{24}FeN_3O_6$ (970.27 g mol <sup>-1</sup> ).
<b>Yield:</b>	61.1 mg (0.063 mmol, 63% of th.), pale yellow crystals.
<b>Elemental analysis:</b>	found (calcd.): C 29.81% (29.71%), H 3.18% (3.32%), N 3.94% (4.33%).
<b>IR:</b> (solid, ATR)	$\tilde{\nu} = 3062vw, 2929vw, 2752vw, 1587vw, 1482m, 1438m, 1395m, 1272sh, 1263s, 1227vs, 1204vs, 1181vs, 1161sh, 1138vs, 1108vs, 1029vs, 997m, 930s, 868s, 843w, 814w, 796w, 758m, 742s, 713vs, 690s$ cm <sup>-1</sup> .
<b>UV-Vis:</b> (solution, MeOH)	$\lambda_{max} = 243, 326$ nm.
<b>UV-Vis:</b> (solid, KBr)	$\lambda_{max} = 325$ nm.

**1a-Ga**

<b>Empirical formula:</b>	$C_{24}H_{32}F_{24}GaN_3O_6$ (984.22 g mol <sup>-1</sup> ).
<b>Yield:</b>	74.8 mg (0.076 mmol, 76% of th.), colorless crystals.
<b>Elemental analysis:</b>	found (calcd.): C 29.01% (29.29%), H 3.02% (3.28%), N 4.36% (4.27%).
<b>IR:</b> (solid, ATR)	$\tilde{\nu} = 3049vw, 2999vw, 2755vw, 1519m, 1482m, 1465w, 1394w, 1263m, 1231vs, 1205vs, 1181vs, 1157s, 1133vs, 1108vs, 1075w, 1009s, 990s, 937vs, 869vs, 841s, 813vw, 781vw, 760m, 743s, 731w, 713s, 692w, 680w, 654w$ cm <sup>-1</sup> .
<b>UV-Vis:</b> (solution, MeOH)	$\lambda_{max} =$ no absorptions.

**1a-In**

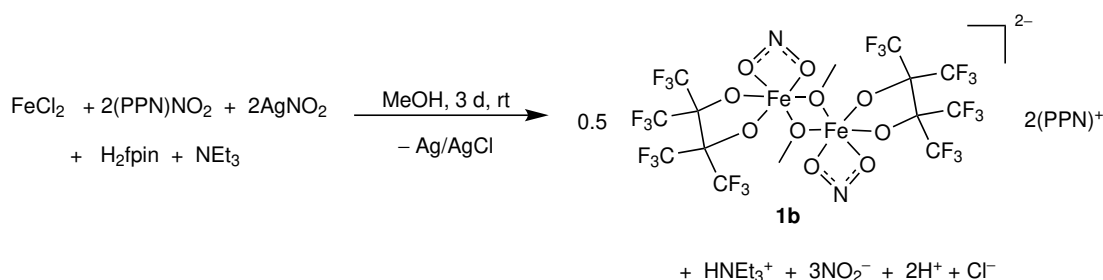
<b>Empirical formula:</b>	$C_{24}H_{32}F_{24}InN_3O_6$ (1029.31 g mol <sup>-1</sup> ).
<b>Yield:</b>	91.6 mg (0.089 mmol, 89% of th.), colorless crystals.
<b>Elemental analysis:</b>	found (calcd.): C 27.75% (28.01%), H 3.08% (3.13%), N 4.05% (4.08%).
<b>IR:</b> (solid, ATR)	$\tilde{\nu} = 3039vw, 2991vw, 2750vw, 1482w, 1465w, 1395w, 1259m, 1227vs, 1201s, 1175s, 1150vs, 1139vs, 1126s, 1104s, 1075w, 1060w, 1014m, 987m, 933s, 890w, 866s, 843m, 813w, 783w, 757m, 740m, 730m, 712s, 676vw, 657vw$ cm <sup>-1</sup> .
<b>UV-Vis:</b> (solution, MeOH)	$\lambda_{max} = 288$ nm.

**1a-Tl**

<b>Empirical formula:</b>	$C_{24}H_{32}F_{24}TlN_3O_6$ (1118.88 g mol <sup>-1</sup> ).
<b>Yield:</b>	36.9 mg (0.033 mmol, 33% of th.), colorless crystals.
<b>Elemental analysis:</b>	found (calcd.): C 25.21% (25.76%), H 3.07% (2.88%), N 3.56% (3.76%).
<b>IR:</b> (solid, ATR)	$\tilde{\nu} = 3033vw, 2918vw, 2753vw, 1670m, 1486m, 1465m, 1450m, 1434m, 1395m, 1253s, 1225vs, 1209vs, 1180vs, 1147vs, 1134vs, 1098vs, 1035w, 1013m, 985m, 938s, 865vs, 846s, 818vw, 794vw, 757m, 740s, 730m, 712vs, 665m\text{ cm}^{-1}$ .
<b>UV-Vis:</b> (solution, MeOH)	$\lambda_{max} = 260\text{ nm}$ .

**1a-Bi**

<b>Empirical formula:</b>	$C_{24}H_{32}F_{24}BiN_3O_6$ (1123.48 g mol <sup>-1</sup> ).
<b>Yield:</b>	55 mg (0.049 mmol, 49% of th.), yellowish crystals.
<b>Elemental analysis:</b>	found (calcd.): C 25.26% (25.66%), H 3.03% (2.87%), N 4.36% (3.74%).
<b>IR:</b> (solid, ATR)	$\tilde{\nu} = 3006vw, 2736vw, 2508vw, 1476m, 1426w, 1394m, 1254s, 1217vs, 1201vs, 1182vs, 1160vs, 1132vs, 1105vs, 1018m, 986m, 966w, 931s, 866s, 842m, 813m, 782w, 757m, 739s, 730m, 712s, 667m\text{ cm}^{-1}$ .
<b>UV-Vis:</b> (solution, MeOH)	$\lambda_{max} = 357\text{ nm}$ .

5.6.2 (PPN)<sub>2</sub>[Fe<sub>2</sub>(fpin)<sub>2</sub>(NO<sub>2</sub>-κ<sup>2</sup>O,O')<sub>2</sub>(μ-OCH<sub>3</sub>)<sub>2</sub>] (1b)

**Starting materials:**

Iron(II) chloride, silver nitrite, (PPN)NO<sub>2</sub>, H<sub>2</sub>fpin, triethylamine, methanol.

**Procedure:**

Iron(II) chloride (15.8 mg, 0.13 mmol, 1.0 equiv.), silver nitrite (38.5 mg, 0.25 mmol, 2.0 equiv.) and (PPN)NO<sub>2</sub> (146 mg, 0.25 mmol, 2.0 equiv.) were stirred in methanol (10 mL) at -20°C for 30 min. Then, H<sub>2</sub>fpin (44.0 μL, 0.25 mmol, 2.0 equiv.) and triethylamine (34.0 μL, 0.25 mmol, 2.0 equiv.) were added to the yellow suspension. The mixture was stirred for 3 d at room temperature whereby the solution changed its color from yellow, over brown to a pale orange while the precipitate turned dark gray. The solid was filtered off and the filtrate was narrowed under reduced pressure. After two days at 5°C pale orange crystals of **1b** were obtained. The mother liquid was removed by syringe, the crystals were washed three times with ice-cold methanol and dried *in vacuo*.

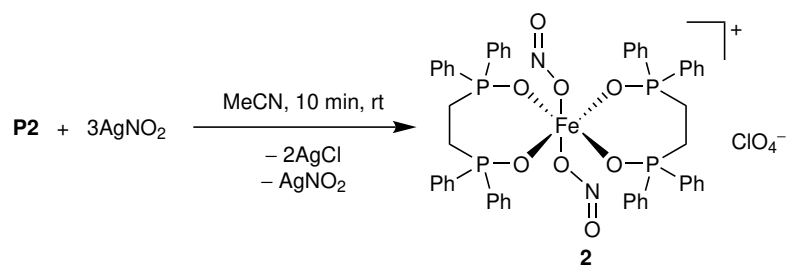
**Empirical formula:** C<sub>86</sub>H<sub>66</sub>F<sub>24</sub>Fe<sub>2</sub>N<sub>4</sub>O<sub>10</sub>P<sub>4</sub> (2007.0 g mol<sup>-1</sup>).

**Yield:** 34.3 mg (0.017 mmol, 26% of th.), pale orange crystals.

**Elemental analysis:** found (calcd.): C 54.65% (51.47%), H 3.50% (3.31%), N 2.45% (2.79%).

**IR:** (solid, ATR)  $\tilde{\nu} = 3060\text{w}, 1589\text{w}, 1483\text{m}, 1481\text{w}, 1438\text{m}, 1295\text{m}, 1282\text{m}, 1256\text{sh}, 1232\text{vs}, 1202\text{vs}, 1176\text{vs}, 1169\text{s}, 1145\text{s}, 1113\text{vs}, 1026\text{m}, 997\text{m}, 928\text{s}, 866\text{s}, 834\text{w}, 823\text{w}, 799\text{m}, 745\text{m}, 722\text{s}, 689\text{s cm}^{-1}$ .

**UV-Vis:** (solution, MeOH)  $\lambda_{\text{max}} = 225, 320 \text{ nm}$ .

5.6.3 [Fe(dppe(O)<sub>2</sub>)<sub>2</sub>(NO<sub>2</sub>-κO)<sub>2</sub>](ClO<sub>4</sub>) · MeCN (2 · MeCN)

**Starting materials:**

**P2**, silver nitrite, acetonitrile, methanol.

**Procedure:**

**P2** (109 mg, 0.10 mmol, 1.0 equiv.) was dissolved in a mixture of acetonitrile (16 mL) and methanol (2 mL) before a surplus of silver nitrite (46.2 mg, 0.30 mmol, 3.0 equiv.) was added. The mixture was stirred for 10 min at room temperature before the precipitating silver chloride and remaining silver nitrite were filtered off. The product was obtained as pale orange powder by complete evaporation of the solvent. In order to obtain crystals, the orange solution was narrowed under reduced pressure. At this, almost the whole product precipitated as pale orange powder. The suspension was stored at 5°C for two weeks. Few block-shaped, red crystals of **2** · MeCN were found between the powder.

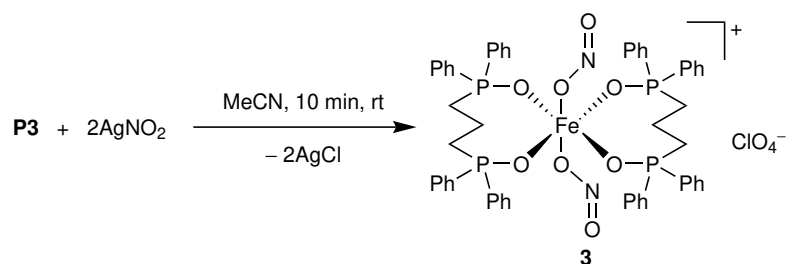
**Empirical formula:** C<sub>52</sub>H<sub>48</sub>ClFeN<sub>2</sub>O<sub>12</sub>P<sub>4</sub> (1108.15 g mol<sup>-1</sup>).

**Yield:** quantitative, orange powder and few red, block-shaped crystals.

**Elemental analysis:** found (calcd.): C 55.82% (56.36%), H 4.54% (4.37%), N 2.54% (2.53%).

**IR:** (solid, ATR)  $\tilde{\nu} = 2363\text{vw}, 1591\text{w}, 1560\text{m}, 1542\text{m}, 1472\text{m}, 1439\text{m}, 1404\text{w}, 1331\text{vw}, 1313\text{vw}, 1286\text{vw}, 1129\text{vs}, 1087\text{vs}, 1027\text{m}, 997\text{s}, 985\text{s}, 972\text{sh}, 929\text{w}, 858\text{vw}, 809\text{m}, 736\text{s}, 724\text{vs}, 689\text{vs}, 674\text{s cm}^{-1}$ .

**UV-Vis:** (solid, KBr)  $\lambda_{\text{max}} = 350, 450 \text{ nm}$ .

5.6.4 [Fe(dppp(O)<sub>2</sub>)<sub>2</sub>(NO<sub>2</sub>-κO)<sub>2</sub>](ClO<sub>4</sub>) · 2MeCN (3 · 2MeCN)

**Starting materials:**

**P3**, silver nitrite, acetonitrile.

**Procedure:**

**P3** (112 mg, 0.10 mmol, 1.0 equiv.) was dissolved in acetonitrile (10 mL) and silver nitrite (30.8 mg, 0.20 mmol, 2.0 equiv.) was added. The mixture was stirred for 20 min at room temperature. The precipitating silver chloride was filtered off. The product was obtained as orange powder by complete evaporation of the solvent. In order to obtain crystals, the orange solution was narrowed under reduced pressure. At this point, almost the whole product precipitated as powder. When stored at 5°C for several days, few red, block-shaped crystals of **3** · 2MeCN were found between the powder.

**Empirical formula:**

C<sub>52</sub>H<sub>48</sub>ClFeN<sub>2</sub>O<sub>12</sub>P<sub>4</sub> (1108.15 g mol<sup>-1</sup>).

**Yield:**

quantitative, orange powder and few red, block-shaped crystals.

**Elemental analysis:**

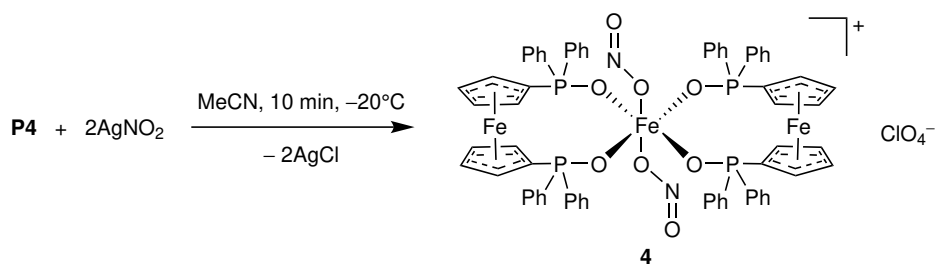
found (calcd.): C 55.88% (57.08%), H 4.58% (4.61%), N 3.51% (2.47%).

**IR:** (solid, ATR)

$\tilde{\nu} = 3058\text{vw}, 1590\text{w}, 1469\text{m}, 1438\text{m}, 1406\text{w}, 1353\text{vw}, 1302\text{w}, 1236\text{w}, 1182\text{m}, 1143\text{m}, 1121\text{vs}, 1088\text{vs}, 1068\text{vs}, 1027\text{m}, 995\text{s}, 981\text{sh}, 942\text{m}, 805\text{m}, 746\text{m}, 719\text{s}, 693\text{s}, 665\text{m cm}^{-1}$ .

**UV-Vis:** (solution, MeCN)

$\lambda_{\text{max}} = 259, 265, 272, 348 \text{ nm}$ .

5.6.5  $[\text{Fe}(\text{dppf}(\text{O})_2)_2(\text{NO}_2-\kappa\text{O})_2](\text{ClO}_4) \cdot 3\text{MeCN}$  ( $4 \cdot 3\text{MeCN}$ )

**Starting materials:**

**P4**, silver nitrite, acetonitrile.

**Procedure:**

**P4** (140 mg, 0.10 mmol, 1.0 equiv.) was dissolved in acetonitrile (10 mL) and the solution was cooled down to  $-20^\circ\text{C}$ . Silver nitrite (30.8 mg, 0.20 mmol, 2.0 equiv.) was added and the mixture was stirred for 10 min before the precipitating silver chloride was filtered off.  $4 \cdot 3\text{MeCN}$  was obtained as orange, diamond-shaped crystals by storing the reaction solution at  $-25^\circ\text{C}$  for a week.

**Empirical formula:**

$\text{C}_{70}\text{H}_{59}\text{ClFe}_3\text{N}_3\text{O}_{12}\text{P}_4$  ( $1461.13 \text{ g mol}^{-1}$ ).

**Yield:**

21.9 mg (0.015 mmol, 15% of th.), orange, diamond-shaped crystals.

**Elemental analysis:**

found (calcd.): C 56.62% (57.54%), H 3.76% (4.07%), N 3.27% (2.88%).

**IR:** (solid, ATR)

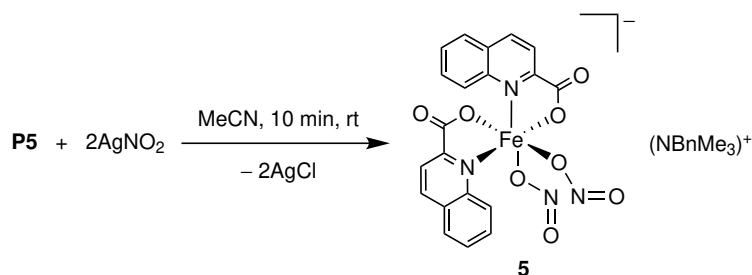
$\tilde{\nu} = 3087\text{vw}, 3055\text{vw}, 1590\text{w}, 1475\text{m}, 1460\text{m}, 1438\text{s}, 1388\text{w}, 1369\text{w}, 1356\text{w}, 1306\text{w}, 1188\text{m}, 1142\text{vs}, 1121\text{s}, 1089\text{vs}, 1027\text{s}, 1006\text{sh}, 996\text{s}, 900\text{w}, 880\text{w}, 852\text{w}, 818\text{m}, 748\text{m}, 728\text{s}, 703\text{s}, 690\text{s cm}^{-1}$ .

**UV-Vis:** (solution, MeCN)

$\lambda_{\text{max}} = 265, 272, 306, 435 \text{ nm}$ .

## 5.7 Synthesis of nitrito complexes with N,O-donor co-ligands

### 5.7.1 (NBnMe<sub>3</sub>)[Fe(NO<sub>2-κO</sub>)<sub>2</sub>(qu)<sub>2</sub>] · 2MeCN (5 · 2MeCN)



#### Starting materials:

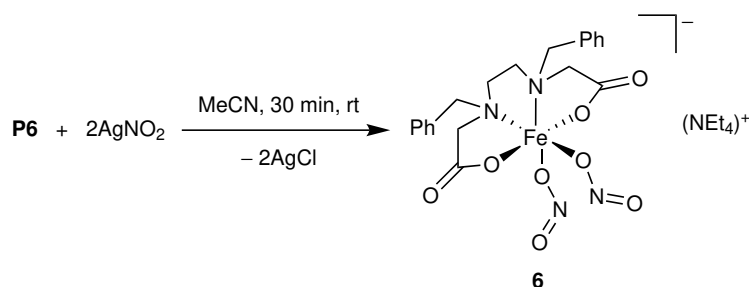
**P5**, silver nitrite, acetonitrile.

#### Procedure:

**P5** (62.1 mg, 0.10 mmol, 1.0 equiv.) was dissolved in acetonitrile (6 mL). Silver nitrite (30.8 mg, 0.20 mmol, 2.0 equiv.) was added and the mixture was stirred for 10 min at room temperature. The precipitating silver chloride was filtered off resulting in an orange solution which was narrowed under reduced pressure and stored at 5°C for crystallization. After a few hours, the mother liquor was decanted yielding few red-orange, very volatile, crystal platelets of **5** · 2MeCN.

**Empirical formula:** C<sub>34</sub>H<sub>34</sub>FeN<sub>7</sub>O<sub>8</sub> (724.18 g mol<sup>-1</sup>).

**Yield:** few red-orange, crystal platelets.

5.7.2 (NEt<sub>4</sub>)[Fe(Bn<sub>2</sub>edda)(NO<sub>2</sub>-κO)<sub>2</sub>] (6)

**Starting materials:**

**P6**, silver nitrite, acetonitrile.

**Procedure:**

**P6** (61.1 mg, 0.10 mmol, 1.0 equiv.) was dissolved in acetonitrile (6 mL). The opaque solution was filtered through a syringe filter to remove remaining sodium chloride from the synthesis. Afterwards, silver nitrite (30.8 mg, 0.20 mmol, 2.0 equiv.) was added under vigorous stirring. The mixture was stirred for 30 min at room temperature before the precipitating silver chloride was filtered off. The resulting orange solution was narrowed under reduced pressure and stored at 5°C for crystallization. After 4 d, the mother liquor was decanted and the remaining red-orange, rod-shaped crystals were washed with diethyl ether and dried *in vacuo*.

**Empirical formula:**

C<sub>28</sub>H<sub>42</sub>FeN<sub>5</sub>O<sub>8</sub> (632.52 g mol<sup>-1</sup>).

**Yield:**

34.3 mg (0.054 mmol, 54% of th.), red-orange, rod-shaped crystals.

**Elemental analysis:**

found (calcd.): C 52.21% (53.17%), H 7.03% (6.69%), N 10.82% (11.07%).

**IR:** (solid, ATR)

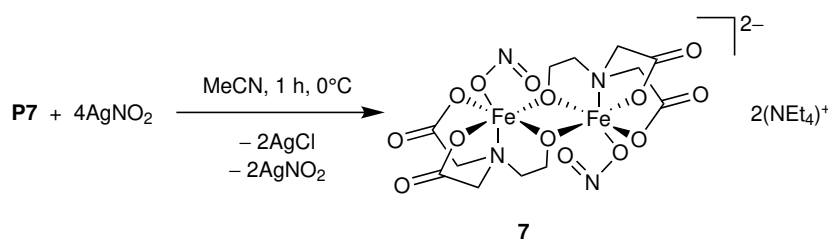
$\tilde{\nu}$  = 2981vw, 2931vw, 1654vs, 1577w, 1487m, 1462m, 1426w, 1394m, 1333s, 1298vs, 1282vs, 1225w, 1204w, 1173m, 1077w, 1064m, 1001s, 983vs, 968vs, 935m, 910s, 843m, 814sh, 799vs, 783vs, 755vs, 705vs, 669vw, 660vw cm<sup>-1</sup>.

**UV-Vis:** (solution, MeCN)

$\lambda_{max}$  = 276 nm.

**UV-Vis:** (solid, KBr)

$\lambda_{max}$  = 300, 350, 500 nm.

5.7.3  $(\text{NEt}_4)_2[\text{Fe}_2(\mu\text{-heida})_2(\text{NO}_2\text{-}\kappa\text{O})_2]$  (**7**)

**Starting materials:**

**P7**, silver nitrite, acetonitrile.

**Procedure:**

**P7** (79.1 mg, 0.10 mmol, 1.0 equiv.) was dissolved in acetonitrile (15 mL). A surplus of silver nitrite (61.6 mg, 0.40 mmol, 4.0 equiv.) was added and the mixture was stirred for 1 h at 0°C before the precipitating silver chloride and remaining silver nitrite were filtered off. The resulting greenish solution was carefully layered with diethyl ether. After one week, the supernatant was decanted yielding the product as green, block-shaped crystals which were dried *in vacuo*.

**Empirical formula:**

$\text{C}_{28}\text{H}_{56}\text{Fe}_2\text{N}_6\text{O}_{14}$  (812.47 g mol<sup>-1</sup>).

**Yield:**

60.0 mg (0.074 mmol, 74% of Th.), green, block-shaped crystals.

**Elemental analysis:**

found (calcd.): C 41.27% (41.39%), H 6.95% (6.95%), N 10.34% (10.34%).

**IR:** (solid, ATR)

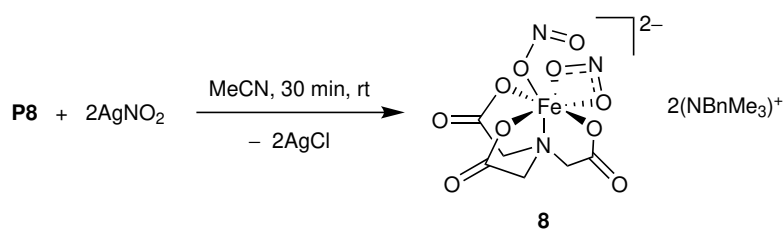
$\tilde{\nu} = 2977\text{vw}, 2918\text{vw}, 2847\text{vw}, 1635\text{vs}, 1482\text{m}, 1452\text{m}, 1411\text{m}, 1381\text{m}, 1359\text{s}, 1345\text{s}, 1318\text{s}, 1251\text{w}, 1215\text{m}, 1182\text{m}, 1146\text{m}, 1107\text{m}, 1072\text{s}, 1034\text{m}, 1004\text{s}, 968\text{vw}, 931\text{w}, 912\text{s}, 903\text{s}, 824\text{m}, 803\text{m}, 784\text{m}, 724\text{m}, 687\text{vw}, 668\text{vw cm}^{-1}$ .

**UV-Vis:** (solution, MeCN)

$\lambda_{max} = 251 \text{ nm}$ .

**UV-Vis:** (solid, KBr)

$\lambda_{max} = 470, 590 \text{ nm}$ .

5.7.4 (NBnMe<sub>3</sub>)<sub>2</sub>[Fe(NO<sub>2</sub>-κ<sup>2</sup>O,O')(NO<sub>2</sub>-κO)(nta)] (8)

**Starting materials:**

P8, silver nitrite, acetonitrile.

**Procedure:**

P8 (61.8 mg, 0.10 mmol, 1.0 equiv.) was suspended in acetonitrile (10 mL) and silver nitrite (30.8 mg, 0.20 mmol, 2.0 equiv.) was added. The mixture was stirred for 30 min at room temperature before the precipitating silver chloride was filtered off. The resulting yellow-orange filtrate was narrowed under reduced pressure and stored at 5°C for crystallization. After 1 d the product was obtained as pale orange, crystal platelets.

**Empirical formula:**

C<sub>26</sub>H<sub>38</sub>FeN<sub>5</sub>O<sub>10</sub> (636.46 g mol<sup>-1</sup>).

**Yield:**

35.2 mg (0.055 mmol, 55% of th.), pale orange, crystal platelets.

**Elemental analysis:**

found (calcd.): C 45.13% (45.01%), H 5.63% (5.52%), N 10.01% (10.09%). (calcd. for 8 · 0.4AgCl)

**IR:** (solid, ATR)

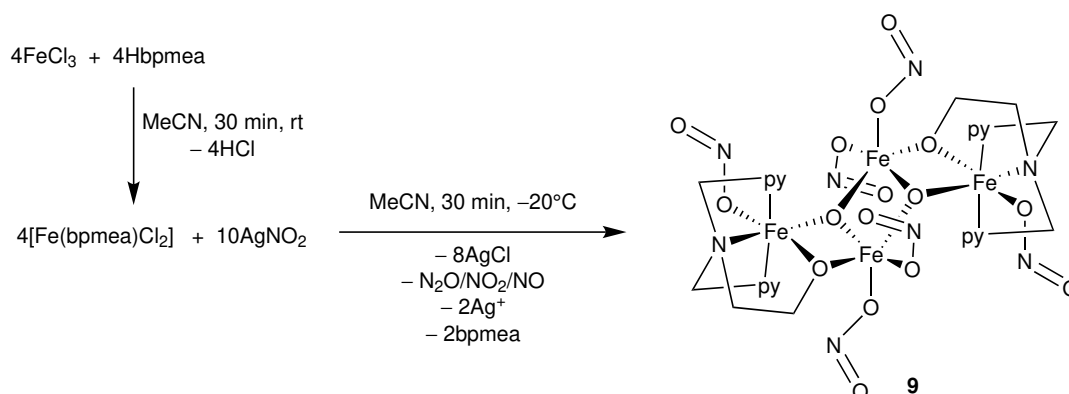
$\tilde{\nu} = 3032\text{vw}, 2967\text{vw}, 2923\text{vw}, 2251\text{vw}, 1642\text{s}, 1615\text{vs}, 1488\text{m}, 1459\text{m}, 1396\text{s}, 1379\text{vs}, 1357\text{s}, 1256\text{sh}, 1219\text{m}, 1156\text{vw}, 1125\text{m}, 1080\text{vw}, 1036\text{vw}, 990\text{m}, 975\text{m}, 918\text{s}, 890\text{s}, 863\text{m}, 806\text{m}, 784\text{vs}, 728\text{vs}, 706\text{s cm}^{-1}$ .

**UV-Vis:** (solution, MeCN)

$\lambda_{\text{max}} = 256, 300 \text{ nm}$ .

**UV-Vis:** (solid, KBr)

$\lambda_{\text{max}} = 300, 340, 400, 470 \text{ nm}$ .

5.7.5  $[\text{Fe}_4(\mu\text{-bpmea})_2(\text{Z-NO}_2\text{-}\kappa\text{O})_2(\text{E-NO}_2\text{-}\kappa\text{O})_4(\mu_3\text{-O})_2] \cdot 2\text{MeCN}$  (**9** · 2MeCN)

**Starting materials:**

Iron(III) chloride, Hbpmea, silver nitrite, acetonitrile.

**Procedure:**

Iron(III) chloride (16.2 mg, 0.10 mmol, 1.0 equiv.) and Hbpmea (24.3 mg, 0.10 mmol, 1.0 eq) were dissolved in acetonitrile (10 mL) and stirred for 30 min at room temperature. The solvent was evaporated completely to remove dissolved hydrogen chloride. The yellow-brown residue was redissolved in acetonitrile (10 mL) and cooled down to  $-20^\circ\text{C}$ . A surplus of silver nitrite (154 mg, 10.0 mmol, 10 equiv.) was added and the mixture was stirred for 1 h at  $-20^\circ\text{C}$  before the brown precipitate was filtered off. The resulting gold-brown solution was stored for two weeks at  $-25^\circ\text{C}$  resulting in the growth of yellow-brown, needle-shaped crystals of **9** · 2MeCN.

Alternatively, **9** can be synthesized starting from **P9** (83.9 mg, 0.10 mmol, 1.0 eq) in acetonitrile (10 mL) with silver nitrite (123 mg, 0.80 mmol, 8.0 equiv.). Further steps are analogue to the previously described procedure.

**Empirical formula:**

$\text{C}_{32}\text{H}_{38}\text{Fe}_4\text{N}_{14}\text{O}_{18}$  ( $1098.12 \text{ mol}^{-1}$ ).

**Yield:**

few yellow-brown, needle-shaped crystals.

**Elemental analysis:**

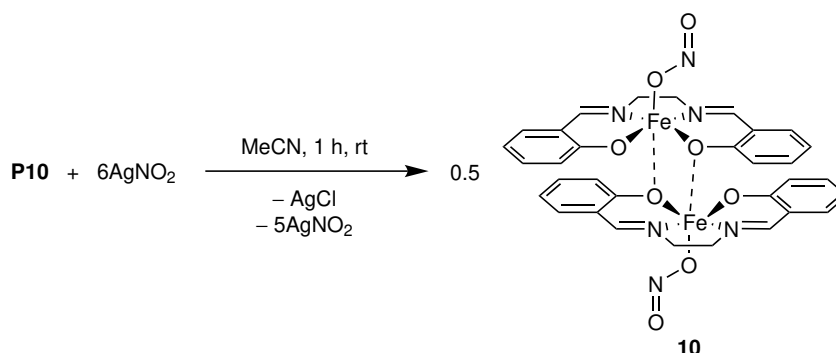
found (calcd.): C 32.72% (33.10%), H 3.08% (3.17%), N 16.49% (16.54%). (calcd. for **9** · MeCN)

**IR:** (solid, ATR)

$\tilde{\nu} = 2928\text{vw}, 2872\text{vw}, 1608\text{m}, 1572\text{w}, 1484\text{s}, 1464\text{m}, 1445\text{s}, 1352\text{vw}, 1343\text{vw}, 1320\text{vw}, 1301\text{w}, 1182\text{br}, 1179\text{m}, 1160\text{m}, 1077\text{m}, 1043\text{s}, 1024\text{vs}, 993\text{vs}, 968\text{vs}, 960\text{sh}, 905\text{m}, 863\text{w}, 814\text{sh}, 801\text{vs}, 764\text{vs}, 729\text{m}, 695\text{vs cm}^{-1}$ .

**UV-Vis:** (solution, MeOH)

$\lambda_{\text{max}} = 338 \text{ nm}$ .

5.7.6 [ $\{\text{Fe}(\text{NO}_2\text{-}\kappa\text{O})(\text{salen})\}_2\] \cdot 2\text{MeCN} (\mathbf{10} \cdot 2\text{MeCN})$ 

**Starting materials:**

**P10**, silver nitrite, acetonitrile.

**Procedure:**

**P10** (35.7 mg, 0.10 mmol, 1.0 equiv.) was dissolved in acetonitrile (40 mL) resulting in a dark purple solution. A surplus of silver nitrite (92.3 mg, 0.60 mmol, 6.0 equiv.) was added and the mixture was stirred for 10 min at room temperature. The precipitating silver chloride and remaining silver nitrite were filtered off and the black filtrate was stored for two weeks at  $-25^\circ\text{C}$  resulting in the growth of black, block-shaped crystals of **10** \cdot 2MeCN.

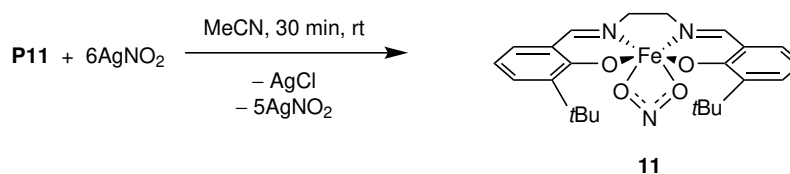
**Empirical formula:**  $\text{C}_{36}\text{H}_{34}\text{Fe}_2\text{N}_8\text{O}_8$  (818.41 g mol $^{-1}$ ).

**Yield:** 30.2 mg (0.037 mmol, 74% of th.), black, block-shaped crystals.

**Elemental analysis:** found (calcd.): C 52.65% (52.72%), H 3.78% (4.12%), N 13.62% (13.27%). (calcd. for **10** \cdot 1.6MeCN)

**IR:** (solid, ATR)  $\tilde{\nu} = 2915\text{vw}, 2251\text{vw}, 1646\text{m}, 1626\text{s}, 1597\text{s}, 1558\text{m}, 1542\text{m}, 1464\text{m}, 1440\text{s}, 1388\text{m}, 1371\text{w}, 1328\text{w}, 1304\text{m}, 1271\text{m}, 1244\text{m}, 1227\text{m}, 1212\text{m}, 1152\text{m}, 1126\text{m}, 1092\text{m}, 1028\text{vs}, 980\text{m}, 957\text{m}, 903\text{m}, 889\text{m}, 880\text{m}, 811\text{s}, 801\text{s}, 780\text{vs}, 768\text{vs}, 667\text{vw cm}^{-1}$ .

**UV-Vis:** (solution, MeCN)  $\lambda_{\text{max}} = 234, 257, 290, 330, 502\text{nm}$ .

5.7.7 [Fe(NO<sub>2</sub>-κ<sup>2</sup>O,O')(tBu<sub>2</sub>salen)] (11)

**Starting materials:**

**P11**, silver nitrite, acetonitrile.

**Procedure:**

**P11** (47.0 mg, 0.1 mmol, 1.0 equiv.) was dissolved in acetonitrile (10 mL) resulting in a black solution. A surplus of silver nitrite (92.4 mg, 0.60 mmol, 6.0 equiv.) was added under vigorous stirring and the mixture was stirred for 30 min at room temperature. The precipitating silver chloride and remaining silver nitrite were filtered off and the purple filtrate was stored for 3 d at  $-25^\circ\text{C}$  resulting in the growth of black, block-like crystals.

**Empirical formula:**

C<sub>24</sub>H<sub>30</sub>FeN<sub>3</sub>O<sub>4</sub> (480.37 g mol<sup>-1</sup>).

**Yield:**

34.59 mg (0.072 mmol, 72% of th.), black, block-like crystals.

**Elemental analysis:**

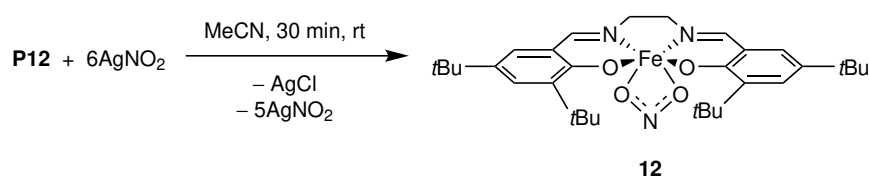
found (calcd.): C 57.61% (60.01%), H 6.56% (6.30%), N 8.21% (8.75%).

**IR:** (solid, ATR)

$\tilde{\nu}$  = 2950w, 2907w, 2865w, 1630s, 1610vs, 1587vs, 1546vs, 1440m, 1414s, 1386s, 1355m, 1336m, 1317m, 1293s, 1264m, 1232m, 1209s, 1197vs, 1146m, 1088m, 1073w, 1044m, 1024w, 977m, 964w, 932w, 868vs, 811m, 801m, 763vs, 752vs, 689s, 660w cm<sup>-1</sup>.

**UV-Vis:** (solution, MeCN)

$\lambda_{max}$  = 217, 234, 263, 297, 322, 527 nm.

5.7.8 [Fe(NO<sub>2</sub>-κ<sup>2</sup>O,O')(tBu<sub>4</sub>salen)] (12)

**Starting materials:**

**P12**, silver nitrite, acetonitrile.

**Procedure:**

**P12** (58.2 mg, 0.1 mmol, 1.0 equiv.) was dissolved in acetonitrile (14 mL) resulting in a dark red solution. A surplus of silver nitrite (92.4 mg, 0.60 mmol, 6.0 equiv.) was added under vigorous stirring and the mixture was stirred for 30 min at room temperature. The precipitating silver chloride and remaining silver nitrite were filtered off and the black filtrate was stored for 2 h at 5°C resulting in the growth of black, block-like crystals.

**Empirical formula:**

C<sub>32</sub>H<sub>46</sub>FeN<sub>3</sub>O<sub>4</sub> (592.58 g mol<sup>-1</sup>).

**Yield:**

52.7 mg (0.089 mmol, 89% of th.), black, block-like crystals.

**Elemental analysis:**

found (calcd.): C 64.95% (64.86%), H 7.74% (7.82%), N 7.23% (7.09%).

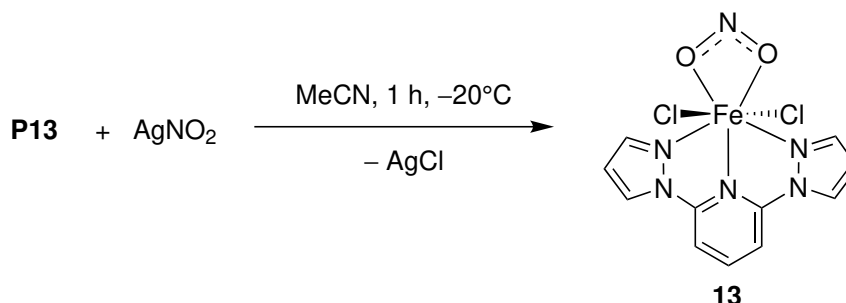
**IR:** (solid, ATR)

$\tilde{\nu}$  = 2950m, 2902m, 2867m, 1631s, 1615vs, 1536vs, 1463m, 1432m, 1410m, 1386s, 1360m, 1331m, 1298s, 1272s, 1252s, 1232vs, 1211s, 1174s, 1135m, 1095m, 1041m, 1027m, 975m, 930m, 912m, 875m, 866m, 835s, 811m, 780s, 745s, 704vw cm<sup>-1</sup>.

**UV-Vis:** (solution, MeCN)

$\lambda_{max}$  = 241, 268, 300, 327, 551 nm.

## 5.8 Synthesis of nitrito complexes with N-donor co-ligands

5.8.1  $[\text{Fe}(\text{bipzpy})\text{Cl}_2(\text{NO}_2-\kappa^2\text{O},\text{O}')]\cdot\text{MeCN}$  (**13** · MeCN)**Starting materials:**

**P14**, silver nitrite, acetonitrile, diethyl ether.

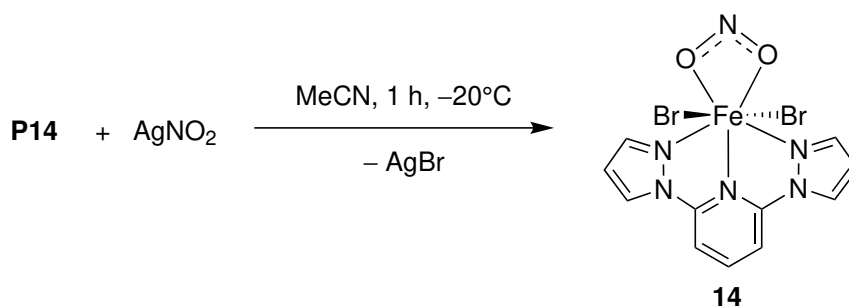
**Procedure:**

**P14** (37.3 mg, 0.10 mmol, 1.0 equiv.) was dissolved in acetonitrile (5 mL) and cooled down to  $-20^\circ\text{C}$ . Silver nitrite (15.4 mg, 0.10 mmol, 1.0 equiv.) was added and the mixture was stirred for 1 h before the precipitating silver chloride was filtered off. The orange solution was layered with ice-cold diethyl ether (10 mL) and quickly transferred to the freezer. After two weeks at  $-25^\circ\text{C}$ , **13** · MeCN was obtained as small, red, diamond-shaped crystals. The mother liquor was decanted, the crystals were washed with cold diethyl ether and carefully dried *in vacuo*.

**Empirical formula:**  $\text{C}_{13}\text{H}_{12}\text{Cl}_2\text{FeN}_7\text{O}_2$  (425.05 g mol $^{-1}$ ).

**Yield:** few, red, diamond-shaped crystals.

**IR:** (solid, ATR)  $\tilde{\nu} = 3116\text{vw}, 3092\text{vw}, 1618\text{s}, 1585\text{m}, 1520\text{s}, 1497\text{m}, 1478\text{s}, 1399\text{s}, 1345\text{m}, 1308\text{s}, 1230\text{vs}, 1206\text{vs}, 1182\text{s}, 1173\text{vs}, 1123\text{vs}, 1076\text{m}, 1061\text{vs}, 1030\text{sh}, 1013\text{w}, 977\text{vs}, 911\text{m}, 888\text{m}, 870\text{m}, 797\text{s}, 775\text{s}, 745\text{m}, 717\text{m}, 669\text{m cm}^{-1}$ .

5.8.2 [Fe(bipzpy)Br<sub>2</sub>(NO<sub>2</sub>-κ<sup>2</sup>O,O')] · MeCN (14 · MeCN)

**Starting materials:**

**P15**, silver nitrite, acetonitrile.

**Procedure:**

**P15** (50.6 mg, 0.10 mmol, 1.0 equiv.) was dissolved in acetonitrile (10 mL) and cooled down to  $-20^\circ\text{C}$ . Silver nitrite (15.4 mg, 0.10 mmol, 1.0 equiv.) was added and the mixture was stirred for 1 h before the precipitating silver chloride was filtered off. The dark red solution was quickly transferred to the freezer and stored for two weeks at  $-25^\circ\text{C}$ . **14** · MeCN was obtained as dark red, diamond-shaped crystals.

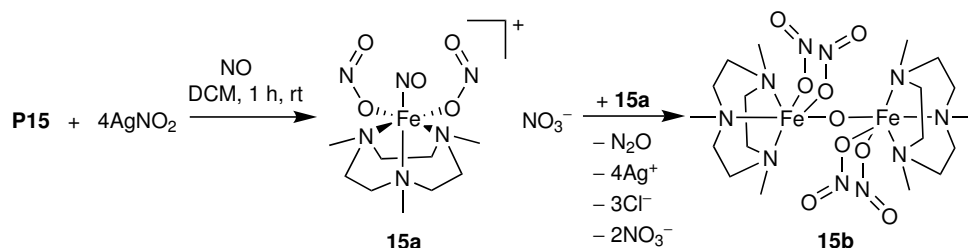
**Empirical formula:** C<sub>13</sub>H<sub>12</sub>Br<sub>2</sub>FeN<sub>7</sub>O<sub>2</sub> (513.95 g mol<sup>-1</sup>).

**Yield:** 3.9 mg (7.59 μmol, 7.6% of th.), dark red, diamond-shaped crystals.

**Elemental analysis:** found (calcd.): C 26.81% (30.38%), H 2.12% (2.35%), N 17.06% (19.08%).

**IR:** (solid, ATR)  $\tilde{\nu}$  = 3149w, 3118w, 3099m, 1623s, 1588s, 1502s, 1479vs, 1400s, 1347s, 1319m, 1284s, 1212m, 1179m, 1156w, 1138w, 1077m, 1059s, 1032m, 1019w, 976vs, 910w, 869w, 798wv, 785s, 767vs, 753s, 725m, 670m cm<sup>-1</sup>.

**UV-Vis:** (solution, MeCN)  $\lambda_{max}$  = 238, 244, 263, 270, 304, 395, 468 nm.

5.8.3 [Fe(Me<sub>3</sub>tacn)(NO)(NO<sub>2-κ</sub>O)<sub>2</sub>](NO<sub>3</sub>) · 0.5DCM (15a · 0.5DCM)

**Starting materials:**

**P15**, silver nitrite, dichloromethane, nitric oxide.

**Procedure:**

**P15** (133 mg, 0.40 mmol, 1.0 equiv.) was suspended in dichloromethane (10 mL) and silver nitrite (246 mg, 1.60 mmol, 4.0 equiv.) was added under vigorous stirring. Then, the nitrogen atmosphere was replaced by nitric oxide and the mixture was stirred for 1 h at room temperature before the red suspension was stored with the precipitated silver chloride at 5°C. The color of the solution turned to orange within one day and orange crystal platelets formed on the interface between solution and nitric oxide within a week.

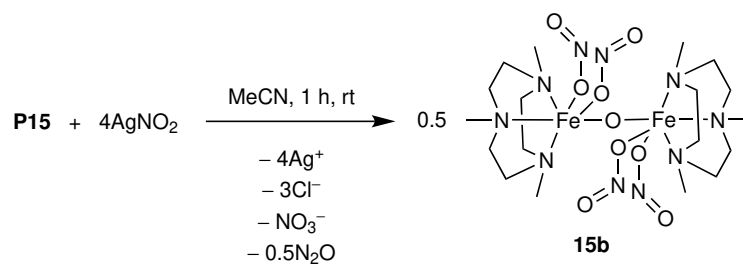
Alternative **15a** could be obtained by running the reaction without adding nitric oxide. After addition of the silver nitrite, the reaction solution was stirred for 4 h and then directly stored at 5°C. Few crystals of **15a** were isolated between many red crystals of **15b**.

**Empirical formula:**  $\text{C}_{9.5}\text{H}_{22}\text{ClFeN}_7\text{O}_8$  (453.62 g mol<sup>-1</sup>).

**Yield:** air sensitive, orange crystals.

**IR:** (solid, ATR)  $\tilde{\nu} = 2923\text{vw}, 1887\text{s}, 1744\text{vw}, 1643\text{w}, 1547\text{w}, 1463\text{sh}, 1439\text{vs}, 1422\text{vs}, 1328\text{vs}, 1291\text{vs}, 1275\text{vs}, 1164\text{m}, 1123\text{m}, 1051\text{s}, 1027\text{sh}, 1007\text{s}, 974\text{m}, 903\text{w}, 822\text{m}, 799\text{s}, 752\text{m}, 737\text{m}, 693\text{w}, 667\text{w cm}^{-1}$ .

**UV-Vis:** (solution, DCM)  $\lambda_{\text{max}} = 251, 302, 395 \text{ nm}$ .

5.8.4  $[\text{Fe}_2(\text{Me}_3\text{tacn})_2(\text{NO}_2-\kappa\text{O})_4(\mu\text{-O})]$  (**15b**)

**Starting materials:**

**P15**, silver nitrite, acetonitrile, diethyl ether, alternatively: dichloromethane.

**Procedure:**

**P15** (33.3 mg, 0.10 mmol, 1.0 equiv.) was dissolved in acetonitrile (10 mL) and silver nitrite (61.6 mg, 0.40 mmol, 4.0 equiv.) was added under vigorous stirring. The mixture was stirred for 1 h at room temperature before the precipitating silver chloride was filtered off. Layering the red solution with diethyl ether (10 mL) resulted in red, needle-shaped crystals of **15b** within two days. Recrystallization from dichloromethane at 5°C yielded in growth of red, diamond-shaped crystals of **15b** · 2DCM.

**Empirical formula:**  $\text{C}_{18}\text{H}_{42}\text{Fe}_2\text{N}_{10}\text{O}_9$  (654.29 g mol<sup>-1</sup>).

**Yield:** 15.7 mg (0.024 mmol, 48% of th.), red, needle-shaped crystals.

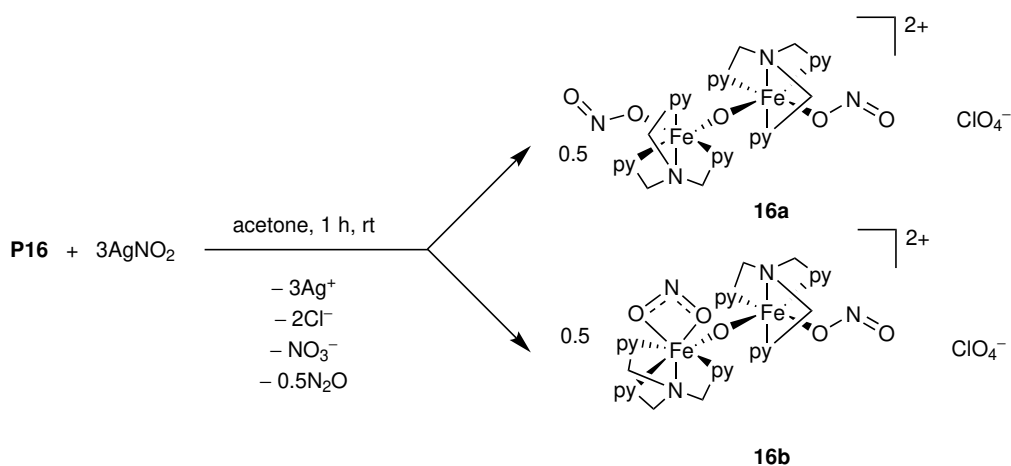
**Elemental analysis:** found (calcd.): C 32.91% (33.04%), H 6.32% (6.47%), N 21.22% (21.41%).

**IR:** (solid, ATR)  $\tilde{\nu} = 2849\text{w}, 2367\text{vw}, 1503\text{w}, 1486\text{w}, 1465\text{m}, 1439\text{s}, 1366\text{w}, 1285\text{s}, 1207\text{w}, 1159\text{s}, 1128\text{s}, 1051\text{m}, 1030\text{vs}, 1003\text{s}, 988\text{vs}, 894\text{m}, 811\text{s}, 793\text{s}, 759\text{vs}, 675\text{m}, 665\text{m cm}^{-1}$ .

**UV-Vis:** (solution, MeCN)  $\lambda_{\text{max}} = 284, 360 \text{ nm}$ .

**UV-Vis:** (solid, KBr)  $\lambda_{\text{max}} = 290, 320, 375, 520 \text{ nm}$ .

5.8.5  $[\text{Fe}_2(\text{NO}_2\text{-}\kappa\text{O})_2(\text{tpya})_2(\mu\text{-O})](\text{ClO}_4)_2 \cdot 2\text{C}_3\text{H}_6\text{O}$  (**16a** ·  $2\text{C}_3\text{H}_6\text{O}$ ) and  $[(\text{NO}_2\text{-}\kappa\text{O})(\text{tpya})\text{Fe}(\mu\text{-O})\text{Fe}(\text{NO}_2\text{-}\kappa^2\text{O},\text{O}')(\text{tpya})](\text{ClO}_4)_2 \cdot 3\text{C}_3\text{H}_6\text{O}$  (**16b** ·  $3\text{C}_3\text{H}_6\text{O}$ )



**Starting materials:**

**P16**, silver nitrite, acetone.

**Procedure:**

**P16** (51.6 mg, 0.10 mmol, 1.0 equiv.) was dissolved in acetone (8 mL) and silver nitrite (46.2 mg, 0.30 mmol, 3.0 equiv.) was added. After 1 h at room temperature the precipitating silver chloride and remaining silver nitrite were filtered off. The red filtrate was transferred to the freezer and stored for a week at  $-25^\circ\text{C}$ . Crystals with two different habitus grew in the reaction vessel. The mother liquor was removed and the products were dried *in vacuo*. **16a** ·  $2\text{C}_3\text{H}_6\text{O}$  was obtained as red, crystal aggregates, while **16b** ·  $3\text{C}_3\text{H}_6\text{O}$  was obtained as orange, block-like crystals.

**Empirical formula:**  $\text{C}_{42}\text{H}_{48}\text{Cl}_2\text{Fe}_2\text{N}_{10}\text{O}_{15}$  (**16a** ·  $2\text{C}_3\text{H}_6\text{O}$ ; 1113.54 g mol $^{-1}$ ).

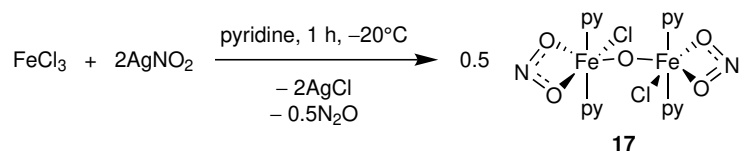
$\text{C}_{45}\text{H}_{54}\text{Cl}_2\text{Fe}_2\text{N}_{10}\text{O}_{16}$  (**16b** ·  $3\text{C}_3\text{H}_6\text{O}$ ; 1173.58 g mol $^{-1}$ ).

**Yield:** 39.4 mg; mixture of orange, block-like crystals and red, crystal aggregates.

**Elemental analysis:** found (calcd.): C 43.42% (43.54%), H 3.53% (3.73%), N 13.65% (13.82%). (calcd. for **16** ·  $0.25\text{C}_3\text{H}_6\text{O}$ )

**IR:** (solid, ATR)  $\tilde{\nu} = 3086\text{vw}, 2924\text{vw}, 1708\text{s}, 1605\text{s}, 1573\text{w}, 1506\text{w}, 1471\text{m}, 1439\text{m}, 1394\text{vw}, 1359\text{m}, 1314\text{w}, 1290\text{m}, 1274\text{sh}, 1253\text{vw}, 1224\text{m}, 1160\text{sh}, 1078\text{vs}, 1020\text{s}, 997\text{m}, 909\text{w}, 895\text{w}, 818\text{s}, 795\text{s}, 765\text{vs}, 733\text{m cm}^{-1}$ .

**UV-Vis:** (solution, DCM)  $\lambda_{\text{max}} = 315, 362, 495 \text{ nm}$ .

5.8.6  $[\text{Fe}_2\text{Cl}_2(\text{NO}_2-\kappa^2\text{O},\text{O}')_2(\text{py})_4(\mu\text{-O})] \cdot \text{py}$  (17 · py)

**Starting materials:**

Iron(III) chloride, silver nitrite, pyridine.

**Procedure:**

Iron(III) chloride (16.2 mg, 0.10 mmol, 1.0 equiv.) was dissolved in pyridine (5 mL) and cooled down to  $-20^\circ\text{C}$  before silver nitrite (30.8 mg, 0.20 mmol, 2.0 equiv.) was added. The mixture was stirred for 1 h at and quickly transferred to the freezer. After one week, small, red, block-shaped crystals were found between many colorless needles.

**Empirical formula:**  $\text{C}_{25}\text{H}_{25}\text{Cl}_2\text{Fe}_2\text{N}_7\text{O}_5$  (686.12 g mol $^{-1}$ ).

**Yield:** few, red, block-shaped crystals.

**IR:** (solid, ATR)  $\tilde{\nu} = 3056\text{vw}, 1635\text{vw}, 1601\text{m}, 1531\text{vw}, 1501\text{vw}, 1302\text{w}, 1232\text{s}, 1213\text{s}, 1197\text{m}, 1149\text{m}, 1118\text{m}, 1067\text{m}, 1038\text{m}, 1003\text{m}, 980\text{s}, 856\text{w}, 827\text{m}, 746\text{vs}, 692\text{vs}, 671\text{s cm}^{-1}$ .

## 6 Appendix

### 6.1 Packing diagrams of the crystal structures

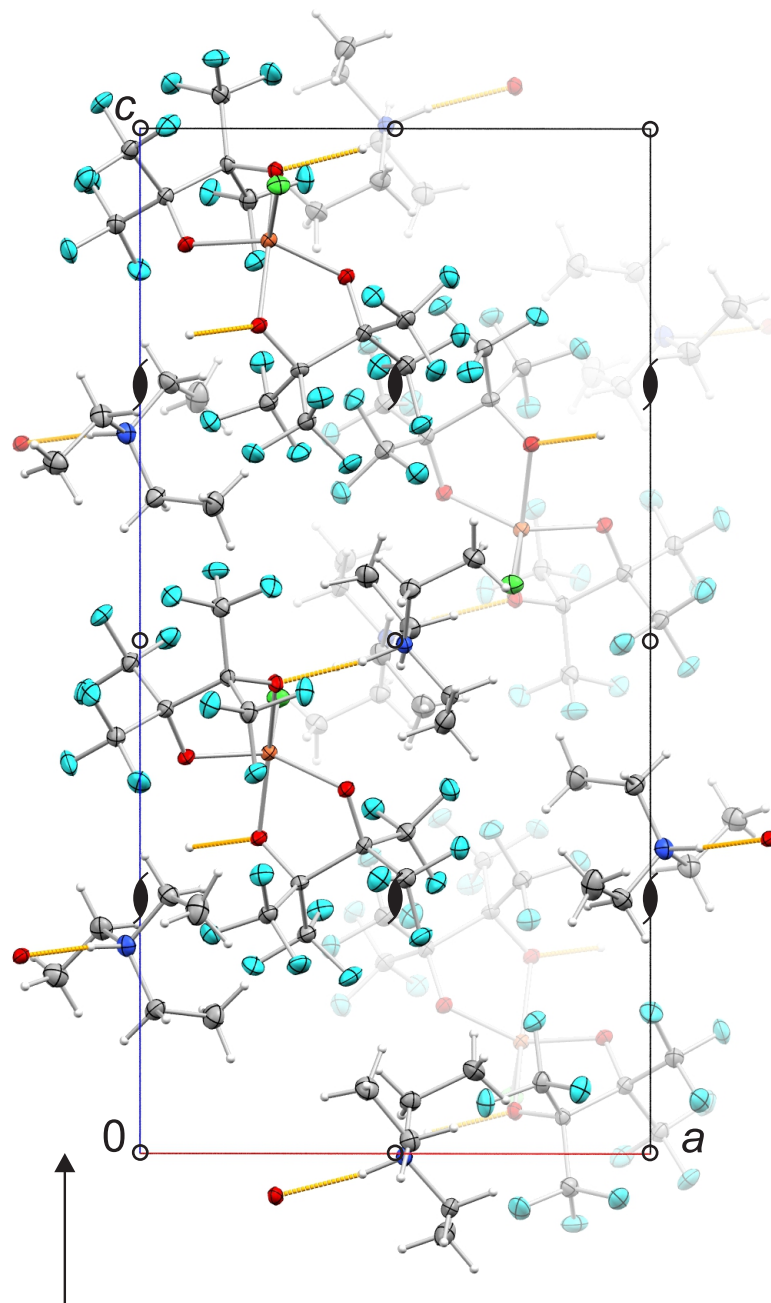


**Figure 6.74:** Packaging diagram of **P1** in the monoclinic space group  $P2_1/c$  with view along  $[010]$ . Symmetry elements of the respective space group are overlaid. Atoms: carbon(gray), hydrogen(white), chlorine(green), fluorine(turquoise), iron(orange), nitrogen(blue), oxygen(red).

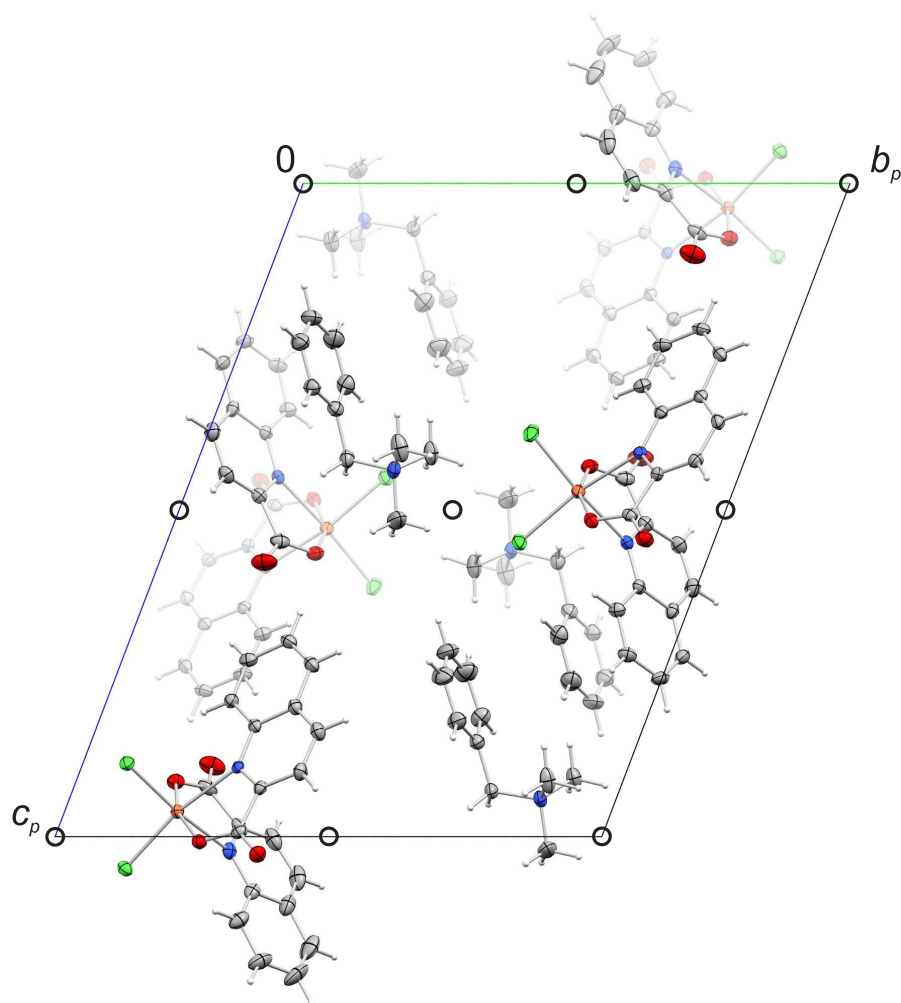


**Figure 6.75:** Packaging diagram of **P5** in the triclinic space group  $P\bar{1}$  with view along  $[100]$ . Symmetry elements of the respective space group are overlaid. Atoms: carbon(gray), hydrogen(white), chlorine(green), iron(orange), nitrogen(blue), oxygen(red).

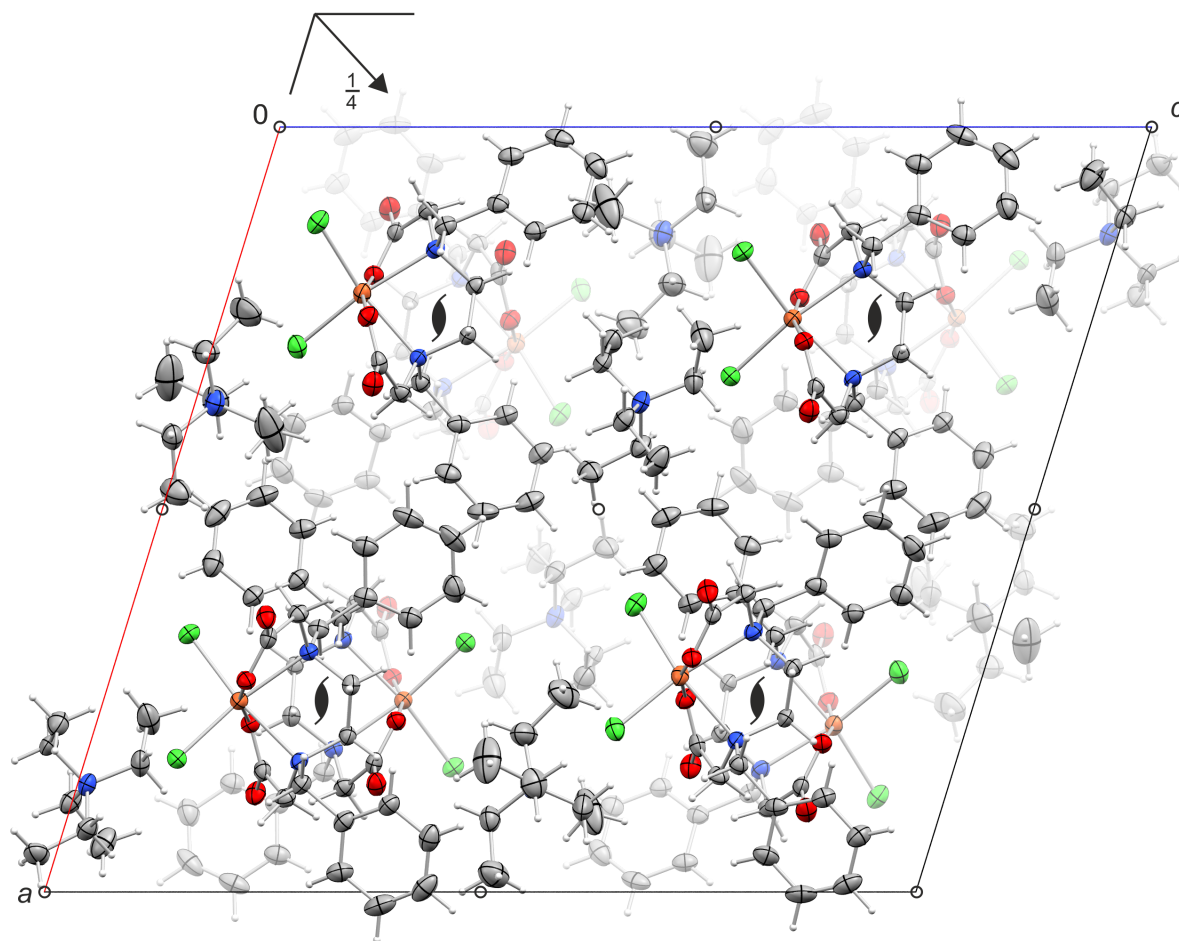


**Figure 6.76:** Packaging diagram of **P6** in the monoclinic space group  $P2_1/n$  with view along  $[010]$ . Symmetry elements of the respective space group are overlaid. Atoms: carbon(gray), hydrogen(white), chlorine(green), iron(orange), nitrogen(blue), oxygen(red).

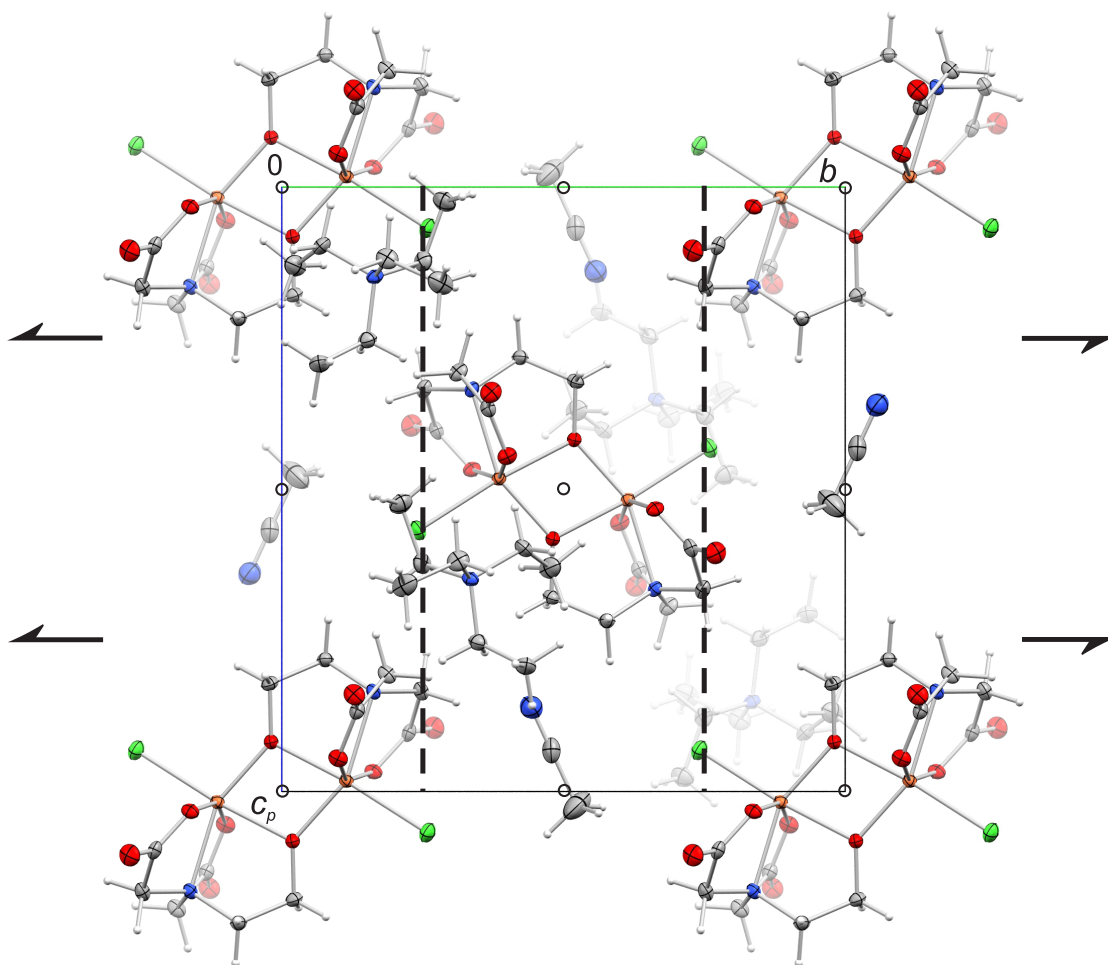


**Figure 6.77:** Packaging diagram of  $P7 \cdot 2MeCN$  in the monoclinic space group  $P2_1/c$  with view along  $[100]$ . Symmetry elements of the respective space group are overlaid. Atoms: carbon(grey), hydrogen(white), chlorine(green), iron(orange), nitrogen(blue), oxygen(red).

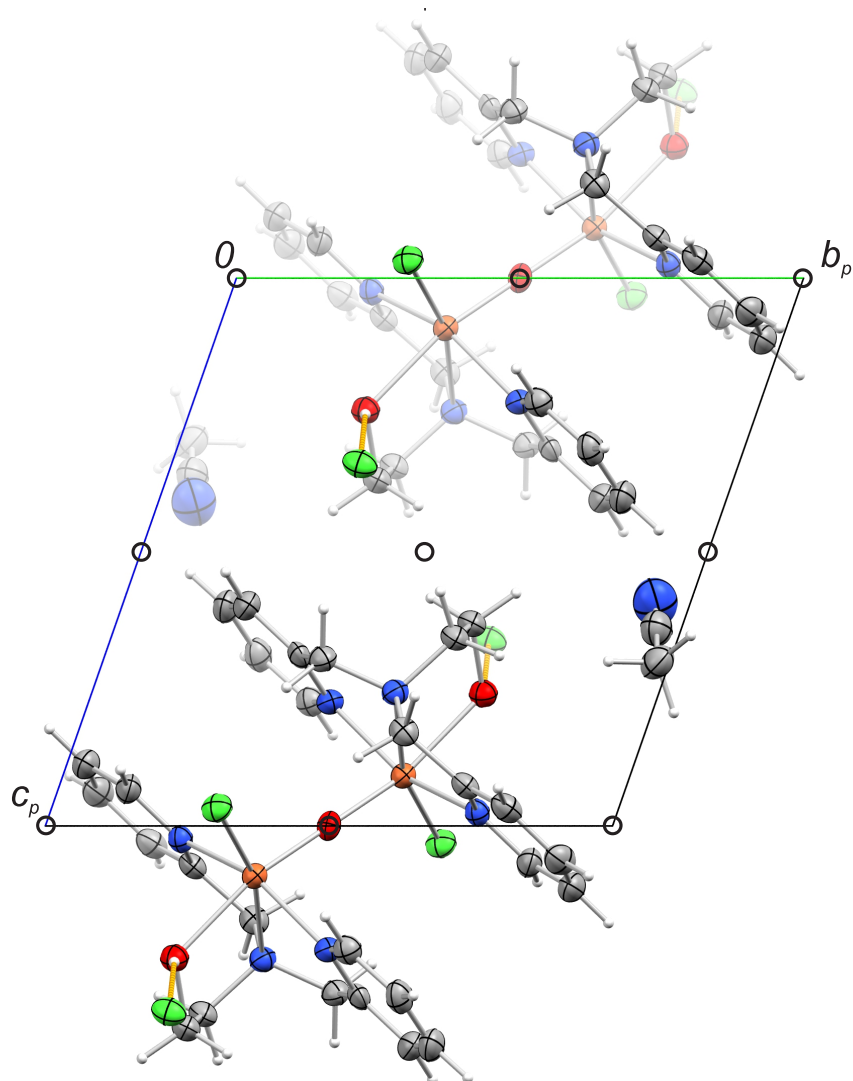


**Figure 6.78:** Packaging diagram of  $P9 \cdot 2MeCN$  in the triclinic space group  $P\bar{1}$  with view along  $[100]$ . Symmetry elements of the respective space group are overlaid. Atoms: carbon(grey), hydrogen(white), chlorine(green), iron(orange), nitrogen(blue), oxygen(red).

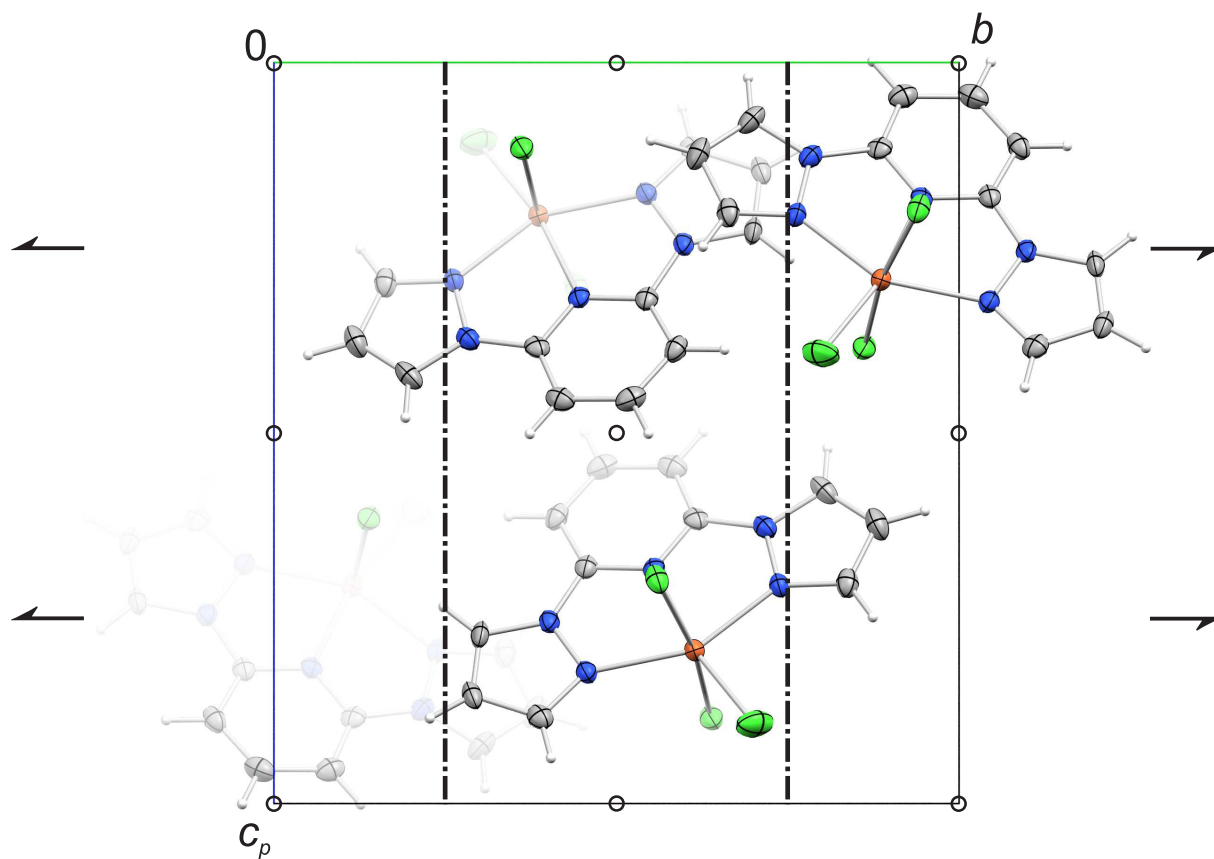


**Figure 6.79:** Packaging diagram of **P13** in the monoclinic space group  $P2_1/n$  with view along  $[100]$ . Symmetry elements of the respective space group are overlaid. Atoms: carbon(gray), hydrogen(white), chlorine(green), iron(orange), nitrogen(blue).

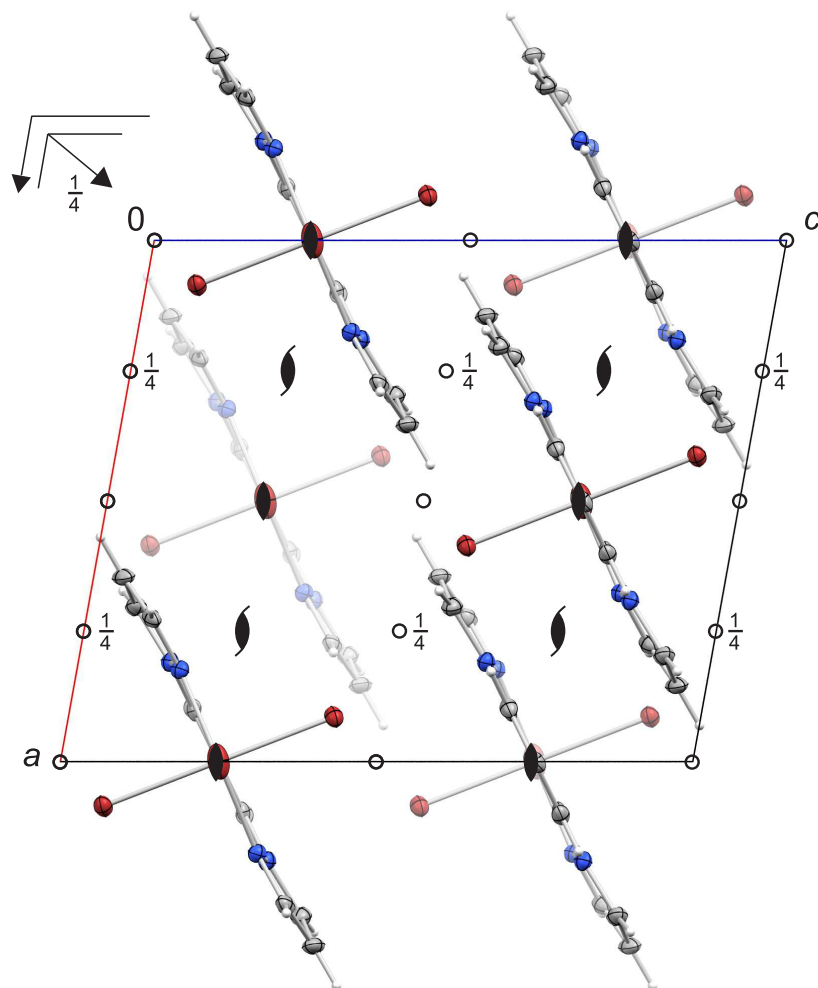


**Figure 6.80:** Packaging diagram of **P14** in the monoclinic space group  $C2/c$  with view along  $[010]$ . Symmetry elements of the respective space group are overlaid. Atoms: carbon(gray), hydrogen(white), bromine(red), iron(orange), nitrogen(blue).

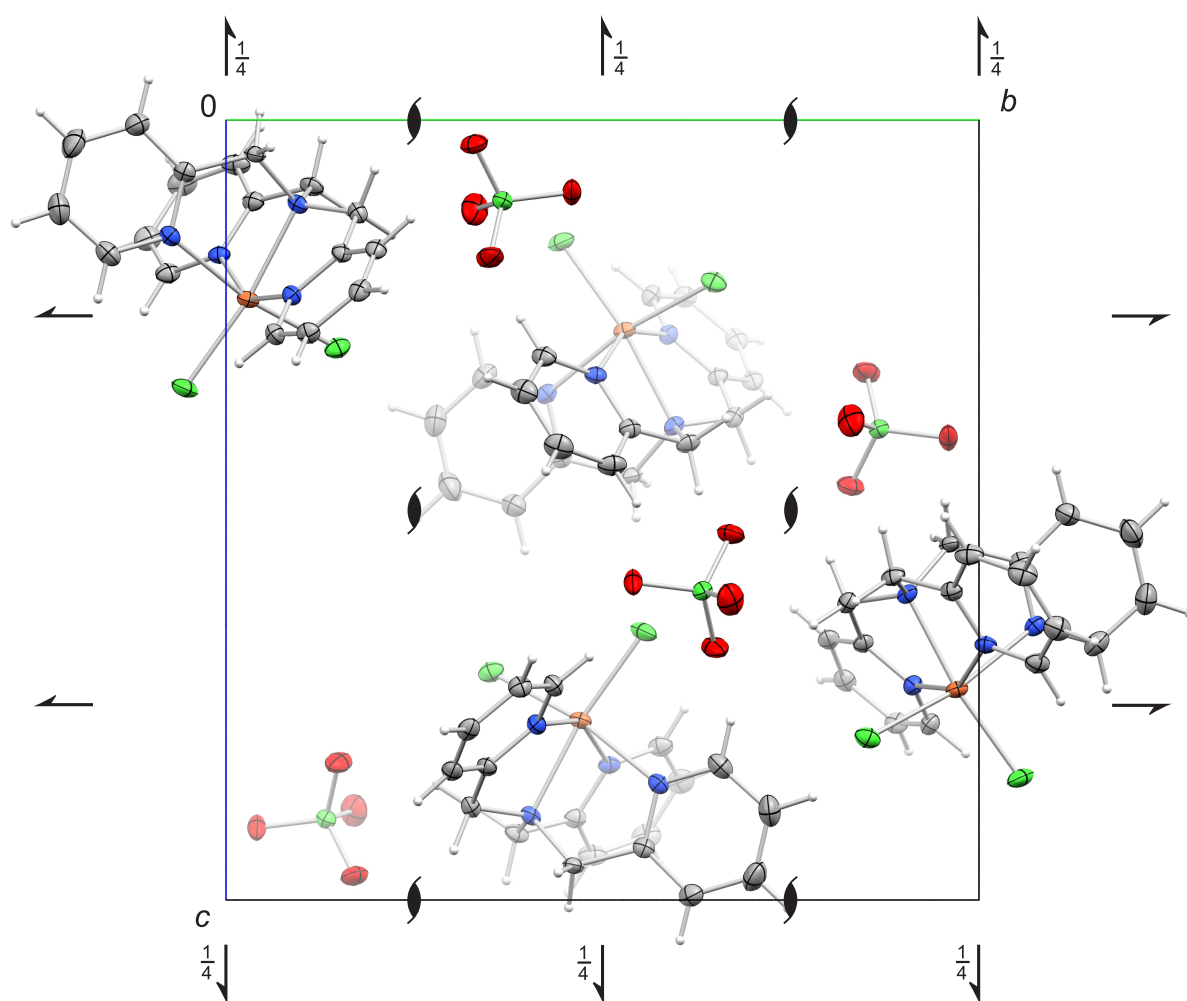


**Figure 6.81:** Packaging diagram of **P16** in the orthorhombic space group  $P2_12_12_1$  with view along [100]. Symmetry elements of the respective space group are overlaid. Atoms: carbon(grey), hydrogen(white), chlorine(green), iron(orange), nitrogen(blue), oxygen(red).

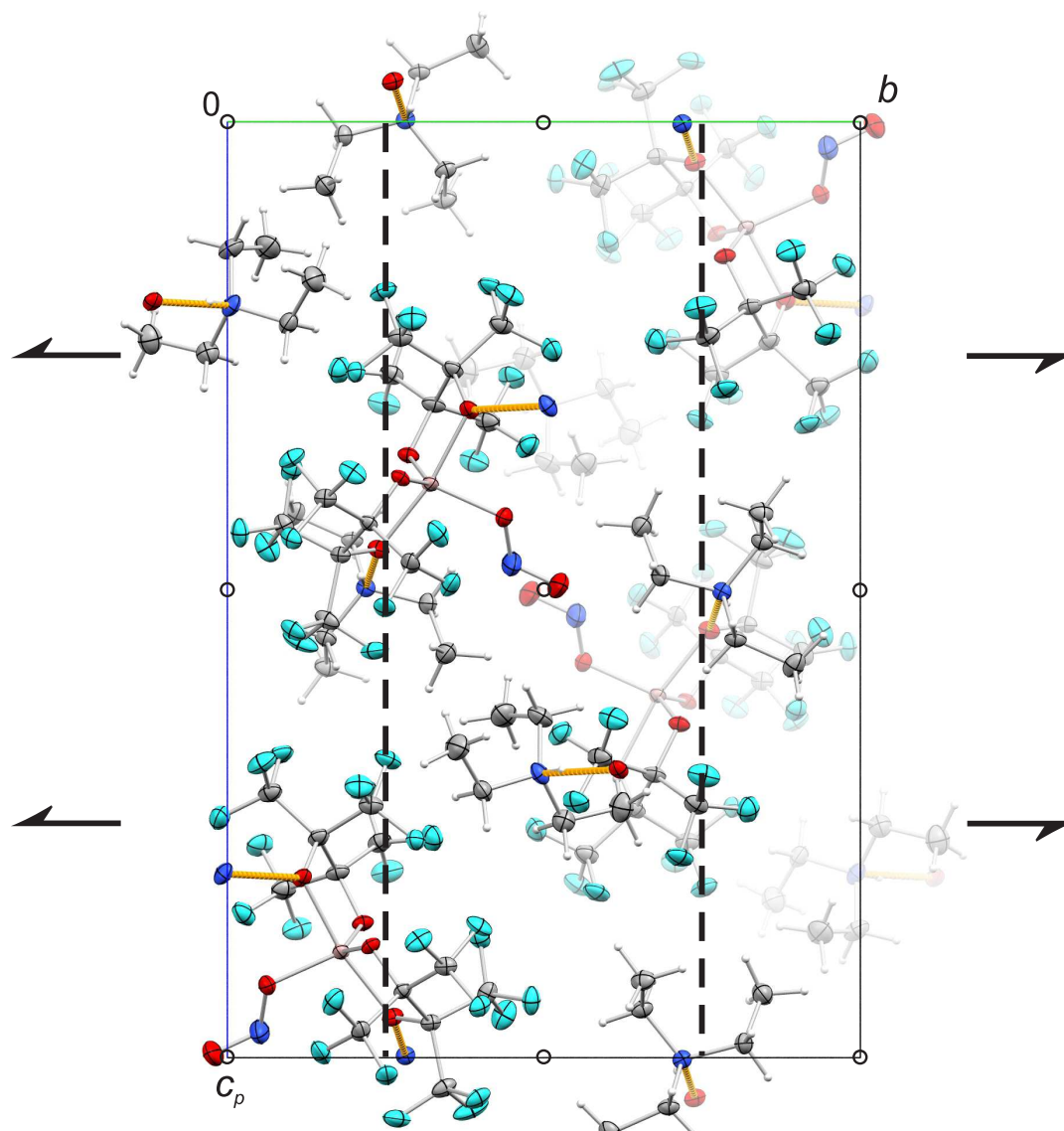


**Figure 6.82:** Packaging diagram of **1a-Al**, **1a-Cr** ( $\kappa O$ ) and **1a-Ga** (representative) in the monoclinic space group  $P2_1/c$  with view along [100]. Symmetry elements of the respective space group are overlaid. Atoms: carbon(gray), hydrogen(white), fluorine(turquoise), gallium(pink), nitrogen(blue), oxygen(red).

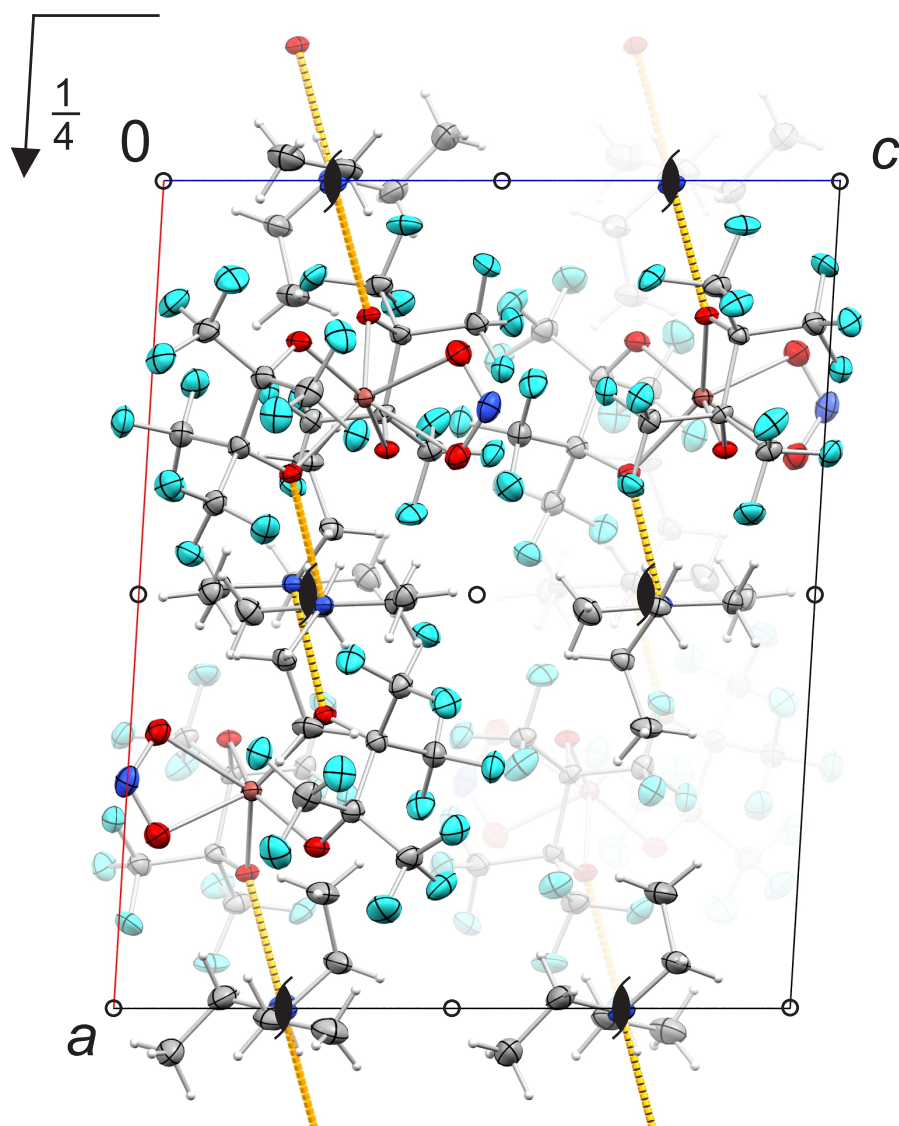


**Figure 6.83:** Packaging diagram of **1a-Tl** in the monoclinic space group  $P2_1/c$  with view along  $[010]$ . Symmetry elements of the respective space group are overlaid. Atoms: carbon(gray), hydrogen(white), fluorine(turquoise), thallium(brown), nitrogen(blue), oxygen(red).

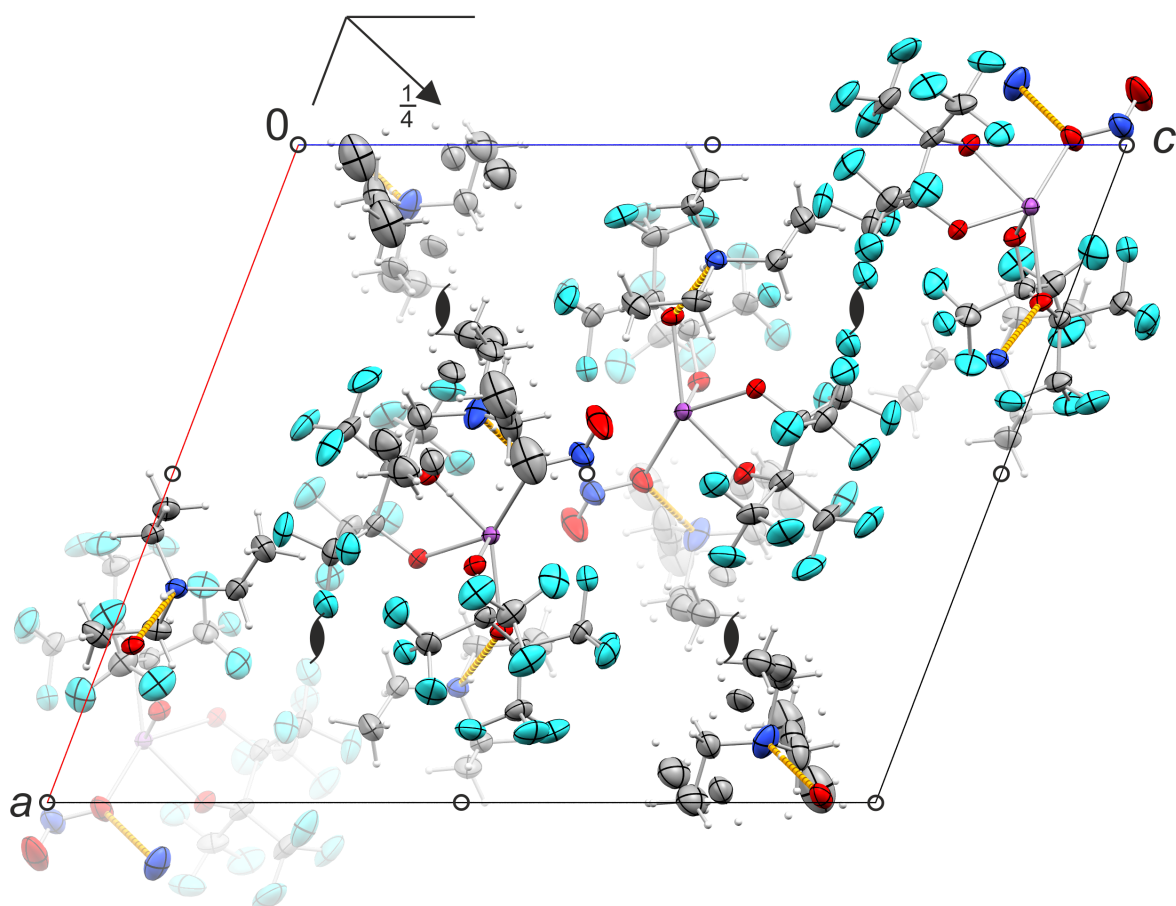


**Figure 6.84:** Packaging diagram of **1a-Bi** in the monoclinic space group  $P2_1/n$  with view along  $[010]$ . Symmetry elements of the respective space group are overlaid. Atoms: carbon(gray), hydrogen(white), fluorine(turquoise), bismuth(purple), nitrogen(blue), oxygen(red).

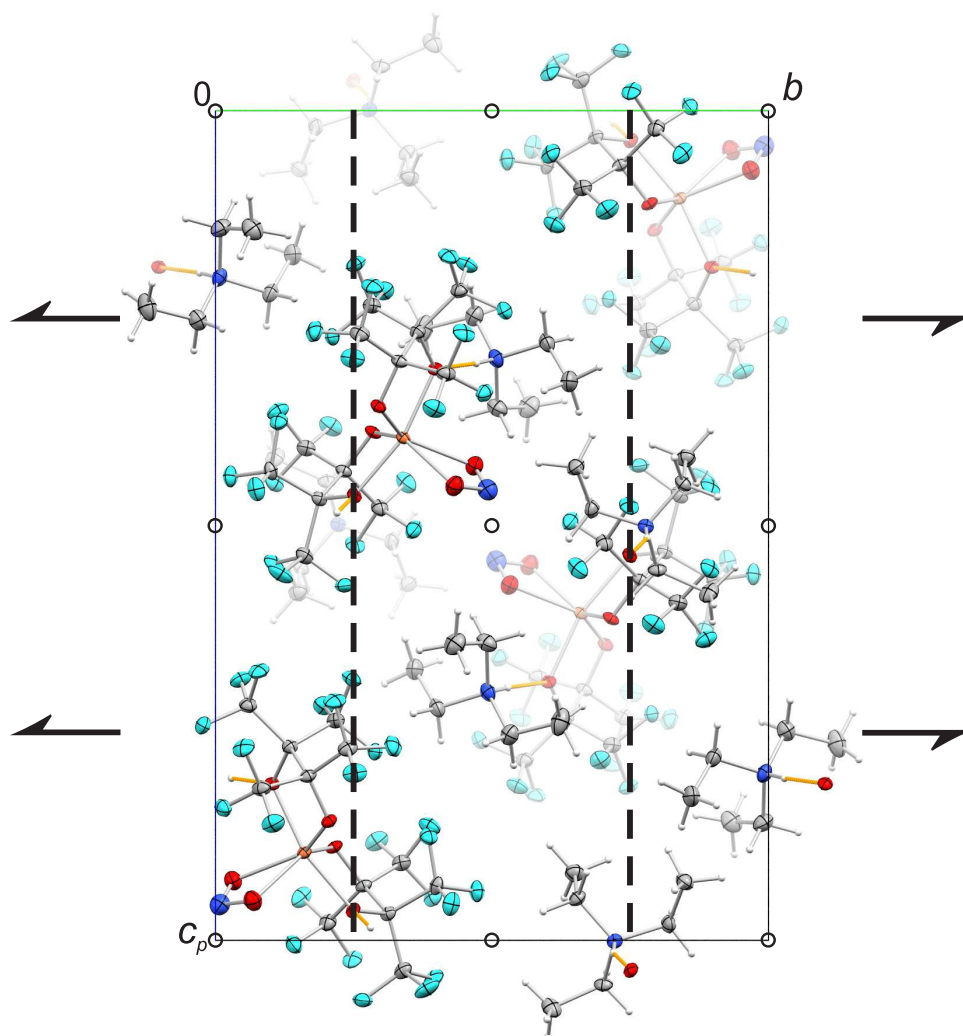


**Figure 6.85:** Packaging diagram of **1a-Sc**, **1a-Cr** ( $\kappa^2O, O'$ ), **1a-Fe** (representative) and **1a-In** in the monoclinic space group  $P2_1/c$  with view along [100]. Symmetry elements of the respective space group are overlaid. Atoms: carbon(gray), hydrogen(white), fluorine(turquoise), iron(orange), nitrogen(blue), oxygen(red).

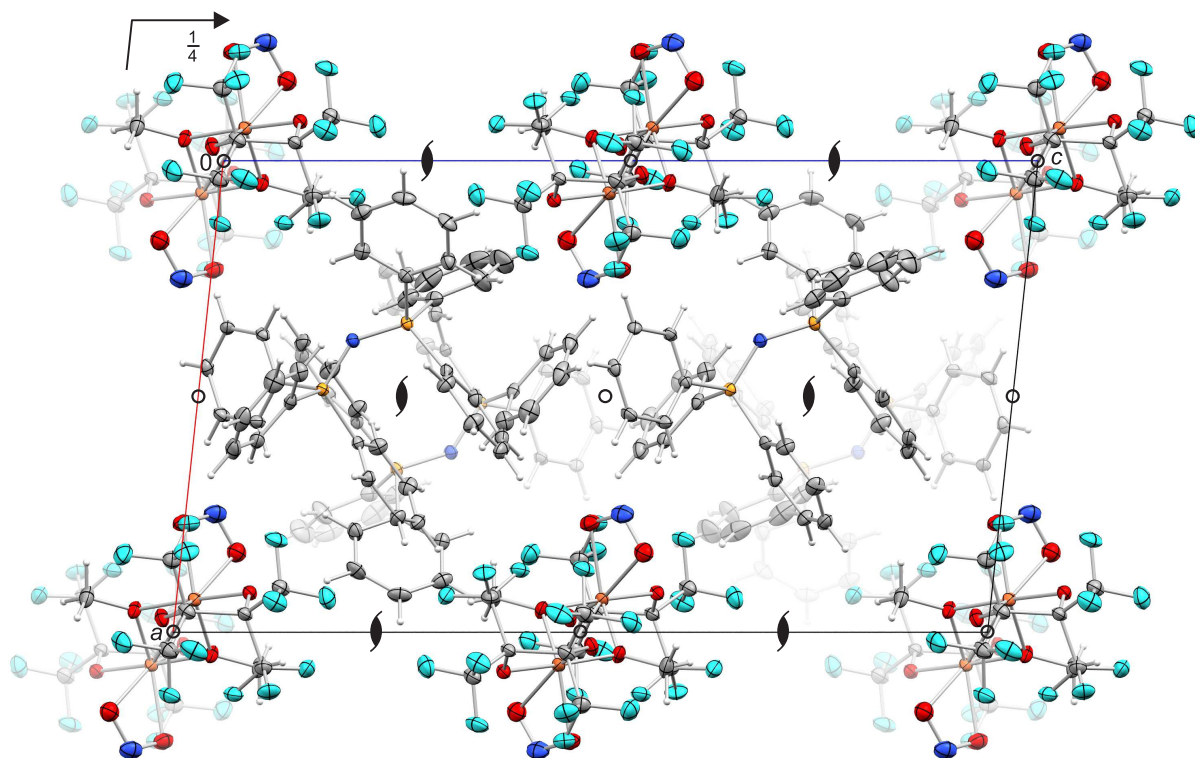


**Figure 6.86:** Packaging diagram of **1b** in the monoclinic space group  $P2_1/c$  with view along  $[010]$ . Symmetry elements of the respective space group are overlaid. Atoms: carbon(gray), hydrogen(white), fluorine(turquoise), iron(orange), nitrogen(blue), oxygen(red), phosphorous(yellow-orange).

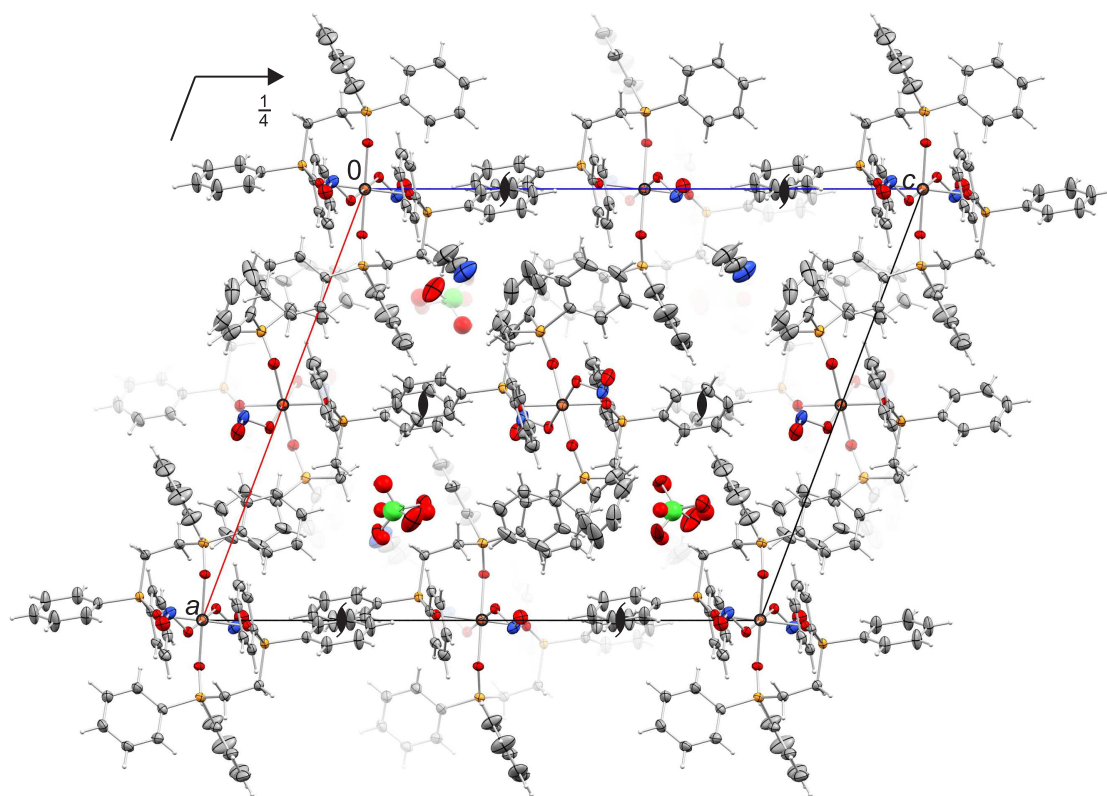


**Figure 6.87:** Packaging diagram of  $2 \cdot \text{MeCN}$  in the monoclinic space group  $P2_1/c$  with view along  $[010]$ . Symmetry elements of the respective space group are overlaid. Atoms: carbon(grey), hydrogen(white), chlorine(green), iron(orange), nitrogen(blue), oxygen(red), phosphorous(yellow-orange).

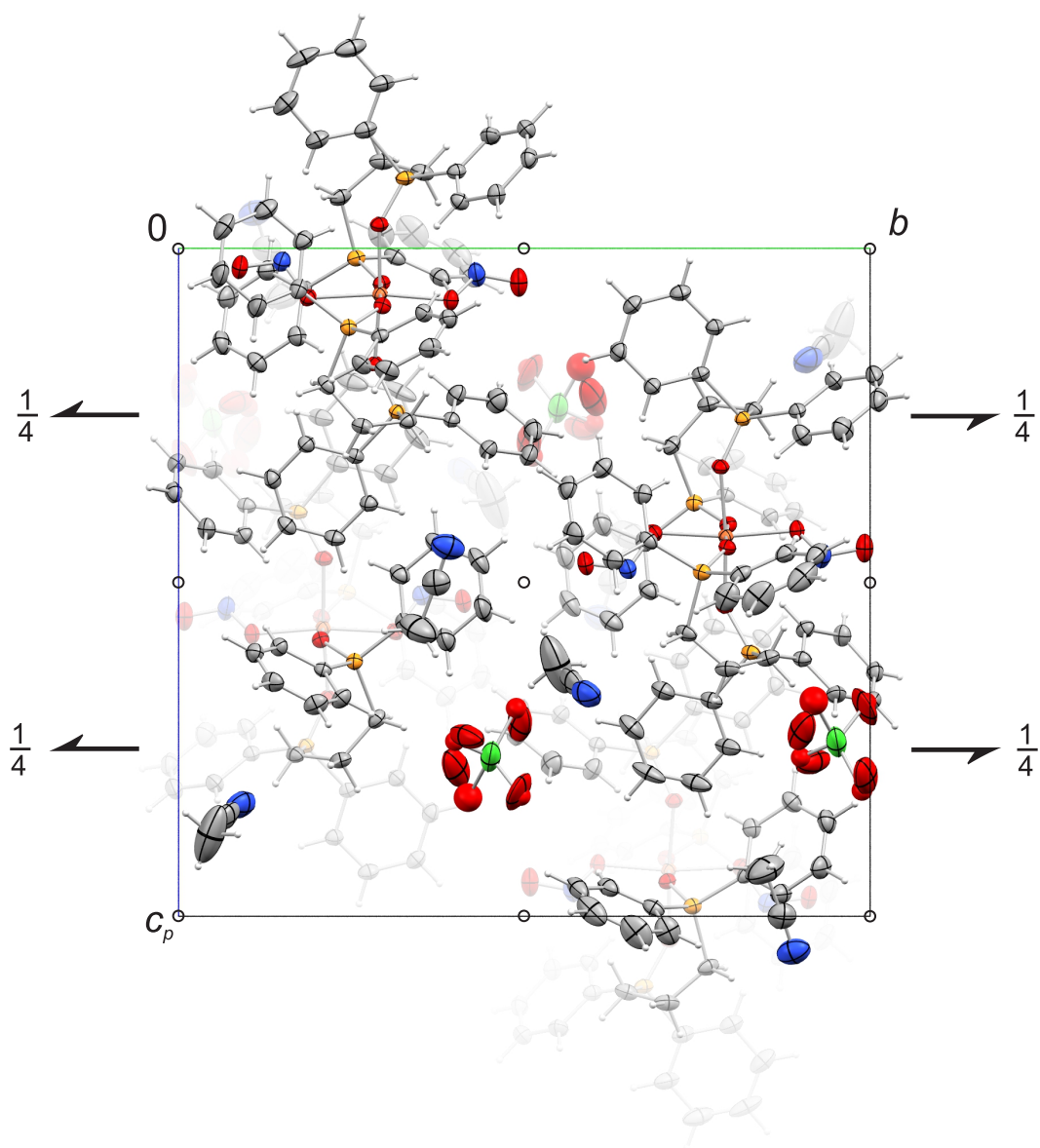


**Figure 6.88:** Packaging diagram of  $3 \cdot 2\text{MeCN}$  in the monoclinic space group  $P2_1/n$  with view along  $[100]$ . Symmetry elements of the respective space group are overlaid. Atoms: carbon(grey), hydrogen(white), chlorine(green), iron(orange), nitrogen(blue), oxygen(red), phosphorous(yellow-orange).

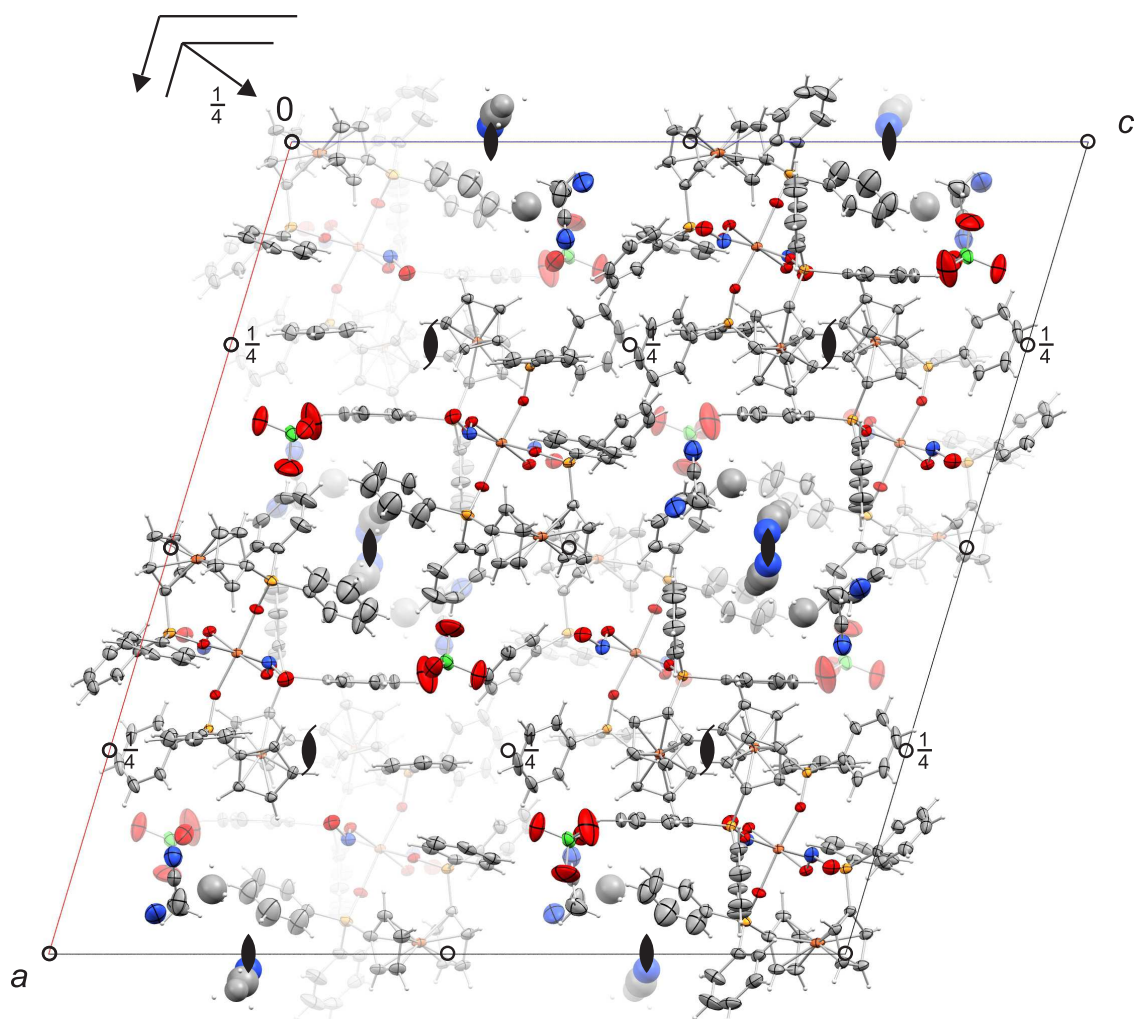


**Figure 6.89:** Packaging diagram of  $4 \cdot 3\text{MeCN}$  in the monoclinic space group  $C2/c$  with view along  $[010]$ . Symmetry elements of the respective space group are overlaid. Atoms: carbon(grey), hydrogen(white), chlorine(green), iron(orange), nitrogen(blue), oxygen(red), phosphorous(yellow-orange).

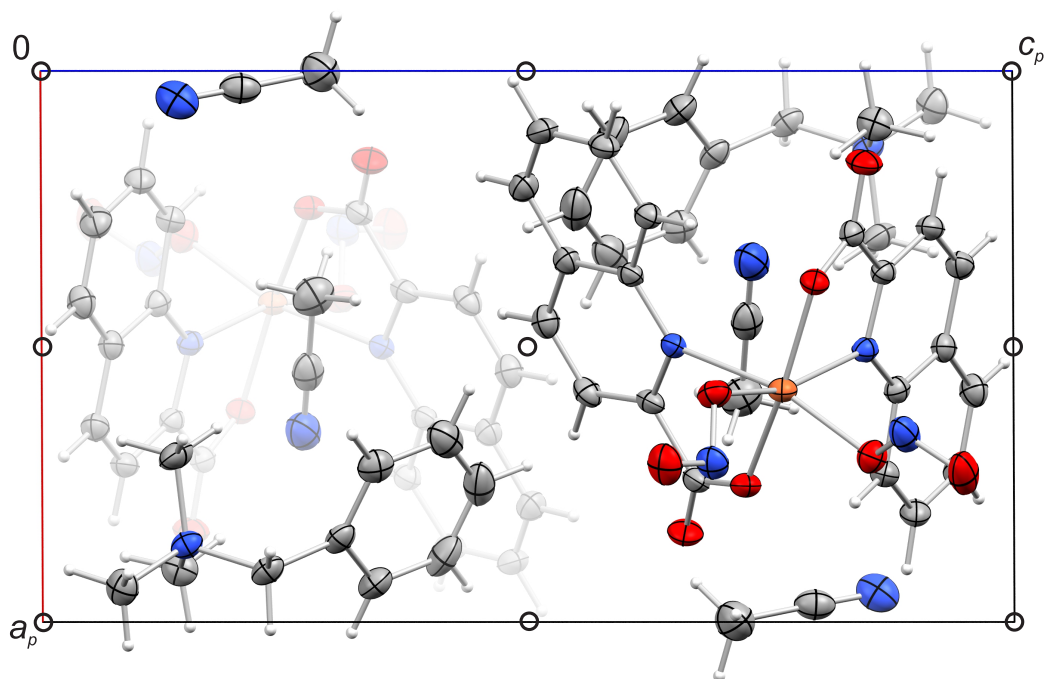


**Figure 6.90:** Packaging diagram of  $5 \cdot 2\text{MeCN}$  in the triclinic space group  $P\bar{1}$  with view along  $[010]$ . Symmetry elements of the respective space group are overlaid. Atoms: carbon(grey), hydrogen(white), iron(orange), nitrogen(blue), oxygen(red).

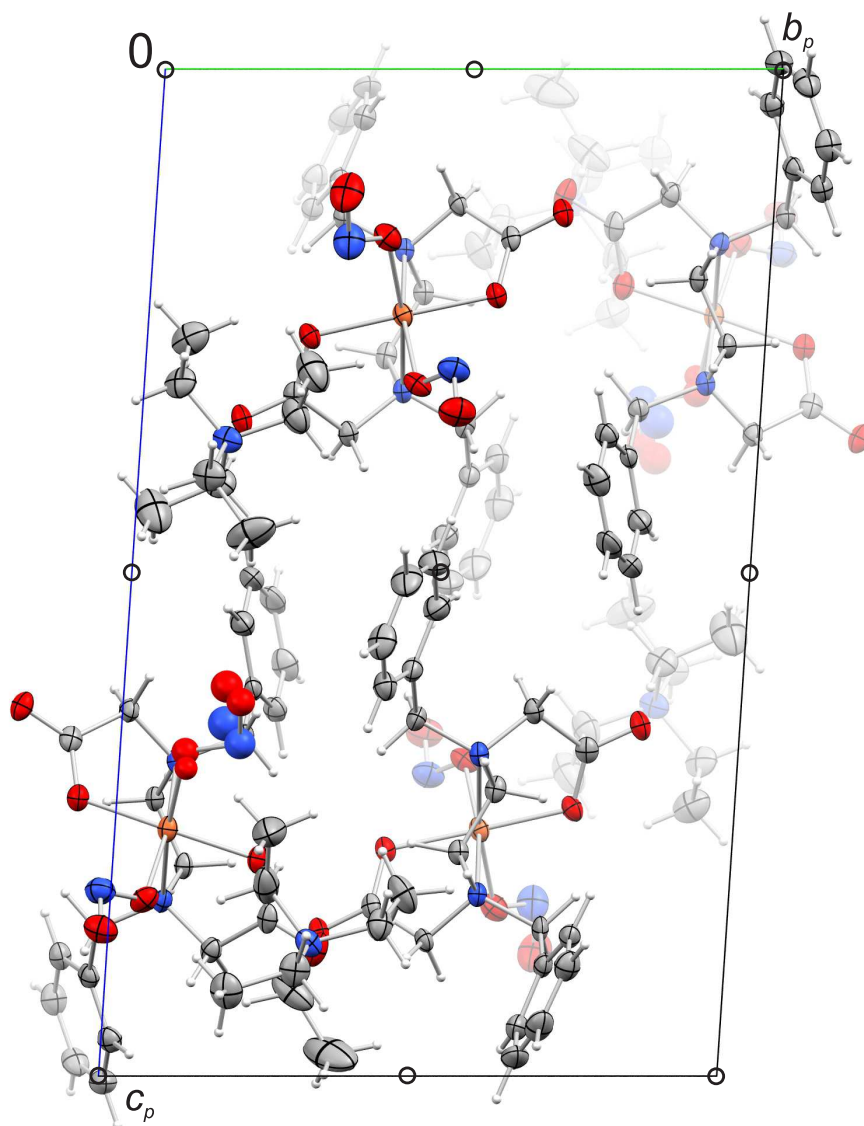


**Figure 6.91:** Packaging diagram of **6** in the triclinic space group  $P\bar{1}$  with view along  $[100]$ . Symmetry elements of the respective space group are overlaid. Atoms: carbon(grey), hydrogen(white), iron(orange), nitrogen(blue), oxygen(red).

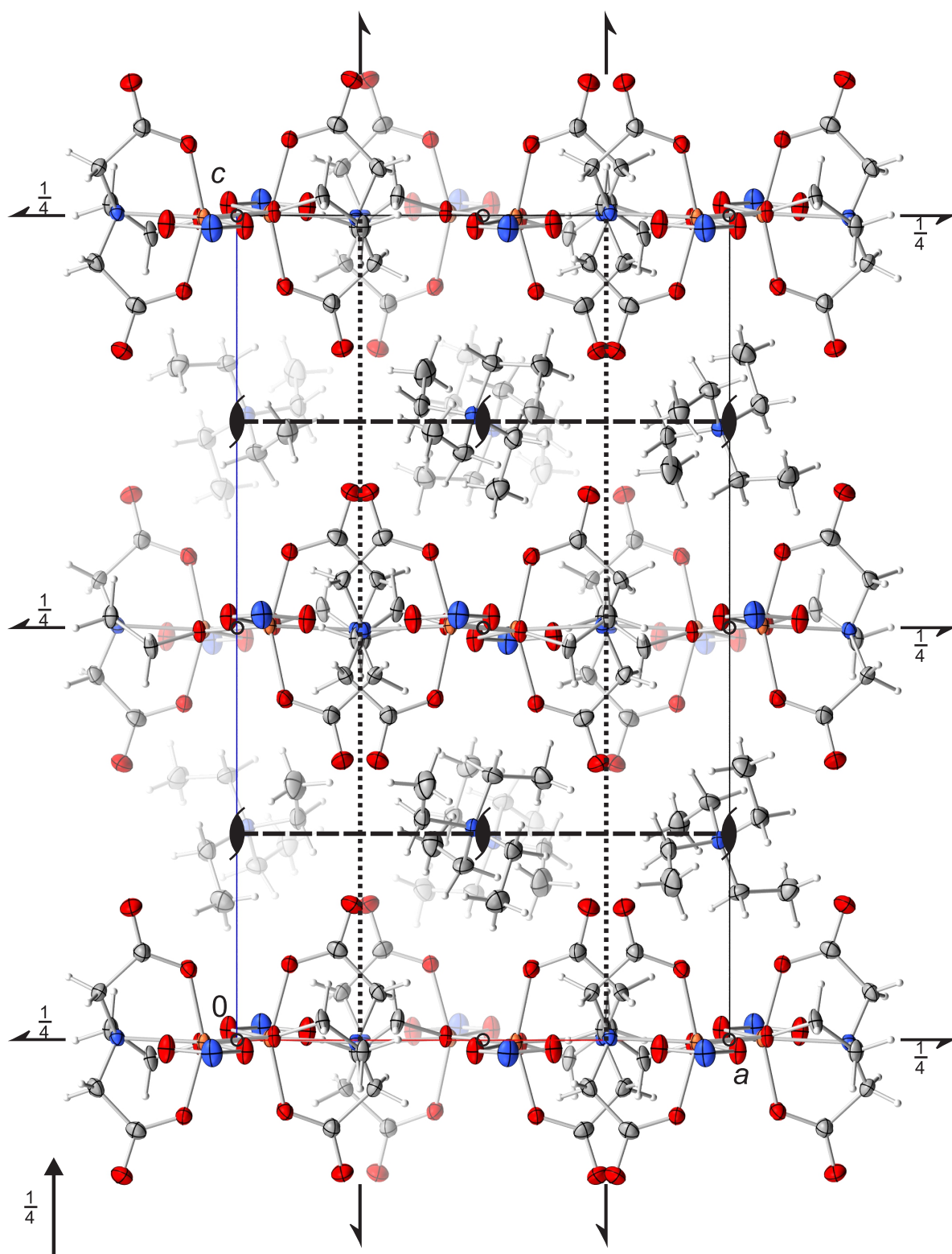


**Figure 6.92:** Packaging diagram of **7** in the orthorhombic space group  $Pbca$  with view along  $[010]$ . Symmetry elements of the respective space group are overlaid. Atoms: carbon(grey), hydrogen(white), iron(orange), nitrogen(blue), oxygen(red).

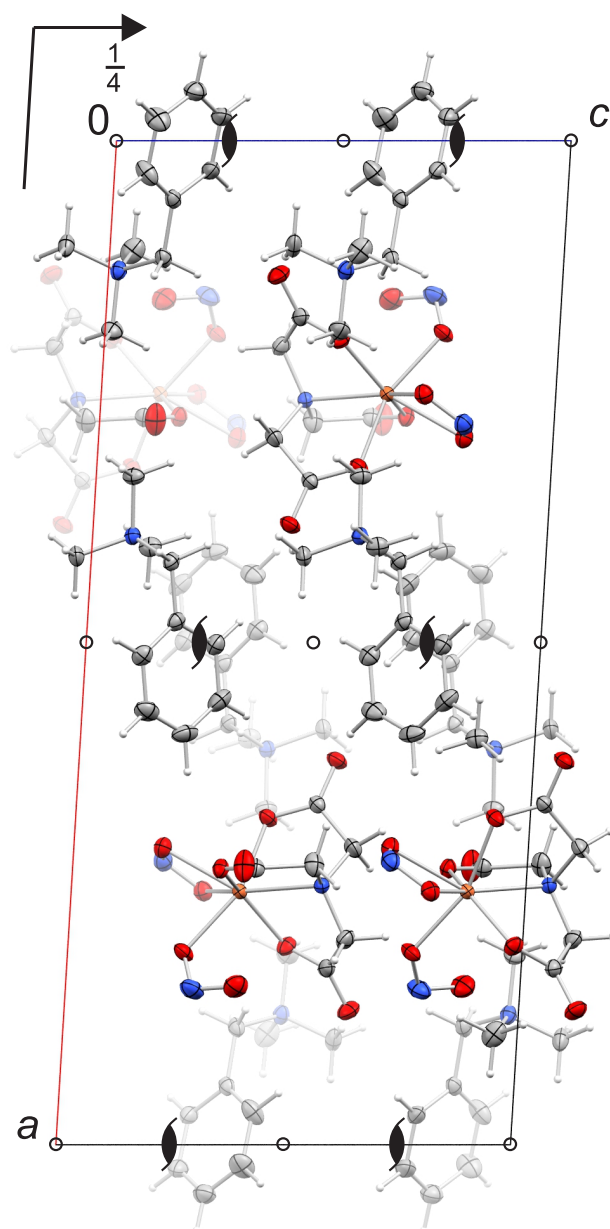


**Figure 6.93:** Packaging diagram of **8** in the monoclinic space group  $P2_1/c$  with view along  $[010]$ . Symmetry elements of the respective space group are overlaid. Atoms: carbon(grey), hydrogen(white), iron(orange), nitrogen(blue), oxygen(red).

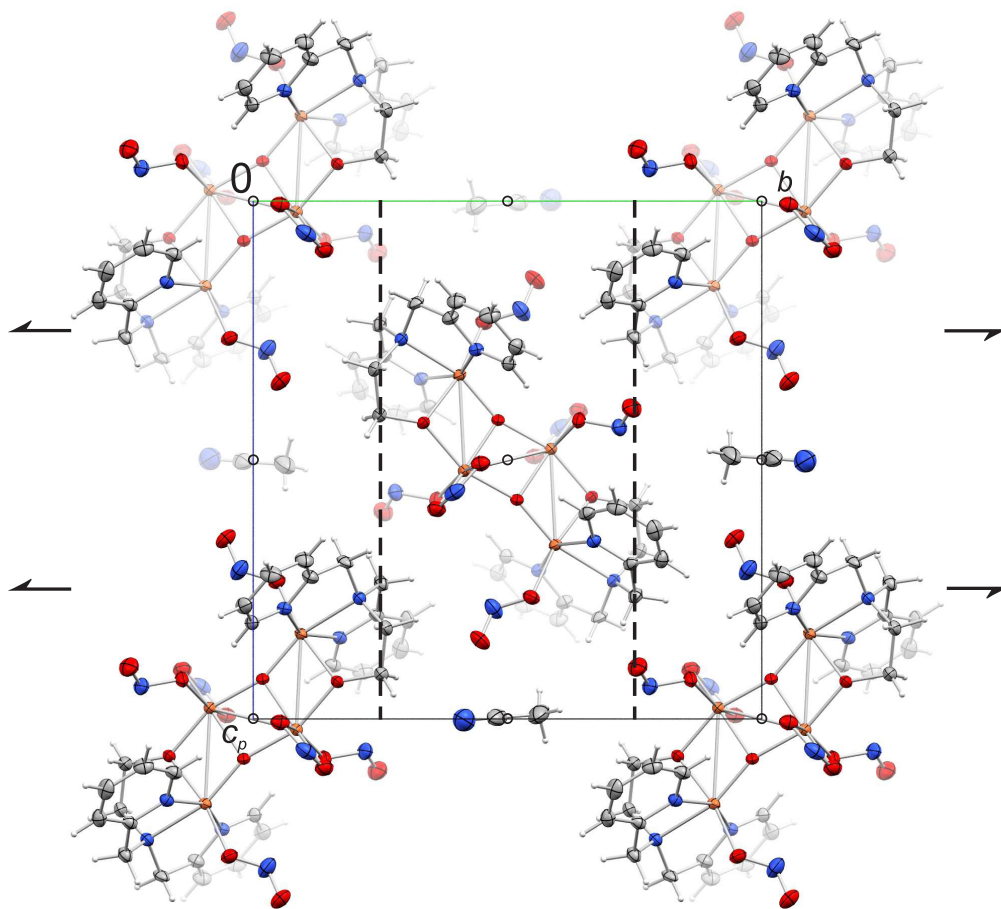


**Figure 6.94:** Packaging diagram of  $9 \cdot 2\text{MeCN}$  in the monoclinic space group  $P2_1/c$  with view along  $[100]$ . Symmetry elements of the respective space group are overlaid. Atoms: carbon(grey), hydrogen(white), iron(orange), nitrogen(blue), oxygen(red).

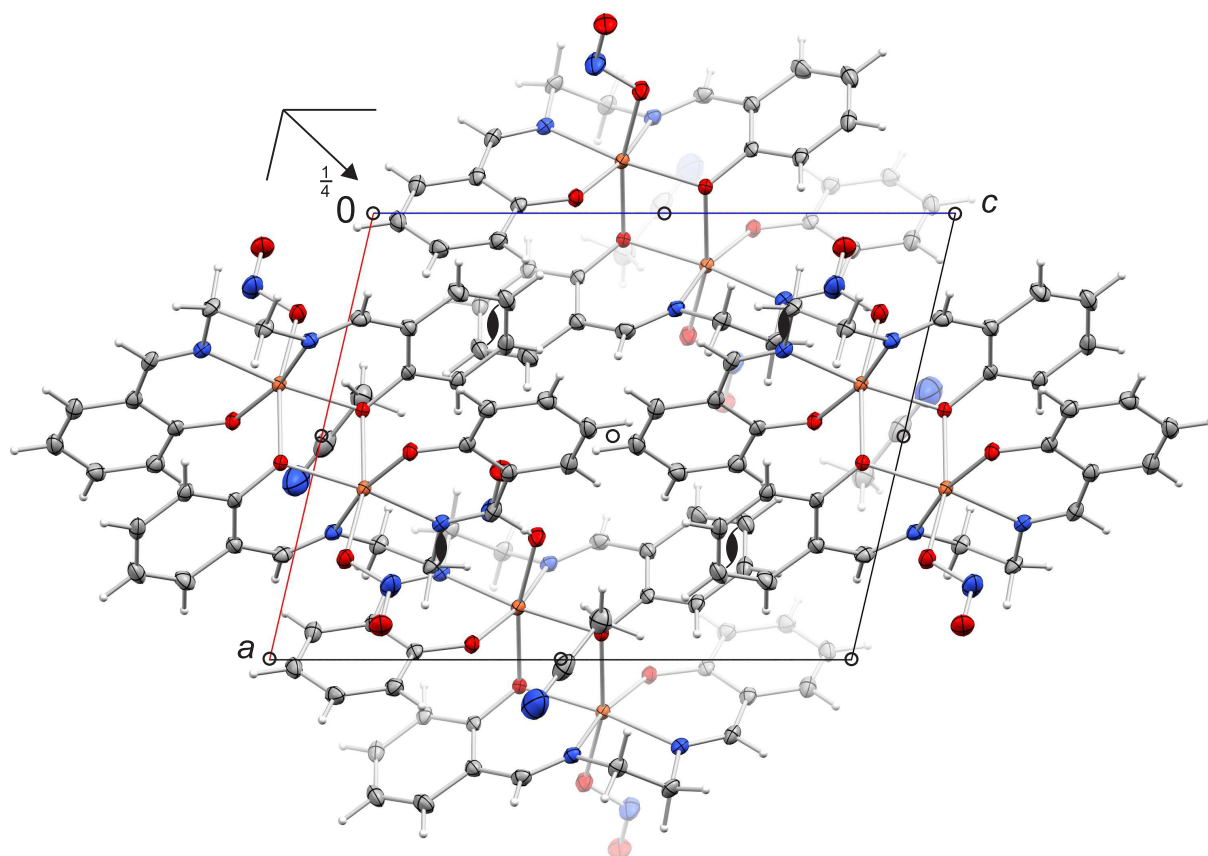


**Figure 6.95:** Packaging diagram of  $10 \cdot 2\text{MeCN}$  in the monoclinic space group  $P2_1/n$  with view along  $[010]$ . Symmetry elements of the respective space group are overlaid. Atoms: carbon(grey), hydrogen(white), iron(orange), nitrogen(blue), oxygen(red).







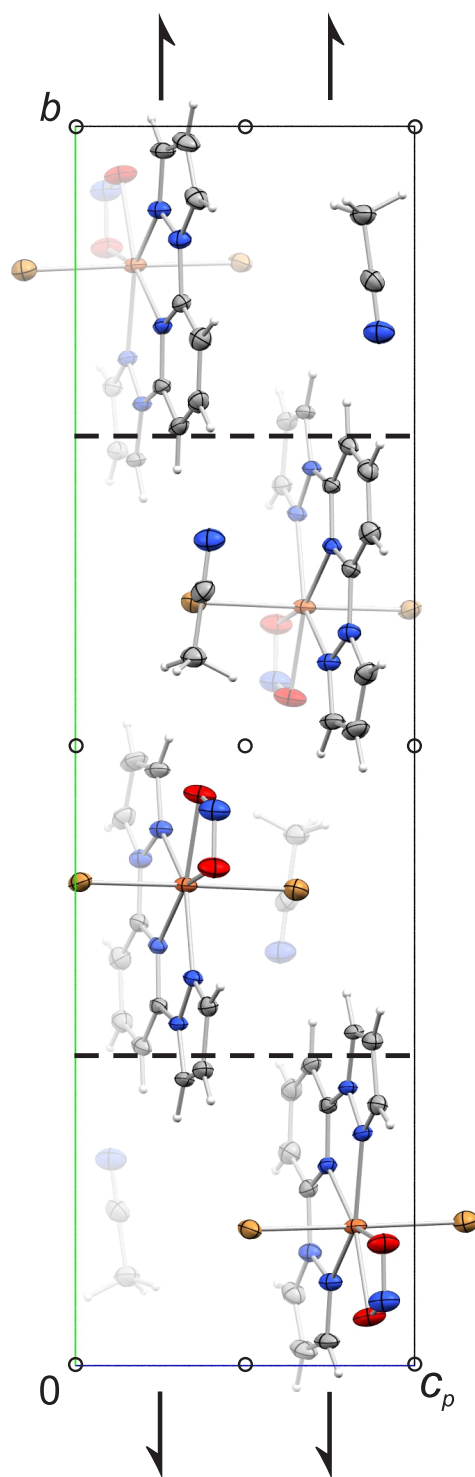


**Figure 6.99:** Packaging diagram of  $14 \cdot \text{MeCN}$  in the monoclinic space group  $P2_1/c$  with view along  $[100]$ . Symmetry elements of the respective space group are overlaid. Atoms: carbon(grey), hydrogen(white), bromine(yellow-orange), iron(orange), nitrogen(blue), oxygen(red).

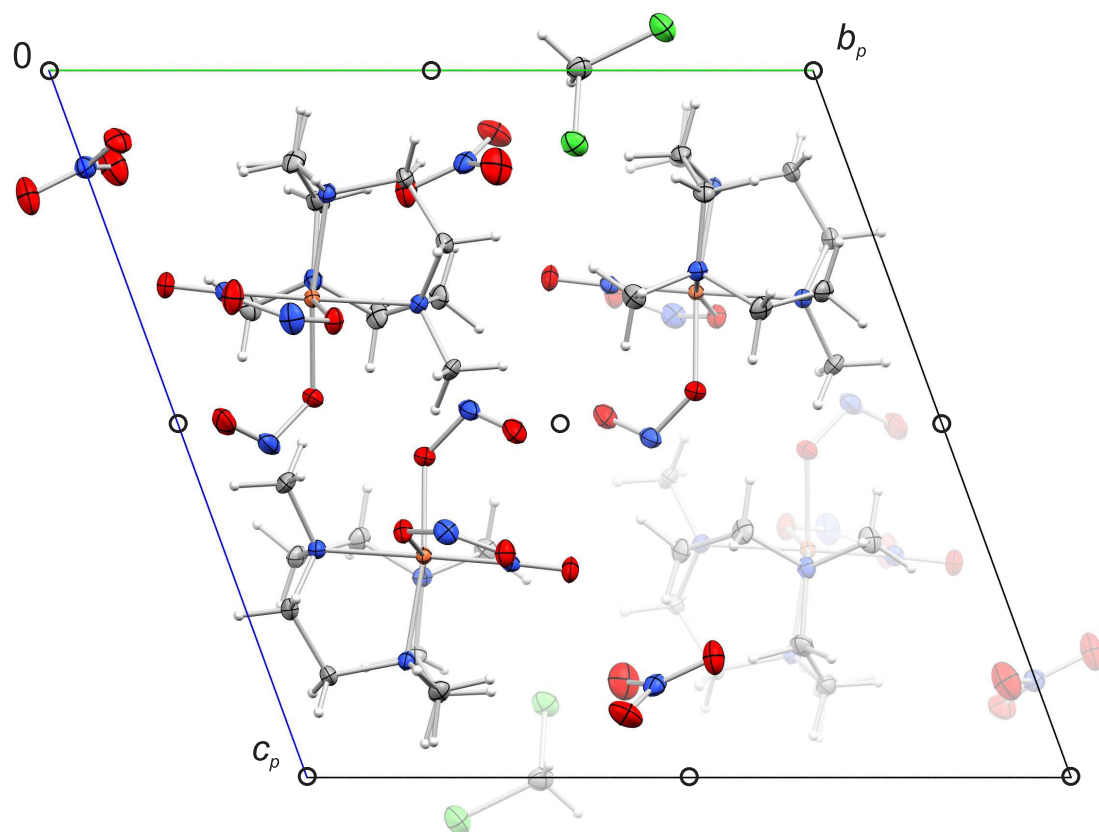


**Figure 6.100:** Packaging diagram of **15a** · 0.5DCM in the triclinic space group  $P\bar{1}$  with view along [100]. Symmetry elements of the respective space group are overlaid. Atoms: carbon(grey), hydrogen(white), chlorine(green), iron(orange), nitrogen(blue), oxygen(red).

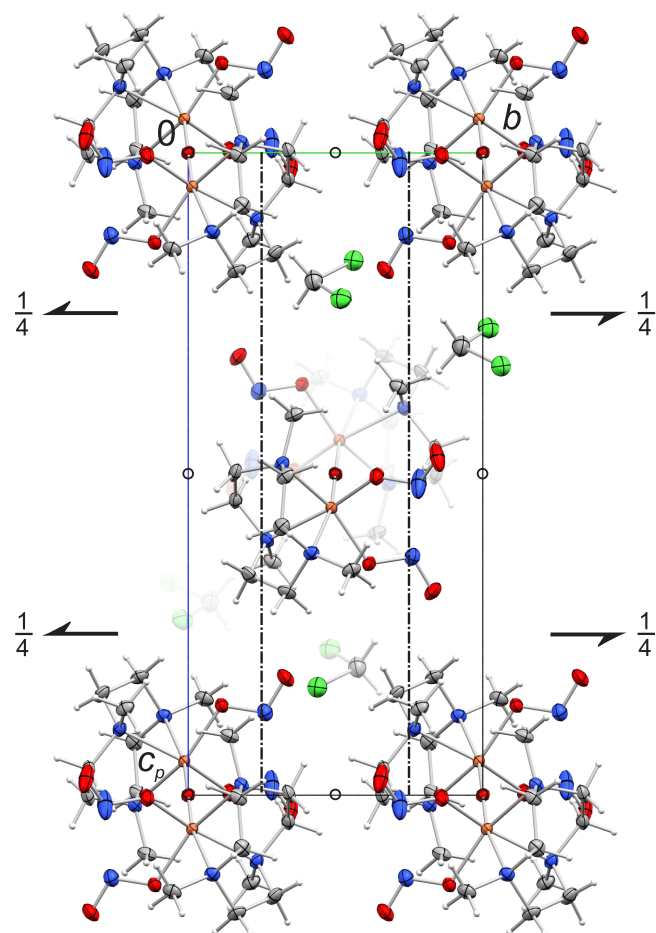


**Figure 6.101:** Packaging diagram of  $15b \cdot 2DCM$  in the monoclinic space group  $P2_1/n$  with view along  $[100]$ . Symmetry elements of the respective space group are overlaid. Atoms: carbon(grey), hydrogen(white), chlorine(green), iron(orange), nitrogen(blue), oxygen(red).

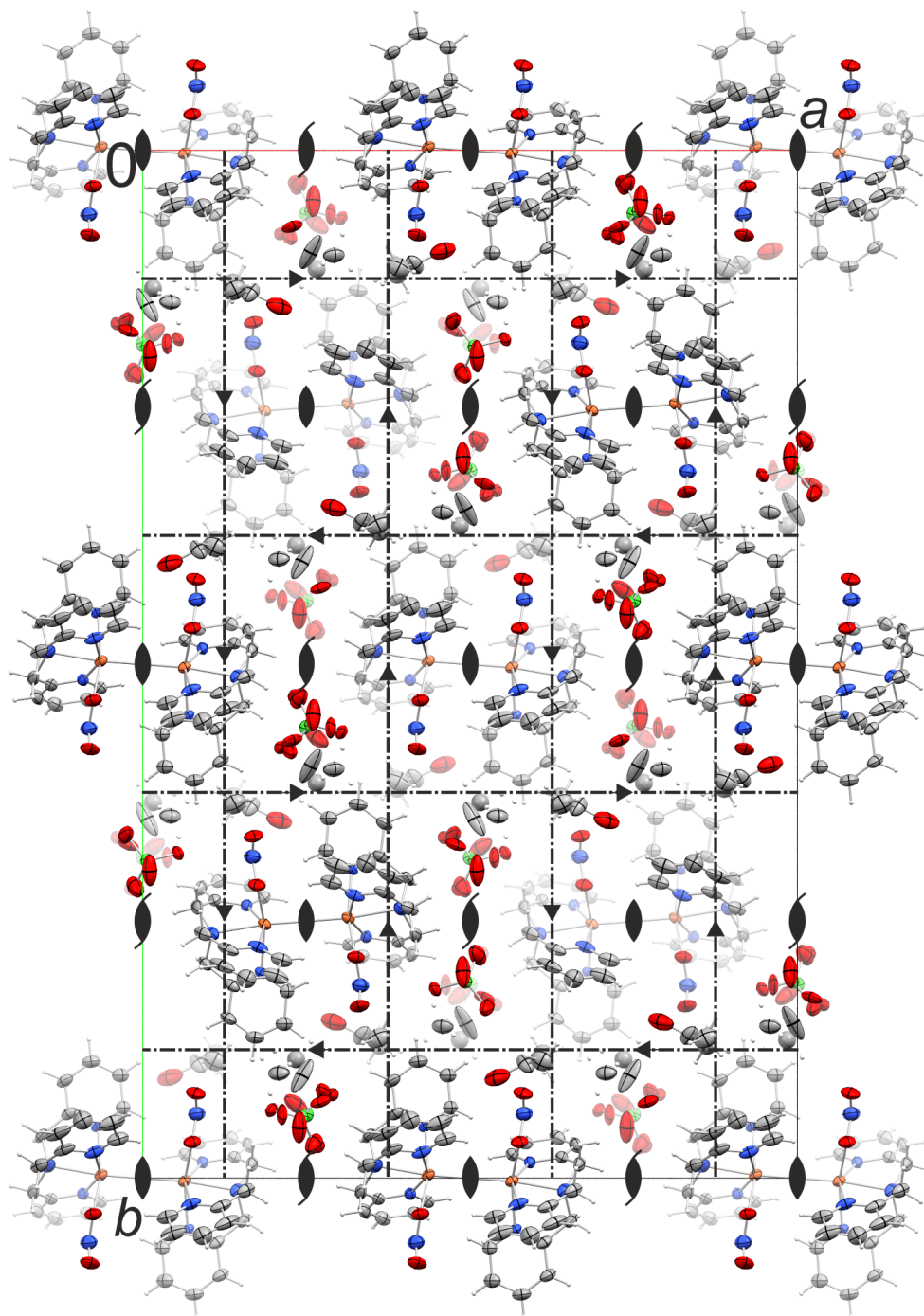


**Figure 6.102:** Packaging diagram of  $16a \cdot 2C_3H_6O$  in the orthorhombic space group  $Fdd2$  with view along  $[001]$ . Symmetry elements of the respective space group are overlaid. Atoms: carbon(grey), hydrogen(white), chlorine(green), iron(orange), nitrogen(blue), oxygen(red).

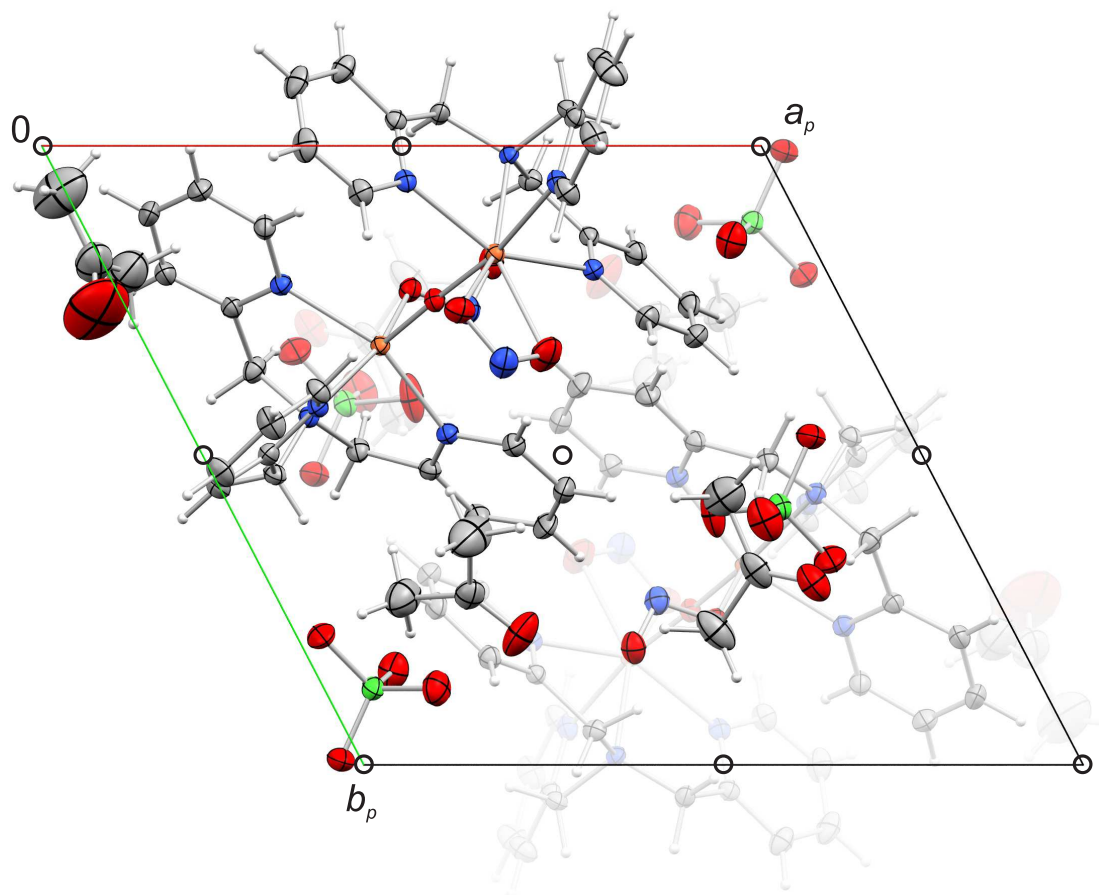


**Figure 6.103:** Packaging diagram of **16b** · 3C<sub>3</sub>H<sub>6</sub>O in the triclinic space group  $P\bar{1}$  with view along [001]. Symmetry elements of the respective space group are overlaid. Atoms: carbon(grey), hydrogen(white), chlorine(green), iron(orange), nitrogen(blue), oxygen(red).

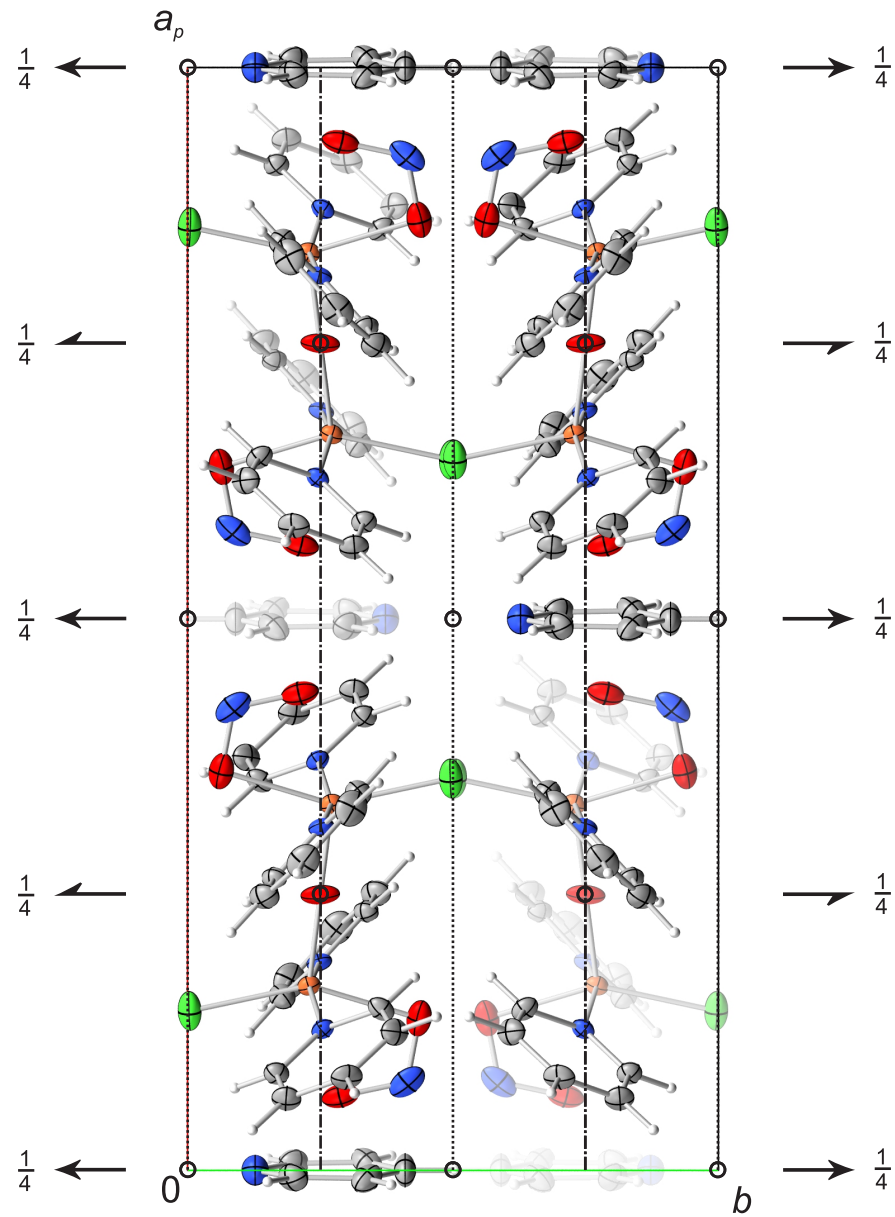


**Figure 6.104:** Packaging diagram of  $17 \cdot \text{py}$  in the monoclinic space group  $C2/c$  with view along  $[001]$ . Symmetry elements of the respective space group are overlaid. Atoms: carbon(grey), hydrogen(white), chlorine(green), iron(orange), nitrogen(blue), oxygen(red).

## 6.2 Crystallographic tables

	<b>P1</b>	<b>P5</b>	<b>P6</b>
empirical formula	C <sub>24</sub> H <sub>32</sub> ClF <sub>24</sub> FeN <sub>2</sub> O <sub>4</sub>	C <sub>30</sub> H <sub>28</sub> Cl <sub>2</sub> FeN <sub>3</sub> O <sub>4</sub>	C <sub>28</sub> H <sub>42</sub> Cl <sub>2</sub> FeN <sub>3</sub> O <sub>4</sub>
M <sub>r</sub> /g mol <sup>-1</sup>	959.81	621.3	611.39
crystal system	monoclinic	triclinic	monoclinic
space group	<i>P</i> 2 <sub>1</sub> / <i>c</i>	<i>P</i> $\bar{1}$	<i>P</i> 2 <sub>1</sub> / <i>n</i>
a/Å	10.9477(5)	9.2507(4)	21.1203(11)
b/Å	14.3274(6)	16.0287(5)	13.0032(7)
c/Å	21.9917(9)	20.6735(7)	23.0163(12)
α/°	90	110.262(1)	90
β/°	90.074(2)	97.971(1)	107.141(2)
γ/°	90	92.101(1)	90
V/Å <sup>3</sup>	3449.4(3)	2836.07(2)	6040.2(6)
Z	4	4	8
ρ <sub>calc</sub> /g cm <sup>-3</sup>	1.848	1.455	1.345
μ/mm <sup>-1</sup>	0.681	0.761	0.713
crystal size/mm	0.10×0.10×0.05	0.04×0.04×0.02	0.09×0.08×0.07
T/K	102(2)	102(2)	102(2)
diffractometer	Bruker D8Venture	Bruker D8Venture	Bruker D8Venture
radiation	MoK <sub>α</sub>	MoK <sub>α</sub>	MoK <sub>α</sub>
anode	rotating anode	rotating anode	rotating anode
rated input/kW	2.5	2.5	2.5
Θ-range/°	2.987–27.12	2.506–27.13	2.829–26.41
reflexes for metric	9895	7078	9131
absorption correction	multi-scan	multi-scan	multi-scan
transmission factors	0.6937–0.7455	0.6919–0.7455	0.5613–0.7454
reflexes measured	78227	53075	93675
independent reflexes	7609	12421	12375
R <sub>int</sub>	0.0774	0.0577	0.0604
mean σ(I)/I	0.080	0.084	0.084
reflexes with I ≥ 2σ(I)	5672	7926	8247
x,y (weighting scheme)	0.0221, 2.8838	0.0384, 2.1854	0.0456, 13.8857
hydrogen refinement	<i>a</i>	<i>a</i>	<i>a</i>
parameter	511	727	693
restraints	0	0	0
R(F <sub>obs</sub> )	0.0376	0.0484	0.0541
R <sub>w</sub> (F <sup>2</sup> )	0.0864	0.1197	0.1498
S	1.090	1.017	1.072
shift/error <sub>max</sub>	0.001	0.001	0.001
max. el. density/eÅ <sup>-3</sup>	0.473	0.911	0.654
min. el. density/eÅ <sup>-3</sup>	-0.445	-0.532	-0.627
measurement code	yv112	yv446	xv714

**Table 22:** Crystallographic data of (HNEt<sub>3</sub>)<sub>2</sub>[FeCl(fpin)<sub>2</sub>] (**P1**), (NBnMe<sub>3</sub>)[FeCl<sub>2</sub>(qu)<sub>2</sub>] (**P5**) and (NEt<sub>4</sub>)[Fe(Bn<sub>2</sub>edda)Cl<sub>2</sub>] (**P6**). <sup>a</sup> All hydrogen atoms were calculated in idealized positions, riding on their parent atoms. U<sub>iso</sub> was always coupled to the parent atom.

	<b>P7</b> · 2MeCN	<b>P9</b> · 2MeCN	<b>P13</b>
empirical formula	C <sub>32</sub> H <sub>62</sub> Cl <sub>2</sub> Fe <sub>2</sub> N <sub>6</sub> O <sub>10</sub>	C <sub>32</sub> H <sub>40</sub> Cl <sub>4</sub> Fe <sub>2</sub> N <sub>8</sub> O <sub>3</sub>	C <sub>11</sub> H <sub>9</sub> Cl <sub>3</sub> FeN <sub>5</sub>
M <sub>r</sub> /g mol <sup>-1</sup>	873.47	838.22	373.43
crystal system	monoclinic	triclinic	monoclinic
space group	<i>P2</i> <sub>1</sub> / <i>c</i>	<i>P</i> $\bar{1}$	<i>P2</i> <sub>1</sub> / <i>n</i>
a/Å	10.6230(2)	9.0073(6)	7.6746(5)
b/Å	13.3929(2)	10.4438(8)	13.1478(7)
c/Å	14.3952(2)	11.4709(8)	14.4541(8)
α/°	90	107.712(2)	90
β/°	93.288(6)	111.349(2)	100.501(2)
γ/°	90	90.389(3)	90
V/Å <sup>3</sup>	2044.7(5)	948.95(12)	1434.05(14)
Z	2	1	4
ρ <sub>calc</sub> /g cm <sup>-3</sup>	1.419	1.467	1.730
μ/mm <sup>-1</sup>	0.898	1.090	1.605
crystal size/mm	0.04×0.04×0.02	0.05×0.05×0.02	0.08×0.07×0.06
T/K	108(2)	102(2)	110(2)
diffractometer	Bruker D8Venture	Bruker D8Venture	Bruker D8Venture
radiation	MoK <sub>α</sub>	MoK <sub>α</sub>	MoK <sub>α</sub>
anode	rotating anode	rotating anode	rotating anode
rated input/kW	2.5	2.5	2.5
Θ-range/°	3.217–26.37	2.988–26.38	2.816–25.36
reflexes for metric	7116	5610	8465
absorption correction	multi-scan	multi-scan	multi-scan
transmission factors	0.6110–0.7454	0.6814–0.7454	0.6090–0.7452
reflexes measured	30743	19437	20106
independent reflexes	4181	3892	2605
R <sub>int</sub>	0.0828	0.0542	0.0450
mean σ(I)/I	0.081	0.092	0.096
reflexes with I ≥ 2σ(I)	3351	2925	2099
x,y (weighting scheme)	0.0394, 1.1938	0.0645, 0.3880	0.0274, 5.1331
hydrogen refinement	<i>a</i>	<i>b</i>	<i>a</i>
parameter	240	228	181
restraints	0	0	0
R(F <sub>obs</sub> )	0.0402	0.0456	0.0437
R <sub>w</sub> (F <sup>2</sup> )	0.1065	0.1287	0.1002
S	1.030	1.081	1.062
shift/error <sub>max</sub>	0.001	0.001	0.001
max. el. density/eÅ <sup>-3</sup>	0.420	0.588	0.870
min. el. density/eÅ <sup>-3</sup>	-0.482	-0.668	-0.534
measurement code	xv028	xv569	wv416

**Table 23:** Crystallographic data of (NEt<sub>4</sub>)<sub>2</sub>[Fe<sub>2</sub>Cl<sub>2</sub>(μ-heida)<sub>2</sub>] · 2MeCN (**P7** · 2MeCN), [Fe<sub>2</sub>Cl<sub>2</sub>(Hbpmca)<sub>2</sub>(μ-O)]Cl<sub>2</sub> · 2MeCN (**P9** · 2MeCN) and [Fe(bipzpy)Cl<sub>3</sub>] (**P13**). <sup>a</sup> All hydrogen atoms were calculated in idealized positions, riding on their parent atoms. U<sub>iso</sub> was always coupled to the parent atom. <sup>b</sup> Coordinates of hydrogen atoms bonded to oxygen were refined freely. All other hydrogen atoms were calculated in idealized positions, riding on their parent atoms. U<sub>iso</sub> was always coupled to the parent atom.

	<b>P14</b>	<b>P16</b>
empirical formula	C <sub>11</sub> H <sub>9</sub> Br <sub>3</sub> FeN <sub>5</sub>	C <sub>18</sub> H <sub>18</sub> Cl <sub>3</sub> FeN <sub>4</sub> O <sub>4</sub>
M <sub>r</sub> /g mol <sup>-1</sup>	506.81	516.56
crystal system	monoclinic	orthorhombic
space group	<i>C</i> 2/ <i>c</i>	<i>P</i> 2 <sub>1</sub> 2 <sub>1</sub> 2 <sub>1</sub>
a/Å	10.8180(7)	8.6201(3)
b/Å	11.1248(7)	15.4581(6)
c/Å	12.9176(11)	16.0030(5)
α/°	90	90
β/°	100.205(4)	90
γ/°	90	90
V/Å <sup>3</sup>	1530.01(2)	2132.41(13)
Z	4	4
ρ <sub>calc</sub> /g cm <sup>-3</sup>	2.200	1.609
μ/mm <sup>-1</sup>	8.816	1.116
crystal size/mm	0.08×0.08×0.06	0.10×0.02×0.02
T/K	107(2)	112(2)
diffractometer	Bruker D8Venture	Bruker D8Venture
radiation	MoK <sub>α</sub>	MoK <sub>α</sub>
anode	rotating anode	rotating anode
rated input/kW	2.5	2.5
Θ-range/°	3.205–27.17	2.990–26.48
reflexes for metric	4500	9975
absorption correction	multi-scan	multi-scan
transmission factors	0.6439–0.7455	0.6839–0.7454
reflexes measured	15520	32198
independent reflexes	1693	4362
R <sub>int</sub>	0.0713	0.0542
mean σ(I)/I	0.131	0.056
reflexes with I ≥ 2σ(I)	1401	3947
x,y (weighting scheme)	0.0144, 3.8710	0.0170, 0.7181
hydrogen refinement	<i>a</i>	<i>a</i>
Flack-parameter	-	0.005(11)
parameter	93	271
restraints	0	0
R(F <sub>obs</sub> )	0.0282	0.0287
R <sub>w</sub> (F <sup>2</sup> )	0.0624	0.0636
S	1.041	1.070
shift/error <sub>max</sub>	0.001	0.001
max. el. density/eÅ <sup>-3</sup>	0.569	0.242
min. el. density/eÅ <sup>-3</sup>	-0.625	-0.293
measurement code	wv549	wv651

**Table 24:** Crystallographic data of [Fe(bipzpy)Br<sub>3</sub>] (**P14**) and [FeCl<sub>2</sub>(tpya)](ClO<sub>4</sub>) (**P16**). <sup>a</sup> All hydrogen atoms were calculated in idealized positions, riding on their parent atoms. U<sub>iso</sub> was always coupled to the parent atom.

	<b>1a-Al</b>	<b>1a-Sc</b>	<b>1a-Cr</b>
empirical formula	C <sub>24</sub> H <sub>32</sub> AlF <sub>24</sub> N <sub>3</sub> O <sub>6</sub>	C <sub>24</sub> H <sub>32</sub> F <sub>24</sub> N <sub>3</sub> O <sub>6</sub> Sc	C <sub>24</sub> H <sub>32</sub> CrF <sub>24</sub> N <sub>3</sub> O <sub>6</sub>
M <sub>r</sub> /g mol <sup>-1</sup>	941.5	959.48	966.52
crystal system	monoclinic	monoclinic	monoclinic
space group	<i>P</i> 2 <sub>1</sub> / <i>c</i>	<i>P</i> 2 <sub>1</sub> / <i>c</i>	<i>P</i> 2 <sub>1</sub> / <i>c</i>
a/Å	10.8307(6)	11.0065(8)	11.3258(8)
b/Å	14.7714(7)	14.6336(10)	14.4332(10)
c/Å	21.8101(12)	22.0791(18)	21.8219(16)
α/°	90	90	90
β/°	90.363(2)	90.265(3)	90.386(2)
γ/°	90	90	90
V/Å <sup>3</sup>	3489.2(3)	3556.1(5)	3567.1(4)
Z	4	4	4
ρ <sub>calc</sub> /g cm <sup>-3</sup>	1.792	1.792	1.800
μ/mm <sup>-1</sup>	0.231	0.376	0.490
crystal size/mm	0.06×0.05×0.04	0.09×0.08×0.07	0.10×0.03×0.03
T/K	104(2)	102(2)	102(2)
diffractometer	Bruker D8Venture	Bruker D8Venture	Bruker D8Venture
radiation	MoK <sub>α</sub>	MoK <sub>α</sub>	MoK <sub>α</sub>
anode	rotating anode	rotating anode	rotating anode
rated input/kW	2.5	2.5	2.5
Θ-range/°	1.867–26.40	2.966–27.14	2.601–27.17
reflexes for metric	8316	9856	9979
absorption correction	multi-Scan	multi-scan	multi-Scan
transmission factors	0.6692–0.7454	0.6934–0.7455	0.6946–0.7455
reflexes measured	62742	66085	87249
independent reflexes	7131	7813	7901
R <sub>int</sub>	0.0754	0.0428	0.0684
mean σ(I)/I	0.082	0.055	0.057
reflexes with I ≥ 2σ(I)	5053	6634	5511
x,y (weighting scheme)	0.0672, 2.2418	0.0311, 2.2122	0.0362, 3.4853
hydrogen refinement	<sup>a</sup>	<sup>a</sup>	<sup>a</sup>
parameter	565	533	897
restraints	3	0	450
R(F <sub>obs</sub> )	0.0513	0.0322	0.0443
R <sub>w</sub> (F <sup>2</sup> )	0.1357	0.0837	0.1156
S	1.024	1.053	1.064
shift/error <sub>max</sub>	0.001	0.001	0.001
max. el. density/eÅ <sup>-3</sup>	0.503	0.411	0.399
min. el. density/eÅ <sup>-3</sup>	−0.369	−0.326	−0.426
measurement code	yv576	xv758	yv250

**Table 25:** Crystallographic data of (HNEt<sub>3</sub>)<sub>2</sub>[Al(fpin)<sub>2</sub>(NO<sub>2</sub>-κ<sup>2</sup>O)] (**1a-Al**), (HNEt<sub>3</sub>)<sub>2</sub>[Sc(fpin)<sub>2</sub>(NO<sub>2</sub>-κ<sup>2</sup>O, O')] (**1a-Sc**) and (HNEt<sub>3</sub>)<sub>2</sub>[Cr(fpin)<sub>2</sub>(NO<sub>2</sub>)] (**1a-Cr**). <sup>a</sup> Coordinates of hydrogen atoms bonded to nitrogen were refined freely. All other hydrogen atoms were calculated in idealized positions, riding on their parent atoms. U<sub>iso</sub> was always coupled to the parent atom.

	<b>1a-Fe</b>	<b>1a-Ga</b>	<b>1a-In</b>
empirical formula	C <sub>24</sub> H <sub>32</sub> F <sub>24</sub> FeN <sub>3</sub> O <sub>6</sub>	C <sub>24</sub> H <sub>32</sub> F <sub>24</sub> GaN <sub>3</sub> O <sub>6</sub>	C <sub>24</sub> H <sub>32</sub> F <sub>24</sub> InN <sub>3</sub> O <sub>6</sub>
M <sub>r</sub> /g mol <sup>-1</sup>	970.37	984.24	1029.34
crystal system	monoclinic	monoclinic	monoclinic
space group	<i>P2<sub>1</sub>/c</i>	<i>P2<sub>1</sub>/c</i>	<i>P2<sub>1</sub>/c</i>
a/Å	10.9462(4)	10.8409(2)	10.9806(16)
b/Å	14.6043(6)	14.8151(4)	14.6346(18)
c/Å	21.8919(7)	21.8825(6)	22.101(3)
α/°	90	90	90
β/°	90.5270(10)	91.0440(10)	90.424(5)
γ/°	90	90	90
V/Å <sup>3</sup>	3499.5(2)	3513.94(15)	3551.4(8)
Z	4	4	4
ρ <sub>calc</sub> /g cm <sup>-3</sup>	1.842	1.860	1.925
μ/mm <sup>-1</sup>	0.603	0.955	0.835
crystal size/mm	0.07×0.03×0.03	0.07×0.03×0.03	0.05×0.05×0.01
T/K	100(2)	102(2)	102(2)
diffractometer	Bruker D8Venture	Bruker D8Venture	Bruker D8Venture
radiation	MoK <sub>α</sub>	MoK <sub>α</sub>	MoK <sub>α</sub>
anode	rotating anode	rotating anode	rotating anode
rated input/kW	2.5	2.5	2.5
Θ-range/°	3.121–25.71	2.903–27.11	2.932–27.12
reflexes for metric	9985	9983	9832
absorption correction	multi-scan	multi-scan	multi-scan
transmission factors	0.7002–0.7453	0.6868–0.7455	0.8866–0.9538
reflexes measured	49841	72651	74027
independent reflexes	6676	7736	7827
R <sub>int</sub>	0.0447	0.0634	0.0793
mean σ(I)/I	0.065	0.078	0.105
reflexes with I ≥ 2σ(I)	5341	6099	6710
x,y (weighting scheme)	0.0234, 3.9118	0.0345, 5.6556	0.0424, 5.7292
hydrogen refinement	<i>a</i>	<i>a</i>	<i>a</i>
parameter	537	563	536
restraints	3	3	0
R(F <sub>obs</sub> )	0.0377	0.0411	0.0372
R <sub>w</sub> (F <sup>2</sup> )	0.0785	0.099	0.0999
S	1.048	1.038	1.034
shift/error <sub>max</sub>	0.001	0.001	0.004
max. el. density/eÅ <sup>-3</sup>	0.644	0.987	1.394
min. el. density/eÅ <sup>-3</sup>	-0.411	-0.439	-0.476
measurement code	wv136	yv588	yv596

**Table 26:** Crystallographic data of (HNEt<sub>3</sub>)<sub>2</sub>[Fe(fpin)<sub>2</sub>(NO<sub>2</sub>-κ<sup>2</sup>O,O')] (**1a-Fe**), (HNEt<sub>3</sub>)<sub>2</sub>[Ga(fpin)<sub>2</sub>(NO<sub>2</sub>-κO)] (**1a-Ga**) and (HNEt<sub>3</sub>)<sub>2</sub>[In(fpin)<sub>2</sub>(NO<sub>2</sub>-κ<sup>2</sup>O,O')] (**1a-In**). <sup>a</sup> Coordinates of hydrogen atoms bonded to nitrogen were refined freely. All other hydrogen atoms were calculated in idealized positions, riding on their parent atoms. U<sub>iso</sub> was always coupled to the parent atom.

	<b>1a-Tl</b>	<b>1a-Bi</b>
empirical formula	C24H32F24N3O6Tl	C24H32BiF24N3O6
$M_r/\text{g mol}^{-1}$	1118.89	1123.5
crystal system	monoclinic	monoclinic
space group	$P2_1/c$	$P2_1/n$
$a/\text{\AA}$	16.7040(18)	17.5150(14)
$b/\text{\AA}$	15.5840(18)	10.8211(9)
$c/\text{\AA}$	13.6332(15)	20.6268(15)
$\alpha/^\circ$	90	90
$\beta/^\circ$	93.465(4)	110.915(3)
$\gamma/^\circ$	90	90
$V/\text{\AA}^3$	3542.4(7)	3651.8(5)
$Z$	4	4
$\rho_{\text{calc}}/\text{g cm}^{-3}$	2.098	2.043
$\mu/\text{mm}^{-1}$	4.73	4.993
crystal size/mm	0.09×0.05×0.05	0.07×0.06×0.02
$T/\text{K}$	100(2)	173(2)
diffractometer	Bruker D8Venture	Bruker D8Venture
radiation	MoK $_{\alpha}$	MoK $_{\alpha}$
anode	rotating anode	rotating anode
rated input/kW	2.5	2.5
$\Theta$ -range/ $^\circ$	2.994–27.11	2.831–30.56
reflexes for metric	9808	9870
absorption correction	multi-scan	multi-scan
transmission factors	0.5680–0.7455	0.6294–0.7461
reflexes measured	63061	74493
independent reflexes	7836	11171
$R_{\text{int}}$	0.0356	0.0451
mean $\sigma(\text{I})/\text{I}$	0.109	0.093
reflexes with $\text{I} \geq 2\sigma(\text{I})$	6320	9318
x,y (weighting scheme)	0.000, 12.3494	0.0115, 2.4694
hydrogen refinement	$a$	$a$
parameter	537	595
restraints	0	6
$R(F_{\text{obs}})$	0.0272	0.0265
$R_w(F^2)$	0.0567	0.0538
$S$	1.06	1.012
shift/error $_{\text{max}}$	0.001	0.003
max. el. density/ $\text{e}\text{\AA}^{-3}$	2.897	0.448
min. el. density/ $\text{e}\text{\AA}^{-3}$	−1.599	−0.737
measurement code	yv638	yv698

**Table 27:** Crystallographic data of (HNEt $_3$ ) $_2$ [Tl(fpin) $_2$ (NO $_2$ - $\kappa^2$ O, O')] (**1a-Tl**) and (HNEt $_3$ ) $_2$ [Bi(fpin) $_2$ (NO $_2$ - $\kappa^2$ O, O')] (**1a-Bi**). <sup>a</sup> Coordinates of hydrogen atoms bonded to nitrogen were refined freely. All other hydrogen atoms were calculated in idealized positions, riding on their parent atoms.  $U_{\text{iso}}$  was always coupled to the parent atom.

	<b>1b</b>	<b>2 · MeCN</b>	<b>3 · 2MeCN</b>
empirical formula	C <sub>86</sub> H <sub>66</sub> F <sub>24</sub> Fe <sub>2</sub> N <sub>4</sub> O <sub>10</sub> P <sub>4</sub>	C <sub>54</sub> H <sub>51</sub> ClFeN <sub>3</sub> O <sub>12</sub> P <sub>4</sub>	C <sub>58</sub> H <sub>58</sub> ClFeN <sub>4</sub> O <sub>12</sub> P <sub>4</sub>
M <sub>r</sub> /g mol <sup>-1</sup>	2007.00	1149.16	1218.26
crystal system	monoclinic	monoclinic	monoclinic
space group	<i>P2</i> <sub>1</sub> / <i>c</i>	<i>P2</i> <sub>1</sub> / <i>c</i>	<i>P2</i> <sub>1</sub> / <i>n</i>
a/Å	12.9585(6)	19.5425(10)	16.0610(11)
b/Å	15.0913(5)	12.6144(6)	19.3959(13)
c/Å	22.2898(8)	23.6664(11)	18.8560(13)
α/°	90	90	90
β/°	96.1150(10)	110.673(2)	96.792(2)
γ/°	90	90	90
V/Å <sup>3</sup>	4334.2(3)	5458.5(5)	5832.8(7)
Z	2	4	4
ρ <sub>calc</sub> /g cm <sup>-3</sup>	1.538	1.398	1.387
μ/mm <sup>-1</sup>	0.521	0.506	0.479
crystal size/mm	0.06×0.05×0.05	0.06×0.06×0.05	0.10×0.10×0.10
T/K	100(2)	108(2)	109(2)
diffractometer	Bruker D8Venture	Bruker D8Venture	Bruker D8Venture
radiation	MoK <sub>α</sub>	MoK <sub>α</sub>	MoK <sub>α</sub>
anode	rotating anode	rotating anode	rotating anode
rated input/kW	2.5	2.5	2.5
Θ-range/°	2.884–27.11	2.448–26.41	2.365–27.13
reflexes for metric	9978	9964	9791
absorption correction	multi-scan	multi-scan	multi-scan
transmission factors	0.6817–0.7455	0.7056–0.7454	0.6612–0.7455
reflexes measured	51568	82266	93273
independent reflexes	9546	11192	12875
R <sub>int</sub>	0.0297	0.0633	0.0551
mean σ(I)/I	0.067	0.071	0.081
reflexes with I ≥ 2σ(I)	7567	8477	9430
x,y (weighting scheme)	0.0401, 3.6227	0.0432, 6.4176	0.0498, 11.8815
hydrogen refinement	<i>a</i>	<i>a</i>	<i>a</i>
parameter	587	702	741
restraints	0	42	0
R(F <sub>obs</sub> )	0.0403	0.0449	0.0524
R <sub>w</sub> (F <sup>2</sup> )	0.1046	0.1210	0.1490
S	1.054	1.054	1.063
shift/error <sub>max</sub>	0.001	0.001	0.001
max. el. density/eÅ <sup>-3</sup>	0.447	0.599	0.562
min. el. density/eÅ <sup>-3</sup>	-0.406	-0.471	-0.861
measurement code	wv114	xv094	xv381

**Table 28:** Crystallographic data of (PPN)<sub>2</sub>[Fe<sub>2</sub>(fpin)<sub>2</sub>(NO<sub>2</sub>-κO)<sub>2</sub>(μ-OMe)<sub>2</sub>] (**1b**), [Fe(dppe(O)<sub>2</sub>)<sub>2</sub>(NO<sub>2</sub>-κO)<sub>2</sub>](ClO<sub>4</sub>) · MeCN (**2 · MeCN**) and [Fe(dppp(O)<sub>2</sub>)<sub>2</sub>(NO<sub>2</sub>-κO)<sub>2</sub>](ClO<sub>4</sub>) · 2MeCN (**3 · 2MeCN**). <sup>a</sup> All hydrogen atoms were calculated in idealized positions, riding on their parent atoms. U<sub>iso</sub> was always coupled to the parent atom.

Appendix

	<b>4 · 3MeCN</b>	<b>5 · 2MeCN</b>	<b>6</b>
empirical formula	$C_{142}H_{121}Cl_2Fe_6N_7O_{24}P_8$	$C_{34}H_{34}Cl_{0.2}FeN_{6.8}O_{7.6}$	$C_{28}H_{42}FeN_5O_8$
$M_r/g\ mol^{-1}$	2963.21	722.28	632.51
crystal system	monoclinic	triclinic	triclinic
space group	$C2/c$	$P\bar{1}$	$P\bar{1}$
$a/\text{\AA}$	34.9829(10)	9.8863(6)	11.6282(6)
$b/\text{\AA}$	12.1116(3)	11.4903(9)	12.7866(7)
$c/\text{\AA}$	32.8815(10)	16.3644(11)	21.2804(12)
$\alpha/^\circ$	90	80.472(2)	93.708(2)
$\beta/^\circ$	106.6420(10)	86.184(2)	101.410(2)
$\gamma/^\circ$	90	67.842(2)	90.094(2)
$V/\text{\AA}^3$	13348.3(7)	1697.9(2)	3094.7(3)
$Z$	4	2	4
$\rho_{calc}/g\ cm^{-3}$	1.475	1.413	1.358
$\mu/mm^{-1}$	0.845	0.521	0.542
crystal size/mm	0.04×0.04×0.03	0.06×0.06×0.05	0.06×0.02×0.02
$T/K$	106(2)	102(2)	102(2)
diffractometer	Bruker D8Venture	Bruker D8Venture	Bruker D8Venture
radiation	MoK $_{\alpha}$	MoK $_{\alpha}$	MoK $_{\alpha}$
anode	rotating anode	rotating anode	rotating anode
rated input/kW	2.5	2.5	2.5
$\Theta$ -range/ $^\circ$	2.012–27.15	2.803–27.11	3.120–26.47
reflexes for metric	9965	9435	9871
absorption correction	multi-Scan	multi-scan	multi-scan
transmission factors	0.7019–0.7455	0.7027–0.7455	0.6677–0.7454
reflexes measured	123217	31926	72997
independent reflexes	14677	7454	11711
$R_{int}$	0.0544	0.0431	0.0611
mean $\sigma(I)/I$	0.100	0.054	0.080
reflexes with $I \geq 2\sigma(I)$	11789	5998	8687
x,y (weighting scheme)	0.0432, 116.0389	0.0263, 0.9033	0.0210, 12.1333
hydrogen refinement	$a$	$a$	$a$
parameter	876	475	763
restraints	21	0	0
$R(F_{obs})$	0.0663	0.0382	0.0678
$R_w(F^2)$	0.1565	0.0935	0.1496
$S$	1.089	1.044	1.101
shift/error $_{max}$	0.001	0.001	0.001
max. el. density/ $e\text{\AA}^{-3}$	1.842	0.316	0.577
min. el. density/ $e\text{\AA}^{-3}$	−0.824	−0.512	−0.637
measurement code	yv574	yv459	xv753

**Table 29:** Crystallographic data of  $[\text{Fe}(\text{dppf}(\text{O})_2)_2(\text{NO}_2\text{-}\kappa\text{O})_2](\text{ClO}_4) \cdot 3\text{MeCN}$  (**4 · 3MeCN**),  $(\text{NBnMe}_3)[\text{Fe}(\text{NO}_2\text{-}\kappa\text{O})_2(\text{qu})_2] \cdot 2\text{MeCN}$  (**5 · 2MeCN**) and  $(\text{NEt}_4)[\text{Fe}(\text{Bn}_2\text{edda})(\text{NO}_2\text{-}\kappa\text{O})_2]$  (**6**). <sup>a</sup> All hydrogen atoms were calculated in idealized positions, riding on their parent atoms.  $U_{iso}$  was always coupled to the parent atom.

Appendix

	<b>7</b>	<b>8</b>	<b>9 · 2MeCN</b>
empirical formula	C <sub>28</sub> H <sub>56</sub> Fe <sub>2</sub> N <sub>6</sub> O <sub>14</sub>	C <sub>26</sub> H <sub>38</sub> FeN <sub>5</sub> O <sub>10</sub>	C <sub>32</sub> H <sub>38</sub> Fe <sub>4</sub> N <sub>14</sub> O <sub>16</sub>
M <sub>r</sub> /g mol <sup>-1</sup>	812.48	636.46	1098.16
crystal system	orthorhombic	monoclinic	monoclinic
space group	<i>Pbca</i>	<i>P2<sub>1</sub>/c</i>	<i>P2<sub>1</sub>/c</i>
a/Å	12.749(2)	24.9074(11)	8.6707(6)
b/Å	14.137(2)	10.5084(5)	15.8581(12)
c/Å	21.338(3)	11.2562(4)	16.2885(13)
α/°	90	90	90
β/°	90	93.4590(10)	97.648(2)
γ/°	90	90	90
V/Å <sup>3</sup>	3845.9(9)	2940.8(2)	2219.8(3)
Z	4	4	2
ρ <sub>calc</sub> /g cm <sup>-3</sup>	1.403	1.438	1.643
μ/mm <sup>-1</sup>	0.823	0.576	1.365
crystal size/mm	0.06×0.06×0.02	0.04×0.04×0.01	0.04×0.02×0.02
T/K	111(2)	108(2)	101(2)
diffractometer	Bruker D8Venture	Bruker D8Venture	Bruker D8Venture
radiation	MoK <sub>α</sub>	MoK <sub>α</sub>	MoK <sub>α</sub>
anode	rotating anode	rotating anode	rotating anode
rated input/kW	2.5	2.5	2.5
Θ-range/°	3.036–26.46	2.104–27.10	3.224–27.14
reflexes for metric	5972	9989	9474
absorption correction	multi-scan	multi-scan	multi-Scan
transmission factors	0.7887–0.8620	0.6748–0.7455	0.6570–0.7455
reflexes measured	57494	46959	41062
independent reflexes	3499	6490	4744
R <sub>int</sub>	0.1080	0.0471	0.0645
mean σ(I)/I	0.078	0.061	0.105
reflexes with I ≥ 2σ(I)	2249	5134	3400
x,y (weighting scheme)	0.0326, 5.2537	0.0332, 2.4250	0.0176, 6.1010
hydrogen refinement	<i>a</i>	<i>a</i>	<i>a</i>
parameter	230	385	299
restraints	0	0	0
R(F <sub>obs</sub> )	0.0396	0.0383	0.0509
R <sub>w</sub> (F <sup>2</sup> )	0.1115	0.0931	0.0986
S	1.048	1.042	1.062
shift/error <sub>max</sub>	0.001	0.001	0.001
max. el. density/eÅ <sup>-3</sup>	0.477	0.750	0.511
min. el. density/eÅ <sup>-3</sup>	-0.521	-0.371	-0.555
measurement code	xv041	xv350	xv675

**Table 30:** Crystallographic data of (NEt<sub>4</sub>)<sub>2</sub>[Fe<sub>2</sub>(μ-heida)<sub>2</sub>(NO<sub>2</sub>-κO)<sub>2</sub>] (**7**), (NBnMe<sub>3</sub>)<sub>2</sub>[Fe(NO<sub>2</sub>-κ<sup>2</sup>O,O')(NO<sub>2</sub>-κO)(nta)] (**8**) and [Fe<sub>4</sub>(μ-bpmea)<sub>2</sub>(Z-NO<sub>2</sub>-κO)<sub>2</sub>(E-NO<sub>2</sub>-κO)<sub>4</sub>(μ<sub>3</sub>-O)<sub>2</sub>] · 2MeCN (**9** · 2MeCN). <sup>a</sup> All hydrogen atoms were calculated in idealized positions, riding on their parent atoms. U<sub>iso</sub> was always coupled to the parent atom.

## Appendix

	<b>10</b>	<b>11</b>	<b>12</b>
empirical formula	C <sub>36</sub> H <sub>34</sub> Fe <sub>2</sub> N <sub>8</sub> O <sub>8</sub>	C <sub>24</sub> H <sub>30</sub> FeN <sub>3</sub> O <sub>4</sub>	C <sub>32</sub> H <sub>46</sub> FeN <sub>3</sub> O <sub>4</sub>
M <sub>r</sub> /g mol <sup>-1</sup>	818.41	480.36	592.57
crystal system	monoclinic	monoclinic	monoclinic
space group	<i>P2</i> <sub>1</sub> / <i>n</i>	<i>P2</i> <sub>1</sub> / <i>n</i>	<i>P2</i> <sub>1</sub> / <i>n</i>
a/Å	10.4790(4)	9.8952(3)	9.9319(4)
b/Å	13.2608(4)	16.8620(5)	18.5351(6)
c/Å	13.3112(4)	14.6176(5)	17.4142(6)
α/°	90	90	90
β/°	103.1190(10)	103.0170(10)	104.6980(10)
γ/°	90	90	90
V/Å <sup>3</sup>	1801.45(10)	2376.31(13)	3100.85(19)
Z	2	4	4
ρ <sub>calc</sub> /g cm <sup>-3</sup>	1.509	1.343	1.269
μ/mm <sup>-1</sup>	0.87	0.669	0.526
crystal size/mm	0.09×0.08×0.07	0.10×0.08×0.04	0.04×0.04×0.03
T/K	102(2)	173(2)	105(2)
diffractometer	Bruker D8Venture	Bruker D8Venture	Bruker D8Venture
radiation	MoK <sub>α</sub>	MoK <sub>α</sub>	MoK <sub>α</sub>
anode	rotating anode	rotating anode	rotating anode
rated input/kW	2.5	2.5	2.5
Θ-range/°	3.200–27.12	3.210–27.51	2.656–27.12
reflexes for metric	9932	9907	9876
absorption correction	multi-scan	multi-Scan	multi-scan
transmission factors	0.6894–0.7455	0.7000–0.7456	0.6949–0.7455
reflexes measured	31523	59493	63795
independent reflexes	3962	5444	6834
R <sub>int</sub>	0.044	0.0546	0.0501
mean σ(I)/I	0.061	0.045	0.055
reflexes with I ≥ 2σ(I)	3461	4408	5758
x,y (weighting scheme)	0.0220, 1.2311	0.0299, 1.2634	0.0312, 2.3388
hydrogen refinement	<sup>a</sup>	<sup>a</sup>	<sup>a</sup>
parameter	245	295	373
restraints	0	0	0
R(F <sub>obs</sub> )	0.0284	0.0344	0.0348
R <sub>w</sub> (F <sup>2</sup> )	0.0735	0.0849	0.0851
S	1.080	1.046	1.041
shift/error <sub>max</sub>	0.001	0.001	0.001
max. el. density/eÅ <sup>-3</sup>	0.319	0.266	0.341
min. el. density/eÅ <sup>-3</sup>	-0.374	-0.330	-0.404
measurement code	yv188	zv232	yv567

**Table 31:** Crystallographic data of [{Fe(NO<sub>2</sub>-κO)(salen)}<sub>2</sub>] · 2MeCN (**10** · 2MeCN), [Fe(NO<sub>2</sub>-κ<sup>2</sup>O,O')(tBu<sub>2</sub>salen)] (**11**) and [Fe(NO<sub>2</sub>-κ<sup>2</sup>O,O')(tBu<sub>4</sub>salen)] (**12**). <sup>a</sup> All hydrogen atoms were calculated in idealized positions, riding on their parent atoms. U<sub>iso</sub> was always coupled to the parent atom.

## Appendix

	<b>13</b> · MeCN	<b>14</b> · MeCN	<b>15a</b> · 0.5DCM
empirical formula	C <sub>13</sub> H <sub>12</sub> Cl <sub>2</sub> FeN <sub>7</sub> O <sub>2</sub>	C <sub>13</sub> H <sub>12</sub> Br <sub>2</sub> FeN <sub>7</sub> O <sub>2</sub>	C <sub>19</sub> H <sub>44</sub> Cl <sub>2</sub> Fe <sub>2</sub> N <sub>14</sub> O <sub>16</sub>
M <sub>r</sub> /g mol <sup>-1</sup>	425.05	513.97	907.28
crystal system	monoclinic	monoclinic	triclinic
space group	<i>P</i> 2 <sub>1</sub> / <i>c</i>	<i>P</i> 2 <sub>1</sub> / <i>c</i>	<i>P</i> $\bar{1}$
a/Å	8.5078(7)	8.5801(4)	9.0018(5)
b/Å	26.7705(16)	27.1477(12)	14.5617(9)
c/Å	7.5163(6)	7.6035(4)	14.8367(9)
α/°	90	90	70.494(2)
β/°	102.856(3)	102.220(2)	75.082(2)
γ/°	90	90	89.474(2)
V/Å <sup>3</sup>	1669.0(2)	1730.95(14)	1765.11(18)
Z	4	4	2
ρ <sub>calc</sub> /g cm <sup>-3</sup>	1.692	1.972	1.707
μ/mm <sup>-1</sup>	1.248	5.511	1.062
crystal size/mm	0.03×0.03×0.01	0.05×0.05×0.03	0.10×0.10×0.03
T/K	112(2)	102(2)	108(2)
diffractometer	Bruker D8Venture	Bruker D8Venture	Bruker D8Venture
radiation	MoK <sub>α</sub>	MoK <sub>α</sub>	MoK <sub>α</sub>
anode	rotating anode	rotating anode	rotating anode
rated input/kW	2.5	2.5	2.5
Θ-range/°	3.353–25.70	2.855–27.13	3.011–26.38
reflexes for metric	2345	8150	9928
absorption correction	multi-scan	multi-scan	multi-scan
transmission factors	0.7242–0.8620	0.6408–0.7455	0.6915–0.7454
reflexes measured	8656	43889	36916
independent reflexes	3144	3809	7202
R <sub>int</sub>	0.0471	0.0635	0.0432
mean σ(I)/I	0.096	0.127	0.069
reflexes with I ≥ 2σ(I)	2134	2851	6162
x,y (weighting scheme)	0.0271, 4.1998	0.0347, 8.7421	0.0276, 1.6382
hydrogen refinement	<sup>a</sup>	<sup>a</sup>	<sup>a</sup>
parameter	227	230	484
restraints	0	0	0
R(F <sub>obs</sub> )	0.0559	0.0410	0.0320
R <sub>w</sub> (F <sup>2</sup> )	0.1108	0.1060	0.0811
S	1.058	1.034	1.045
shift/error <sub>max</sub>	0.001	0.001	0.001
max. el. density/eÅ <sup>-3</sup>	0.604	1.225	0.548
min. el. density/eÅ <sup>-3</sup>	-0.575	-1.103	-0.556
measurement code	wv502	yv226	xv133

**Table 32:** Crystallographic data of [Fe(bipzpy)Cl<sub>2</sub>(NO<sub>2</sub>-κ<sup>2</sup>O,O')] · MeCN (**13** · MeCN), [Fe(bipzpy)Br<sub>2</sub>(NO<sub>2</sub>-κ<sup>2</sup>O,O')] · MeCN (**14** · MeCN) and [Fe(Me<sub>3</sub>tacn)(NO)(NO<sub>2</sub>-κO)<sub>2</sub>](NO<sub>3</sub>) · 0.5DCM (**15a** · 0.5DCM). <sup>a</sup> All hydrogen atoms were calculated in idealized positions, riding on their parent atoms. U<sub>iso</sub> was always coupled to the parent atom.

	<b>15b</b> · 2DCM	<b>16a</b> · 2C <sub>3</sub> H <sub>6</sub> O	<b>16b</b> · 3C <sub>3</sub> H <sub>6</sub> O
empirical formula	C <sub>20</sub> H <sub>46</sub> Cl <sub>4</sub> Fe <sub>2</sub> N <sub>10</sub> O <sub>9</sub>	C <sub>42</sub> H <sub>48</sub> Cl <sub>2</sub> Fe <sub>2</sub> N <sub>10</sub> O <sub>15</sub>	C <sub>45</sub> H <sub>54</sub> Cl <sub>2</sub> Fe <sub>2</sub> N <sub>10</sub> O <sub>16</sub>
M <sub>r</sub> /g mol <sup>-1</sup>	824.17	1115.5	1173.58
crystal system	monoclinic	orthorhombic	triclinic
space group	<i>P</i> 2 <sub>1</sub> / <i>n</i>	<i>F</i> dd2	<i>P</i> $\bar{1}$
a/Å	10.6899(4)	27.7590(10)	13.2684(12)
b/Å	8.6186(3)	43.5581(18)	13.4217(12)
c/Å	18.7957(6)	8.4999(3)	17.3982(18)
α/°	90	90	73.162(3)
β/°	91.0450(10)	90	86.555(3)
γ/°	90	90	62.721(3)
V/Å <sup>3</sup>	1731.40(10)	10277.5(7)	2626.1(4)
Z	2	8	2
ρ <sub>calc</sub> /g cm <sup>-3</sup>	1.581	1.442	1.484
μ/mm <sup>-1</sup>	1.206	0.742	0.731
crystal size/mm	0.06×0.06×0.05	0.10×0.03×0.02	0.08×0.07×0.06
T/K	107(2)	111(2)	102(2)
diffractometer	Bruker D8Venture	Bruker D8Venture	Bruker D8Venture
radiation	MoK <sub>α</sub>	MoK <sub>α</sub>	MoK <sub>α</sub>
anode	rotating anode	rotating anode	rotating anode
rated input/kW	2.5	2.5	2.5
Θ-range/°	3.207–27.11	2.872–27.12	2.985–27.10
reflexes for metric	9897	9973	9990
absorption correction	multi-scan	multi-Scan	multi-scan
transmission factors	0.6976–0.7455	0.6723–0.7455	0.6973–0.7455
reflexes measured	35671	41044	47925
independent reflexes	3807	5657	11476
R <sub>int</sub>	0.0344	0.0477	0.0525
mean σ(I)/I	0.061	0.095	0.077
reflexes with I ≥ 2σ(I)	3195	4858	8975
x,y (weighting scheme)	0.0159, 1.8978	0.1015, 20.1168	0.0266, 3.5441
hydrogen refinement	<i>a</i>	<i>a</i>	<i>a</i>
Flack-parameter	-	0.09(3)	-
parameter	208	399	682
restraints	0	108	3
R(F <sub>obs</sub> )	0.0279	0.0538	0.0453
R <sub>w</sub> (F <sup>2</sup> )	0.0645	0.1659	0.1112
S	1.070	1.097	1.032
shift/error <sub>max</sub>	0.001	0.001	0.001
max. el. density/eÅ <sup>-3</sup>	0.465	1.211	0.842
min. el. density/eÅ <sup>-3</sup>	-0.357	-0.390	-0.519
measurement code	xv272	xv294	yv605

**Table 33:** Crystallographic data of [Fe<sub>2</sub>(Me<sub>3</sub>tacn)<sub>2</sub>(NO<sub>2</sub>-κO)<sub>4</sub>(μ-O)] (**15b**), [Fe(NO<sub>2</sub>-κO)(tpya)<sub>2</sub>(μ-O)](ClO<sub>4</sub>)<sub>2</sub> · 2C<sub>3</sub>H<sub>6</sub>O and [(NO<sub>2</sub>-κO)(tpya)Fe(μ-O)Fe(NO<sub>2</sub>-κ<sup>2</sup>O, O')(tpya)](ClO<sub>4</sub>)<sub>2</sub> · 3C<sub>3</sub>H<sub>6</sub>O (**16a** · 2C<sub>3</sub>H<sub>6</sub>O and **16b** · 3C<sub>3</sub>H<sub>6</sub>O). <sup>a</sup> All hydrogen atoms were calculated in idealized positions, riding on their parent atoms. U<sub>iso</sub> was always coupled to the parent atom.

## 17 · py

empirical formula	C <sub>25</sub> H <sub>25</sub> Cl <sub>2</sub> Fe <sub>2</sub> N <sub>7</sub> O <sub>5</sub>
M <sub>r</sub> /g mol <sup>-1</sup>	686.12
crystal system	monoclinic
space group	C2/c
a/Å	21.6553(7)
b/Å	9.8810(4)
c/Å	14.7161(5)
α/°	90
β/°	108.413(2)
γ/°	90
V/Å <sup>3</sup>	2987.68(2)
Z	4
ρ <sub>calc</sub> /g cm <sup>-3</sup>	1.525
μ/mm <sup>-1</sup>	1.197
crystal size/mm	0.05×0.05×0.04
T/K	109(2)
diffractometer	Bruker D8Venture
radiation	MoK <sub>α</sub>
anode	rotating anode
rated input/kW	2.5
Θ-range/°	2.965–26.03
reflexes for metric	7243
absorption correction	multi-scan
transmission factors	0.6823–0.7453
reflexes measured	29439
independent reflexes	2941
R <sub>int</sub>	0.0855
mean σ(I)/I	0.109
reflexes with I ≥ 2σ(I)	2273
x,y (weighting scheme)	0.0237, 18.7533
hydrogen refinement	<sup>a</sup>
parameter	188
restraints	0
R(F <sub>obs</sub> )	0.0526
R <sub>w</sub> (F <sup>2</sup> )	0.1192
S	1.158
shift/error <sub>max</sub>	0.001
max. electron density/eÅ <sup>-3</sup>	1.071
min. electron density/eÅ <sup>-3</sup>	-0.546
measurement code	wv577

**Table 34:** Crystallographic data of [Fe<sub>2</sub>Cl<sub>2</sub>(NO<sub>2</sub>-κ<sup>2</sup>O,O')<sub>2</sub>(py)<sub>4</sub>(μ-O)] · py (17 · py). <sup>a</sup> All hydrogen atoms were calculated in idealized positions, riding on their parent atoms. U<sub>iso</sub> was always coupled to the parent atom.

## 7 Bibliography

- [1] J. Enemark, R. Feltham, *Coord. Chem. Rev.* **1974**, *13*, 339–406, DOI: 10.1016/s0010-8545(00)80259-3.
- [2] M. C. Stuart, M. Kouimtzi, S. Hill (Eds.), *WHO model formulary 2008*, World Health Organization, **2009**, 60–66.
- [3] V. Ngala, C. Page, M. Page, *Corros. Sci.* **2002**, *44*, 2073–2087, DOI: 10.1016/S0010-938X(02)00012-4.
- [4] H. Beyer, W. Walter, W. Francke, *Lehrbuch der organischen Chemie 24th ed.*, S. Hirzel Verlag, Stuttgart, **2004**, 171–173.
- [5] N. Kornblum, R. A. Smiley, R. K. Blackwood, D. C. Iffland, *J. Am. Chem. Soc.* **1955**, *77*, 6269–6280, DOI: 10.1021/ja01628a064.
- [6] J. H. Silver, *J. Neurol. Neurophy.* **2016**, *7*, 1–7, DOI: 10.4172/2155-9562.1000370.
- [7] J. L. Miljkovic, I. Kenkel, I. Ivanović-Burmazović, M. R. Filipovic, *Angew. Chem. Int. Ed.* **2013**, *52*, 12061–12064, DOI: 10.1002/anie.201305669.
- [8] K. O. Honikel, *Handbook of Fermented Meat and Poultry*, F. Toldra (Ed.), Wiley-Blackwell, Hoboken, New Jersey, United states, **2007**, chapter Principles of Curing, pp. 17–30.
- [9] E. Polenske, *Arbeiten aus dem Kaiserlichen Gesundheitsamte* **1891**, *7*, 471–474, DOI: 10.25646/6387.
- [10] M. D. Pierson, L. A. Smoot, M. C. Robach, *Crit. Rev. Food Sci. Nutr.* **1983**, *17*, 141–187, DOI: 10.1080/10408398209527346.
- [11] L. Siekmann, M. Plötz, C. Krischek, *Curr. Clin. Microbiol. Rep.* **2021**, *8*, 40–48, DOI: 10.1007/s40588-021-00164-w.
- [12] E. Binkerd, O. Kolari, *Food Cosmet. Toxicol.* **1975**, *13*, 655–661, DOI: 10.1016/0015-6264(75)90157-1.
- [13] D. Greenwood, R. C. B. Slack, M. R. Barer, W. L. Irving, *A Guide to Microbial Infections: Pathogenesis, Immunity, Laboratory Diagnosis and Control 18th ed.*, Elsevier Health Sciences, London, United Kingdom, **2012**, 245–255.
- [14] J. E. Grass, L. H. Gould, B. E. Mahon, *Foodborne Pathog. Dis.* **2013**, *10*, 131–136, DOI: 10.1089/fpd.2012.1316.
- [15] K. Katabami, M. Hayakawa, S. Gando, *Case Rep. Emerg. Med.* **2016**, *2016*, 1–3, DOI: 10.1155/2016/9013816.
- [16] W. J. Gowans, *Br. J. Gen. Pract.* **1990**, *40*, 470–471, PMID: 2271282.
- [17] A. Holleman, E. Wiberg, N. Wiberg, *Lehrbuch der anorganischen Chemie 102nd ed.*, Walter de Gruyter, Berlin, **2007**, 723–726.

- [18] M. Baidya, H. Yamamoto, *J. Am. Chem. Soc.* **2011**, *133*, 13880–13882, DOI: 10.1021/ja206736q.
- [19] J. Heinecke, P. C. Ford, *J. Am. Chem. Soc.* **2010**, *132*, 9240–9243, DOI: 10.1021/ja102221e.
- [20] J. C. Beard, T. M. Swager, *J. Org. Chem.* **2021**, *86*, 2037–2057, DOI: 10.1021/acs.joc.0c02774.
- [21] S. Veena, S. Rashmi, *Int. J. Toxicol. Pharmacol. Res.* **2014**, *6*, 86–96.
- [22] Bundesministerium der Justiz und für Verbraucherschutz, <https://www.gesetze-im-internet.de/lmzdv/LMZDV.pdf> **2021**, (access: 20.09.2021).
- [23] The European Parliament and the Council of the European Union, *OJEU* **2008**, 16–34, <https://eur-lex.europa.eu/legal-content/DE/TXT/?uri=OJ:L:2008:354:TOC> (access: 20.09.2021).
- [24] L. B. Maia, J. J. G. Moura, *Chem. Rev.* **2014**, *114*, 5273–5357, DOI: 10.1021/cr400518y.
- [25] A. Rajta, R. Bhatia, H. Setia, P. Pathania, *J. Appl. Microbiol.* **2020**, *128*, 1261–1278, DOI: 10.1111/jam.14476.
- [26] M. Schobert, D. Jahn, *Int. J. Med. Microbiol.* **2010**, *300*, 549–556, DOI: 10.1016/j.ijmm.2010.08.007.
- [27] M. Rudolf, Ph.D. thesis, Universität Konstanz, Konstanz, **2004**.
- [28] A. Werner, *Z. Anorg. Chem.* **1893**, *3*, 267–330, DOI: 10.1002/zaac.18930030136.
- [29] A. Werner, *Z. Anorg. Chem.* **1898**, *16*, 109–166, DOI: 10.1002/zaac.18980160114.
- [30] S. M. Jørgensen, *Z. Anorg. Chem.* **1894**, *5*, 147–196, DOI: 10.1002/zaac.18940050119.
- [31] P. Kar, R. Biswas, M. G. B. Drew, Y. Ida, T. Ishida, A. Ghosh, *Dalton Trans.* **2011**, *40*, 3295–3304, DOI: 10.1039/C0DT01521K.
- [32] R. Kia, F. Safari, *Inorg. Chim. Acta* **2016**, *453*, 357–368, DOI: 10.1016/j.ica.2016.08.041.
- [33] S. K. Brayshaw, T. L. Easun, M. W. George, A. M. E. Griffin, A. L. Johnson, P. R. Raithby, T. L. Savarese, S. Schiffers, J. E. Warren, M. R. Warren, S. J. Teat, *Dalton Trans.* **2012**, *41*, 90–97.
- [34] S. Hematian, I. Kenkel, T. E. Shubina, M. Dürr, J. J. Liu, M. A. Siegler, I. Ivanovic-Burmazovic, K. D. Karlin, *J. Am. Chem. Soc.* **2015**, *137*, 6602–6615, DOI: 10.1021/jacs.5b02174.
- [35] J. Pitarch López, F. W. Heinemann, R. Prakash, B. A. Hess, O. Horner, C. Jeandey, J.-L. Oddou, J.-M. Latour, A. Grohmann, *Chem. Eur. J.* **2002**, *8*, 5709–5722, DOI: 10.1002/1521-3765(20021216)8:24<5709::AID-CHEM5709>3.0.CO;2-I.

- [36] W.-Y. Wu, M.-L. Tsai, Y.-A. Lai, C.-H. Hsieh, W.-F. Liaw, *Inorg. Chem.* **2021**, DOI: 10.1021/acs.inorgchem.1c00541.
- [37] C. R. Groom, I. J. Bruno, M. P. Lightfoot, S. C. Ward, *Acta Cryst. B* **2016**, *72*, 171–179, DOI: 10.1107/S2052520616003954.
- [38] M. A. Hitchman, G. L. Rowbottom, *Coord. Chem. Rev.* **1982**, *42*, 55 – 132, DOI: 10.1016/S0010-8545(00)80527-5.
- [39] D. M. M. M. Dissanayake, B. E. Petel, W. W. Brennessel, K. L. Bren, E. M. Matson, *J. Coord. Chem.* **2020**, *73*, 2664–2676, DOI: 10.1080/00958972.2020.1821373.
- [40] L. Beyer, J. A. Cornejo, *Koordinationschemie*, Vieweg+Teubner Verlag,, **2012**, 21–50.
- [41] I. Levin, *NIST Inorganic Crystal Structure Database (ICSD)*, National Institute of Standards and Technology, **2018**, (Accessed 2021–15–08), DOI: 10.18434/M32147.
- [42] U. Hauser, V. Oestreich, H. D. Rohrweck, *Z. Physik A* **1977**, *280*, 17–25, DOI: 10.1007/BF01438104.
- [43] U. Hauser, V. Oestreich, H. D. Rohrweck, *Z. Physik A* **1977**, *280*, 125–130, DOI: 10.1007/BF01409539.
- [44] U. Hauser, V. Oestreich, H. D. Rohrweck, *Z. Physik A* **1978**, *284*, 9–19, DOI: 10.1007/BF01433868.
- [45] M. D. Carducci, M. R. Pressprich, P. Coppens, *J. Am. Chem. Soc.* **1997**, *119*, 2669–2678, DOI: 10.1021/ja9625743.
- [46] M. R. Warren, T. L. Easun, S. K. Brayshaw, R. J. Deeth, M. W. George, A. L. Johnson, S. Schiffers, S. J. Teat, A. J. Warren, J. E. Warren, C. C. Wilson, C. H. Woodall, P. R. Raithby, *Chem. Eur. J.* **2014**, *20*, 5468–5477, DOI: 10.1002/chem.201302053.
- [47] L. E. Hatcher, J. M. Skelton, M. R. Warren, P. R. Raithby, *Acc. Chem. Res.* **2019**, *52*, 1079–1088, DOI: 10.1021/acs.accounts.9b00018.
- [48] B. Adell, *Z. Anorg. Chem.* **1944**, *252*, 272–280, DOI: 10.1002/zaac.19442520512.
- [49] I. Grenthe, E. Nordin, *Inorg. Chem.* **1979**, *18*, 1109–1116, DOI: 10.1021/ic50194a042.
- [50] D. Schaniel, N. Mockus, T. Woike, A. Klein, D. Sheptyakov, T. Todorova, B. Delley, *Phys. Chem. Chem. Phys.* **2010**, *12*, 6171–6178, DOI: 10.1039/B921723A.
- [51] J. M. Cole, *Chem. Soc. Rev.* **2004**, *33*, 501–513, DOI: 10.1039/b205339j.
- [52] D. Schaniel, M. Imlau, T. Weisemoeller, T. Woike, K. Krämer, H.-U. Güdel, *Adv. Mater.* **2007**, *19*, 723–726, DOI: 10.1002/adma.200601378.
- [53] N. L. Fry, P. K. Mascharak, *Acc. Chem. Res.* **2011**, *44*, 289–298, DOI: 10.1021/ar100155t.

- [54] D. Schaniel, T. Woike, *Phys. Chem. Chem. Phys.* **2009**, *11*, 4391–4395, DOI: 10.1039/b900546c.
- [55] T. Ishikawa, K. Tanaka, *Z. Kristallogr.* **2008**, *223*, 334–342, DOI: 10.1524/zkri.2008.0033.
- [56] M. D. Cohen, *Angew. Chem. Int. Ed.* **1975**, *14*, 386–393, DOI: 10.1002/anie.197503861.
- [57] M. J. Petersson, W. A. Loughlin, I. D. Jenkins, *Chem. Commun.* **2008**, 4493–4494, DOI: 10.1039/B807695B.
- [58] C. R. Hilliard, N. Bhuvanesh, J. A. Gladysz, J. Blümel, *Dalton Trans.* **2012**, *41*, 1742–1754, DOI: 10.1039/c1dt11863c.
- [59] F. F. Arp, N. Bhuvanesh, J. Blümel, *Dalton Trans.* **2019**, *48*, 14312–14325, DOI: 10.1039/c9dt03070k.
- [60] S. Ménage, J.-B. Galey, J. Dumats, G. Hussler, M. Seité, I. G. Luneau, G. Chottard, M. Fontecave, *J. Am. Chem. Soc.* **1998**, *120*, 13370–13382, DOI: 10.1021/ja981123a.
- [61] T. J. Boyle, J. M. Sears, J. A. Greathouse, D. Perales, R. Cramer, O. Staples, A. L. Rheingold, E. N. Coker, T. M. Roper, R. A. Kemp, *Inorg. Chem.* **2018**, *57*, 2402–2415, DOI: 10.1021/acs.inorgchem.7b01350.
- [62] E. C. M. Ording-Wenker, M. A. Siegler, M. Lutz, E. Bouwman, *Dalton Trans.* **2015**, *44*, 12196–12209, DOI: 10.1039/c5dt01041a.
- [63] G. J. P. Britovsek, J. England, A. J. P. White, *Inorg. Chem.* **2005**, *44*, 8125–8134, DOI: 10.1021/ic0509229.
- [64] S. Kundu, W. Y. Kim, J. A. Bertke, T. H. Warren, *J. Am. Chem. Soc.* **2016**, *139*, 1045–1048, DOI: 10.1021/jacs.6b11332.
- [65] D. C. Povey, T. S. Lobana, P. K. Bhatia, *J. Cryst. Spectrosc.* **1991**, *21*, 13–19, DOI: 10.1007/bf01158967.
- [66] W. Zhang, T. S. A. Hor, *Dalton Trans.* **2011**, *40*, 10725–10730, DOI: 10.1039/c1dt10920k.
- [67] M. A. Walters, J. Chaparro, T. Siddiqui, F. Williams, C. Ulku, A. L. Rheingold, *Inorg. Chim. Acta* **2006**, *359*, 3996–4000, DOI: 10.1016/j.ica.2006.03.043.
- [68] T. Matsushita, H. Kono, M. Nishino, T. Shono, *Bull. Chem. Soc. Jpn.* **1982**, *55*, 2581–2587, DOI: 10.1246/bcsj.55.2581.
- [69] R. Duan, C. Hu, X. Li, X. Pang, Z. Sun, X. Chen, X. Wang, *Macromolecules* **2017**, *50*, 9188–9195, DOI: 10.1021/acs.macromol.7b01766.
- [70] D. Gong, X. Jia, B. Wang, X. Zhang, L. Jiang, *J. Organomet. Chem.* **2012**, *702*, 10–18, DOI: 10.1016/j.jorganchem.2011.11.025.
- [71] A. In-Iam, Ph.D. thesis, Ludwig-Maximilians-Universität München, **2020**.

- [72] P. Chaudhuri, M. Winter, K. Wieghardt, S. Gehring, W. Haase, B. Nuber, J. Weiss, *Inorg. Chem.* **1988**, *27*, 1564–1569, DOI: 10.1021/ic00282a011.
- [73] F.-T. Tsai, P.-L. Chen, W.-F. Liaw, *J. Am. Chem. Soc.* **2010**, *132*, 5290–5299, DOI: 10.1021/ja100849r.
- [74] K. Nakamoto, *Infrared and Raman spectra of inorganic and coordination compounds 4th ed.*, John Wiley & Sons, Hoboken, New Jersey, United States, Hoboken, **1986**, 221–227.
- [75] S. Lu, T.-W. Chiou, W.-L. Li, C.-C. Wang, Y.-M. Wang, W.-Z. Lee, T.-T. Lu, W.-F. Liaw, *Inorg. Chem.* **2020**, *59*, 8308–8319, DOI: 10.1021/acs.inorgchem.0c00691.
- [76] B. Aßmann, H. Homborg, *Z. anorg. allg. Chem.* **1996**, *622*, 766–770, DOI: 10.1002/zaac.19966220503.
- [77] B. Aßmann, G. Ostendorp, H. Homborg, *Z. anorg. allg. Chem.* **1995**, *621*, 1708–1714, DOI: 10.1002/zaac.19956211016.
- [78] K. Schweiger, M. Göldner, H. Hückstädt, H. Homborg, *Z. anorg. allg. Chem.* **1999**, *625*, 1693–1699, DOI: 10.1002/(SICI)1521-3749(199910)625:10<1693::AID-ZAAC1693>3.0.CO;2-C.
- [79] J. Heinemann, P. Klüfers, *Z. anorg. allg. Chem.* **2021**, *647*, 1815–1818, DOI: 10.1002/zaac.202000449.
- [80] F. Edelmann, H. Plenio, K. Keller, H. W. Roesky, U. Behrens, *Z. anorg. allg. Chem.* **1988**, *565*, 111–117, DOI: 10.1002/zaac.19885650112.
- [81] A. A. Danopoulos, C. Redshaw, A. Vaniche, G. Wilkinson, B. Hussain-Bates, M. B. Hursthouse, *Polyhedron* **1993**, *12*, 1061–1071, DOI: 10.1016/s0277-5387(00)87185-5.
- [82] J. K. Elinburg, A. S. Hyre, J. McNeely, T. M. Alam, S. Klenner, R. Pöttgen, A. L. Rheingold, L. H. Doerrer, *Dalton Trans.* **2020**, *49*, 13773–13785, DOI: 10.1039/d0dt02837a.
- [83] F.-X. Wurzenberger, Ph.D. thesis, Ludwig-Maximilians-Universität München, **2014**.
- [84] S. Alvarez, *Chem. Rev.* **2015**, *115*, 13447–13483, DOI: 10.1021/acs.chemrev.5b00537.
- [85] L. T. Elrod, E. Kim, *Inorg. Chem.* **2018**, *57*, 2594–2602, DOI: 10.1021/acs.inorgchem.7b02956.
- [86] C. J. White, A. L. Speelman, C. Kupper, S. Demeshko, F. Meyer, J. P. Shanahan, E. E. Alp, M. Hu, J. Zhao, N. Lehnert, *J. Am. Chem. Soc.* **2018**, *140*, 2562–2574, DOI: 10.1021/jacs.7b11464.
- [87] E. Ruiz, J. Cirera, S. Alvarez, *Coord. Chem. Rev.* **2005**, *249*, 2649–2660, DOI: 10.1016/j.ccr.2005.04.010.

- [88] M. Hesse, H. Meier, B. Zeeh, *Spektroskopische Methoden in der organischen Chemie 8th ed.*, Thieme, New York, Stuttgart, **2011**, 40–82.
- [89] N. Arulsamy, D. S. Bohle, B. Hansert, A. K. Powell, A. J. Thomson, S. Wocaldo, *Inorg. Chem.* **1998**, *37*, 746–750, DOI: 10.1021/ic9709537.
- [90] L. Gmelin, *Gmelins Handbuch der Anorganischen Chemie; Eisen, B.*, Verlag Chemie, Berlin, **1932**, 157f.
- [91] P. C. Ford, *Inorg. Chem.* **2010**, *49*, 6226–6239, DOI: 10.1021/ic902073z.
- [92] I. Ivanovic-Burmazovic, M. R. Filipovic, *Inorg. Chem.* **2019**, *58*, 4039–4051, DOI: 10.1021/acs.inorgchem.8b02592.
- [93] D. S. Bolotin, N. A. Bokach, M. Y. Demakova, V. Y. Kukushkin, *Chem. Rev.* **2017**, *117*, 13039–13122, DOI: 10.1021/acs.chemrev.7b00264.
- [94] G. Olah, H. Lin, J. Olah, S. Narang, *Proc. Natl. Acad. Sci. USA* **1978**, *75*, 1045–1049, DOI: 10.1073/pnas.75.3.1045.
- [95] G. Robertson, *Contemp. Org. Synth.* **1995**, *2*, 357–363, DOI: 10.1039/CO9950200357.
- [96] L. Cambi, A. Ferrari, *Gazz. Chim. Ital.* **1951**, 1162–1180.
- [97] G. Monsch, Ph.D. thesis, Ludwig-Maximilians-Universität München, **2020**.
- [98] J. Heinemann, Master's thesis, Ludwig-Maximilians-Universität München, **2018**.
- [99] S. Hong, J. J. Yan, D. G. Karmalkar, K. D. Sutherlin, J. Kim, Y.-M. Lee, Y. Goo, P. K. Mascharak, B. Hedman, K. O. Hodgson, K. D. Karlin, E. I. Solomon, W. Nam, *Chem. Sci.* **2018**, *9*, 6952–6960, DOI: 10.1039/c8sc01962b.
- [100] F.-T. Tsai, Y.-C. Lee, M.-H. Chiang, W.-F. Liaw, *Inorg. Chem.* **2012**, *52*, 464–473, DOI: 10.1021/ic3023437.
- [101] C.-C. Tsou, W.-L. Yang, W.-F. Liaw, *J. Am. Chem. Soc.* **2013**, *135*, 18758–18761, DOI: 10.1021/ja4105864.
- [102] A. C. McQuilken, H. Matsumura, M. Dürr, A. M. Confer, J. P. Sheckelton, M. A. Siegler, T. M. McQueen, I. Ivanović-Burmazović, P. Moënne-Loccoz, D. P. Goldberg, *J. Am. Chem. Soc.* **2016**, *138*, 3107–3117, DOI: 10.1021/jacs.5b12741.
- [103] G. Villar-Acevedo, E. Nam, S. Fitch, J. Benedict, J. Freudenthal, W. Kaminsky, J. A. Kovacs, *J. Am. Chem. Soc.* **2011**, *133*, 1419–1427, DOI: 10.1021/ja107551u.
- [104] C. K. Brozek, J. T. Miller, S. A. Stoian, M. Dincă, *J. Am. Chem. Soc.* **2015**, *137*, 7495–7501, DOI: 10.1021/jacs.5b03761.
- [105] S. Metz, *Inorg. Chem.* **2017**, *56*, 3820–3833, DOI: 10.1021/acs.inorgchem.6b02551.
- [106] S. Ghosh, H. Deka, Y. B. Dangat, S. Saha, K. Gogoi, K. Vanka, B. Mondal, *Dalton Trans.* **2016**, *45*, 10200–10208, DOI: 10.1039/C6DT00826G.

- [107] K. J. Franz, S. J. Lippard, *J. Am. Chem. Soc.* **1999**, *121*, 10504–10512, DOI: 10.1021/ja991664f.
- [108] E. G. Abucayon, D. R. Powell, G. B. Richter-Addo, *J. Am. Chem. Soc.* **2017**, *139*, 9495–9498, DOI: 10.1021/jacs.7b05209.
- [109] F. Bottomley, W. V. F. Brooks, S. G. Clarkson, S.-B. Tong, *J. Chem. Soc. Chem. Commun.* **1973**, 919–920, DOI: 10.1039/C39730000919.
- [110] K. A. Hofmann, *Z. Anorg. Chem.* **1896**, *11*, 278–287, DOI: 10.1002/zaac.18960110124.
- [111] K. A. Hofmann, *Z. Anorg. Chem.* **1896**, *12*, 146–168, DOI: 10.1002/zaac.18960120134.
- [112] W. T. Eckenhoff, A. B. Biernesser, T. Pintauer, *Inorg. Chim. Acta* **2012**, *382*, 84–95, DOI: 10.1016/j.ica.2011.10.016.
- [113] T. Kojima, R. A. Leising, S. Yan, L. Que, *J. Am. Chem. Soc.* **1993**, *115*, 11328–11335, DOI: 10.1021/ja00077a035.
- [114] I. J. Bazley, E. A. Erie, G. M. Feiereisel, C. J. LeWarne, J. M. Peterson, K. L. Sandquist, K. D. Oshin, M. Zeller, *J. Chem. Educ.* **2018**, *95*, 876–881, DOI: 10.1021/acs.jchemed.7b00685.
- [115] J. L. Steele, L. Tahsini, C. Sun, J. K. Elinburg, C. M. Kotyk, J. McNeely, S. A. Stoian, A. Dragulescu-Andrasi, A. Ozarowski, M. Ozerov, J. Krzystek, J. Telser, J. W. Bacon, J. A. Golen, A. L. Rheingold, L. H. Doerrer, *Chem. Commun.* **2018**, *54*, 12045–12048, DOI: 10.1039/c8cc04464c.
- [116] T. Ampßler, G. Monsch, J. Popp, T. Riggermann, P. Salvador, D. Schröder, P. Klüfers, *Angew. Chem. Int. Ed.* **2020**, *59*, 12381–12386, DOI: 10.1002/anie.202003122.
- [117] G. Monsch, P. Klüfers, *Angew. Chem. Int. Ed.* **2019**, *58*, 8566–8571, DOI: 10.1002/anie.201902374.
- [118] K. Sundaravel, E. Suresh, K. Saminathan, M. Palaniandavar, *Dalton Trans.* **2011**, *40*, 8092–8107, DOI: 10.1039/c0dt01598a.
- [119] Y. Nishida, T. Okuno, S. Ito, A. Harada, S. Ohba, H. Matsushima, T. Tokii, *Chem. Lett.* **1995**, *24*, 885–886, DOI: 10.1246/cl.1995.885.
- [120] S. Itoa, T. Okuno, H. Itoha, S. Ohbab, H. Matsushima, T. Tokiic, Y. Nishida, *Z. Naturforsch.* **1997**, *52b*, 719–727.
- [121] G. L. Parrilha, S. S. Ferreira, C. Fernandes, G. C. Silva, N. M. F. Carvalho, O. A. C. Antunes, V. Drago, A. J. Bortoluzzi, A. H. Jr., *J. Braz. Chem. Soc.* **2010**, *21*, 603–613, DOI: 10.1590/s0103-50532010000400004.
- [122] S. Tanase, C. Foltz, R. de Gelder, R. Hage, E. Bouwman, J. Reedijk, *J. Mol. Catal. A: Chem.* **2005**, *225*, 161–167, DOI: 10.1016/j.molcata.2004.09.002.

- [123] G. Cahiez, V. Habiak, C. Duplais, A. Moyeux, *Angew. Chem. Int. Ed.* **2007**, *46*, 4364–4366, DOI: 10.1002/anie.200700742.
- [124] W. Uhl, F. Hannemann, W. Saak, R. Wartchow, *Eur. J. Inorg. Chem.* **1998**, *1998*, 921–926, DOI: 10.1002/(SICI)1099-0682(199807)1998:7<921::AID-EJIC921>3.0.CO;2-5.
- [125] T. Darshani, T. K. Weldeghiorghis, F. R. Fronczek, T. Perera, *J. Mol. Struct.* **2020**, *1216*, 128310, DOI: 10.1016/j.molstruc.2020.128310.
- [126] D. L. Ankers, J. C. Fanning, *Polyhedron* **2001**, *20*, 623–625, DOI: 10.1016/s0277-5387(00)00662-8.
- [127] D. Awasabisah, G. B. Richter-Addo, *NO<sub>x</sub> Related Chemistry*, J. A. O. Rudi van Eldik (Ed.), Elsevier, **2015**, chapter NO<sub>x</sub> Linkage Isomerization in Metal Complexes, pp. 1–86.
- [128] J. C. Fanning, *Coord. Chem. Rev.* **1991**, *110*, 235–273, DOI: 10.1016/0010-8545(91)80007-Z.
- [129] J. W. Pyrz, A. L. Roe, L. J. Stern, L. Que, *J. Am. Chem. Soc.* **1985**, *107*, 614–620, DOI: 10.1021/ja00289a013.
- [130] B. Weber, *Koordinationschemie: Grundlagen und aktuelle Trends*, Springer, Berlin, Heidelberg, **2014**.
- [131] A. K. Patra, R. K. Afshar, J. M. Rowland, M. M. Olmstead, P. K. Mascharak, *Angew. Chem. Int. Ed.* **2003**, *115*, 4655–4659, DOI: 10.1002/ange.200352070.
- [132] R. K. Afshar, A. A. Eroy-Reveles, M. M. Olmstead, P. K. Mascharak, *Inorg. Chem.* **2006**, *45*, 10347–10354, DOI: 10.1021/ic0614115.
- [133] A. L. Feig, M. T. Bautista, S. J. Lippard, *Inorg. Chem.* **1996**, *35*, 6892–6898, DOI: 10.1021/ic960552b.
- [134] O. Einsle, A. Messerschmidt, R. Huber, P. M. H. Kroneck, F. Neese, *J. Am. Chem. Soc.* **2002**, *124*, 11737–11745, DOI: 10.1021/ja0206487.
- [135] C. Hauser, T. Glaser, E. Bill, T. Weyhermüller, K. Wieghardt, *J. Am. Chem. Soc.* **2000**, *122*, 4352–4365, DOI: 10.1021/ja994161i.
- [136] C. Kupper, J. A. Rees, S. Dechert, S. DeBeer, F. Meyer, *J. Am. Chem. Soc.* **2016**, *138*, 7888–7898, DOI: 10.1021/jacs.6b00584.
- [137] D. Schweitzer, J. J. Ellison, S. C. Shoner, S. Lovell, J. A. Kovacs, *J. Am. Chem. Soc.* **1998**, *120*, 10996–10997, DOI: 10.1021/ja981117e.
- [138] S. Chatel, A.-S. Chauvin, J.-P. Tuchagues, P. Leduc, E. Bill, J.-C. Chottard, D. Mansuy, I. Artaud, *Inorg. Chim. Acta* **2002**, *336*, 19–28, DOI: 10.1016/s0020-1693(02)00818-6.

- [139] A. Dey, A. M. Confer, A. C. Vilbert, P. Moënne-Loccoz, K. M. Lancaster, D. P. Goldberg, *Angew. Chem. Int. Ed.* **2018**, *57*, 13465–13469, DOI: 10.1002/anie.201806146.
- [140] M. Wolf, Ph.D. thesis, Ludwig-Maximilians-Universität München, **2016**.
- [141] B. M. Aas, Ph.D. thesis, Ludwig-Maximilians-Universität München, **2018**.
- [142] A. Majumdar, S. J. Lippard, *Inorg. Chem.* **2013**, *52*, 13292–13294, DOI: 10.1021/ic4019508.
- [143] M. G. Finnegan, A. G. Lappin, W. R. Scheidt, *Inorg. Chem.* **1990**, *29*, 181–185, DOI: 10.1021/ic00327a008.
- [144] M. Januszczuk, J. Janicki, H. Wojakowska, R. Krzyminiewski, J. Pietrzak, *Inorg. Chim. Acta* **1991**, *186*, 27–31, DOI: 10.1016/s0020-1693(00)87926-8.
- [145] F. Lissel, F. Schwarz, O. Blacque, H. Riel, E. Lörtscher, K. Venkatesan, H. Berke, *J. Am. Chem. Soc.* **2014**, *136*, 14560–14569, DOI: 10.1021/ja507672g.
- [146] T. D. Harris, T. A. Betley, *J. Am. Chem. Soc.* **2011**, *133*, 13852–13855, DOI: 10.1021/ja2052655.
- [147] O. A. Ileperuma, R. D. Feltham, *Inorg. Chem.* **1977**, *16*, 1876–1883, DOI: 10.1021/ic50174a011.
- [148] B. C. Sanders, S. M. Hassan, T. C. Harrop, *J. Am. Chem. Soc.* **2014**, *136*, 10230–10233, DOI: 10.1021/ja505236x.
- [149] T. Woike, U. Himmelreich, H. Henke, H. Bärnighausen, *Z. Kristallogr.* **2002**, *217*, 119–126, DOI: 10.1524/zkri.217.3.119.20648.
- [150] B. Weber, I. Käßlinger, H. Görls, E.-G. Jäger, *Eur. J. Inorg. Chem.* **2005**, *2005*, 2794–2811, DOI: 10.1002/ejic.200400759.
- [151] A. K. Patra, M. J. Rose, M. M. Olmstead, P. K. Mascharak, *J. Am. Chem. Soc.* **2004**, *126*, 4780–4781, DOI: 10.1021/ja040015n.
- [152] M. J. Rose, A. K. Patra, M. M. Olmstead, P. K. Mascharak, *Inorg. Chim. Acta* **2010**, *363*, 2715–2719, DOI: 10.1016/j.ica.2010.04.023.
- [153] F.-T. Tsai, T.-S. Kuo, W.-F. Liaw, *J. Am. Chem. Soc.* **2009**, *131*, 3426–3427, DOI: 10.1021/ja808743g.
- [154] A. M. Tondreau, J. M. Boncella, *Polyhedron* **2016**, *116*, 96–104, DOI: 10.1016/j.poly.2016.04.007.
- [155] M. A. Andrews, T. C. T. Chang, C. W. F. Cheng, T. J. Emge, K. P. Kelly, T. F. Koetzle, *J. Am. Chem. Soc.* **1984**, *106*, 5913–5920, DOI: 10.1021/ja00332a027.
- [156] F. Xie, Z. Qi, X. Li, *Angew. Chem. Int. Ed.* **2013**, *52*, 11862–11866, DOI: 10.1002/anie.201305902.

- [157] Y. Kashiwame, M. Watanabe, K. Araki, S. Kuwata, T. Ikariya, *Bull. Chem. Soc. Jpn.* **2011**, *84*, 251–258, DOI: 10.1246/bcsj.20100331.
- [158] I. Bernal, J. Cetrullo, J. Cai, R. A. Geanangel, J. H. Worrell, *J. Chem. Soc., Dalton Trans.* **1995**, 99–104, DOI: 10.1039/dt9950000099.
- [159] R. D. Shannon, *Acta Cryst. A* **1976**, *32*, 751–767, DOI: 10.1107/s0567739476001551.
- [160] J. Pouessel, P. Thuéry, J.-C. Berthet, T. Cantat, *Dalton Trans.* **2014**, *43*, 4415–4425, DOI: 10.1039/c3dt52703d.
- [161] B. Alič, A. Štefančič, G. Tavčar, *Dalton Trans.* **2017**, *46*, 3338–3346, DOI: 10.1039/C6DT04909E.
- [162] V. Kavun, A. Udovenko, A. Slobodyuk, N. Makarenko, E. Kovaleva, L. Zemnukhova, *J. Fluorine Chem.* **2019**, *217*, 50–57, DOI: 10.1016/j.jfluchem.2018.11.004.
- [163] M. Head-Gordon, J. A. Pople, M. J. Frisch, *Chem. Phys. Lett.* **1988**, *153*, 503–506, DOI: 10.1016/0009-2614(88)85250-3.
- [164] A. In-Iam, M. Wolf, C. Wilfer, D. Schaniel, T. Woike, P. Klüfers, *Chem. Eur. J.* **2018**, *25*, 1304–1325, DOI: 10.1002/chem.201804565.
- [165] A. A. Raheem, M. Wilke, M. Borgwardt, N. Engel, S. I. Bokarev, G. Grell, S. G. Aziz, O. Kühn, I. Y. Kiyani, C. Merschjann, E. F. Aziz, *Struct. Dyn.* **2017**, *4*, 044031, DOI: 10.1063/1.4990567.
- [166] B. Delley, *Z. Kristallogr. Cryst. Mater.* **2008**, *223*, 329–333, DOI: 10.1524/zkri.2008.0032.
- [167] T. Kerscher, Ph.D. thesis, Ludwig-Maximilians-Universität München, **2010**, DOI: 10.5282/edoc.12085.
- [168] J. T. Muya, H. Chung, S. U. Lee, *RSC Advances* **2018**, *8*, 3328–3342, DOI: 10.1039/c7ra11603a.
- [169] S. A. Cotton, *Comments Inorg. Chem.* **1999**, *21*, 165–173, DOI: 10.1080/02603599908020421.
- [170] K. J. Fisher, *Comprehensive coordination chemistry II: from biology to nanotechnology*, Vol. 35, J. A. McCleverty, T. Meyer (Eds.), Elsevier Pergamon, **2004**, chapter Scandium and Yttrium, pp. 1–29.
- [171] S. A. Cotton, *Encyclopedia of Inorganic Chemistry 2nd ed.*, R. B. King, R. H. Crabtree, C. M. Lukehart, D. A. Atwood, R. Scott (Eds.), John Wiley & Sons, Ltd, Hoboken, New Jersey, United States, **2006**, chapter Scandium, Yttrium & the Lanthanides: Inorganic & Coordination Chemistry, pp. 1–38, DOI: 10.1002/0470862106.ia211.
- [172] J. Lee, A. Y. Kovalevsky, I. V. Novozhilova, K. A. Bagley, P. Coppens, G. B. Richter-Addo, *J. Am. Chem. Soc.* **2004**, *126*, 7180–7181, DOI: 10.1021/ja0488986.

- [173] I. V. Novozhilova, P. Coppens, J. Lee, G. B. Richter-Addo, K. A. Bagley, *J. Am. Chem. Soc.* **2006**, *128*, 2093–2104, DOI: 10.1021/ja0567891.
- [174] N. Xu, J. Yi, G. B. Richter-Addo, *Inorg. Chem.* **2010**, *49*, 6253–6266, DOI: 10.1021/ic902423v.
- [175] D. Schaniel, E.-E. Bendeif, T. Woike, H.-C. Böttcher, S. Pillet, *CrystEngComm* **2018**, *20*, 7100–7108, DOI: 10.1039/C8CE01345D.
- [176] T. S. Kurtikyan, A. A. Hovhannisyanyan, G. M. Gulyan, P. C. Ford, *Inorg. Chem.* **2007**, *46*, 7024–7031, DOI: 10.1021/ic700846x.
- [177] Sigma-Aldrich, Ascarite II Adsorbents, <https://www.sigmaaldrich.com/DE/de/-product/aldrich/223921> **2021**, (access: 08.09.2021).
- [178] P. G. Potvin, M. Knapp, U. Jordis, *JASPER v2.0*, <https://www.yorku.ca/pgpotvin/public/Jasper/jasper2.htm> **2021**, (access: 08.09.2021).
- [179] W. Kopycki, J. Binkowski, *Microchim. Acta* **1984**, *84*, 149–157, DOI: 10.1007/BF01204166.
- [180] JASCO Corporation, *Spectra Manager 2.07.00*, **2002–2008**.
- [181] Mestrelab Research S.L., *MestReNova 12.0.0-20080*, **2017**.
- [182] G. M. Sheldrick, *Acta Cryst. A* **2008**, *64*, 112–122, DOI: 10.1107/s0108767307043930.
- [183] A. L. Spek, *Acta Cryst. D* **2009**, *65*, 148–155, DOI: 10.1107/S0907444490804362X.
- [184] C. B. Hübschle, G. M. Sheldrick, B. Dittrich, *J. Appl. Crystallogr.* **2011**, *44*, 1281–1284, DOI: 10.1107/S0021889811043202.
- [185] L. J. Farrugia, *J. Appl. Crystallogr.* **2012**, *45*, 849–854, DOI: 10.1107/s0021889812029111.
- [186] C. F. Macrae, P. R. Edgington, P. McCabe, E. Pidcock, G. P. Shields, R. Taylor, M. Towler, J. van de Streek, *J. Appl. Crystallogr.* **2006**, *39*, 453–457, DOI: 10.1107/S002188980600731X.
- [187] Persistence of Vision Pty. Ltd., *Persistence of Vision Raytracer (Version 3.7)*, Williamstown, VIC, AUS, **1991–2013**.
- [188] F. Neese, *WIREs Comput. Mol. Sci.* **2018**, *8:e1327*, DOI: 10.1002/wcms.1327.
- [189] J. P. Perdew, *Phys. Rev. B* **1986**, *33*, 8822–8824, DOI: 10.1103/physrevb.33.8822.
- [190] A. D. Becke, *Phys. Rev. A* **1988**, *38*, 3098–3100, DOI: 10.1103/physreva.38.3098.
- [191] J. Tao, J. P. Perdew, V. N. Staroverov, G. E. Scuseria, *Phys. Rev. Lett.* **2003**, *91*, 346–354, DOI: 10.1103/physrevlett.91.146401.

- [192] J. P. Perdew, Y. Wang, *Phys. Rev. B* **1992**, *45*, 13244–13249, DOI: 10.1103/physrevb.45.13244.
- [193] V. N. Staroverov, G. E. Scuseria, J. Tao, J. P. Perdew, *J. Chem. Phys.* **2003**, *119*, 12129–12137, DOI: 10.1063/1.1626543.
- [194] F. Weigend, R. Ahlrichs, *Phys. Chem. Chem. Phys.* **2005**, *7*, 3297–3305, DOI: 10.1039/b508541a.
- [195] K. Eichkorn, F. Weigend, O. Treutler, R. Ahlrichs, *Theor. Chem. Acc.* **1997**, *97*, 119–124, DOI: 10.1007/s002140050244.
- [196] F. Weigend, *Phys. Chem. Chem. Phys.* **2006**, *8*, 1057–1065, DOI: 10.1039/b515623h.
- [197] O. Treutler, R. Ahlrichs, *J. Chem. Phys.* **1995**, *102*, 346–354, DOI: 10.1063/1.469408.
- [198] M. Sierka, A. Hogekamp, R. Ahlrichs, *J. Chem. Phys.* **2003**, *118*, 9136–9148, DOI: 10.1063/1.1567253.
- [199] S. Grimme, J. Antony, S. Ehrlich, H. Krieg, *J. Chem. Phys.* **2010**, *132*, 154104, DOI: 10.1063/1.1567253.
- [200] V. Barone, M. Cossi, *J. Phys. Chem. A* **1998**, *102*, 1995–2001, DOI: 10.1021/jp9716997.
- [201] G. A. Andrienko, *Chemcraft - Graphical Program for Visualization of Quantum Chemistry Computations*, **2021**.
- [202] M. D. Hanwell, D. E. Curtis, D. C. Lonie, T. Vandermeersch, E. Zurek, G. R. Hutchison, *J. Cheminf.* **2012**, *4*, 1–17, DOI: 10.1186/1758-2946-4-17.

# Danksagung

An erster Stelle danke ich meinem Doktorvater Prof. Dr. Peter Klüfers für die freundliche Aufnahme in seinen Arbeitskreis, die guten Arbeitsbedingungen, den großen wissenschaftlichen Freiraum und seine hilfsbereite Art.

Prof. Dr. Hans-Christian Böttcher danke ich für das Erstellen des Zweitgutachtens, seine generell herzliche und offene Art und den guten Rote-Bete-Salat. Besonders danke ich ihm für die Chance mit ihm zusammen zu forschen, publizieren und mein Wissen über Metallcluster auszubauen.

Für das Mitwirken in der Promotionskommission danke ich Prof. Dr. Andreas Kornath, Prof. Dr. Oliver Trapp, Prof. Dr. Wolfgang Schnick und Prof. Dr. Thomas M. Klapötke.

Lida Holowatyj-den Toom danke ich für die erstklassige Organisation, ihre hilfsbereite, besonnene Art und die sprachliche Korrektur meiner Arbeit.

Christine Neumann danke ich für ihr unvergleichbares Labormanagement, die langen Gespräche über Gott, die Welt und Little Britain, die guten Tipps und die lustige Arbeitsatmosphäre.

Viel Dank geht auch Dr. Peter Mayer, dafür dass er mich in die Praxis der Einkristalldiffraktometrie eingelernt hat und immer hilfsbereit war, falls es mal Probleme mit Zwillingen und Fehlordnungen gab.

Dem Analytikteam der Fakultät danke ich für die gewissenhafte Bearbeitung meiner Proben.

Prof. Dr. Dominik Schaniel von der Université de Lorraine danke ich für die PLI Messungen meiner Substanzen.

Zudem danke ich meinem Laborkollegen Dr. Georg Monsch für die schönen gemeinsamen  $\text{km h}^{-1}$  und die unzähligen wertvollen Tipps am Anfang meiner Masterarbeit.

Daniel Schröder, Torsten Ampßler und Jens Popp danke ich für das Korrigieren dieser Arbeit und dafür, dass wir als der "Rest" des AK Klüfers noch so eine schöne Zeit verbringen konnten. Shorty danke ich hierbei besonders für die viele Hilfe bei computer-chemischen Angelegenheiten. Thorsten und Jans danke ich außerdem für den entspannten Laboralltag, die Memes, die unzähligen Feierabendbiere und das Wo-Ist-Ronny Spiel.

Allen Doktoranden und Ehemaligen des AK Klüfers danke ich dafür, dass sie meine Promotion durch die vielen lustigen Abende, Feiern, AK-Hütten und Kaffeeküchengespräche zu einer unvergesslichen Zeit gemacht haben. Namentlich zu nennen sind dabei vor allem Dr. Areenan In-Iam, Helen und Dr. Markus Funk, Dr. Tobias Mayer, Tobias Riggemann Sezen Hollweck, Luca Theresa Rieder sowie Dr. Bianca Aas. Ein besonderer Dank geht dabei an Dr. Oliver Richter und Dr. Sebastian Brück, die dafür gesorgt haben, dass ich mich ab dem Beginn meiner Masterarbeit sofort im Arbeitskreis wohlfühlt habe.

Sophie Gutenthaler danke ich für die vielen spannenden fachlichen und außerfachlichen Diskussionen, motivierenden Gespräche und Katzenbilder.

Auch ein herzliches Dankeschön geht an die Mitglieder des AK Ivanović-Burmazović mit denen gerade am Ende meiner Promotionszeit noch ein paar lustige Abende möglich waren. Dank geht auch an Annette Rogge für die freundliche Hilfe bei organisatorischen Dingen bezüglich meiner Prüfung.

Ich danke außerdem meinen Praktikanten, die mich während den letzten drei Jahren bei meiner Forschung unterstützt haben. Allen voran Carla Hofer und Sonja Wiens, die durch ihren Fleiß und gewissenhafte Arbeitsweise meine Ergebnisse sehr aufgewertet haben.

Meinen Kommilitonen Christoph Seifert, Florian Binder, Sebastian Steiner und Thomas Juli danke ich für die wirklich schöne Studienzeit. Natürlich geht mein Dank auch an Lorenz Wollring, der nach all den Jahren noch immer ein gudder boy ist.

Allen meinen Freunden danke ich dafür, dass sie den Ausgleich zu meinem Arbeitsalltag dargestellt haben. Allen voran danke ich dabei Franzy, Christoph, Christian, Bibi, Timo, Daniel und Johannes. Natürlich danke auch jenen, die sich hier angesprochen fühlen und nicht namentlich erwähnt sind.

Melanie danke ich dafür, dass sie trotz meiner doch sehr anstrengenden Arbeitseinstellung zu mir gehalten und mich immer moralisch unterstützt hat.

Zuletzt danke ich noch meiner Familie – vor allem meinen Eltern, Beate und Helge Heine-  
mann – für die unentwegte Unterstützung, Motivation und dafür, dass sie mir das Studium erst möglich haben.